ORGANIC GEOCHEMICAL INVESTIGATION OF SEDIMENTS IN THE JAPAN SEA: TRACKING PALEOCEANOGRAPHIC AND PALEOCLIMATIC CHANGES SINCE THE MID-MIOCENE

by

Frederike Wittkopp

A thesis submitted to the University of Birmingham for the degree of

DOCTOR OF PHILOSOPHY

School of Geography. Earth and Environmental Sciences

College of Life and Environmental Sciences

University of Birmingham

March 2017

Wir sind nicht der erste Organismus, der die Atmosphäre verändert, aber wir sind der erste Organismus, der über die Konsequenzen seines Handelns nachdenken kann.

–Dr. Thomas Reiter - ESA Koordinator Internationale Agenturen

We are not the first organism to change the atmosphere, but we are the first organism that is able to understand the consequences of its actions.

–Dr. Thomas Reiter - ESA Interagency Coordinator

Everything not saved will be lost.

–Nintendo 'Quit Screen' message

Abstract

The mid- to late Miocene marks one of the last warm periods of the Neogene, before the descent in to the ice house climate of the late Pliocene and Pleistocene. The mid- to late Miocene climate was long overlooked, but receives increasingly more interest. Previously, this part of the Miocene was considered to be a period of sustained warmth on land, and warm sea surface temperatures, but with an atmosphere low in CO_2. This notion is now slowly changing. Increasing evidence shows that pCO_2 in the late Miocene might have been higher than previously thought. This makes the mid- to late Miocene a key interval for the investigation of the link between changing atmospheric CO_2 levels and global climate.

Existing studies have shown that the Japan Sea is particularly sensitive to glacio-eustatic sea level change, and it is suspected that this marginal sea is very sensitive to other global climate changes. Furthermore, the Japan Sea lies downwards of the westerly jet, and therefore receives a considerable dust flux derived from the central Asian interior. During the late Miocene, the uplift of the Himalaya-Tibetan-Plateau (HTP) is thought to have triggered the onset

of the modern Asian monsoon system. The uplift was also thought to have triggered the onset of C_4 plant expansion during the late Miocene (from 8 Ma onwards), leading to the enhanced cooling and aridification of central Asia. Additionally, enhanced HTP uplift from 3.6 Ma to Present is suspected to have forced the westerly jet to flow in two discrete modes, affecting the monsoon intensity on a millennial scale. Sediments derived from the Japan Sea thus are suitable to reconstruct these vegetation and climate changes in the central Asian interior, associated with the HTP uplift. Furthermore, these sediments can also be used to reconstruct the impact of climate change on the East Asian monsoon.

Bulk sedimentary parameters, terrestrial *n*-alkanes, hopanoids, alkenones, and branched and isoprenoidal glycerol dialkyl glycerol tetraether from a sediment core from the Japan Sea were analyzed with an average resolution of 120 kyr. The studied interval spans the last 10 million years, with some exceptions even spanning the last 18 Ma. The investigated compounds were used to compile biomarker-based records of terrestrial and marine environmental changes since the mid-Miocene. Sea surface temperature (SST) reconstructions, using unsaturation index of C_{37}-ketones ($U^{K'}_{37}$) and tetraether index of tetraethers consisting of 86 carbons (TEX_{86}), show a distinctive cooling trend of up to 10 °C since the mid-Miocene. The good agreement between the SST record from the Japan Sea, and proxy records from the northern Pacific and the $\delta^{18}O$ global stack of benthic foraminifera indicates that the Japanese Sea cooled in response to the global descent into today's ice house climate. Both

SST reconstructions record the late Miocene cooling quite well. The observed climate deterioration was likely driven by globally operating climate mechanisms, most likely decreasing atmospheric CO_2 concentrations. During the Pleistocene, repeated opening and closure of the Tsugaru Strait restricted the inflow of the Tsushima Warm Current and a concomitant expansion of cold waters from the northern Japan Sea led to extreme SST variations.

The Japan Sea does record the onset of the Asian monsoon system, and the late Miocene C_4 plant expansion in the central Asian interior. A strong summer monsoon, indicated by the δD signature of *n*-alkanes, persisted with interruptions from 3 Ma to 5 Ma. In correspondence to the enhanced HTP uplift at around 3.6 Ma, the source area of *n*-alkanes begins to vary between Siberia and the continental Asian margin, it is hypothesized that this fluctuation occurs in sync with the switch between glacial and interglacial cycles. The fluctuation is detectable in the carbon and deuterium isotopic signature of terrestrial *n*-alkanes.

Mixing models were applied to reconstruct the influx of terrestrial organic matter into the Japan Sea over time. The four mixing models give contrasting results, also because the terrestrial end member of each mixing model cannot be constrained for the Japan Sea. It was therefore impossible to reconstruct the variable influx of terrestrial organic matter under changing environmental and climatic conditions. Biomarkers for anoxic depositional environments, such as the lycopane/nC_{31} ratio or the presence of 28,30-Dinorhopane agree with the record of redox sensitive minerals.

Atmospheric pCO_2 reconstructions based on alkenone $\delta^{13}C$ values show a substantial pCO_2 decline from 8 Ma to 6 Ma, from >500 to around 300 µatm. This is the required range for C_4 plants to become competitive over C_3 plants. Furthermore, the decline in pCO_2 matches the onset of C_4 plant expansion across Asia, as indicated by the ^{13}C signature of terrestrial *n*-alkanes. It also falls into the time where other studies indicate CO_2 limitation in large coccolithophores, suggesting that a critical threshold of <500 µatm of CO_2 in the atmosphere was reached. It is suggested that good temperature control and well constrained $\delta^{13}C$ record of benthic foraminfera improve late Miocene atmospheric CO_2 reconstructions, which was not the case for previous alkenone paleobarometry studies spanning this interval.

Acknowledgments

I am most grateful to my supervisor, **Dr. Tom Dunkley Jones**. It is safe to say that there would be no dissertation without you, and some of the astonishing results found in this dissertation would have remained buried at IODP Site U1425. Thank you for sticking with me and helping me through the very difficult times. Then, I want to thank **Dr. Heiko Moossen** (MPI-BGC) for 'midwifing' this thesis, and for his reassurance and inexhaustible patience when going through my drafts, especially in times when I lacked it. Which was pretty much all the time. Not less important to this thesis was the contribution of **Dr. James Bendle** and **Dr. Andrew C.G. Henderson**. I want to acknowledge both for setting up the topic, and for discussion and advice during writing up the thesis and SST paper.

GDGTs are one important building block, not only of Archaea, but also of this thesis, and I want to thank **Dr. Masanobu YAMAMOTO** for providing valuable instrument time and money to measure them at the University of Hokkaido, Sapporo. I want to thank Dr. Yamamoto for his hospitality during my stay in Japan, and for taking a lot of time to discuss the results. I also want

to thank **Dr. Osamu SEKI**, and **Dr. Tomohisa IRINO** for their contribution to the discussion, and advice on the age model, as well as isotope measurements. This thesis has benefited tremendously from their input. Furthermore, I would like to acknowledge the **Great Britain Sasakawa Foundation**, Grant-No. GBSF4603 was gratefully received and used to travel to Japan. Bulk sediment parameters were measured at the Max-Planck-Institute for Biogeochemistry (MPI-BGC) in Jena, Germany. I want to thank **Ines Hilke** and Heiko Moossen and their staff for analyzing the samples for me.

Whilst mass spectra of *n*-alkanes and ketones are straight forward to read, the identification of triterpenoids and the implications of their presence were a different story. I therefore want to specifically acknowledge **Prof. Jan Schwarzbauer** (RWTH Aachen University), **Prof. Jaap Sinnighe Damsté** (Royal NIOZ), and **Hans-Peter Nytoft** (GEUS Denmark) for their prompt and extensive responses to my queries, as well as their advice and discussion on structure identification. I also want to thank **Dr. Marcel van der Meer** (Royal NIOZ) for advice on the protocol modifications for alkenone separation using silver nitrate silica gel columns. **Dr. Ken Peters** is thanked for the Biomarker Guide Vol. 2 he gave me during my first Gordon's Research Conference. I have referred to it a lot, and I am glad I have it stacked on my shelf.

I also want to thank the two men who prepared me very well for this thesis experience, **Prof. Stefan Schouten** (Royal NIOZ) and **Prof. Jack Middelburg** (Utrecht University). I have really benefited from your outstanding mentoring and supervision skills. I am also very grateful that you gave me the opportu-

nity to network with other young scientists, even though I was 'just' a M.Sc. student.

I am also very grateful to **my family** and **Heiko** for their love and support over these straining 3.5 years, and for never asking when I'll be finished or what the hell I am going to do with this degree. I want to apologize to my friends at home and abroad for neglecting them, things will now change for the better. Shout out to my colleagues at the University of Birmingham for all the entertaining lunch and coffe breaks and good laugh at the pub. I am very grateful to have met **Ulrike** Baranowski, **Alan** Hastie, **Gaël** Lymer, **Carlos** D'Apolito, **Rodrigo** Neregato, **Simiao** Sun, **Plamen** Andreev, **Joanne** Murray, **Murray** Hogget, and **Gary** Clarke. The food was always plenty, and the nights were long, and the laughter never ending. These were great moments I will always look back to. A special mention also for **Andy** Rees, teaching me the fine arts of ranting. A special thank you also goes out to **Richard** and **Christine Butler**, for the lovely dinners at their fab p(a)lace, and for inspiring us to buy a black Weber BBQ monster, as well as introducing me to the only pub in Birmingham serving my beloved Bitburger. None of the parties mentioned here received money for this surreptitious advertising. I also want to thank **Bethany Chamberlain**, **Carrie Walker**, and **Dr. Helen MacKay** - you were fantastic fume hood buddies and my work would have been quite boring without you. **Dr. Ian Boomer**, **Prof. Tim Reston**, and **Dr. James Wheeley** are thanked for dragging me out of the lab into the field every now and then, and giving me a much needed break. Also, I do not think it is a secret how

much I have enjoyed the caravan inspections. I want to say thank you to **Gretchel Coldicott**, **Aruna Mistry** and **Sara Kinahan** for their kind and encouraging words, and open ears when I needed them. Last but not least, I want to thank the **MPI BGC 'Mahlzeit' crew**, Heike, Michael, Birgit, Ines, Sonja, Jürgen and Willi, for keeping me socialized when I was deep down in the writing progress. **Linda** and **Kirsten** are thanked for letting me use the MPI-CE/BGC library facilities.

Acronyms

ACL average chain length

amoA ammonia monooxygenase

BIT branched index of tetraethers

BHP Bacteriohopanepolyol

CBT cyclization of branched tetraethers

CLP Chinese Loess Plateau

CoA Coenzyme A

CRB Columbia River Basalt

DCM Dichloromethane

DIC dissolved inorganic carbon

DOXP 1-deoxyxylulose 5-phosphate

EASM East Asian summer monsoon

EAWM East Asian winter monsoon

ECS East China Sea

ECSCW East China Sea Coastal Water

FID Flame Ionization Detector

GC gas chromatography

GC-MS gas chromatography-mass spectrometry

brGDGT branched Glycerol Dialkyl Glycerol Tetraether

iGDGT isoprenoidal Glycerol Dialkyl Glycerol Tetraether

GGGP geranylgeranylglyceryl phosphate

GHGs Greenhouse gases

HPLC-MS high-pressure liquid chromatography/mass spectrometry

HTP Himalaya-Tibetan-Plateau

IODP International Ocean Discovery Program

IPP Isopentyl diphosphate

ITCZ Inner Tropical Convergence Zone

JSPW Japan Sea Proper Water

LMC late Miocene cooling

MAR mass accumulation rate

MAT mean annual air temperature

MBT methylation of branched tetraethers

MeOH Methanol

MEP methylerythritol-pathway

MI Methane Index

MMCO mid-Miocene Climate Optimum

MMCT mid-Miocene Climate Transition

m-PWP mid-Pliocene Warm Period

MVA mevalonate

NADP-ME nicotineamide adenine dinucleotide phosphate-malic enzyme

NAD-ME nicotineamide adenine dinucleotide

ODP Ocean Drilling Program

OEP odd-over-even predominance

OM organic matter

OMZ oxygen minimum zone

PCK PEP carboxykinase

POC particulate organic carbon

psu practical salinity units

RI Ring Index

Rubisco ribulose 1,5-biphosphate carboxylase/oxygenase

SCS South China Sea

SIM selective ion mode

SSS sea surface salinity

SST sea surface temperature

TEX_{86} tetraether index of tetraethers consisting of 86 carbons

TLE total lipid extract

TOC total organic carbon

TWC Tsushima Warm Current

$U^{K'}_{37}$ unsaturation index of C_{37}-ketones

VPDB Vienna Pee Dee Belemnite

WJ westerly jet

Contents

List of Figures

List of Tables

1. Introduction and Outline

The data derived for this PhD project stems from sediment cores retrieved during International Ocean Discovery Program (IODP) Expedition 346 and Ocean Drilling Program (ODP) leg 127/128. The main motivation of Expedition 346 was to understand the evolution of the Asian monsoon in response to the Himalaya-Tibetan-Plateau (HTP) uplift, which is poorly understood (Tada et al. 2016). This is mostly due to the lack of marine sediment cores available for paleoenvironmental studies on this issue. Thus, IODP Expedition 346 marked the beginning of a series of IODP expeditions around SE-Asia, in an attempt to understand the evolution of the Asian monsoon system and its impact on the environment. The Japan Sea lies downwind of the westerly jet, and, additionally, is under the influence of the winter monsoon. On this basis, the Japan Sea is an ideal archive to study the Asian monsoon evolution. Subsequently, IODP Expedition 346 had two aims: to specify the onset timing and reconstruct the variability of the East Asian monsoon (summer monsoon, winter monsoon, and westerly jet), and to reconstruct their spatial pattern and interrelationship. Second, to reconstruct changes in surface- and deep-water

circulations in the Japan Sea, and examine their relationship to variation in the East Asian monsoon and glacio-eustatic sea level changes (Tada et al. 2013).

The Japan Sea is very unique in its juxtaposition with the worlds' largest continent, Eurasia, and its largest ocean, the Pacific. Furthermore, the Japan Sea is under the influence of one of the largest western boundary currents, the Kuroshio Current, as well as the worlds' largest cold air circulation - the Siberian High. Currently, the Japan Sea is considered to be a global warming hot spot, as it is warming twice as fast as the surrounding oceans and marginal seas (Rhein et al. 2013). This distinctive warming trend was related to the warming and expansion of western boundary currents as a result of the Hadley-Cell expansion (Wu et al. 2012; Yang et al. 2016). One branch of the Kuroshio Current enters the Japan Sea as the Tsushima Warm Current (TWC) via the Tsushima Strait. Furthermore, winter wind stress in the Japan Seas has decreased between 1960 and 1990, which results in reduced sensible heat loss and accelerated surface temperature increase (Gamo 1999; Yeh et al. 2010). Reduced wind speeds across the Japan Sea could be related to the decreasing strength of the East Asian winter monsoon (EAWM), which is modelled to weaken with increasing pCO_2 (Hori and Ueda 2006). As a result, the continent-sea-air interaction characterizing the Japan Sea is admittedly complex, but the Japan Sea could serve as potential archive of changes in these interactions. Extracting these archives could aid the understanding of changes for example in atmospheric circulation, or western boundary currents, which in turn also affect the global climate state (Wang and Chen 2014). The recon-

struction of atmospheric circulation pattern is subsequently one opportunity emerging from IODP Expedition 346. Since for the first time it is possible to generate long-term climate records, such as sea surface temperatures, the generation of such records will allow to assess the past hot-spot potential of the Japan Sea. This can be achieved by comparing the generated records to other records of the same kind, i.e. from the open Pacific. Current climate analogues for the modern global warming focus on the Pliocene, although it is now becoming clear that pCO_2 levels were lower in the Pliocene (Pagani et al. 2010; Seki et al. 2010; Badger et al. 2013b) than what we can expect for the future (Rhein et al. 2013; 900–1000ppm, IPCC scenario RCP8.5). Thus, the paleoenvironment of the mid-Miocene climate is becoming increasingly interesting to investigate. The mid-Miocene has long been overlooked, mostly because of controversial boundary conditions: sustained warmth, small ice sheets, and low atmospheric CO_2 (see section 1.1), and thus, climate records spanning the mid-Miocene to Present are sparse. Organic SST proxies spanning the mid Miocene to Present do not exist at all. Tada et al. (1999) considers the Japan Sea to show greater response to interhemispheric climatic perturbations, and its high sedimentation rate offers a much higher resolution, compared to open ocean sediments. Since marginal seas like the Japan Sea also receive a terrestrial sedimentary component, they are ideal places to study land-ocean-climate linkages (Tada et al. 1999). Therefore, sediment cores retrieved during Expedition 346 and leg 127/128 are ideal to study long-term climate trends, and increase our understanding of climatic evolution from the mid-Miocene to

Present.

1.1. Mid- and late Miocene climate change

Three important parameters are used to describe global climate conditions: surface temperatures, ice volume and atmospheric CO_2 content (pCO_2) (Foster et al. 2012). Since the 1970s, a growing volume of paleoclimate records have been compiled, mostly based on the stable isotopic compositions of marine carbonates ($\delta^{18}O$ and $\delta^{13}C$) (e.g. Shackleton and Opdyke 1973; Shackleton and Kennett 1976; Hays et al. 1976). Most notably, long-term records of the oxygen isotopic composition of deep-ocean benthic foraminifera have given an insight into global scale changes in ice volume and deep-water temperatures ($\delta^{18}O$). Likewise, changes in the global carbon cycle can be derived from the measurement of inorganic and organic $\delta^{13}C$ with the combination of both records giving an insight into transfers between both carbon pools. A detailed $\delta^{18}O$ record compiled by Zachos et al. (2001; 2008) reveals a 60 Ma cooling trend since the Cretaceous, but also short term climate perturbations in the Cenozoic. Such perturbations include the mid-Miocene Climate Optimum (MMCO) (17–15 Ma), mid-Miocene Climate Transition (MMCT) (~14.5 Ma), and millennial scale dynamics of Plio-Pleistocene ice sheet growth. The Miocene represents one of the last warm periods of the Neogene, before the development of a world with bipolar ice caps in the Plio-Pleistocene (Zachos et al. 2001). The Miocene is characterized by significant global climate variations,

in particular by the MMCO, with very warm sea surface temperatures (SSTs) and warm deep waters (Woodruff et al. 1981). The MMCO coincides with a small Antarctic ice sheet, increased pCO_2 (Foster et al. 2012), and also the main eruptive phase of the Columbia River Basalt (CRB) between 16.1 and 15 Ma (Hodell and Woodruff 1994; Kürschner et al. 2008; Foster et al. 2012). The injection of CO_2 into the atmosphere by the CRBs has led some authors to hypothesise that this injection prevented immediate cooling of the climate by counteracting the increased carbon removal at this time (Vincent and Berger 1985; Hodell and Woodruff 1994; Kender et al. 2009). McKay et al. (2014) successfully models the carbon cycle perturbation, and also adds in the factor of LIPs, their outgassing coinciding with episodes of cooling during MMCO (Mi-stages). As a result of this outgassing, the sustained warmth fostered the growth of subtropical rain forests in Western and Central Europe, as well as East Asia (Zachos et al. 2008; Hamon et al. 2011; Utescher et al. 2011; Pound et al. 2011). Evidence of sustained sea surface temperatures can be found in the Japan Sea and its surrounding area (Ogasawara 1994). The MMCO is then followed by the MMCT, at around 14.5 Ma when surface temperatures dropped substantially, and the Antarctic ice sheets started to grow again (Foster et al. 2012; Badger et al. 2013a). The cause for this ice sheet growth is presently unknown. The drastic cooling of the MMCT is also visible in the paleontological record of the Japan Sea (Ogasawara 1994). One favoured hypothesis is the draw down of pCO_2 due to the onset of silica weathering of the fresh basalt deposits, as well as increased organic carbon burial (Monterey

Hypothesis (Vincent and Berger 1985)). Uncertainties and limitations of multi site correlations of carbon isotopic excursion (CIE) events stem from the differences in onset timing, termination and magnitude of CIEs (Diester-Haass et al. 2006).

The late Miocene (12–5 Ma) remains equally enigmatic, as reconstructed CO_2 concentrations were low: 200–350 µatm (Pagani et al. 1999b) with the North Pole being nearly ice free (Zachos et al. 2001), and the continents were warmer than today (Micheels et al. 2011; Utescher et al. 2011; Pound et al. 2011). The late Miocene C_4 plant expansion (Cerling et al. 1997) also falls into this period of already low atmospheric CO_2 concentrations. Without the clear trigger of a major CO_2 decline, this expansion is thought to have another driver, such as the uplift of the Himalaya Plateau (Pagani et al. 1999b). Reconciling the sustained warmth of the late Miocene with the relatively low reconstructed atmospheric pCO_2 values has been problematic (Pagani et al. 1999a; LaRiviere et al. 2012). LaRiviere et al. (2012) suggested that cloud and water vapor feedbacks helped to sustain a warm climate. Furthermore, observed late Miocene perturbations in the terrestrial environment show no or limited corresponding signal within the deep-ocean $\delta^{18}O$ record (Zachos et al. 2001). A recent advance in deciphering the late Miocene climate is presented in a study by Herbert et al. (2016), who found substantial cooling of SSTs across both hemispheres at around 7 Ma. The authors suggest that surface ocean cooling is acting as a positive feedback mechanism for the CO_2 decline, due to the effect of temperature on the solubility of CO_2 in water. Subsequently, atmo-

spheric CO_2 concentrations descended from above 500 to around 350 µatm, a critical CO_2 level associated with C_4 plant expansion (Ehleringer et al. 1997; Herbert et al. 2016). As mentioned before, there is no direct proxy evidence for CO_2 suggesting such a drop, although the onset of size-specific carbon isotope fractionation in coccoliths at circa 7 Ma has been interpreted as a response to carbon dioxide limitation (Bolton and Stoll 2013). Interestingly, this size fractionation becomes very pronounced in the late Miocene, in sync with the C_4 plant expansion, and this is the first study to link changes in the marine and terrestrial environment as a global response to a carbon dioxide limitation (Bolton and Stoll 2013).

Due to the lack of good proxy data for MMCO atmospheric CO_2 levels and continuous SST records from the MMCO to Present (LaRiviere et al. 2012; Seki et al. 2012; Herbert et al. 2016), one of the aims of this thesis is the generation of a multi-proxy long-term SST record, to improve the understanding of late Miocene climate change. Compiling records of past vegetation change, and changes in the hydrological cycle will also contribute to the understanding of the late Miocene environment.

1.2. Outline of this thesis

Amongst contributing to the Expedition 346 outlines, this thesis aims at providing more insight into the paleoceanography of the Japan Sea for the last 17 million years and the impact of climate change on the marine and terrestrial

realm.

Chapter 4 describes the sea surface temperature change in the Japan Sea over the last 17 million years, using $U^{K'}_{37}$ and TEX_{86}, with a focus on the MMCO and the late Miocene cooling (LMC). As the Japan Sea opened up at the same time of the studied interval, it is the aim to disentangle the local (tectonic) signal from the global (climate) signal in order to understand the surface temperature evolution in the Japan Sea.

Changes in the $\delta^{13}C$ and δD signature of long-chain *n*-alkanes for the last 8 Ma are used to reconstruct the evolution of the Asian monsoon in relation to the Himalaya-Tibetan-Plateau (HTP) uplift. The changes in the compound specific isotopic signature will reveal changes in precipitation and vegetation in the central Asian source region. The combination of both stable isotopic signatures will reveal changes in the origin of *n*-alkanes in the Japan Sea. Furthermore, **Chapter 5** will describe the use of *n*-alkane δD signatures to indicate changes in the dominant moisture source for plants in the source region.

Chapter 6 discusses the efficacy of various mixing models for the reconstruction of terrestrial organic matter delivery to the Japan Sea. Furthermore, biomarker records of 28,30-Dinorhopane and the Lycopane/nC_{31} ratio were compared to records of redox sensitive minerals to evaluate their use as markers of anoxic depositional conditions.

Chapter 7 presents a pCO_2 record of the Japan Sea, based on the $\delta^{13}C$ signature of long-chain ketones, which are produced by haptophytes. Since they are thought to rely on the passive diffusion of CO_2 into their cell, they are

considered to record changes in pCO_2. The generated data in this chapter is used to understand the role of CO_2 as driving force of sea surface temperatures in the Japan Sea and vegetation change in central Asia.

1.3. The biomarker concept

Organic geochemistry employs aspects of chemistry, biology and geology to study the fate, constituents, and distribution of organic matter (OM) throughout Earth's history. Its application has shed light on energy sources of microbes, sources of fossil fuels, evolution of life on Earth and its climatic history (Bianchi and Canuel 2011). Because of its disciplinary overlap between biology, chemistry, geology and physics, the application of organic geochemistry is versatile and is applied to many pertinent questions in Geosciences, such as past atmospheric CO_2 levels or the effects and causes of past climate changes. In contrast to inorganic matter, sedimentary OM deposited on the ocean floor is generally not affected by the chemical and isotopic properties of sea water, or ice volume. Hence, they are very powerful tools to reconstruct past environments.

Two principal sources contribute organic matter to the marine environment: marine organic matter, and terrestrial organic carbon (OC_{terr}) which is transported by eolian and fluvial processes from the continents to the ocean (Hedges et al. 1997). Oceanic sediments integrate these two signals, enabling the study of past environmental changes in both realms. A third source of organic carbon

in marine sediments stems from prokaryotic organisms, such as cyanobacteria, heterotrophic, sulphate reducing and methane oxidising bacteria. However, their role in producing and processing organic matter in the marine carbon cycle is not well understood (Sinninghe Damsté and Schouten 1997; Eglinton and Repeta 2003). Evidence from their contribution to the sedimentary OM record stems from the presence of hopanoids (Ourisson and Albrecht 1992), but the proportion of their abundance is not necessarily a reflection of their input (Sinninghe Damsté and Schouten 1997). OM that escaped recycling in the surface layer of the water column or at the sediment surface and subsequently preserved in the geological record is subject to a variety of preservation factors. This OM is a mixture of marine algae, vascular plants and OM reworked from sedimentary rocks (Eglinton and Repeta 2003). The OM can be physically protected, by binding to an inorganic matrix such as opal, calcium carbonates, and detrital aluminosilicates (Hedges et al. 2001), smectites (Ransom et al. 1998) and therefore escapes remineralisation (Keil et al. 1994). Since the inorganic matrix makes up 80% of sinking particles in the ocean (Hedges et al. 2001), it acts as ballast and helps the OM to bypass the oxygenated water column and pore water quite rapidly before it is added to the anoxic parts of the sediment (Eglinton and Repeta 2003; and references therein). Another way of physical protection is the encapsulation of labile organic matter in more refractory polymers (Tegelaar et al. 1989). With regard to oxygen deficient or anoxic depositional environments, the precise controls of enhanced OM burial are still debated. By studying the organic matter content on the Washington

continental slope, Hedges et al. (1999) pointed out the importance of oxygen exposure time. The organic carbon to mineral surface area ratio decreased with increasing distance from the continental slope and increasing oxygen exposure time, indicating that the sedimentary OM responds to an 'oxic effect' (Hedges et al. 1999). Furthermore, anoxia slows down burrowing activities by benthic fauna (bioturbation), which otherwise aids oxidation of organic matter in the sediment (Hulthe et al. 1998), providing fidelity in its potential as archive for past environmental changes. The concept of selective preservation (Tegelaar et al. 1989) is often applied, where the preservation of OM does not fall into either of the above described criteria. The little OM that is being detected in sediments exposed to oxygen for prolonged times is considered to be refractory, and its structure might be inherent to its resistance towards degradation. The selective preservation of some compounds can best be studied in environments experiencing post depositional oxidation, i.e. Hoefs et al. (1998a), where these compounds comparatively enrich in the oxic layer of a turbidite. Selective preservation is particularly relevant when applying biomarker ratios, i.e. to assess the relative input of of one variable to another. Selective preservation can affect these ratios and subsequently lead to a biased interpretation. Another way of chemical protection is the formation of organosulfur compounds, which applies to OM deposited under anoxic and euxinic conditions. The OM reacts with sulfides, and can result in intramolecular or intermolecular incorporation of sulphur: the prior mechanism leads to the formation of cyclic organic sulphur compounds (Werne et al. 2000). The intermolecular incorpo-

ration of sulfur leads to the formation of macromolecules (Sinninghe Damsté et al. 1989), which due to their size become unavailable for the biogeochemical analysis, unless their bond is broken up prior to instrumental analysis. In terms of the geolgical and paleoceanographic evolution of the Japan Sea (Tada 1994), all three preservation factors could become important. A more detailed discussion will be conducted in the respective chapters where necessary.

The measurement of bulk OM properties of these sediments is fast and simple, as it does not require time intensive work-up of sediments. Bulk sedimentary parameters can already give information about the source of sedimentary OM and its respective changes over time via their $\delta^{13}C_{org}$ signature. On geological time scales, caution should be exercised with regard to changes in the ^{13}C signature. It should always be considered that the in-situ bacterial biomass caused the changes the $\delta^{13}C_{org}$ signature (Lehmann et al. 2002), by removing organic matter, and contributing their own biomass to the sedimentary record, which can be reflected in the ^{13}C signature (Sinninghe Damsté and Schouten 1997). As discussed above, selective preservation and physical protection of OM also governs its sequestration in marine sediments. Hence, the bulk composition of the OM is constantly modified (Harvey et al. 1995), with implications for the $\delta^{13}C_{org}$ record, as shown in incubation experiments by Lehmann et al. (2002): a continuous decrease in $\delta^{13}C_{org}$ was attributed to the selective preservation of compounds depleted in $\delta^{13}C$. The addition of compound specific isotopic analysis is usually recommended to further elucidate different sources in the sedimentary record (Bianchi and Canuel 2011).

Molecular indicators of environmental changes require sediment extraction and separation into different compound classes, but are more specific in their representation of particular organic matter sources and environments of production. Biomarker lipids are amongst these molecular indicators, and are unique compounds produced by specific organisms, serving as indicators for the presence of their producers. Biomarkers can retain their source information even after undergoing diagenesis over geological time scales (Bianchi and Canuel 2011). The presence of biomarker lipids are then used to make inferences about certain environmental conditions (Tab. 1.1). The largest contributors of OM to the ocean sedimentary record are phytoplankton. As primary producers, the phytoplankton are only dependent on light and nutrients, and can have a high net production in terms of reproduction and growth rate (Arrigo 2005). Fresh OM consists of proteins, carbohydrates, nucleic acids and lipids. The small part of OM escaping nutrient recycling in the surface layer, sinks down the water column whilst being subject to varying degrees of decomposition (Meyers 1997; and references therein). The amount of OM reaching the sea floor is dependent on the length of the water column and the primary production rate (Müller and Suess 1979). Once the OM is deposited on the sea floor, it is incorporated into the sediment. The first three compound groups (proteins, nucleic acids and carbohydrates) are easily degraded in the water column and in the sediment (Bianchi and Canuel 2011), while lipids remain relatively stable (Harvey et al. 1995). Diagenesis of organic matter in sediments occurs post burial, in geochemical terms it is the process that

affects the produced compounds during burial, at relatively low temperatures (60–100 °C) and low pressure (Killops and Killops 2005). Diagenesis occurs through processes such as defunctionalization, stereochemical alteration and aromatization, leading to the formation of more stable substances (Ourisson and Albrecht 1992; Koopmans et al. 1996), although some functional groups are able to survive diagenesis such as in fatty acids or ketones. Cranwell (1981) was able to establish the following order of stability to diagenesis: *n*-alkanes > alkenones > sterols > alcohols, with important effects on the information content of biomarker contained in the sedimentary archives (Sinninghe Damsté et al. 2002).

1.3.1. Terrestrial biomarkers

n-Alkanes

Higher land plant epicuticular waxes form a protective layer on leaves and stems (Eglinton and Hamilton 1967), preventing water loss due to evaporation (Jetter, R., Kunst, L. and Samuels 2006), and protecting plants from mechanical and biological damage (Eglinton and Hamilton 1967). Long-chain *n*-alkanes (nC$_{27}$-nC$_{35}$), alcohols and fatty acids (Bianchi and Bianchi 1990; Rommerskirchen et al. 2006) are main constituents of this wax layer. Plant *n*-alkane production leads to odd-over-even predominance (OEP) with one or two preferably produced *n*-alkanes (Eglinton and Hamilton 1967; Fig. 2.3). The OEP in *n*-alkanes is a result of enzymatic decarboxylation of fatty acids

Table 1.1.: Overview of biomarker lipids used in this study.

Compound	**Origin**	**Indication**	**Reference**
C_{28} bisnorhopane	Chemoautotrophs	anoxic-oxic interface	Moldowan et al. (1984)
C_{29-31} *n*-alkanes	Higher plants	Contributing plant	Eglinton and Hamilton (1967)
$\delta^{13}C$ C_{29-31} *n*-alkanes	Higher plants	Metabolism	Hayes (1993)
δD C_{29-31} *n*-alkanes	Higher plants	Precipitation	Sachse et al. (2006)
C_{37} alkenones	Haptophytes	Sea surface temperature	Brassell et al. (1986)
$\delta^{13}C$ C_{37} alkenones	Haptophytes	CO_2	Pagani et al. (1999a)
δD C_{37} alkenones	Haptophytes	Sea surface salinity	Schouten et al. (2006)
GDGTs	Thaumarcheota	Sea surface temperature	Schouten et al. (2002)
Lycopane/C_{31} *n*-alkane	Algae	Paleoxicity	Sinninghe Damsté et al. (2003)

which are mainly produced with even amounts of carbon in their chain. These *n*-alkanes are readily extractable from sediments, and the lack of functional groups makes them resistant to degradation. The average chain length (ACL) (Eq. 1.1) distribution of *n*-alkanes serves as proxy for aridity and/or air temperature (Rommerskirchen et al. 2003; Schefuß et al. 2003; Castañeda et al. 2009; Moossen et al. 2015). In Eq. 1.1, C_n is the peak area of the respective *n*-alkane *n*. Only the most frequent *n*-alkanes are used for the ACL calculation.

$$\mathrm{ACL} = \frac{(C_n \times n)}{\sum n} \tag{1.1}$$

n-Alkanes carry a wealth of information about plant community structure, as C_3 and C_4 plants fractionate CO_2 differently (Farquhar et al. 1989), with consequences for their carbon isotopic signature (Farquhar et al. 1989; Chikaraishi and Naraoka 2003; Sage 2004). Since C_4 plants generally have a competitive advantage over C_3 plants in low CO_2 environments (Sage 2004), the compound specific carbon isotope analysis of *n*-alkanes carries subsequent information about CO_2 levels in the past (Farquhar et al. 1989). While the isotopic composition of these lipids are readily available, the climatic implication in particular over geological time scales is more difficult to disentangle. The largest influence on the $^{13}C/^{12}C$ ratio of *n*-alkanes results from the metabolic pathway for CO_2 fixation (Farquhar et al. 1989; Fig. 1.1). The $\delta^{13}C$ signature of long-chain *n*-alkanes is used to differentiate between C_3 and C_4 vegetation, which gives clues about the ancient climate. Almost all trees, the majority

of grasses and shrubs utilize the C_3 (Benson-Calvin) pathway, in which CO_2 and ribulose 1,5-biphosphate carboxylase/oxygenase (Rubisco) are converted to 3-phosphoglycerate (therefore C_3-pathway) using the Rubisco enzyme. The Rubisco enzyme preferentially utilizes the lighter ^{12}C isotope-containing CO_2. This leaves C_3 plants more depleted (-28 ‰) than C_4 plants (Sage 2004). In the C_4 (Hatch-Slack) pathway, plants start with the conversion of CO_2 to oxaloacetate (consists of four carbon atoms, hence C_4 pathway) via PEP-carboxylase in the mesophyll cell (Fig. 1.1). Subsequently, the CO_2 is split off in the shear bundle cells using one of three enzymes (Sage 2004; nicotineamide adenine dinucleotide phosphate-malic enzyme (NADP-ME), nicotineamide adenine dinucleotide (NAD-ME), or PEP carboxykinase (PCK)). Then, the released CO_2 is fed into the Calvin cycle by Rubisco (Sage 2004). Plants utilizing the C_4 pathway are grasses, sedges, as well as dicots (Sage 2004). Since C_4 plants pre-concentrate CO_2, they have a competitive advantage in arid, hot and low CO_2 environments although the active uptake of CO_2 requires more energy. C_3 plants let CO_2 passively diffuse through their cell membranes, making them vulnerable to water loss in hot and arid environments. The difference in metabolic pathways leads to differential isotopic fractionation of CO_2, leaving C_4 plants about 16 ‰ more enriched in ^{13}C than C_3 plants (Collister et al. 1994; Chikaraishi and Naraoka 2003; Chikaraishi et al. 2004). Rubisco preferably fixes ^{12}C, while the PEP-carboxylase does not discriminate between the two carbon isotopes. The Rubisco fixation in the shear bundle of C_4 plants has little effect on the isotopic value. Since fatty acids and *n*-alkanes are slightly

more depleted than the plant tissue (−33 ‰ (C_3, *n*-alkanes), −21.7 ‰ (C_4, *n*-alkanes)), further isotopic discrimination occurs during their synthesis, which is higher for C_4 plants than for C_3 plants (Collister et al. 1994). This isotopic signal detected in the sedimentary *n*-alkane record can be taken as indicator of plant community change and therefore changes in environment and climate, by applying a binary end member mixing model (Schefuß et al. 2003; Bendle et al. 2006; 2007; Vogts et al. 2012). Apart from the metabolic pathway involved, the atmospheric concentration of CO_2 also influences the carbon isotopic fractionation of C_3 plants (Schubert and Jahren 2012; 2015). This is an important key parameter, as pCO_2 exhibits great variability over the last 40 Ma (Beerling and Royer 2011; Zhang et al. 2013). Growth chamber experiments have shown that the isotopic fractionation increases with increasing pCO_2 (0.4–3‰ per 100 ppm change in CO_2). These experiments were carried out under constant light, nutrient and humidity conditions (Schubert and Jahren 2012), but in the outside world it is possible that the effect of humidity and moisture availability masks the effect of changing pCO_2 on the $\delta^{13}C$ record. However, Schubert and Jahren (2015) emphasize that changes in pCO_2 and its subsequent effect on the $\delta^{13}C$ record of higher land plants should be considered first, before conclusions about the environmental parameters (humidity, temperature) are drawn. The isotopic signature of CO_2 ($\delta^{13}C_{CO2}$) also influences the $\delta^{13}C$ signature of *n*-alkanes (Farquhar et al. 1989). Over the last 65 Ma, $\delta^{13}C_{CO2}$ varied greatly, which also shifts the C_3/C_4 end members to either more enriched or depleted isotopic compositions over the same timescales

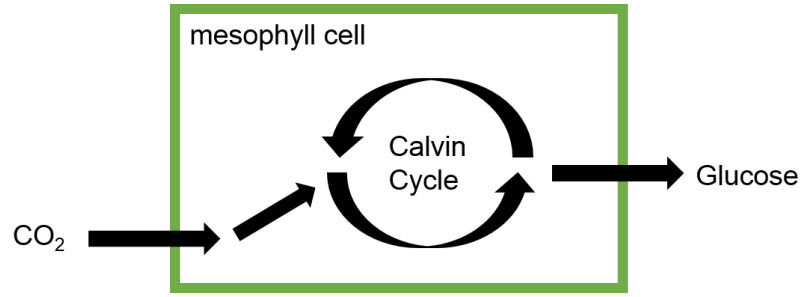

(a) Metabolic pathway of a C_3 plant

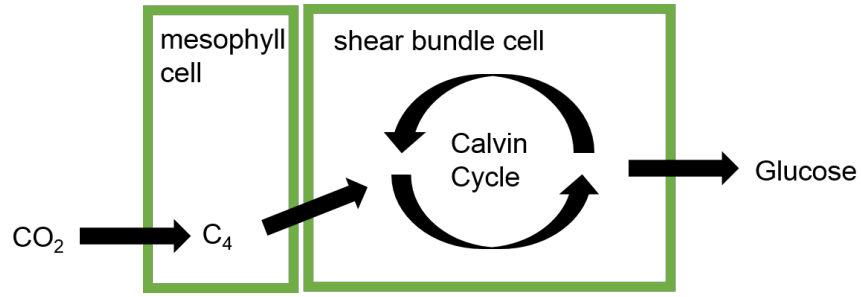

(b) Metabolic pathway of a C_4 plant

Figure 1.1.: Simplified C_3 and C_4 plant metabolism pathways, which affect the ^{13}C sequestration and leads to isotopic differences in C_3 and C_4 plants.

(Tipple et al. 2010). When reconstructing past plant community changes based on the $\delta^{13}C$ signature of *n*-alkanes over long time scales, the variations in $\delta^{13}C_{CO2}$ need to be taken into consideration to avoid over- or underestimation of contributors.

Meteoric water is the primary hydrogen source for plants, which is subsequently used for lipid synthesis within the plant, including the synthesis of *n*-alkanes (Sachse et al. 2012; and references therein). Hence, the compound specific hydrogen analysis of *n*-alkanes provides insight into changes of the

global hydrogen cycle, and therefore precipitation and climate (Sachse et al. 2012). δD variations of long-chain *n*-alkanes show a good correlation with mean annual precipitation δD values (Sachse et al. 2006; 2012), and thus have been used in a variety of settings to reconstruct precipitation patterns (Zhuang et al. 2014; Moossen et al. 2015). Other studies (Mügler et al. 2008; 2010; Thomas et al. 2016) tried to reconstruct the source of atmospheric moisture using the δD signature of *n*-alkanes, but on geological time scales, the δD signature of the moisture source might have changed. This has to be kept in mind when working with these records. The isotopic composition of precipitation is the fundamental control on the hydrogen isotopic ratio of *n*-alkanes, and there are several regional climatic factors that influence this composition (Liu and Huang 2005; Sachse et al. 2012; Zhuang et al. 2014). These factors are (a) the temperature effect: leaving the source water depleted in D with decreasing temperatures, (b) the amount effect: leaving source water D depleted with increasing amount of precipitation, and (c) the continental effect: increased depletion of source water D further land inwards (Sachse et al. 2012; and references therein). Locally, the δD signature of higher plants is influenced by the fractionation between lipids and source water: $\epsilon_{wax/water}$, which is mainly driven by the available moisture and temperature (Smith and Freeman 2006). $\epsilon_{wax/water}$ incorporates three different fractionation factors: the D/H fractionation during biosynthesis, fractionation of D/H during soil-water transpiration and leaf-water transpiration (Mügler et al. 2008; Feakins and Sessions 2010; Sachse et al. 2012), although these fractionation factors are poorly understood

at the moment (Sachse et al. 2012). Subsequently, global and local factors can influence any δD record substantially, therefore careful evaluation of the dataset prior to interpretation is necessary. All these factors, biosynthetic pathways, biosynthesis of plant lipids, $\delta^{13}C_{CO2}$ and $\epsilon_{wax/water}$, must be considered when interpreting δD and $\delta^{13}C$ records of *n*-alkanes over long time scales.

Branched glycerol dialkyl glycerol tetraethers

The origin of branched Glycerol Dialkyl Glycerol Tetraethers (brGDGTs) (Fig. 1.2) is still uncertain; minor abundance of GDGT-I were found in cultures of Acidobacteria (Schouten et al. 2013). These bacterial GDGTs differ from archaeal GDGTs because they possess a basic 13,16-dimethyloctacosane as alkyl chain (Fig. 1.2). Furthermore, the stereochemistry of the glycol moiety is inverse to that of isoprenoidal GDGTs, marking an evolutionary difference between bacterial and archaeal lipids (Koga et al. 1998; Figs 1.2, 1.3). Weijers et al. (2006a) found increased brGDGT in the anoxic zone of soils, suggesting that they are synthesized by anaerobic bacteria. Since in the terrestrial environment, brGDGT production takes place only in soils, their contribution probably does not reflect the total terrestrial OM input, but rather soil OM input into marine sediments only (Hopmans et al. 2004; Weijers et al. 2006b; Moossen et al. 2013). However, the relative abundance of brGDGTs has been utilized as a proxy for the relative abundance of terrestrial OM in the ocean: the branched index of tetraethers (BIT) (Hopmans et al. 2004; Eq. 1.2). A ratio

close to 0 is considered to reflect an open marine environment, a ratio close to 1 indicates a soil dominated environment. However, the utilization of BIT is complicated by the fact that brGDGTs are also produced in marine sediments (Fietz et al. 2012), thus the BIT ratio rarely approaches 0. Variable BIT values are found for coastal marine settings (Hopmans et al. 2004). Other studies then took advantage of BIT as soil OM proxy. Soil organic matter is mostly comprised of degrading plant OM, which can alter the C/N ratios and $\delta^{13}C_{org}$ signatures of plant OM that is actually used to track terrestrial OM matter. It was shown, that soil OM can have C/N ratios close to the marine end member (Gordon and Goñi 2003), hence the soil OM contribution to marine sediments remains overlooked. Obviously, other proxies than the chemical fingerprints of higher plants are necessary, preferably from organisms living in the soil layer. These would accurately track the transport and recycling of soil organic matter in the marine environment. Amongst branched GDGTs, these can be bacteriohopanepolyols (BHPs) (Rohmer et al. 1984), stemming from bacteria which in contrast to the brGDGT producing Acidobacteria reside in the upper, oxic part of the soil. The subsequent development of the soil proxy R_{soil} index by Zhu et al. (2011) facilitates a new approach to tracking soil OM in marine sediments. Due to the lack of appropriate analytical facilities, and the application to a limited time scale (centennial to millennial), the R_{soil} index will not be further discussed here.

Studies have shown that BIT is also affected by soil pH, as the BIT is lowered with increasing soil pH (Weijers et al. 2007), giving false estimates for

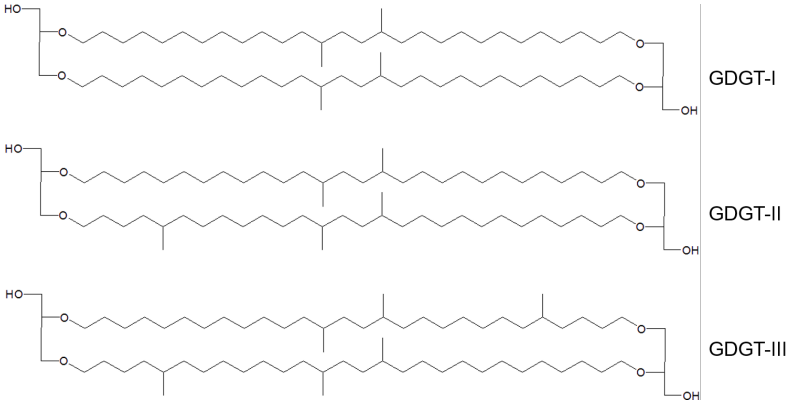

Figure 1.2.: Structures of branched GDGTs used for calculation of the BIT.

BIT reconstructions in marine environments.

Weijers et al. (2007) found a significant relationship between branched GDGT distribution, and mean annual air temperature (MAT) and soil pH (Eqs 1.3,1.4). The amount of methyl groups are negatively correlated with MAT and soil pH, yielding the index of methylation of branched tetraethers (MBT). The amount of cyclopentane moieties is negatively correlated with soil pH, yielding the index of cyclization of branched tetraethers (CBT). Subsequently, the MBT and CBT proxies were developed.

$$\text{BIT} = \frac{\text{GDGT-I} + \text{GDGT-II} + \text{GDGT-III}}{\text{GDGT-I} + \text{GDGT-II} + \text{GDGT-III} + \text{Crenarchaeol}} \tag{1.2}$$

$$\text{MBT} = \frac{[\text{I} + \text{Ib} + \text{Ic}]}{[\text{I} + \text{Ib} + \text{Ic}] + [\text{II} + \text{IIb} + \text{IIc}] + [\text{III} + \text{IIIb} + \text{IIIc}]} \tag{1.3}$$

$$\mathrm{CBT} = \frac{\mathrm{Ib} + \mathrm{IIb}}{\mathrm{I} + \mathrm{II}} \tag{1.4}$$

$$\mathrm{MBT} = 0.867 - 0.096 \times \mathrm{pH} + 0.021 \times \mathrm{MAT} \tag{1.5}$$

$$\mathrm{CBT} = 3.33 - 0.38 \times \mathrm{pH} \tag{1.6}$$

These were later refined by Peterse et al. (2012; Eqs 1.7,1.8) with lower correlation coefficients and subsequently giving a higher uncertainty of MBT. But soils are very heterogeneous, thus a scatter in a global soil calibrations can be expected (Schouten et al. 2013).

$$\mathrm{MBT}' = \frac{[\mathrm{I} + \mathrm{Ib} + \mathrm{Ic}]}{[\mathrm{I} + \mathrm{Ib} + \mathrm{Ic}] + [\mathrm{II} + \mathrm{IIb} + \mathrm{IIc}] + [\mathrm{III}]} \tag{1.7}$$

$$\mathrm{MAT}(\pm 5\,^{\circ}\mathrm{C}) = 0.81 - 5.67 \times \mathrm{CBT} + 31.0 \times \mathrm{MBT}' \tag{1.8}$$

Some constrains on the application of these proxies are defined by Schouten et al. (2013) and Weijers et al. (2011): branched GDGTs produced in soils probably reflect soil instead of air temperature, and as for other temperature proxies, the MBT/CBT ratio might be biased towards a certain season, at least at high latitudes (Rueda et al. 2009; Moossen et al. 2015). Furthermore, when applying the MBT/CBT proxy to marine sediments it should be considered

that branched GDGTs arrive pre-aged at the sampling locality, thus the subsequent time lag can cause an offset between branched GDGT proxies and marine proxies (Schouten et al. 2013).

1.3.2. Marine biomarkers

Alkenones

One important variable in the climate system is the sea surface temperature (SST). Changes in the atmospheric circulation and global heat distribution are linked to changes in SSTs (Bjerknes 1964). For climate models it is therefore important to estimate the temperature change in the oceans in order to predict large-scale reorganizations of the atmosphere.

The first organic geochemical SST proxy was developed by Brassell et al. (1986), based on the unsaturation index of C_{37}-ketones ($U^{K'}_{37}$). Long-chain ketones (known as alkenones) contain 2-4 double bonds. The carbonyl group is usually located at the second or third carbon atom (Volkman 2006). The notation $C_{x:y}$ indicates the chain length of the ketone (x) and the number of double bonds (y). Depending on the surrounding temperature, the ketones are more (warm) or less (cold) unsaturated. The production of alkenones in the marine realm is thought to be limited to members of the haptophyte algae within the Order Isochysidales. The actual function of these ketones is not known. It is speculated that they serve as energy storage for the organism (Eltgroth et al. 2005). The initial proxy, U^{K}_{37}, also included the tetra-unsaturated heptatriacon-

tane, but since it is only present in fresh and cold waters, it was excluded from the proxy (Prahl and Wakeham 1987; Eq. 1.9). Prahl and Wakeham (1987) modified the U^{K}_{37} proxy, and calibrated it with laboratory cultures of *Emiliania huxleyi*. Global core top calibrations were performed by Müller et al. (1998) and Conte et al. (2006), and to date these are the most extensive calibrations of $U^{K'}_{37}$ versus SST. $U^{K'}_{37}$ is likely to reflect SST, although the haptophyte production depth is tied to light penetration, giving a depth range of 0–200 m. However, core top calibrations indicate that paleo-SST reconstructions reflect SSTs at a depth of 10 m (Müller et al. 1998; Ohkouchi et al. 1999). Generally, $U^{K'}_{37}$ agrees with the mean annual SST, with the exception of high latitude regions, where a seasonal production of phytoplankton is observed (Müller et al. 1998; Moossen et al. 2015).

Distribution of differently unsaturated C_{37}-alkenones varies with the surrounding sea surface temperature (SST) (Prahl and Wakeham 1987; Prahl et al. 1988; Müller et al. 1998) and is expressed as Eq. 1.9. The most recent calibration was established by Conte et al. (2006), and is used in this study (Eq. 1.10.

$$U^{K'}_{37} = \frac{C_{37:2}}{C_{37:2} + C_{37:3}} \tag{1.9}$$

$$SST(\pm 1.1\,^{\circ}C) = 29.876 \times (U^{K'}{}_{37}) - 1.334 \tag{1.10}$$

Alkenone paleobarometry Reconstructing pCO_2 over geological time scales of great interest, for which many proxies available, but only four are deemed most promising by IPCC 2007 (Solomon 2007). Within the terrestrial environment, the abundance of stomata on fossil leaves (Woodward 1987) and $\delta^{13}C$ of soil carbonates (Cerling 1991) can provide insight into past changes in atmospheric carbon dioxide. The fossil leaves proxy is based on the observation that stomatal density decreases with increasing CO_2 in the atmosphere (Woodward 1987; Kürschner et al. 2008). Soil carbonates from arid to semi humid areas precipitating at the soil-atmosphere interface are in equilibrium with atmospheric CO_2 (Cerling 1991; Breecker et al. 2010). Down sides of both proxies exist, in example fossil leaves are rather scarce and cannot cover a continous time span, and the use of soil carbonates is limited to deserts.

The marine environment also provides pCO_2 proxies, via the $\delta^{11}B$ signature of foraminfera. The idea behind this proxy is that ^{11}B in sea water is incorporated in microfossils as a function of sea water pH and alkalinity (Foster and Rae 2016; and references therein). The main draw back is that reconstructions are not reliable on time scales longer than the last 3 Ma (Foster and Rae 2016). The second marine proxy for pCO_2 is the $\delta^{13}C$ signature of alkenones. Since the discovery that CO_2 concentrations have a major control on the $\delta^{13}C$ variation in alkenones (Goericke and Fry 1994; Riebesell et al. 2000), the alkenone $\delta^{13}C$ signature has been used to reconstruct atmospheric CO_2 concentrations (pCO_2, (Jasper and Hayes 1990; Pagani et al. 1999b; Eq. 1.11). ϵ_p describes the photosynthetic fractionation factor between the inor-

ganic substrate; the dissolved CO_2, and organic matter produced by the algae. ϵ_f reflects the fractionation during carbon fixation, and depends on the enzyme involved; in the case for haptophytes this is Rubisco ID (Pagani 2014). *b* is the sum of all biological factors affecting the carbon isotopic fractionation. It has been shown that *b* is strongly correlated to oceanic PO_4^{3-} concentrations, or another micronutrient causing the same variation as PO_4^{3-} on *b* (Pagani et al. 1999a; Pagani 2014). The most obvious problem with PO_4^{3-} as proxy for *b* is the inability to reconstruct past phosphate concentrations of the ocean, adding uncertainty to the pCO_2 reconstruction (see section 7.4.2).

$$\epsilon_{\mathrm{p}} = \epsilon_{\mathrm{f}} - \frac{\mathrm{b}}{[\mathrm{CO}_{2(aq)}]} \tag{1.11}$$

Haptophytes are thought to rely on passive diffusion of CO_2 into the cell (Pagani 2014). Therefore, the carbon isotopic signature of the alkenone is determined by the isotopic signature of the substrate; $\delta^{13}C_{CO2}$. Additionally, the isotopic fractionation of carbon inside the cell is determined by the enzymes involved. The understanding of the associated fractionation with the respective enzyme is also crucial to understand ϵ_f, which is necessary for alkenone based pCO_2 reconstructions (Pagani 2014). ϵ_f estimates for paleoclimate reconstructions usually range between 25 and 28‰ (Pagani et al. 1999a; Seki et al. 2010; Pagani et al. 2011). The diffusion of CO_2 into the cell is based on the principle of diffusion of CO_2 in C_3 plants (Farquhar et al. 1989; Pagani et al. 1999a), and is expressed as:

$$CO_{2(e)} \underset{k_{-1}}{\overset{k_1}{\rightleftharpoons}} CO_{2(i)} \xrightarrow{k_2} C_{org}$$

$CO_{2(e)}$ represents external CO_2, $CO_{2(i)}$ the internal $CO_{2(aq)}$, and k_1,k_{-1} and k_2 are the rate constants for the CO_2 fluxes involved (Pagani 2014). The principle enzyme involved with carbon fixation in coccoliths is the subform 'Rubisco ID' (Pagani 2014; and references therein). A recent analysis of this enzyme has shown that it only accounts for a maximum fractionation of 11‰ (Pagani 2014; and references therein), which is in stark contrast to the established 25-28‰ fractionation found by Goericke and Fry (1994) and applied in alkenone pCO_2 studies (Pagani et al. 1999b; Seki et al. 2010). Currently, no process is known that would remove additional ^{13}C from coccolithophores, in order to reach a photosynthetic fractionation factor (ϵ_p) of 7-25‰, as established in paleoclimate and batch culture studies (Bidigare et al. 1997; Pagani et al. 1999a; Riebesell et al. 2000; Rost et al. 2002; Pagani 2014). Batch cultures and chemostat experiments have shown that alkenone ^{13}C is not always determined by $CO_{2(aq)}$, but also by irradiance (Rost et al. 2002), cell size (Burkhardt S; Riebesell 1999), cell geometry (Popp et al. 1998) and growth rates (Riebesell et al. 2000). Furthermore, the *b*-factor is calibrated to modern ocean $[PO_4^{3-}]$ and therefore does not necessarily reflect ancient ocean $[PO_4^{3-}]$, affecting the alkenone paleobarometry. Thus, when alkenones are used for estimates of ancient pCO_2 concentrations, *b* and ϵ_f need to be carefully evaluated, since they exert the largest control on the reconstructed outcome. Furthermore, growth rates should be constrained in order to enhance the fidelity in the alkenone

paleobarometry method. No study so far has constrained growth rate and cell size and the subsequent impact on the alkenone paleobarometry.

Paleosalinity Recently, the δD variations in C_{37} alkenones were used to reconstruct salinity changes in a variety of marine settings (van der Meer et al. 2008; Kasper et al. 2014; Warden et al. 2016). The concept behind the utilization of organic hydrogen is that it functions as proxy for the δD composition of the source water at the time of photosynthesis (Sachse et al. 2012; and references therein). Indeed, δD signatures of biolipids are offset, but highly correlated with δD of the source water (Chikaraishi and Naraoka 2003; Sachse et al. 2006; 2012). Culture studies by Schouten et al. (2006) have shown that the deuterium isotopic signature of alkenones changes by 3-4‰ per salinity unit. The correlation between salinity and the alkenone hydrogen isotopic signature is attributed to restricted exchange with extracellular water at higher salinity, increased production of osmolytes, or lower growth rates at higher salinity (Sachse et al. 2012; and references therein). As for the ^{13}C signature, alkenone δD signatures also seem to be influenced by the growth rate: Schouten et al. (2006) found the best correlation for the fractionation between alkenones and salinity when growth rates were divided by salinity. Chivall et al. (2014) studied the effect of salinity and growth phase on the hydrogen isotopic composition, and found a reduced sensitivity of the fractionation factor $\alpha_{alkenone-water}$ to salinity after the exponential growth phase. Presently, the predominant growth phase of haptophytes is unknown and this also applies to

the geological past, which adds the factor growth phase as uncertainty to this paleosalinity proxy. Furthermore, the alkenone distribution influences their hydrogen signature: a differential hydrogen isotopic fractionation occurs between differently unsaturated alkenones (van der Meer et al. 2013). The best explanation seem to lie within the biosynthesis of these alkenones: the $C_{37:3}$ alkenone is formed by desaturation of the $C_{37:2}$ alkenone, which will lead to a D-depletion of the $C_{37:3}$ alkenone (Chikaraishi et al. 2004; van der Meer et al. 2013). Subsequently, it was suggested to conduct a combined measurement of $C_{37:2}$ and $C_{37:3}$ alkenones for sea surface salinity reconstructions. In contrast to $U^{K'}_{37}$ a shift in alkenone producing species does not seem to hamper its use as paleosalinity proxy (Warden et al. 2016). Irradiance also influences the hydrogen isotopic composition of alkenones, the fractionation decreases with increasing irradiance (van der Meer et al. 2015). However, this is not considered to be problematic for the use of alkenone δD as surface salinity proxy, since haptophytes tend to bloom at high irrandiance levels close to the surface, where irradiance is relatively high and constant (van der Meer et al. 2015). Obviously, the application of alkenone δD as salinity proxy is relatively novel, and caution should be exercised when interpreting these records, with a special focus on alkenone distributions (van der Meer et al. 2013), and growth phases (Chivall et al. 2014).

Isoprenoid glycerol dialkyl glycerol tetraethers

An alternative proxy to reconstructing SSTs is the Tetraether index of Tetraethers consisting of 86 carbons (TEX_{86}) proxy which is based on the relative abundance of isoprenoidal Glycerol Dialkyl Glycerol Tetraethers (iGDGTs) in marine sediments (Schouten et al. 2002; Fig. 1.3). Unlike $U^{K'}_{37}$, the biomarkers used for TEX_{86} are produced by a large range of Archaea, not just Thaumarchaeota which are assumed to have the largest influence on TEX_{86}. This vast array of GDGT producers makes environmental effects on this temperature proxy much more difficult to constrain (Schouten et al. 2013; and references therein). The relative distribution of isoprenoidal GDGTs with differing amounts (0–4) of cyclopentyl moieties is thought to reflect ambient growth temperature (De Rosa and Gambacorta 1988; Uda et al. 2001; Schouten et al. 2002; Zhu et al. 2016). The additional GDGT Crenarchaeol and its regioisomer contains an additional cyclohexyl moiety (Schouten et al. 2002). GDGTs are membrane constituents of marine Thaumarchaeota which are ubiquitous in the world's oceans. Thaumarchaeota represent a substantial fraction of the picoplankton, and are involved in ammonium oxidation and therefore probably play a major role in ocean nutrient cycling (Tierney 2014; and references therein). Since Archaea are such versatile organisms, they successfully inhabit every part of the ocean, from surface water to extreme environments. It was found that Euryachaeota dominate in surface waters, while the marine Thaumarchaeota, relevant for the TEX_{86} proxy, reside in the mesopelagic zone

below the photic zone (Massana et al. 1997). Furthermore, Thaumarchaeota can be divided into 'shallow water' and 'deep water' Thaumarchaeota, based on the differences in ammonia monooxygenase (amoA) and geranylgeranylglyceryl phosphate (GGGP) synthase, possibly affecting GDGT distributions, and therefore the TEX_{86} outcome (Villanueva et al. 2015). While this observation agrees with the nitrifying trait of marine Thaumarchaeota, it clashes with the idea that their relative GDGT distribution correlates best with temperatures of the 0–100 m (Tierney 2014). Early into the TEX_{86} proxy development this phenomenon was explained by rapid export of surface GDGTs to the sea floor, which in contrast to their deeper produced counterparts are incorporated into faecal pallets and therefore sink faster (Wakham et al. 2003). An alternative explanation for the correlation between GDGT distribution and SST is provided by Tierney (2014): temperatures at 100 m are closely correlated to SST, thus TEX_{86} records SST changes over time merely due to this close relation. Reconstructions of SSTs using TEX_{86} show that it records changes in SSTs, but there are also studies where TEX_{86} seems to record subsurface temperatures, especially in upwelling regions (Tierney 2014; and references therein). To date, it is not possible to resolve the effect of surface dwelling Euryarcheota on the sedimentary GDGT record. Since marine Thaumarcheota are most active when no other phytoplankton blooms are active (Wuchter et al. 2005; 2006), their productivity peak should result in a seasonal SST record. However, most sediment trap studies and paleoclimate reconstructions find good agreement with annual SSTs (Yamamoto et al. 2012; Turich et al. 2013;

Chen et al. 2014). Recently, some studies have shown that marine Thaumarchaeota react sensitive to the redox state of the water column (Qin et al. 2015; Zhu et al. 2016). These ecological characteristics of marine Thaumarcheota would obviously have an impact on TEX_{86} and its calibration to sea surface temperatures.

Since their discovery as potential SST proxy, various calibrations of GDGTs against SSTs have been proposed (Tab. 1.2). Furthermore, Tierney and Tingley (2014) provided a Bayesian regression model for TEX_{86}, to assess the spatial relationship between GDGTs and SSTs. However, rather than a new calibration, this Bayesian model is a re-assessment of existing calibrations. Calibrations used for this study include the calibration by Kim et al. (2008), who established a linear TEX_{86} calibration (Eqs 1.12, 1.13) based on a global data set of core top samples.

$$TEX_{86} = \frac{\text{GDGT-2} + \text{GDGT-3} + \text{cren}'}{\text{GDGT-1} + \text{GDGT-2} + \text{GDGT-3} + \text{cren}'} \tag{1.12}$$

$$\text{SST}(\pm 1.7\,^{\circ}\text{C}) = -10.78 + 56.2 \times TEX_{86} \tag{1.13}$$

Furthermore, Kim et al. (2010) developed an exponential TEX_{86} proxy as expression for oceans with an annual sea surface temperature of $\leq 15\,^{\circ}$C, TEX_{86}^{L}, and the respective calibration equation 1.15:

$$TEX_{86}^{L} = \frac{\text{GDGT-2}}{\text{GDGT-1} + \text{GDGT-2} + \text{GDGT-3}} \tag{1.14}$$

Table 1.2.: Overview of different global TEX_{86} calibrations, compiled by Tierney (2014)

Study	**Equation**	**Error(°C)**
Schouten et al. (2002)	TEX_{86}=0.0158T+0.28	N/A
Kim et al. (2008)	T=-10+56.2×TEX_{86}	1.7
Liu et al. (2009)	T=50.475-16.332×(1/TEX_{86})	3.7
Kim et al. (2010)	T=49.9+67.5×TEX^{L}_{86}	4
Kim et al. (2010)	T=38.6+68.4×TEX^{H}_{86}	2.5

$$\text{SST-L}(\pm 4.0\,^{\circ}\text{C}) = 67.5 \times \log \text{TEX}^{\text{L}}{}_{86} + 46.9 \tag{1.15}$$

Kim et al. (2010) also established a TEX_{86} expression, for oceans with an annual sea surface temperature of ≥15 °C, TEX^{H}_{86}, and the respective calibration equation 1.17:

$$\text{TEX}^{\text{H}}{}_{86} = \frac{\text{GDGT-2} + \text{GDGT-3} + \text{cren}'}{\text{GDGT-1} + \text{GDGT-2} + \text{GDGT-3} + \text{cren}'} \tag{1.16}$$

$$\text{SST-H}(\pm 2.5\,^{\circ}\text{C}) = 68.4 \times \log \text{TEX}^{\text{H}}{}_{86} + 38.6 \tag{1.17}$$

These calibrations are established by correlating the relative GDGT distribution with overlying SSTs. This approach captures the full range of the living conditions of Thaumarchaeota and the associated uncertainty, which makes the respective calibration applicable, even on geological time scales (Tierney 2014). Examining the spatial distribution of the residual error shows that

$TEX_{86}^{H/L}$ derived SSTs tend to underestimate tropical SSTs, while polar SSTs are usually overestimated. Tierney (2014) attributes this latitudinal bias to the biogeochemical variability affecting GDGT production. This bias of TEX_{86} is possibly not meaningful during geological times when the continental configuration was different from modern times. On the other hand, the calibration of modern-day SSTs to GDGT distributions might not be applicable to the past (Tierney 2014). Based on these uncertainties, it is not a straightforward decision which of the proposed calibrations (Tab. 1.2) are suitable for paleoclimatic reconstructions. These uncertainties are presently difficult to constrain. The newly proposed sensitivity to the redox state of the water column (Qin et al. 2015; Zhu et al. 2016), as well as genetic control on depth-related GDGT production (Villanueva et al. 2015) show that a better understanding of the ecology of marine Thaumarchaeota is required.

Isoprenoidal GDGTs derived from soils and delivered to the oceans via fluvial processes can bias TEX_{86} (Weijers et al. 2006b; Schouten et al. 2013), and the contribution is expressed as branched versus isoprenoid tetraether index (BIT, Eq. 1.2) (Hopmans et al. 2004). The cut-off point for TEX_{86} SSTs not biased by soil derived GDGTs lies at a BIT value of 0.3. However, Tierney (2014) points out that BIT is a non-linear proxy for soil input and sensitive to absolute changes of Crenarchaeol and branched GDGTs, thus the cut-off point for BIT will depend on the soil type and varies from basin to basin. Thus, even with a BIT larger than 0.3 TEX_{86}-SSTs can still be reasonable (Schouten et al. 2013).

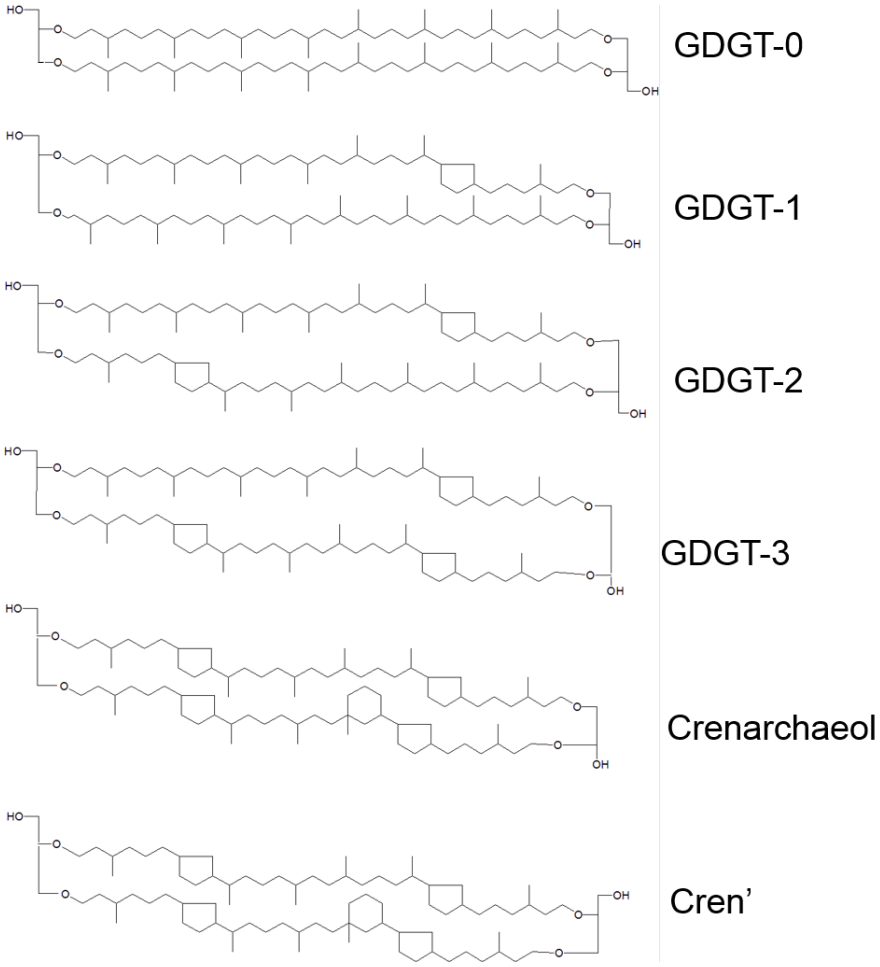

Figure 1.3.: Isoprenoidal GDGTs used for calculation of TEX_{86}

Thermal maturity of the sediment affects the GDGT abundance, and thus biases TEX_{86} towards colder temperatures (Schouten et al. 2004). The impact of thermal maturity on GDGTs can be measured. Thermal maturity of a sediment can be established by studying the stereochemical characteristics of hopanoids, for example the racemic mixture or the 17β,21β configuration of hopanes (Seifert and Moldowan 1980). Schouten et al. (2004) established that GDGTs start to disappear at 17α,21β(H)-hopane distribution of ≤0.5 (Eq. 1.18).

$$\frac{\beta\beta}{\alpha\beta + \beta\beta + \beta\alpha} \tag{1.18}$$

Methanotrophic/metanogenic archea in the sediment can add in-situ produced GDGTs to the sedimentary record, biasing the TEX_{86} reconstructions (Lipp and Hinrichs 2009; Zhang et al. 2011). To determine the influence of methanogenic/methanotrophic archeal membrane lipids on the TEX_{86} ratio, the GDGT-0/Crenarchaeol ratio (Inglis et al. 2015; Eq. 1.19) and the Methane Index (MI) (Zhang et al. 2011; Eq. 1.20) can be used.

$$\%\text{GDGT-0} = \frac{\text{GDGT-0}}{\text{GDGT-0} \times \text{Crenarchaeol}} \times 100 \tag{1.19}$$

$$\text{MI} = \frac{\text{GDGT-1} + \text{GDGT-2} + \text{GDGT-3}}{\text{GDGT-1} + \text{GDGT-2} + \text{GDGT-3} + \text{Crenarchaeol} + \text{Cren}'} \tag{1.20}$$

Furthermore, Zhang et al. (2016) also proposed the Ring Index (RI) to as-

sess the influence of non-thermal factors on the TEX_{86}-SST record. The authors argue that its more sensitive than the application of BIT or MI alone (Eq. 1.21). The RI is then used to calculate the difference from the modern TEX_{86}-RI relationship in order to assess non-thermal factors influencing TEX_{86} (Eq. 1.22). RI_{sample} is the RI calculated with Eq. 1.21, and RI_{TEX} is calculated with Equation 1.23. The cut-off point for RI lies at 0.3 (Zhang et al. 2016).

$$\begin{aligned} RI = 0 \times [\text{GDGT-0}] + 1 \times [\text{GDGT-1}] + 2 \times [\text{GDGT-2}] + 3 \times [\text{GDGT-3}] \\ +4 \times [\text{Cren}] + 4 \times [\text{Cren}'] \end{aligned} \tag{1.21}$$

$$\Delta RI = RI_{TEX} - RI_{sample} \tag{1.22}$$

$$RI_{TEX} = -0.77 \times TEX_{86} + 3.22 \times TEX_{86}{}^{2} + 1.59 \tag{1.23}$$

All these ratios help to constrain the fidelity of the produced TEX_{86} record, but cannot account for the most important control on the TEX_{86} record, which is the shift within the vast community of GDGT producers with changing environmental conditions.

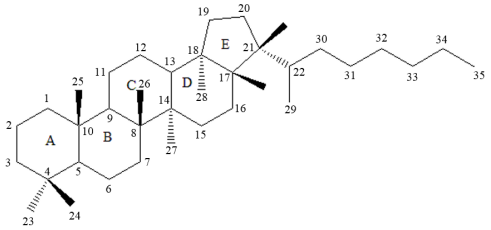

Figure 1.4.: Structure of a C_{35} 17β,21β-hopane (17β(H),21β(H)-pentakishopane), including numbering and ring labeling scheme

Hopanoids

Phytoplankton are the predominant primary producer in the marine realm (Arrigo 2005). Amongst these plankton are: large eukaryotic algae, such as diatoms, dinoflagellates and coccolithophores. But bacteria also contribute significantly to the primary productivity in the oceans (Ourisson et al. 1979; Ourisson and Albrecht 1992). Lipid biomarkers of certain algae and bacteria can be used to track changes in the source of the organic matter deposited at the sea floor. This method is suitable to track changes of the dominant producer, for example a shift from diatoms to coccolithophores. Isoprenoids are essential components of the cell membrane in eukaryotes and some prokaryotes, e.g. as lipid membrane constituents. They are synthesized from the C_5 building block Isopentyl diphosphate (IPP) (Bianchi and Canuel 2011). Isoprenoids are synthesized via the Bloch-Lynen (mevalonate (MVA)) or methyl-erythritol-pathway (MEP) pathway (Peters et al. 2005). The MVA pathway is used by animals, fungi and archaea (Bianchi and Canuel 2011). In this pathway, IPP is synthesized from three molecules of acetyl-Coenzyme A (CoA)

(Bianchi and Canuel 2011). The MEP is used by eubacteria, some algae and land plants (Bianchi and Canuel 2011), and synthesizes IPP by the formation of 1-deoxyxylulose 5-phosphate (DOXP) which is rearranged and reduced to 2-C-methylerythritol 4-phosphate (Bianchi and Canuel 2011). In both pathways, IPP is condensed and synthesized to squalene, the most important precursor for steroids (produced by plants and animals) and hopanoids (produced by eubacteria) (Summons et al. 2006).

Hopanoids are widely distributed among bacteria and cyanobacteria (Ourisson et al. 1979; Summons et al. 1999; 2006), and belong to the class of triterpenoids. They are usually comprised of four 6-carbon and one 5- or 6-carbon ring (Fig. 1.4). They are possible phylogenetic precursors of the steroids (Ourisson et al. 1979). The hopanoid synthesis differs from steroid synthesis at an early stage. Instead of forming epoxysqualene as an intermediate, the squalene-hopene cyclase enzyme catalyzes the conversion from squalene to hopene in a single step (Reinert et al. 2004; Siedenburg and Jendrossek 2011). Like steroids, hopanoids can also be identified by using gas chromatography (GC) and gas chromatography-mass spectrometry (GC-MS) techniques. Although oxygen is not required for the hopane synthesis, the vast majority of hopane producers are aerobic bacteria (Ensminger et al. 1972; Ourisson et al. 1979; Ourisson and Albrecht 1992; Summons et al. 2006; and references therein). The diagenetic steps from the functionalized hopanoid to the aliphatic remains of the precursor include defunctionalization, and loss of carbon atoms at the side chain (Ourisson and Albrecht 1992). Lastly, stereochemical char-

acteristics of the hopanoids are modified, e.g. by changing the racemic mixture of the C_{22} (Seifert and Moldowan 1980), or the 17β,21β configuration (Seifert and Moldowan 1980). These stereochemical changes facilitate the use of R/(R+S) or ββ ratios as thermal maturity indicators (Seifert and Moldowan 1980). Hopanes with 30 and less carbon atoms are thought to be derived from diplopterol (Ourisson et al. 1979). Diplopterol is produced by a variety of marine as well as terrestrial organisms (Ourisson et al. 1979; Venkatesan 1988; Prahl et al. 1992). The extended hopane series with more than 30 carbon atoms is thought to be derived from the Bacteriohopanepolyol (BHP) precursor (Ourisson et al. 1979), and can sometimes be indicative of cyanobacteria (Ourisson and Albrecht 1992; Yamamoto and Watanabe 1995). Since hopanes are synthesized by eubacteria, they serve as excellent biomarkers for the presence of bacteria, and subsequently the depositional environment, i.e. the 28,30-Dinorhopane and its precursor 28,30-Dinorneohop-13(18)-ene (Sinninghe Damsté et al. 2014). Hopanoids can also serve as plant markers, e.g. oleanane as marker for angiosperms. They thus provide useful tools for paleoenvironmental reconstructions.

2. Methods

2.1. Bulk sediment parameters

All bulk sedimentary parameters were measured at the Max-Planck-Institute for Biogeochemistry, Jena (Germany). To obtain total nitrogen data for site U1425, the total carbon/total nitrogen (TC/TN) ratio was measured. The protocol for these measurements was modified after Verado, D. J., Froelich, P.N. and McIntyre (1990). 10 mg of a sample were weighted into tin-cups. Additionally, 3×10 mg of a soil sample with known TC/TN ratios and 5 blanks were measured with the samples. TC/TN ratios were determined using a Carlo Erba NA-1500 analyzer. TOC measurements required 30 mg of sample weighted into silver-cups. 3 drops of Milli-Q water were added to each sample to avoid a strong reaction with the H_2SO_3 treatment. Removing inorganic carbon in form of carbonates, 100 µl of freshly opened 6% H_2SO_3 were added to each sample before they were dried at 60 °C for 12 hours. After this step, five times of 120 µl 6% H_2SO_3 were added to each sample, before they were dried at 60 °C over the weekend. All samples were then re-packed into tin cups prior

to TOC measurements using a Carlo Erba NA-1500 analyzer. Dependent on the TOC content of each sample, 1.5–15 mg of sediment were weighted into tin cups and treated with a total of 120 µl of 6% H_2SO_3 prior to analysis for $\delta^{13}C_{org}$. The samples were stored at 60 °C for a few days prior to analysis on a Delta C prototype IRMS (Finnigan MAT), coupled with an EA 1100. The ^{13}C content of the analyzed bulk sediment was determined by measuring a lab internal standard (Alj-3, caffeine) which is calibrated against Vienna Pee Dee Belemnite (VPDB), along with the samples. Samples were run in duplicates to determine the 1σ error.

2.2. Biomarker extraction and separation

Biomarker extraction and separation was performed at the University of Birmingham, School of Geography, Earth and Environmental Sciences, following an adapted protocol from Kawamura et al. (2003). Glassware and tools used in this process, such as Pasteur pipettes, test tubes, round-bottom flasks, aluminum foil and spatulas were furnaced for 8 h at 450 °C in order to remove organic contaminants.

2.2.1. Extraction and sulfur removal

Ground, freeze dried sediments (3–10 g, depending on availability) were extracted by ultrasonication. The samples were filled into a 30 ml test tube, and

mixed with 20 ml Dichloromethane (DCM):Methanol (MeOH) (DCM:MeOH, 3:1, v/v). The samples were stirred, before they were ultrasonicated for 20 minutes, and then heated at 40 °C for 1 hour. To obtain the supernatant, the samples were centrifuged at 3300 rounds per minute (rpm) for 3 minutes, before the supernatant was decanted into 100 ml tubes. In the subsequent steps, only 10 ml of DCM:MeOH (3:1, v/v) were added to the sample, and the samples were not heated after ultrasonication. This procedure was repeated at least three times or until the supernatant was colorless. The resulting total lipid extract (TLE) was concentrated using a Buechi Sycore connected to a Buechi Vacuum Pump V-700, set to 40 °C, 250 rpm and a pressure of 850 mbar for DCM and 200 mbar for Methanol. The concentrated TLE was transferred into 7 ml vials with a DCM:MeOH 9:1 (v/v) mixture and dried down to approximately 0.5 ml using N_2. To remove sulfur from the samples, activated copper chips were added to the TLE. In order to activate the copper chips, they were first washed with 36% hydrochloric acid, then four times each with MeOH, DCM and *n*-hexane. A few copper chips and 0.5 ml of DCM were added to the TLE and stored for 24 hours. The TLE was then dried over Na_2SO_4 and transferred into pre-weighted GC vials, using a DCM:MeOH 9:1 (v/v) mixture. The TLE was dried under N_2, weighed and stored in a fridge until further analysis.

2.2.2. Silica gel column chromatography

The TLE was separated into four fractions using silica gel (Si-gel) chromatography. The silica gel was furnaced at 450 °C for eight hours in order to activate it prior to every separation. 1 g (circa 4 cm) of Si-gel were filled in to a pasteur pipette plugged with glass wool at the tapered end. The column was conditioned with 4 ml of n-hexane. At the beginning of each fraction, the TLE was redissolved in 4–5 drops of the respective solvent and given on the column. The aliphatic/acyclic fraction were obtained in the first fraction, by eluting with 4 ml of *n*-hexane. Aromatic compounds were eluted in the second fraction, with 2 ml of hexane:DCM (2:1, v/v), the keto-fraction, containing n-alcohols, sterols and alkenones was eluted with 4 ml of DCM, and the polar fraction, containing GDGTs and fatty acids was eluted with 5 ml MeOH. All samples were transferred into GC vials by using the respective solvent of the fraction and then dried under N_2.

2.2.3. Alkenone separation

Prior to isotopic analysis, alkenones require separation into a $C_{37:2}$ and $C_{37:3}$ fraction. For this purpose, the protocol published by D'Andrea et al. (2007) was modified. The alkenone separation was achieved by using silver nitrate (Ag-NO^{3+}) impregnated silica gel columns. A pipette with 0.7 g of Ag-NO^{3+} impregnated silica was prepared, and wrapped in aluminum foil to avoid photoreduction of the Ag-NO^{3+}. The column was conditioned with DCM before

200 µl of sample, redissolved in DCM were given onto the column. Subsequently, the column was washed with 3 ml DCM:ethyl-acetate (9:1, v/v) to elute the $C_{37:2}$-alkenone, and with 4.5 ml DCM:ethyl-acetate (7:3, v/v) to elute the $C_{37:3}$-alkenone. The rest of the compounds were eluted with 5 ml of ethyl acetate. Every fraction was transferred into GC vials with the respective solvent for each fraction and then dried under N_2.

2.2.4. Clean-up of GDGTs

For the analysis of GDGTs, the dried polar fraction (MeOH) was dissolved in 500 µl of hexane:iso-propanol (99:1, v/v) and filtered through a 0.4 µm, 4 mm-diameter polytetrafluorethylene (PFTE) filter prior to analysis using high-pressure liquid chromatography/mass spectrometry (HPLC-MS) (Hopmans et al. 2000; section 2.3.3).

2.3. Identification and quantification of biomarkers

2.3.1. Gaschromatography and mass-spectrometry

Prior to analysis using GC and GC-MS, each fraction was redissolved in 100 µl n-hexane and ultrasonicated, before 50 µl were taken out and filled into a GC vial insert. A known amount (1–2 $\mu g\,\mu l^{-1}$) of Behenic Acid Methy Es-

ter (BAME, Sigma Aldrich, Figure 2.3) was added as an internal standard to the aliphatic fraction. 1.5 $\mu g\,\mu l^{-1}$ of C_{18}-Ketone (Sigma Aldrich, Figure 2.4) was added to the keto-fraction prior to analysis on the GC or GC-MS. Good column working conditions on the GC and GC-MS were ensured by running an external standard prior to every sequence and after every 10 samples (Figure 2.2). 10% of samples were remeasured to determine the 1σ error.

GC analysis was performed on an Agilent 7890B series gas chromatograph, equipped with a 7639ALS Autosampler, a BP5-MS column (SGE Analytical Science, 60 m length × 0.32 mm i.d. × 0.25 µm film thickness) and a Flame Ionization Detector (FID). Hydrogen was used as a carrier gas. Compound separation was achieved by using the following temperature program and in constant flow mode: injection of 1 µl at 70 °C, subsequent heating to 120 °C at 30 $°C\,min^{-1}$ and then to 320 °C at 3 $°C\,min^{-1}$ where the temperature was held for 20 min. GC-Mass spectrometry was performed on an Agilent 7890B series gas chromatograph coupled to an Agilent 5977A MSD with the same autosampler, capillary column and temperature program as for the GC. Helium was used as a carrier gas.

Hopane analysis was performed by running the GC-MS in selective ion mode (SIM)-mode, using m/z 191, a characteristic fragment ion of hopanes (Ourisson et al. 1979). To quantify the hopanes, a 17β,21β-hopane standard (Sigma Aldrich) at concentrations of 1 $mg\,ml^{-1}$, 0.5 $mg\,ml^{-1}$, 0.3 $mg\,ml^{-1}$ and 0.2 $mg\,ml^{-1}$ were injected before every 10 samples (Fig. 2.1). Fernene and Oleanene were both tentatively quantified by expressing the peak area of the

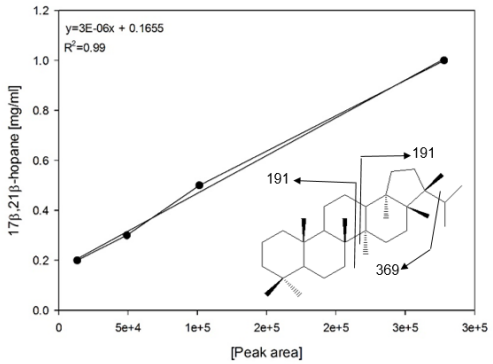

Figure 2.1.: Calibration curve of 17β,21β-hopane (Sigma Aldrich) in order to quantify hopanoids in U1425 samples, and fragmentation pattern of the standard compound.

respective mass fragment relative to m/z 191. The identification of pentacyclic triterpenoids is based on elution order, and mass spectra described in the literature and comparison to retention times (Moldowan et al. 1984; Ageta et al. 1987; Douka et al. 2001; Nytoft and Larsen 2001; Peters et al. 2005; Sinninghe Damsté et al. 2014; Appendix A).

2.3.2. GC-irMS

The hydrogen and carbon isotopic signatures of *n*-alkanes and alkenones were analyzed using an Agilent 7890A-GC interfaced with a GC5 Isoprime furnace and an Isoprime 100 ration Mass Spectrometer. The furnace tube of the GC5 Isoprime was held at 850 °C for $\delta^{13}C$, and was filled with CuO. For δD the furnace tube was filled with Chrome and was held at 1050 °C. A BP5-MS column (SGE Analytical Science; 60 m length × 0.32 mm i.d. × 0.25 µm film thick-

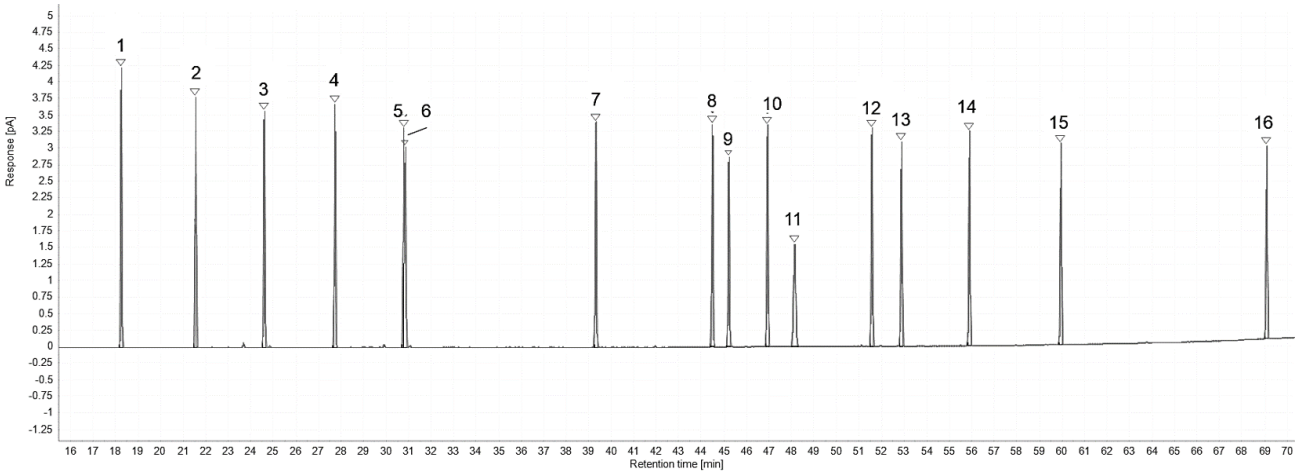

Figure 2.2.: External Standard used for quality control on the GC, and GC-MS. The concentration of all compounds is 10 µg ml^{-1}. Compounds 1-16 are: (1) *n*-hexadecane, (2) Pristane, (3) *n*-octadecane, (4) *n*-nonadecane, (5) *n*-eicosane, (6) octadecan-2-one, (7) *n*-tricosane, (8) *n*-pentacosane, (9) Behenic acid methyl ester, (10) *n*-hexacosane, (11) Squalane, (12) *n*-octacosane, (13) Cholestane, (14) *n*-triacontane, (15) *n*-dotriacontane, (16) *n*-heptatriacontane.

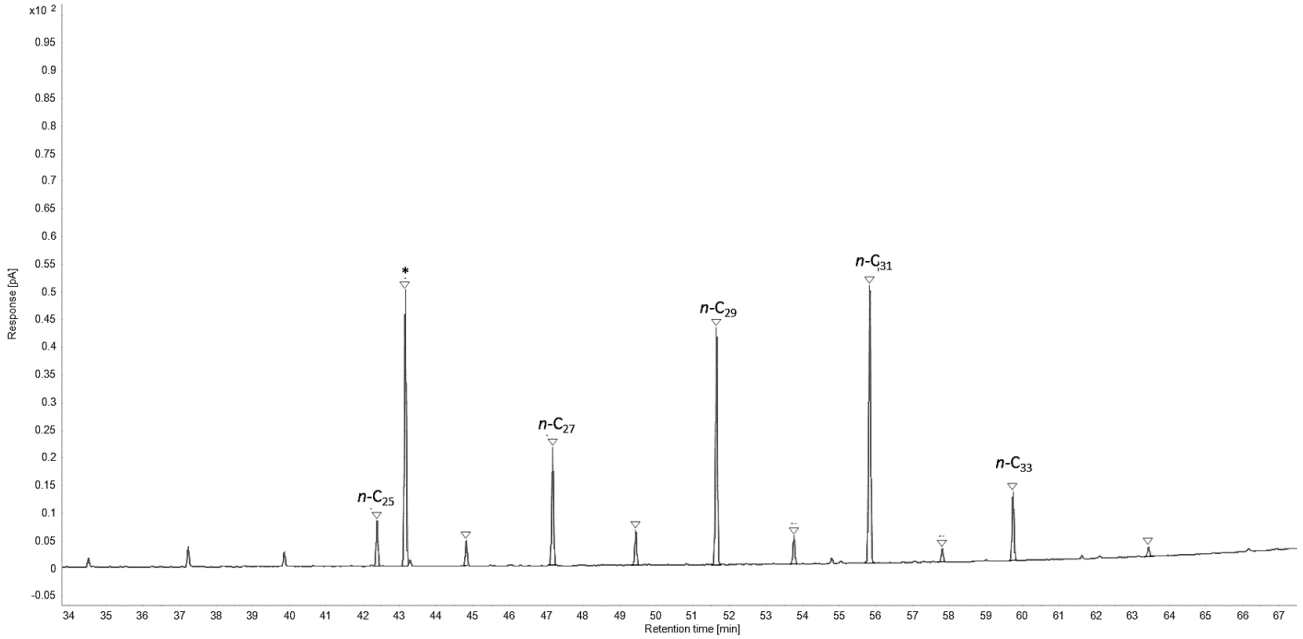

Figure 2.3.: Example of an aliphatic fraction, with the odd *n*-alkanes labeled. ∗ = internal standard, Behenic acid methyl ester (0.1 $\mu g\,\mu l^{-1}$).

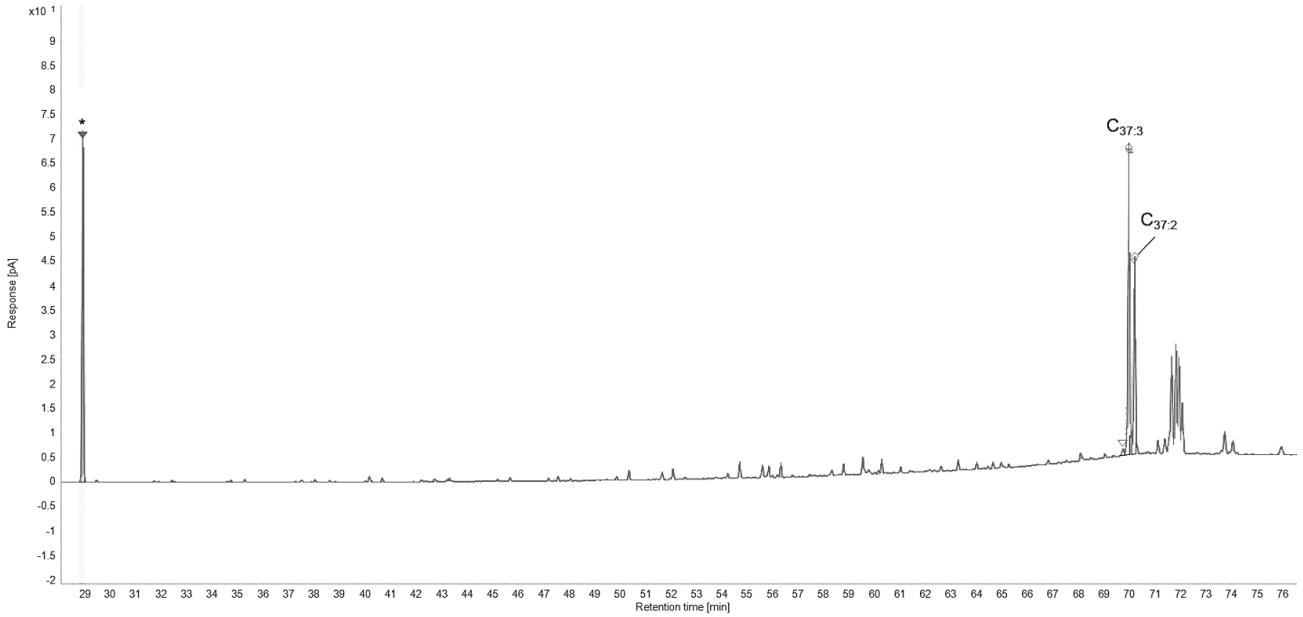

Figure 2.4.: Example of a keto fraction, with the main alkenones labeled. $*$ = internal standard, octadecan-2-one ($1.5\,\mu g\,\mu l^{-1}$).

ness) was used. The same GC temperature program was used as for GC and GC-MS analyses. All samples were analyzed against commercially available *n*-alkane standards (A. Schimmelmann Standard B2 and B4, Indiana University, Eq. 2.1), following the 'principle of identical treatment' (Werner and Brand 2001). These standards were analyzed in duplicates at the start of each measuring sequence, and at the end. The comparison of 'is' (from the B2 or B4 certificate) versus 'actual' (measured) values show no long- or short term systematic offset. The long-term monitoring of the B2/B4 standard revealed no indication of scale contraction, or concentration-effects. The isotopic composition of the *n*-alkanes as well as alkenones for both isotopic signatures, $\delta^{13}C$ and δD, was calculated by adding the difference between the true and measured B2 or B4 standard from the measured sample (Eq. 2.2). The difference between the true and measured standards was recalculated for every 10 samples. All samples were measured in duplicates.

$$\Delta_{standard} = \delta^{13}C_{true-std} - \delta^{13}C_{measured-std} \quad (2.1)$$

$$\delta^{13}C_{sample} = \delta^{13}C_{measured} + \Delta_{standard} \quad (2.2)$$

2.3.3. HPLC-MS

GDGT analyses were performed at the Faculty of Earth Environmental Sciences, Hokkaido University, Sapporo, Japan. The filtered polar fraction was analyzed using HPLC-MS, with an Agilent 1260 Infinity coupled to a 6130

Quadrupole LC/MS, equipped with Chemstation Software. The MS was run in full scan mode. Injection volumes varied between 10–20 µl, and separation was achieved using a Prevail Cyano column (2.1 mm×150 mm, 3 µm film thickness) at 30 °C. The flow rate was 0.2 ml min^{-1}, isocratic with 99% hexane and 1% 2-propanol for the first 5 minutes, followed by am linear gradient to 1.8% 2-propanol. The column was cleaned after each run, by back flushing hexane:2-propanol (90:10, v/v) at 0.2 ml min^{-1} for 10 minutes (Schouten et al. 2007). A working standard was run after every 20 samples. 20 samples (10%) were remeasured to determine the 1σ error.

3. Location and geological history of core site U1425

3.1. Core location and modern day setting

The Japan Sea, located between continental Eurasia and Japan, has a surface of 1×10^6 km^{2}and an average depth of 1350 m (Tada 2004). It consists of the Japan Basin (3700 m deep), Ulleung Basin (2500 m deep) and the Yamato Basin (2900 m deep). This study is based on core samples taken from ODP Site 797 (Leg 127/128, depth: 2862 m) located in the Yamato Basin, and from IODP Expedition 346, Site U1425 (depth: 1909 m) located on the slope of the Yamato Rise. The Yamato Rise is a submerged continental remnant (Xu et al. 2016), only 100 km to the north of Site 797. The Japan Sea is connected to the Pacific via the Tsugaru Strait (130 m depth), to the East China Sea (ECS) via the Tsushima Strait (130 m depth) and to the Okhotsk Sea via the Soya Strait (55 m depth) and the Mamiya Strait (20 m depth). The only

current flowing through the Japan Sea is the Tsushima Warm Current (TWC, Fig. 3.1), which forms due to mixing of Kuroshio Current waters with the East China Sea Coastal Water (ECSCW) at a rate of approximately 7:3 (Tada 2004). The TWC is split in three branches as it flows into the Japan Sea. The most stable branch flows at depths of less than 200 m along the west coast of Honshu Island. The second branch flows along the outer shelf of Honshu Island, and the third branch flows along the Korean shelf. Both these latter branches are unstable and strongly seasonal, with transport fluxes increased in summer and close to zero in winter (Tada 2004; and references therein). The branches merge again at the Tsugaru Strait, and a major part of the TWC flows through the Tsugaru Strait into the Pacific, while a small amount continues to flow through the Soya Strait (Tada 2004). Furthermore, the Liman Current (LC)/North Korean Cold Current (NKCC) flows southwards along the coast of Russia, China and North Korea (Fig. 3.1), and across the Japan Sea. Where the NKCC merges with the TWC, the subpolar front is formed and exits via the Soya strait. Both sampling sites are located within the subpolar front, whilst U1425 is also under the influence of the first branch of the TWC during summer (Fig. 3.1).

Today, the Japan Sea is very well ventilated at all depths, which is due to extensive open-ocean convection and brine rejection due to sea ice formation (Talley et al. 2003; Tada 2004; Talley et al. 2006). The formation of the Japan Sea Proper Water (JSPW) is a result of these processes, and it makes the Japan Sea unique in generating its own deep-water mass (Tada 2004). The JSPW is

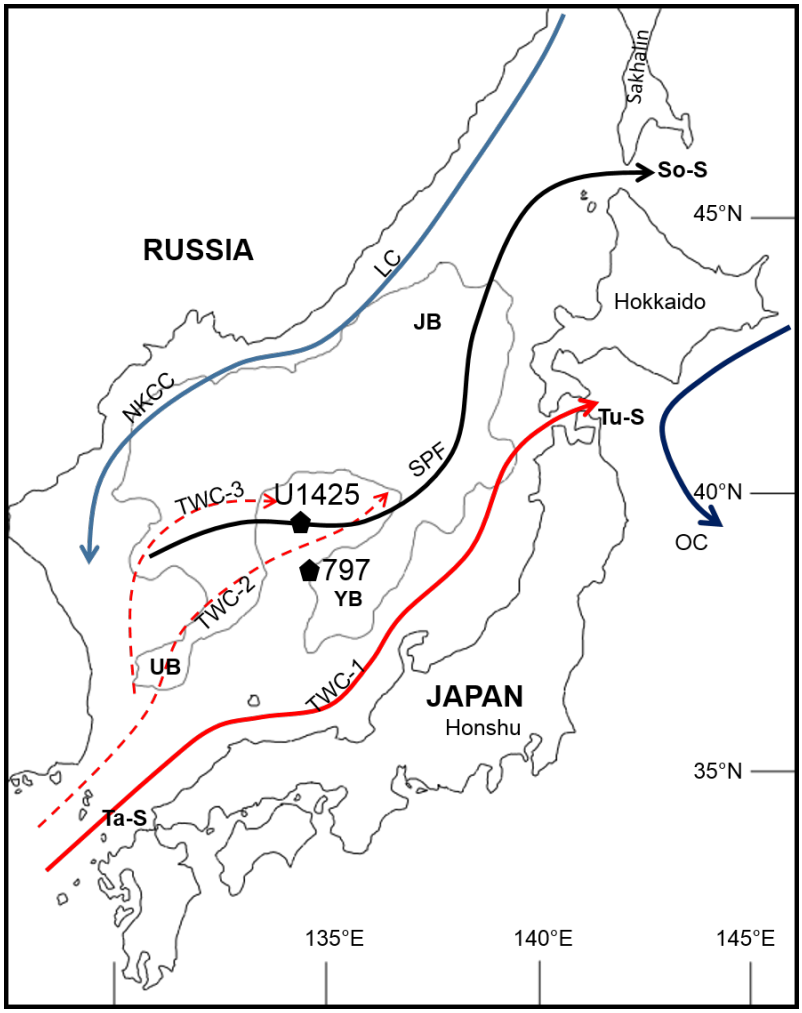

Figure 3.1.: Japan Sea and its major oceanographic currents, the Tsushima Warm Current (TWC-1; red) and its second and third branches, the Tsushima Warm Current-2 and -3 (TWC-2, -3), Liman Current (LC; blue) which becomes the North Korean Cold Current (NKCC), the subpolar front (SPF, black), and the Oyashio Current (OC, dark blue arrow). Also indicated is IODP 346 sampling site U1425 (134.44°E, 39.49°N) and ODP 127/128 site 797 (134.54°E, 38.616°N). Gateways are labelled as Tsushima Strait (Ta-S), Tsugaru Strait (Tu-S), and Soya Strait (So-S). The grey line outlines the Japan Basin (JB), Yamato Basin (YB) and Ulleung Basin (UB).

present at depths below 300 m, and is characterized by a constant salinity of 34.06‰ and temperatures of 0.6 °C. As the formation of this deep water body is heavily dependent on sea ice formation and the average residence time for intermediate and bottom waters in the Japan Sea is 50-100 years, oxygen contents in this deep water are depleted within a few decades (Tada 2004; Talley et al. 2006; and references therein). In the context of climate change, dissolved oxygen contents of these bottom-waters could be completely depleted within the next 200 years (Talley et al. 2006).

3.2. Paleoceanographic history of the Japan Sea

The Japan Sea is widely acknowledged as having evolved during back-arc spreading (Otofuji et al. 1985; Iijima and Tada 1990; Ingle 1992). However, Jolivet et al. (1994) argue, that the evolution of the Japan Sea is a combination of back-arc spreading and the deformation of Asia due to the collision with India, classifying the Japan Sea as a pull-apart basin. The early Oligocene marks the timing of incipient opening of the Japan Sea, which was triggered by crustal thinning and rifting in the northern part of the Japan Sea (Xu et al. 2016). During this early rift stage, non-marine volcanic/sedimentary deposits are deposited in the Japan Basin (Xu et al. 2016). Seafloor spreading started in the late Oligocene, and the south of the Japan Sea experienced expansion

during which the Yamato Basin and Ulleung Basin were formed (Tamaki et al. 1992; Xu et al. 2016). These basins reached lower bathyal depths rapidly (Iijima and Tada 1990). Otofuji and Matsuda (1983) and Otofuji et al. (1985) conclude that the clockwise and anti-clockwise rotation of SW- and NE-Japan stopped at 12 Ma ago, marking the time of back-arc closure which continues until present. Presently, the Japan Sea is in the stage of tectonic destruction (Xu et al. 2016). At 10 Ma, the southern part of the Japan Sea was already lifted above sea level, while the northern part remained below the sea surface. This can be regarded as a paleo-bay stage of the Japan Sea (Fig. 3.2). The Sakhalin Island, today separating the Japan and Okhotsk Sea, was not developed at 10 Ma. The southern Sakhalin Island, including northern Hokkaido displays two distinct marine cycles: from the late Oligocene to early Miocene, and from the mid-Miocene to Pliocene (Xu et al. 2016). Consequently, during these times when the southern Sakhalin Island was submerged, the Okhotsk Sea and Japan Sea were connected with each other, which should be considered when interpreting climate signals derived from sediments in the Japan Sea. The marine cycles are interrupted by an abrupt phase of rapid uplift and subaerial exposure during the early mid Miocene, possibly caused by strike-slip motion (Xu et al. 2016). Rapid subsidence followed this phase at around 15 Ma, and the section reached 2000 m depth at 13 Ma (Xu et al. 2016). Since the beginning of the Pliocene, the southern Sakhalin Island experiences uplift again, causing the depositional environment to transform from bathyal sea to shallow shelf deposits. Non-marine deposits appear during the Pleistocene,

indicating the uplift of the Sakhalin and Hokkaido Islands (Xu et al. 2016; Fig. 3.2). During this time, the proto-Tsugaru Strait also experienced shoaling (Tada 1994). The fact that non-marine deposits appear relatively late in the stratigraphy implies that only from circa 3.6 Ma on, the Japan Sea and Okhotsk Sea were separated from each other (Xu et al. 2016). In the south of the Japan Sea, the Tsushima land bridge blocked the inflow of the TWC from the mid -Miocene through most of the Pliocene (Iijima and Tada 1990; Tada 1994; Fig. 3.2). During the late Pliocene, although the land bridge still existed, it is likely that a shallow waterway opened temporarily through the Tsushima Strait. The land bridge re-opened in the Pleistocene, but due to the shallow sill depth the TWC can only enter the Japan Sea during sea level high stands (Tada 1994). The shallow sill depth and the influx of the TWC had an impact on the ventilation of the Japan Sea in the past. During glacial stages, the relative proportion of the ECSCW increases, because the river mouths of the Yellow River and the Yangtze River move closer to the Tsushima Strait during sea level low stands (Tada 2004). In interglacials, already 40-70% of freshwater contained in the ECS are discharged into the Japan Sea, during glacial stages this proportion increases (Tada 2004). The result is the formation of a thick fresh water cap on top of the water column (Tada 2004; Oba 1991). This density stratification prevents the sinking of overlying water masses during the glacial stages, and the Japan Sea becomes quickly starved in oxygen at intermediate and bottom water depths (Tada 2004; Talley et al. 2003).

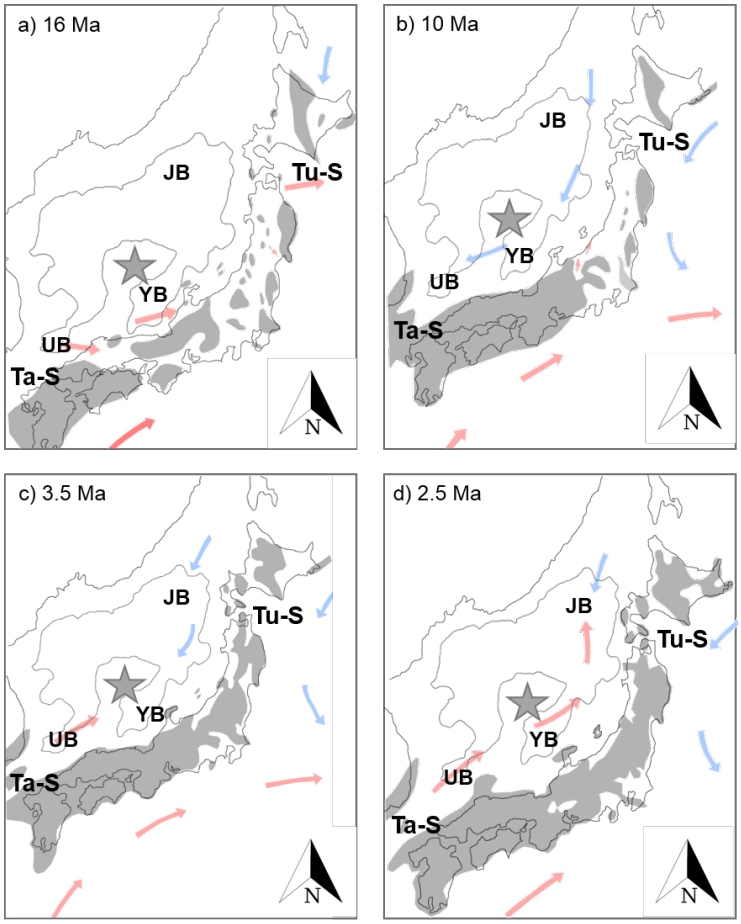

Figure 3.2.: Evolution of the paleogeography of the Japan Sea and surrounding islands, spanning a) 18-15 Ma, b) 12-7 Ma, c) 7-3 Ma, and d) 3-1.7 Ma. Grey shaded areas indicate paleoshorelines of land mass, red arrows indicate paleo-warm currents, blue arrows indicate paleo-cold currents. Star indicates sampling area. Tsushima Strait (Ta-S), Tsugaru Strait (Tu-S). Grey outline indicates the Japan Basin (JB), Yamato Basin (YB), and Ulleung Basin (UB). Star marks the sampling sites. Maps modified after Kano et al. (1991).

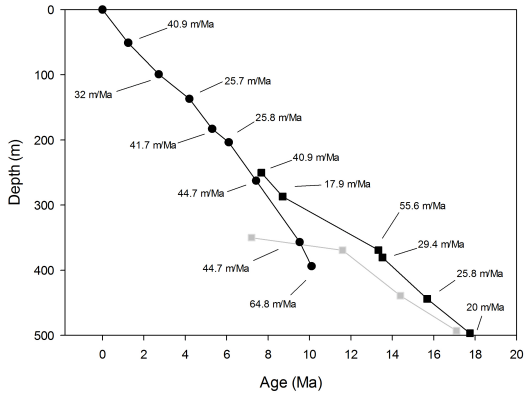

Figure 3.3.: Age model of spliced cores U1425 and 797. Black circles indicate the ages for Site U1425, while black squares indicate the ages for Site 797. Diatom datum levels of Site 797 were standardized to the paleomagnetic reference time scale of Berggren et al. (1985) (Koizumi 1990).

3.3. Age model of core U1425

Age models for both cores are based on the shipboard biostratigraphy (Tamaki et al. 1992; Tada et al. 2015). The biostratigraphy from Site 797 was updated for this study in order to combine the data from the cores at both sites and convert all ages to the Neogene timescale of GTS2012 (Gradstein and Ogg 2012). Microfossils occurring in U1425 were looked for in Site 797. Where diatom fossils were used as tracers, the first/last occurrences (FO/LO) from Koizumi (1990) were then updated with FO/LO as found by Expedition 346. Additionally, FO/LO of nannofossils in Site 797 were adjusted for the orbitally

tuned FO/LO from Backman et al. (2012) and the age model for Site 797 was subsequently recalculated. The re-evaluation of the age model for Site 797 allows the splicing of the data derived from Site 797 and Site 1425 (Fig. 3.3).

4. Evolution of sea surface temperatures in the Japan Sea since the mid-Miocene - a coupled organic temperature proxy approach using $U^{K'}_{37}$ and TEX_{86}

Abstract

The Japan Sea is regarded as a climate change hot spot, warming more rapidly than other seas and oceans and is projected to warm another 3–6 °C by 2100. This study presents the first Japan Sea derived sea surface temperature (SST)

records, spanning the last 18 million years (Ma), from the mid-Miocene to the Pleistocene using the unsaturated alkenone ($U^{K'}_{37}$) and the tetraether (TEX_{86}) indices. Both records show a distinctive cooling trend over the last 18 Ma. The good agreement between the data presented here, and proxy records from the northern Pacific and the $\delta^{18}O$ global stack of benthic foraminifera indicates that the Japan Sea cooled in response to the global descent into today's ice house climate. Throughout the Pliocene/Pleistocene the TEX_{86} and $U^{K'}_{37}$ records show increasing temperature fluctuations at higher frequencies than in the late Miocene. This change may be attributed to the progressive dominance of 100 kyr Milankovich cycles that is also seen in the advent of glacial/interglacial cycles. The sensitivity of the Japan Sea to eustatic sea level change associated with glacial/interglacial cycles led to a restricted influx of Tsushima Current warm water to the Japan Sea, and a concomitant expansion of cold waters from the northern Japan Sea, leading to these stark temperature fluctuations. This study provides important SST estimates for the Miocene and Pliocene, the multi-proxy approach employed here aids the validation of the observed SST trends. The observed climate deterioration, in agreement with other SST records from the mid latitudes, was likely driven by globally operating climate mechanisms, perhaps decreasing atmospheric CO_2 concentrations.

4.1. Introduction

Global near surface ocean temperatures have risen by 0.13 °C per decade (Rhein et al. 2013). The rise in sea surface temperatures (SST) has been attributed to increased anthropogenic greenhouse gas emissions (IPCC 1990; Stocker 2013). In the Japan Sea, bordered by Japan, Korea and Eurasia an even stronger warming trend has been observed, with winter SSTs increasing by 1.6–2.4 °C over the last century (Yamano et al. 2011). As a result, the Japan Sea is regarded as a climate change hot spot, warming more rapidly than any other seas or oceans (Hartman et al. 2013), with a further 3–6 °C warming projected until 2100 (Kolstad and Bracegirdle 2008). With predicted temperatures 2–3 °C warmer than pre-industrial levels, many studies have focused on the Pliocene as an analogue for projected climate change over the coming 200 years (Robinson et al. 2008). However, Pliocene alkenone-derived pCO_2 estimates range from 300 to 400 ppm (Seki et al. 2010), and therefore coincide with current CO_2 levels between 1975 and 2016 (Stocker 2013). By 2100, atmospheric CO_2 concentrations are predicted to reach 900–1000 ppm under the 'business-as-usual' RCP8.5 scenario (Rhein et al. 2013). The most recent geological analogue of similarly high CO_2 concentrations was the Mid-Miocene period, with reconstructed atmospheric CO_2 levels between 400–850 ppm (Kürschner et al. 2008; Beerling and Royer 2011; Zhang et al. 2013). Thus this study presents the first long-term SST record from the Japan Sea spanning the last 18 million years, from the mid-Miocene to the Pleistocene.

The SST records in this study are derived from two widely used and well established temperature proxies, the alkenone unsaturation index ($U^{K'}_{37}$) and the tetraether index of tetraethers consisting of 86 carbons (TEX_{86}) (Brassell et al. 1986; Schouten et al. 2002). A key requirement for organic geochemical temperature proxies is that they can be related to specific source organisms. Ideally the precursor organisms should be ubiquitous and the proxy calibrations should cover a wide temperature range. Brassell et al. (1986) and Prahl and Wakeham (1987) proposed an unsaturation index ($U^{K'}_{37}$), derived from photosynthetic haptophyte algae, as an organic SST proxy. The relative distribution of $C_{37:2}$ and $C_{37:3}$-alkenones produced by these haptophytes varies with the ambient temperature, wherein the relative amount of the more unsaturated alkenone increases with decreasing temperature. The exact function of alkenones within the cell is unknown to this day (Epstein et al. 1998; Eltgroth et al. 2005). The depth at which haptophyte organisms produce alkenones is limited to the photic zone habitat, which in the North Pacific and the Japan Sea typically ranges between the sea surface and 100 m water depth (Lee and Schneider 2005; Lee et al. 2011). However, alkenone-derived SSTs correspond best to the first 10 m of the water column (Müller et al. 1998; Ohkushi et al. 2003). Generally, alkenones reflect mean annual SST except in regions with a shortened season for phytoplankton growth (Sikes et al. 2005; Conte et al. 2006; Yamamoto et al. 2007; Versteegh et al. 2007).

An alternative proxy to reconstructing SSTs is the TEX_{86} proxy which is based on the relative abundance of isoprenoidal glycerol dialkyl glycerol te-

traethers (GDGTs) (Schouten et al. 2002). GDGTs are membrane constituents of Archaea (Schouten et al. 2013; and references therein), but the main isoprenoidal GDGT source for the TEX_{86} proxy are assumed to be marine Thaumarchaeota which are ubiquitous in the world's oceans (Karner et al. 2001). The relative distribution of GDGTs with differing amounts (0–4) of cyclopentyl moieties is thought to reflect ambient growth temperature (De Rosa and Gambacorta 1988; Uda et al. 2001; Schouten et al. 2002; Zhu et al. 2016). The additional GDGT Crenarchaeol and its regio-isomer contains an additional cyclohexyl moiety (Schouten et al. 2002), and are also sensitive to temperature changes. Although GDGTs are produced throughout the entire water column, and TEX_{86} being sometimes affected by other environmental parameters than temperature (Elling et al. 2015; Qin et al. 2015; Hurley et al. 2016), it has been shown that TEX_{86} generally reflects SSTs (Wuchter et al. 2005; Yamamoto et al. 2012; Turich et al. 2013; Chen et al. 2014). $U^{K'}_{37}$ and TEX_{86} indices are ideal tools for temperature reconstruction in the Japan Sea, as it lacks a well preserved microfossil record that could otherwise be used for SST reconstructions (Tamaki et al. 1992). Both organic temperature proxies span a wide range of temperatures, and because of their spatial and temporal occurrence in sediments in the Japan Sea, facilitate the reconstruction of the SST trend in the context of global climate change.

Generating paired SST data sets using these two methodologies provides independent paleothermometer estimates, while allowing an assessment of possible ecological or preservation biases on reconstructed SSTs that would not

be possible with single-proxy studies. This approach aims at disentangling the biological and ecological influences on the proxies from the climate signal itself. This study also considers the most likely driving mechanism for the observed SST variations within the Japan Sea during the last 18 Ma. An improved understanding of driving mechanisms for SST changes in the past may in turn help to generate more accurate projections of the Japan Sea response to ongoing anthropogenic greenhouse gas emissions.

4.2. Methods

The description of the sampling site, the age model, and the biomarker extraction procedure and analysis, can be found in Chapter 3 and 2 respectively.

4.3. Results

$C_{37:2}$- and $C_{37:3}$-alkenones were only detected at Site U1425, in sediments less than 8 million years old (Figure 4.1). The $C_{37:4}$-alkenone was detected in a few samples, and the content (relative to the other alkenones) never exceeds 0.5%. Summed $C_{37:2}$- and $C_{37:3}$-alkenone concentrations vary between 0.1–25 μg dry sediment (DS). The reconstructed $U^{K'}_{37}$-SSTs (Eq. 1.9, 1.10) vary between 8–25 °C throughout the whole record. Late Miocene $U^{K'}_{37}$-SSTs drop from 23 °C to 16 °C. Pliocene and Pleistocene $U^{K'}_{37}$-SSTs vary between 12–20 °C, and 9–18 °C, respectively. The $U^{K'}_{37}$-SST record displays a distinctive trend towards

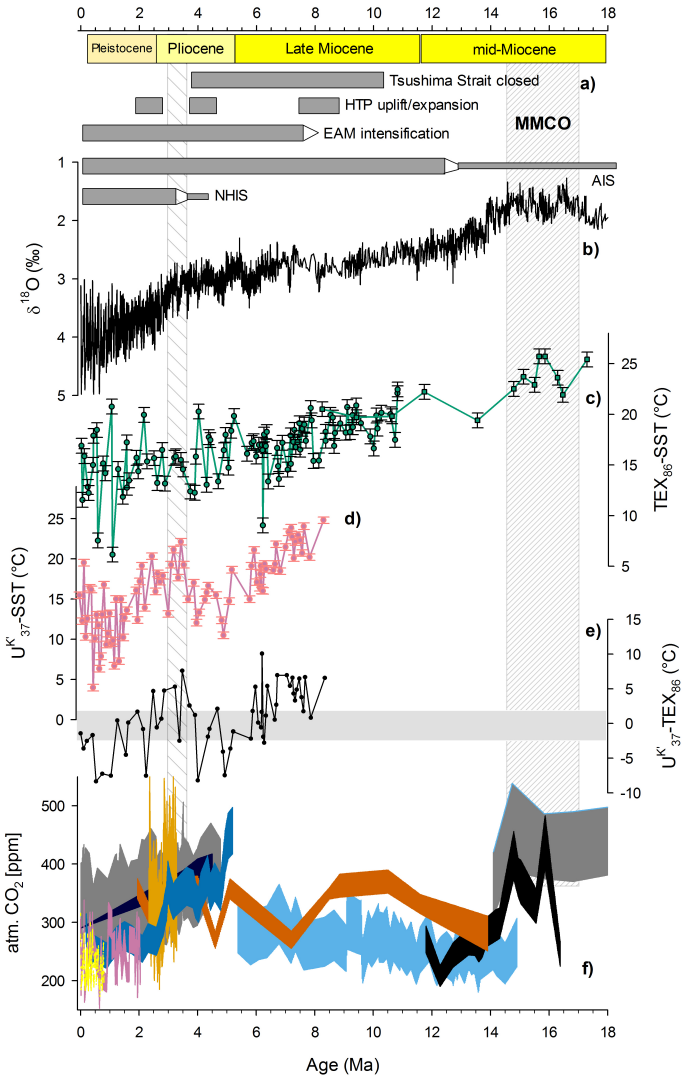

Figure 4.1.: Japan Sea SST records compared to (a) Tectonic and climate events during the studied time interval (after Zachos et al. (2008): Himalaya-Tibet Plateau uplift/expansion (HTP), East Asian Monsoon (EAM) intensification, Antarctic Ice sheet expansion (AIS), Northern Hemisphere Ice sheet expansion (NHIS)), (b) $\delta^{18}O$ benthic foraminifera stack (Zachos et al. 2008), (c) TEX_{86}-SST with 1σ error (d) $U^{K'}_{37}$-SST with 1σ error, (e) ΔSST, grey bar indicates combined calibration error of 2.0 °C, (f) atm. CO_2 reconstructions after Pagani et al. (1999a; green) and Pagani et al. (2010; turquoise), Seki et al. (2010; dark blue), Beerling and Royer (2011; purple), Foster et al. (2012; black), Zhang et al. (2013; grey), Martínez-Botí et al. (2015; red), Hönisch et al. (2009; dark green), Bereiter et al. (2015; yellow). Grey shades refer to mid-Miocene Climate Optimum (MMCO), late Miocene cooling (LMC), mid-Pliocene Warm Period (m-PWP).

colder temperatures from the late Miocene to present. Comparing the TEX_{86}-SST to $U^{K'}_{37}$ shows elevated $U^{K'}_{37}$-SSTs by 5 °C during the late Miocene (6–8 Ma) and mid-to late Pliocene (2.5–4 Ma) (Figure 4.1).

GDGTs were detected in all samples, at Sites U1425 and 797. It is acknowledged that the choice of a TEX_{86} calibration is very controversial, and subject to a lot of uncertainty (Tierney 2014; and references therein). Therefore, the TEX_{86} calibration of Kim et al. (2008) is used to discuss SST changes in the Japan Sea. However, as shown in Fig. 4.2, there is virtually no difference between TEX_{86} (Kim et al. 2008; Eq. 1.12, 1.13), TEX^{H}_{86} (Kim et al. 2010; Eq. 1.16, 1.17), and $TEX^{Bayspar}_{86}$ (Tierney and Tingley 2014). For the period between 10–18 Ma, the different calibrations are off-set by circa 2 °C but have similar overall trends (Figure 4.2). At 6 Ma, TEX^{L}_{86}-SSTs (Eq. 1.14, 1.15) display a sharp temperature drop of 10 °C, which is not observed in the other TEX_{86}-SSTs records (Figure 4.2). The temperature difference between the TEX_{86} records and TEX^{L}_{86}-SSTs is observed for another 2 Ma, before temperatures are briefly similar at 3.5–4 Ma. Subsequently, the trends of the TEX_{86}- and TEX^{L}_{86}-SSTs are similar, but the temperature difference increases once again.

Overall, the reconstructed TEX_{86}-SSTs ranged from 10–25 °C. Mid-Miocene SSTs range between 20–25 °C, while late Miocene temperatures range between 14–22 °C. Pliocene temperatures range from 13–18 °C and Pleistocene temperatures fluctuate between 9–17 °C. The TEX_{86}-SST record displays a general trend towards colder temperatures from mid-Miocene to Present. The

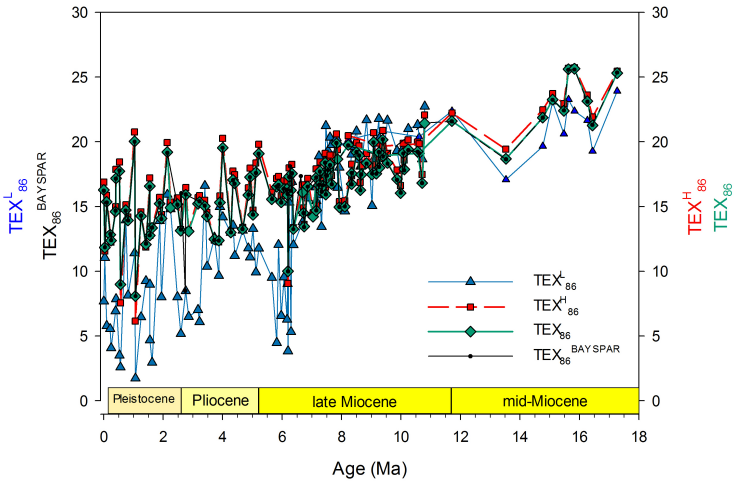

Figure 4.2.: Comparison of TEX^{H}_{86}-SST (red),TEX^{L}_{86}-SST (blue) (both Kim et al. (2010)), TEX_{86} (Kim et al. 2008; black), and Bayspar (Tierney and Tingley 2014; green) calibrations applied to the GDGT distributions in core U1425 and 797.

GDGTs in these samples may be influenced by soil derived isoprenoidal GDGTs, in-situ sedimentary produced GDGTs, and/or variations in growth phase and degree of oxygenation of the water column (Weijers et al. 2006a; Lipp and Hinrichs 2009; Elling et al. 2015; Zhu et al. 2016). The BIT value (Eq. 1.2) for U1425 and 797 ranges between 0 and 0.5 (Fig. 4.3a). The percentage of GDGT-0 (%GDGT-0, Eq. 1.19) increases over the studied interval, from 24% to an average of 50%. Peak %GDGT-0 of 70% and more occur during the mid-Miocene (Fig. 4.3c). The methane index (MI, Eq. 1.20) varies between 0.1 and 0.2. Peak MI values of 0.6 in the mid-Miocene occur at the same time as peak %GDGT-0 and BIT values (Fig. 4.3b). The ring index (Zhang et al. 2016; Eq. 1.21–1.23) varies between 0.1 and 1.6, and most ΔRI>0.3 fall into

the mid- and late Miocene (Fig. 4.3d). Subsequently, data points with a high BIT, MI and/or ΔRI were removed from the data set prior to interpretation. The TEX_{86}-SST record is derived from two spliced sediment cores, from Sites U1425 and 797. There is no visible offset between 7–10 Ma (n=4 (797), n=25 (U1425)) where the samples of both sites overlap. Therefore it is hypothesized that the splicing of the two sediment cores does not introduce artifacts that might lead to a misinterpretation of the results.

4.4. Discussion

4.4.1. Fidelity of the TEX_{86}- and $U_{37}^{K'}$ temperature signal

Modern SSTs (1961-2004) at the drill Sites 797 and U1425 show large intra-annual variability. The SST at Site U1425 is 7 °C in February (coldest month) and 24 °C in August (warmest month), with a mean annual SST of 16 °C. SSTs at Site 797 are 9 °C (February), 24 °C (August), and a mean annual SST of 17 °C (Japan Oceanographic Data Centre, JODC). SSTs in the Japan Sea are thought to have been similar to today throughout the last 5000 years (Lee et al. 2003). The youngest sample at Site U1425 in this study is 3100 years old, and considered a 'surface/modern sample'. The $U_{37}^{K'}$-SST of the modern sample (15 °C±0.4) is in good agreement with modern mean annual temperatures. The TEX_{86}-SST of the modern sample (16.3 °C±0.7) is also in good agreement with the mean annual temperature. Therefore, the youngest parts of the

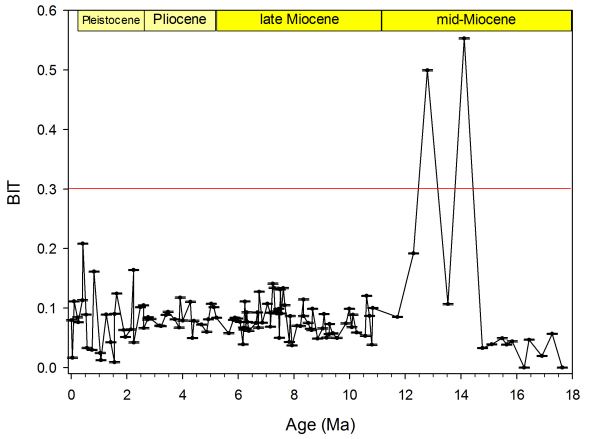

(a) BIT

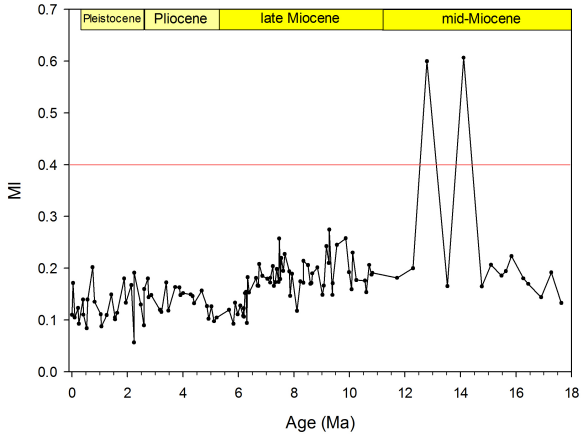

(b) MI

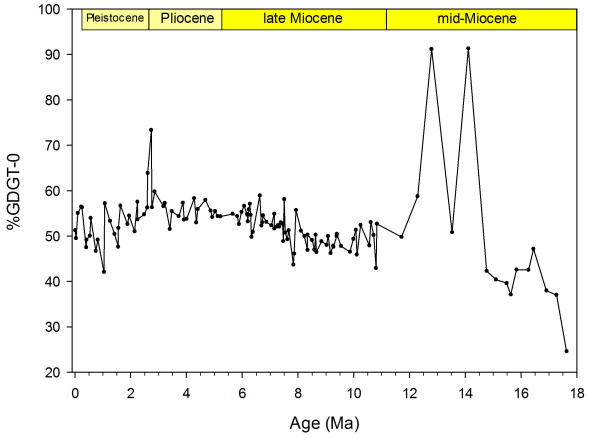

(c) %GDGT-0

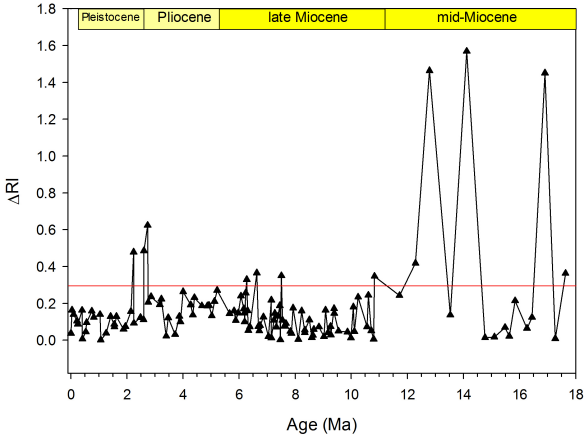

(d) TEX_{86} record, with ΔRI>0.3 marked as red dots

Figure 4.3.: BIT, MI, %GDGT-0 and RI for U1425 and 797. Red lines indicate thresholds given in the literature (Weijers et al. 2006b; Zhang et al. 2011).

TEX_{86}- and $U^{K'}_{37}$-SST records reflect mean annual SSTs in the Japan Sea. Despite the broad agreement between the TEX_{86}- and $U^{K'}_{37}$-SST records, it should be kept in mind that both proxies are derived from different organisms. As a consequence, it can be expected that each proxy reflects SSTs during a certain growing season (Müller et al. 1998; Herfort et al. 2006), although this is usually a post-hoc assumption to explain the mismatch between SSTs and expected mean annual SSTs. Secondly, the depth habitat for Euryachaeota and haptophytes differ. $U^{K'}_{37}$-derived SST reconstructions usually reflect best the temperature of the first 10 m of the water column (Müller et al. 1998; Ohkouchi et al. 1999), while TEX_{86} derived SSTs can correspond to temperatures of depths at around 40–150 m (Mollenhauer et al. 2015; Chen et al. 2016), which is not acknowledged in the calibration (Ho and Laepple 2015) and therefore often causes erroneous SST estimates. These are important factors that should be kept in mind during the interpretation of these SST records or when comparing them to each other.

There are several factors that can affect the robustness of any TEX_{86} record and understanding their role in creating potential biases in any SST reconstruction is essential (Schouten et al. 2013). For example, a TEX_{86} record can be influenced by non-thermal effects such as seasonality (Herfort et al. 2006), water depth (Wei et al. 2011; Taylor et al. 2013; Hernandez-Sanchez et al. 2014; Villanueva et al. 2014), *in-situ* GDGT production in sediments (Lipp and Hinrichs 2009; Zhang et al. 2011), sediment diagenesis (Schouten et al. 2004), and catchment-derived isoprenoid GDGTs from Thaumarchaeota liv-

ing in soils (Weijers et al. 2006b; Tierney 2014). Thaumarcheota production is highest in winter when no other phytoplankton are blooming, and consequently a bias towards winter SSTs can occur in some basins (Herfort et al. 2006). TEX_{86}-SSTs of this study, compared to observed SSTs, show good agreement at the site suggesting that for the modern times, a seasonal bias can be excluded. A sediment trap study from the North Pacific, relatively proximal from the Tsugaru Strait (Yamamoto et al. 2012), found the flux-weighted TEX_{86} to remain constant with depth and corresponding roughly with mean annual sea surface temperature, supporting the idea that surface water Thaumarcheota derived GDGTs are preferably delivered to the sea floor (Yamamoto et al. 2012). As a precautionary measure, seasonal biases for past periods cannot be excluded.

The BIT index for the last 18 Ma shows generally low values, close to 0.1, and in rare cases up to 0.2. This is below the the suggested threshold of 0.3 (Weijers et al. 2006b), and indicates no significant influence of soil-derived isoprenoidal GDGTs on the TEX_{86} record. The exception is the mid-Miocene, where BIT reaches peak values of 0.6. The MI varies around 0.2 for the studied interval, and shows no clear trend over time. During the mid-Miocene, the MI reaches peak values of around 0.5, which is above the 0.4 threshold suggested by Zhang et al. (2011). Interestingly, a high MI occurs at the same time as peak BIT values. The increasing trend in %GDGT-0 over the last 18 Ma is characterized by a sudden spike in %GDGT-0 to up to 90% GDGT-0. This sudden increase also occurs at the same time as increased BIT and MI values. Zhang

et al. (2016) recently introduced the ring index (ΔRI) to determine whether factors other than temperature influence the TEX_{86} proxy. The authors suggest the index is more sensitive than the application of other commonly used ratios, such as the GDGT-0/Crenarchaeol (%) ratio, methane index (MI) or BIT alone (Zhang et al. 2016). In this study, more than 86% of samples show an ΔRI≤0.3. Samples with a ΔRI greater than 0.3 include the BIT, MI and %GDGT-0 excursions discussed above. Subsequently, these excursions were removed from the data set. Interestingly, not all samples with an ΔRI>0.3 in this study are associated with a high MI, %GDGT-0 or high BIT. To avoid a biased TEX_{86}-SST record, all samples with a ΔRI>0.3 were removed from the record, and most of these samples fell within the mid-Miocene (Fig. 4.3d).

The temperature offset between the TEX_{86}- and TEX_{86}^{L}-SST records from 6 Ma onwards is associated with a decrease of the GDGT-2/GDGT-3 ratio (Fig. 4.4). The GDGT-2/GDGT-3 ratio is a focus of ongoing debate as this ratio changes significantly if water depth is either shallower, or deeper than 1000 m at a sediment sample site (Wei et al. 2011; Taylor et al. 2013; Villanueva et al. 2014; Kim et al. 2015). This depth related variation in the GDGT-2/GDGT-3 ratio is thought to be gene-related (Villanueva et al. 2014), thus is used to assess the contribution of deep-water dwelling Archea (Schouten et al. 2012; Taylor et al. 2013). The GDGT-2/GDGT-3 ratio change can cause the TEX_{86}^{H}-index to overestimate (past) SSTs when samples are recovered from depths shallower than 1000 m (Kim et al. 2015). Thus, care must be taken to correctly interpret the TEX_{86}^{H}-SST signal, so as not to confuse a summer-related warm

bias with a depth-related warm bias. In this study, samples are derived from at least 1900 m below the sea surface. Furthermore, the Yamato Basin formed in the late Oligocene by extension of the south Japan Sea (Xu et al. 2016), and rapidly subsided to lower bathyal depths (Iijima and Tada 1990), so that a depth related warm bias can be excluded. The observed GDGT-2/GDGT-3 shift occurs at a time where the proto-Tsugaru Strait shoaled and sealed the Japan Sea off from the open Pacific, followed by a productivity breakdown for approximately 0.5 Ma in the Japan Sea (K. Horikawa, pers. comm.). Primary productivity seems to act as a primary modulator of GDGT distributions in sediment trap studies (Yamamoto et al. 2012), with increased contribution of deep water GDGTs when primary productivity is low (Yamamoto et al. 2012; Taylor et al. 2013). An increase in the GDGT-2/GDGT-3 ratio is therefore associated with a shift in export dynamics, and changes in this ratio are a principal control factor on TEX_{86}^{L}, since the GDGT-3 was removed from the numerator (see Eq. 1.14), which is why this proxy reacts sensitive to changes in GDGT-2/GDGT-3 and not the other TEX_{86} indices (Kim et al. 2010; Taylor et al. 2013). For the Japan Sea, the observation of GDGT-2/GDGT-3 patterns in relation to primary productivity is in stark contrast to the findings of the aforementioned studies. The productivity breakdown did not increase but decrease the GDGT-2/GDGT-3 ratio, and subsequently TEX_{86}^{L} decreases too. It should therefore be considered that the notion of a productivity induced contribution in deep water GDGTs reflected in GDGT-2/GDGT-3 ratios is oversimplified. The GDGT-2/GDGT-3 ratio changes can also reflect a shift in the

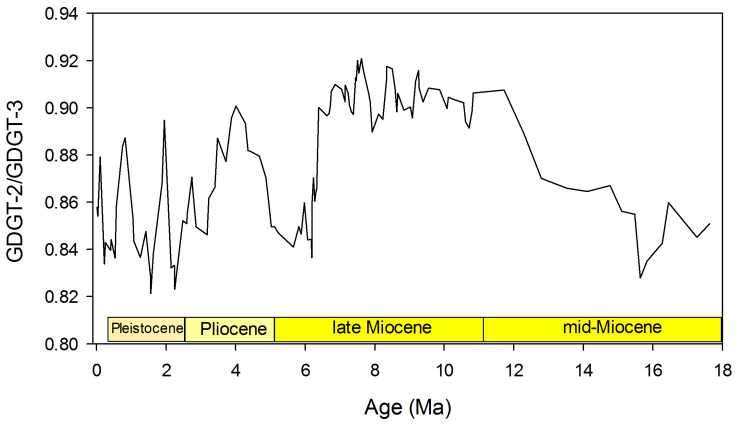

Figure 4.4.: GDGT-2/GDGT-3 ratio for the studied interval, associated with export productivity, and affecting the TEX_{86} records at depths <1000 m.

Thaumarchaeota community, due to changes in nutrient availability or redox state of the water column, which are also related to primary and export productivity, as recent studies have shown (Qin et al. 2015; Zhu et al. 2016). For the Japan Sea it is argued that a change in redox conditions, caused by the uplift of northern Honshu, altered the Thaumarchaeota community to such an extent that it confounds the TEX_{86}^{L} based SST reconstructions. The effect of a change in the redox state on the other TEX_{86} indices cannot be observed (Fig. 4.2).

To test for a potential cold bias of TEX_{86} induced by thermal maturation, the total amount of C_{31}-hopane isomers was calculated. On average, the ββ/(αβ+ββ+βα) ratio of the C_{31}(H)-hopane in all samples is 0.8, exceeding the threshold of ≤0.5, indicating minimal impact of thermal maturation (Schouten et al. 2004). The evaluation of potential biases shows that the TEX_{86}-SST record is not influenced by sedimentary diagenetic processes or water depth.

A bias towards a production season, such as summer or winter, cannot be ruled out with certainty. Nonetheless, it is concluded that the TEX_{86}-proxy reflects genuine temperature changes in the Japan Sea over the last 18 million years.

Factors that can influence the $U^{K'}_{37}$-SST record include changes in the dominant alkenone producers (Volkman et al. 1995), seasonality (Sikes et al. 1997), salinity (Fujine et al. 2006), preferential degradation of the $C_{37:3}$-alkenone (Hoefs et al. 1998b), and nutrient dynamics (Eltgroth et al. 2005; Epstein et al. 1998). The $U^{K'}_{37}$-SST values are 5 °C higher during the late Miocene (6–8 Ma) and mid-to late Pliocene (2.5–4 Ma) (Figure 4.1) compared to the TEX_{86}-SSTs. High (18–19 °C) $U^{K'}_{37}$-SST have previously been reported during marine isotope stage 2 (MIS2), during the last glacial maximum, in various locations in the Japan Sea (Ishiwatari et al. 2001; Fujine et al. 2006). The high reconstructed $U^{K'}_{37}$-SST are attributed to a temperature/summer bias of the dominant alkenone-producers *Emiliania huxleyi* and *Gephryocapsa oceanica*, driven by intensified water column stratification during cold phases (Ishiwatari et al. 2001). Intensified stratification can also be caused by low salinity, evidenced by high concentrations of $C_{34:2}$-alkenoate and $C_{36:2}$-alkenone (Fujine et al. 2006). In this study, neither the $C_{34:2}$-alkenoate nor the $C_{36:2}$-alkenone were found, suggesting that low salinity is not the cause for the deviation of the $U^{K'}_{37}$-SST record from the TEX_{86}-SSTs. Nutrient dynamics can also influence the alkenone producers. Experiments show an increased $U^{K'}_{37}$-SST under nutrient stress (Epstein et al. 1998; Eltgroth et al. 2005). Nutrient concentrations in Japan Sea surface waters are currently low (2 $\mu mol\,kg^{-1}$ NO_2, 0.06 $\mu mol\,kg^{-1}$

NO_3, (Talley et al. 2004)) but still higher than the threshold used in Epstein et al. (1998). While low nutrient levels cannot be excluded to have caused some of the $U^{K'}_{37}$-SST deviation from the TEX_{86}-SST, nutrient constraints do not seem to be a likely driver. This is evidenced by the good agreement between the youngest $U^{K'}_{37}$-SST estimate and observed mean annual SSTs. Last but not least, it is possible that the 5 °C off set stems from the different production depths of the source organism, where alkenone producing haptophytes reside higher in the water column than Euryarcheota (Müller et al. 1998; Mollenhauer et al. 2015).

4.4.2. Long-term Sea Surface Temperature variability throughout the Neogene

The stacked global marine $\delta^{18}O$ benthic foraminifera record offers insight into glacial ice volume, and intermediate to bottom-water temperature variability (Zachos et al. 2001; Lisiecki and Raymo 2005; Zachos et al. 2008)(Figure 4.1). The long term trend towards ^{18}O enriched benthic foraminifera tests signifies the continual global cooling and build-up of glacial sea ice in the southern, and later in the northern hemisphere (Zachos et al. 2008). The TEX_{86}- and $U^{K'}_{37}$-SST records reflect this long term decline towards the current 'ice house' climate (Figure 4.1). Overall, TEX_{86}-SSTs decrease by over 10 °C from the mid-Miocene Climate Optimum (MMCO) to the late Pleistocene. A similar temperature decline is recorded by the $U^{K'}_{37}$ proxy from 8 Ma onwards. There-

fore, it is suggested that the long term Japan Sea SST decline is driven by the same drivers that control the global cooling trend.

The comparison between Japan Sea SST and North Pacific SST records is limited to the period from 13 Ma onwards, as there are no other available organic geochemical SST records spanning the interval 18 Ma to Present. Comparing the SST reconstructions of this study with SST reconstructions from the Pacific (LaRiviere et al. 2012; Seki et al. 2012; O'Brien et al. 2014; Zhang et al. 2014; Herbert et al. 2016) highlights that a temperature gradient of approximately 8 °C persisted across the low to mid latitudes until the end of the mid Miocene (Figure 4.5). Throughout the last 13 Ma, Japan Sea and Pacific Ocean SSTs exhibit the similar cooling trends. The mid-latitude SSTs decrease by 10 °C, to near modern values during the late Miocene cooling (LMC) (7–5 Ma) defined by Herbert et al. (2016). The same LMC trend is observed in the Japan Sea, from circa 22 °C to 13–14 °C, which is in the range of the magnitude of cooling observed by Herbert et al. (2016). By the end of the LMC, the temperature difference between low and mid-latitudes is as large as 15 °C. Temperatures increase again after the LMC, in the mid-latitude Pacific as well as in the Japan Sea. Another cooling episode in the open Pacific and Japan Sea is observed at the onset of the Northern Hemisphere glaciation, at around 2.5 Ma (Figure 4.5). The cooling in the open Pacific ranges around 9 °C relative to modern values. In the Japan Sea, a similar decrease relative to modern values is observed. The overall temperature gradient between the low and mid-latitudes ranges now around 13 °C.

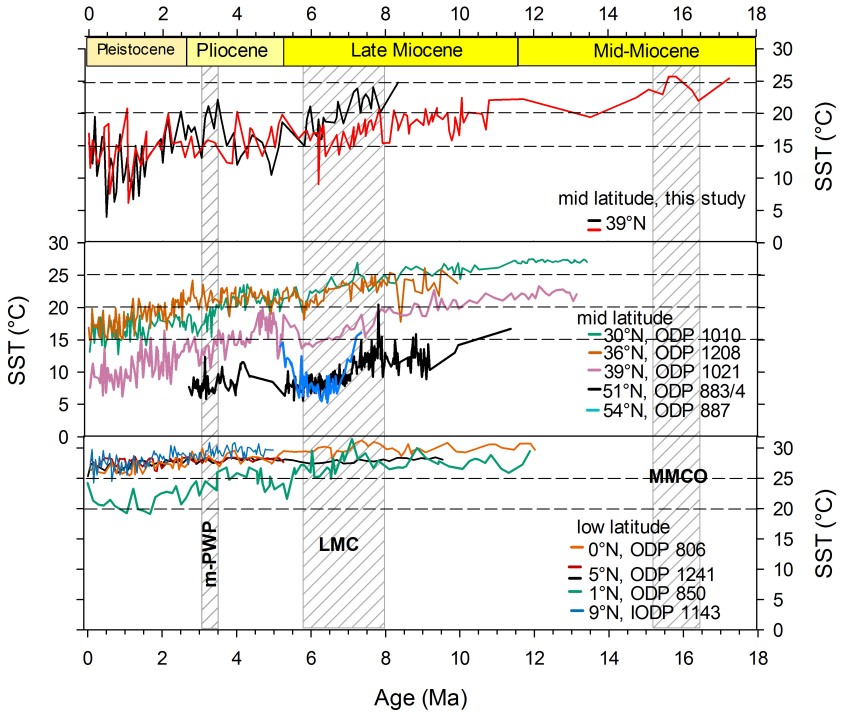

Figure 4.5.: Comparison of SST records from the equatorial and mid-latitudinal Pacific (LaRiviere et al. 2012; Seki et al. 2012; O'Brien et al. 2014; Zhang et al. 2014; Herbert et al. 2016). Grey shades indicate timing of mid-Miocene Climate Optimum (MMCO), late Miocene cooling (LMC), mid-Pliocene Warm Period (m-PWP)

Varying atmospheric CO_2 concentrations are considered to be among the most important drivers of Cenozoic climate change (Beerling and Royer 2011; PALAEOSENS 2012; and references therein). However, there are still large uncertainties regarding the reconstruction of atmospheric CO_2 beyond the Pliocene (Beerling and Royer 2011). This is highlighted by the variable paleo-CO_2 estimates from 18–5 Ma (Fig. 4.1). Several studies highlight the sensitivity of the Japan Sea to variable CO_2 levels (Krapp and Jungclaus 2011; Yamano et al. 2011; Herold et al. 2012; Rhein et al. 2013), which suggests greenhouse gas forcing to be a driver for the observed long-term SST decline in the Japan Sea. Recently, Bolton and Stoll (2013) attributed the onset of strong vital effects in both the $\delta^{18}O$ and carbon isotopes of large coccoliths as a response to limitations on carbon uptake with lower surface ocean dissolved inorganic carbon as atmospheric CO_2 declines. Interestingly, this divergence starts to become very pronounced in the late Miocene, close to the expansion of C_4 plants, and around the same time as the LMC (Herbert et al. 2016). Bolton and Stoll (2013) suggest that terrestrial and marine photosynthesizers show adaptation at a common pCO_2 threshold of circa 500 ppm, and that a decline below such a level caused the synchronous response of both photosynthesizers to this decline. These findings would be the only and indirect evidence of a late Miocene pCO_2 decline from above 500 ppm to less than 500 ppm that is currently available. These results would point towards a decline in atmospheric CO_2 concentration instead of the increase reconstructed by Pagani et al. (1999b). In the early Pliocene, warm SSTs match increased atmospheric CO_2 levels, which

is considered to reflect the high sensitivity of global climate to CO_2 forcing (Pagani et al. 2010). The Japan Sea SST cooling during the Plio/Pleistocene shown in this study coincides with a further drop of atmospheric CO_2, indicating that SSTs were mainly driven by CO_2 forcing throughout the last 5 Ma Pagani et al. (2010) In combination with the findings of Bolton et al. (2016) and Herbert et al. (2016), CO_2 may have acted as a driver for the last 7 Ma at least, by increasing the radiative forcing and the associated feed back mechanisms (Lacis et al. 2010; PALAEOSENS 2012; Rohling et al. 2012; Caballero and Huber 2013). Other climate drivers operating on shorter time scales affecting the TEX_{86}- and $U^{K'}_{37}$-SST records are discussed below.

4.4.3. Short term SST variability

Over shorter time-scales (<1 Ma) Japan Sea SSTs trends deviate from the global $\delta^{18}O$ stack inferred global temperature decline, and from SST reconstructions from other sites during the late Miocene and Pliocene (LaRiviere et al. 2012; Seki et al. 2012; O'Brien et al. 2014; Zhang et al. 2014; Herbert et al. 2016). These deviations can be explained by the dominance of local climate drivers on Japan Sea SSTs, such as changes in the Asian continental climate and tectonic changes affecting ocean current through flow.

Influence of Asian monsoon on SST reconstructions

The East Asian monsoon system can exert control on SSTs in the Japan Sea via the winter and summer monsoon. During winter, sea surface temperatures cool drastically due to increased wind stress from the winter monsoon. This should lead to a cooling signal in SSTs. During the summer monsoon, enhanced fresh water input via precipitation and increased discharge from the Yellow and Yangtze Rivers, leads to the formation of a fresh water lens on the Japan Sea, and the water column becomes stratified. This would be particularly problematic for the application of $U^{K'}_{37}$ (Warden et al. 2016), for which the application is limited in less saline waters. Attributing SST changes to a stronger winter or summer monsoon is not very straight forward; since the winter monsoon is shown to intensify during times of low pCO_2 and glacials (Tada et al. 2016; and references therein), which already would be indicated by comparatively colder SSTs. On the other hand, stronger summer monsoons occur during times of higher pCO_2 and interglacials (Hori and Ueda 2006; Tada et al. 2016), which would be indicated by generally warmer SSTs (Lacis et al. 2010; Caballero and Huber 2013). To pick up a seasonal signal (winter or summer), the here applied SST proxies would have to respond to a certain season, but such a bias was already excluded in the previous discussion. Detailed reconstruction of the Asian continental climate are best inferred from loess deposits (Balsam et al. 2004) and Miocene red clays (Guo et al. 2002). The dominant control on the alternating deposition of loess and paleo-soils is

thought to be the strength of the Asian Monsoon. Xu et al. (2015) analyzed red clays from the East Chinese Loess Plateau (CLP) and identified strong winter monsoons at 5, 5.3, 8.0, 9.6 and 10.5 Ma, as well as a rapid enhancement of the winter monsoon during the late Pliocene. They also found a strong summer monsoon prevailing between 5.6 and 7.5 Ma. The enhanced monsoon episode at 8 Ma is recognized in other paleoclimate records (Rea et al. 1998; Jia et al. 2012). The TEX_{86}-SST record exhibits a temperature minimum at 8 Ma which may reflect enhanced winter monsoons via surface cooling by strong winds. However, there is no evidence in the form of enhanced surface cooling indicating monsoon variations in the SST records during the other events described by Xu et al. (2015). In contrast to TEX_{86}-, $U^{K'}_{37}$-SSTs show elevated temperatures between 5.6 and 7.5 Ma (Fig. 4.1). One assumption is that an enhanced summer monsoon led to excessive fresh water input into the Japan Sea and the subsequent stratification of the water column caused high $U^{K'}_{37}$-SSTs. However, multiple studies point out that an intensified summer monsoon persisted until approximately 4 Ma (Bai et al. 2009; Zhuang et al. 2014; Peng et al. 2016), and so should have elevated $U^{K'}_{37}$-SSTs. The lack of response of the Japan Sea SSTs to a change in the Asian monsoon system could also be attributed to the relatively broad resolution of the SST records, and only a higher SST resolution could indicate such an influence.

Influence of gateway changes on SST reconstructions

As mentioned beforehand, it is important to consider tectonic changes as drivers for short term SST changes. Prior to 10.5 Ma, the Japan Sea was considered to be a paleo-bay, before back-arc closure occurred. The northern Honshu Island was still submerged, and the Japan Sea was able to exchange waters with the open Pacific (Kano et al. 1991; Fig. 3.2). The Tsushima Strait connected Japan to the proto-East China Sea, and the Tsugaru Strait in the North was also open (Tada 1994). This allowed warm waters to flow into the Japan Sea from the southern and eastern channel, and exit to the North (Tada 1994). During the transition from the middle to the late Miocene (10–6.5 Ma), the Japan Sea was tectonically quiescent (Iijima and Tada 1990), and the northern part of Honshu only began to uplift at around 6 Ma, and was mostly completed at 4 Ma (Kano et al. 1991). Only at around this time, colder waters from the Okhotsk Sea could flow into the Japan Sea and influence the SST record. During the LMC, the Japan Sea was still in exchange with the open Pacific, and thus the LMC detected in the Japan Sea is not caused by cold Okhotsk Sea waters, but is a sign of genuine cooling. The brief warmer period shown in the $U^{K'}_{37}$-SST record between 4.1–4.8 Ma is associated with a time of high sea level, where warmer waters entered the Japan Sea briefly (Miller et al. 2005). Thus a complex interplay of sea level, and tectonic change modulated Japan Sea surface temperatures, and is reflected in the $U^{K'}_{37}$-SST record.

The TEX_{86}-SST record shows a similar temperature decline from 10.5 Ma,

but only until 6.7 Ma. Subsequently, the TEX_{86}-SST record diverges from the $U^{K'}_{37}$-SST record between 4.2 Ma until 6.7 Ma, and exhibits comparatively warmer temperatures than $U^{K'}_{37}$. The reason for the $U^{K'}_{37}$-, TEX_{86}-SST discrepancy could be that the TEX_{86}-SST signal may have been confounded by archaeal community shifts. Zhu et al. (2016) have shown that a changing redox state of the water can have an influence on archaeal populations as reflected in RI changes. Tada (1994) showed that the Japan Sea redox state shifted from anoxic to oxic at circa 6 Ma (based on Org-C/Tot-S, Tot-S/Fe_2O_3, and Fe_2O_3/Al_2O_3) where a decrease in fractional abundances of GDGT-1 and -2 is observed (Fig. 4.6). This leads to a warm bias in the TEX_{86}-SST signal. The permanent oxic state prevailed until 2.5 Ma after which it started to fluctuate again between oxic and at least anoxic (Tada 1994). The fractional abundances of GDGT-1 and -2 recover from 4.5 Ma onwards suggesting that the TEX_{86}-SST signal could suffer from a warm bias between 4.5 and 6 Ma.

The TWC re-entered the Japan Sea after 3.5 Ma, via the reopening of the Tsushima Strait (Tada 1994). The re-opening of the Tsushima Strait is reflected by a steep 6 °C $U^{K'}_{37}$-SST increase. The Tsushima Strait was fully reopened from around 2.5 Ma, with an average sill depth of 130 m (Tada 1994). This allowed the TWC to enter the Japan Sea and to leave it via the Tsugaru Strait, but only during interglacial times (Oba 1991; Tada 1994; Kitamura and Kimoto 2006). During glacial periods, eustatic sea levels were too low to allow TWC incursion via the Tsugaru Strait (Miller et al. 2005), and fresh water input via the Yellow and Yangtze rivers dominated (Oba 1991). The forma-

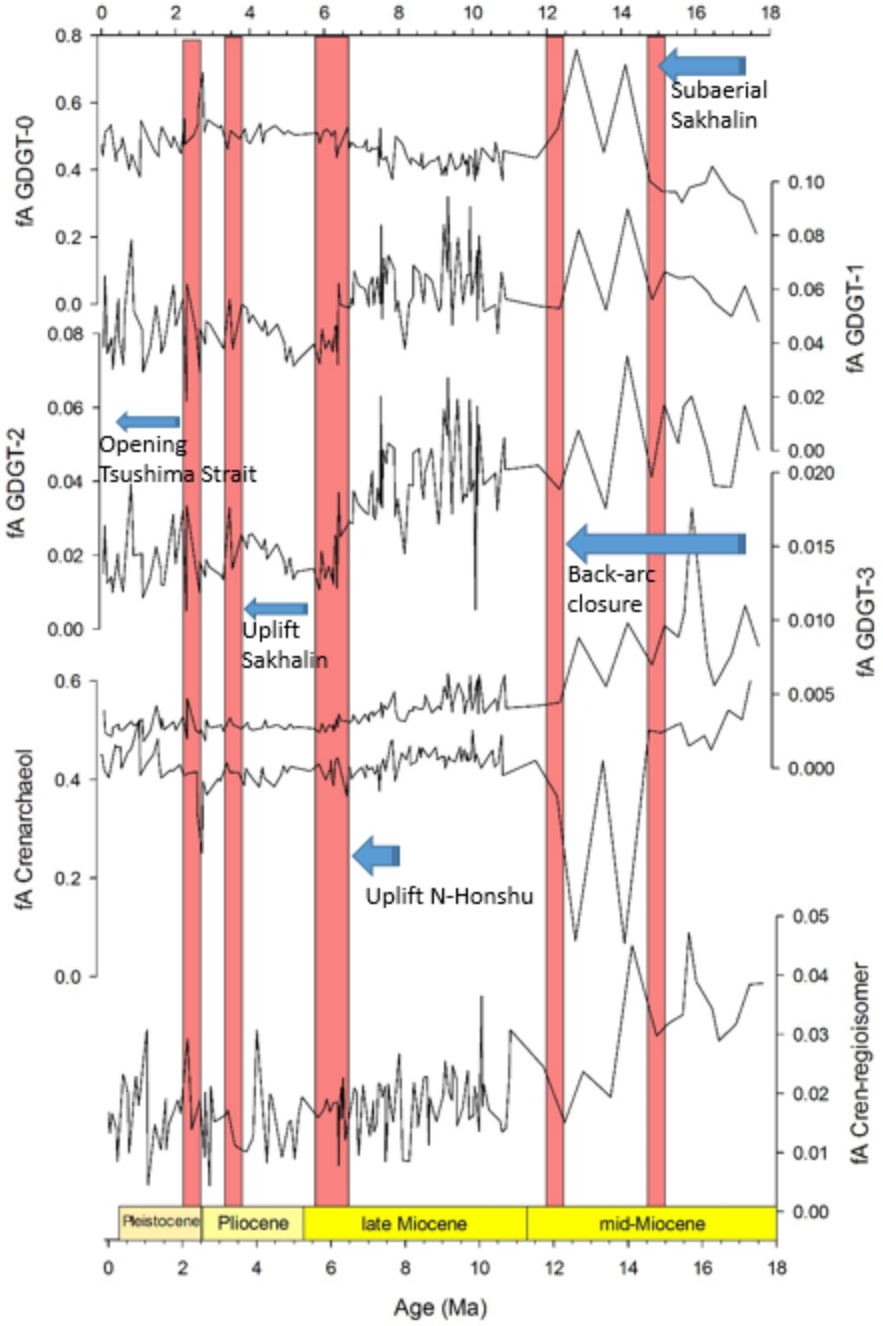

Figure 4.6.: Fractional abundances of GDGT-0,-1,-2,-3, and crenarchaeol. Indicated are also major tectonic and environmental events.

tion of a fresh water lens lead to a strong stratification of the water column, the subsequent heating of this fresh water lens in summer might have forced a haptophyte bloom in summer, with subsequently warmer $U^{K'}_{37}$-SSTs during this time (Ishiwatari et al. 2001). This suggests that $U^{K'}_{37}$-SSTs were more sensitive to changes in surface currents, forced by tectonic changes in the late Miocene to Pliocene, compared to TEX_{86}-SSTs. Nevertheless, the longer term cooling trend is consistent with the TEX_{86}-SST record and the global deep-water $\delta^{18}O$ composite (Zachos et al. 2008) and other SST records from the Pacific (LaRiviere et al. 2012; Seki et al. 2012; O'Brien et al. 2014; Zhang et al. 2014; Herbert et al. 2016).

4.4.4. Plio-Pleistocene variability

The reconstructed TEX_{86}- and $U^{K'}_{37}$-SSTs show increasing variability throughout the last 2.5 Ma. This increased variability is mirrored by the global deep-water $\delta^{18}O$ composite (Figure 4.7), and is attributed to the increased influence of the 100,000 year eccentricity Milankovich cycles during the Pliocene/Pleistocene, and the concomitant intensification of glacial/interglacial cycles (Hays et al. 1976). Unfortunately, the temporal resolution of the records presented here is not sufficiently high to display the 41- to 100 kyr transition for the Japan Sea. Subsequently, only a hypothesis for this variability can be formulated: The average temperature fluctuation in the Japan Sea throughout the Plio/Pleistocene ranges around 5–6 °C relative to the annual mean SST and

most likely represents regional temperature changes amplified by eustatic sea level change within the Japan Sea, as suggested by Tada (1994); Tada et al. (1999). Crucially, the shallow Tsushima Strait (130 m) is the only way for the TWC to enter the Japan Sea. During glacial cycles a drop in eustatic sea level due to global ice sheet growth restricted the TWC from entering the Japan Sea (Iijima and Tada 1990; Tada 1994). Subsequently, the subpolar front extended further southwards into the Japan Sea (Iijima and Tada 1990). Without the countervailing TWC, the extended polar front led to enhanced SSTs cooling in the Japan Sea. In contrast, during interglacials the TWC can enter the Japan Sea, and the consequent heating of the Japan Sea surface waters due to the inflow of these warm waters is also recognized in SST proxies. The oscillation between warm and cold surface waters indicated by the organic SST proxies would also reconcile with micropaleontological studies by Koizumi (1992a;b), who found diatom indicating warm and cold water surface conditions in the Japan Sea over the last 0.8 Ma at least. The sensitivity of the Japan Sea to eustatic sea level change (Tada 1994; Tada et al. 1999) then leads to larger amplitude glacial- interglacial cycles, as reflected in the $U^{K'}_{37}$-, and TEX_{86}-records.

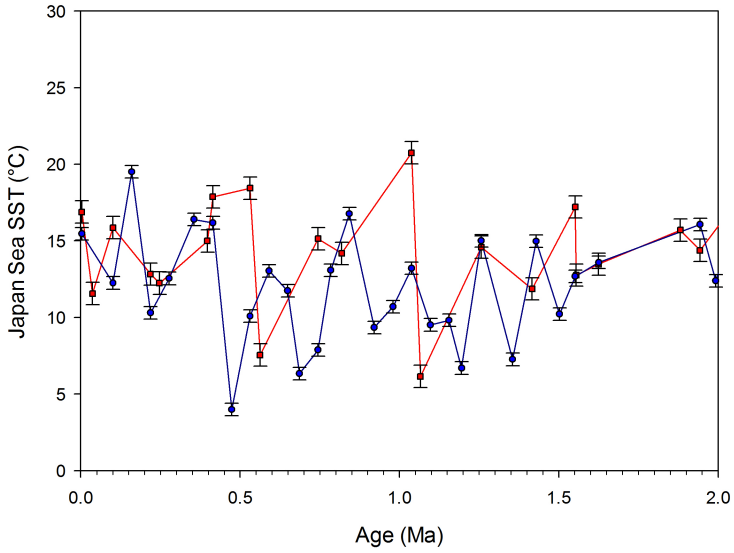

Figure 4.7.: Variation of SST over the last 2 million years. The red squares represent TEX_{86}, and blue circles represent $U^{K'}_{37}$

4.4.5. Changes in Japan Sea SST in comparison to model data

Miocene

There are few fully coupled atmosphere-ocean general circulation model (GCM) simulations of the MMCO climate state. For example, You et al. (2009) suggest a net global surface warming of circa 3 °C, reaching 18 °C with atmospheric CO_2 levels of 460–580 ppm, using the Community Atmosphere Model CAM3.1 and Land Model CLM3.0. Krapp and Jungclaus (2011) and Herold et al. (2012) show that models are currently unable to reproduce the MMCO warmth recorded by paleoclimate data. They compare their model data to

vegetation-based air temperature, and $U^{K'}_{37}$-, planktonic foraminifera $\delta^{18}O$-, and bivalve Mg/Ca ratio derived -SSTs. Krapp and Jungclaus (2011) used an atmosphere-ocean-biosphere GCM to reconstruct the meridional temperature gradient and subsequently compared the model results to continental and marine temperature reconstructions. Herold et al. (2012) used the Community Climate System Model 3 (CCSM3) to model ocean circulation during the Mid-Miocene and compared the results to reconstructed sea surface temperatures. You et al. (2009); Herold et al. (2012) and Krapp and Jungclaus (2011) model temperature differences (MMCO–today) between 3–6 °C, while the TEX_{86}-SST difference reconstructed in this study is approximately 10 °C. The authors (Krapp and Jungclaus 2011; Herold et al. 2012) attribute the model/proxy data offset to a lack of understanding of the boundary conditions used in the models. For example, it is possible that greenhouse gas forcing was larger than assumed. While the models cannot reconstruct the absolute temperature correctly, they do find high anomalous air temperatures over the Japan Sea (Krapp and Jungclaus 2011), and high northwest Pacific SSTs (Herold et al. 2012), at CO_2 concentrations below 400 ppm. These findings are consistent with current observations that the Japan Sea is a SST hot-spot.

Pliocene

Dowsett et al. (2013) modeled mid-Pliocene Warm Period (m-PWP, 3.3–3.1 Ma) SST anomalies, and all of their PlioMIP models spanned a range of 1–5 °C

mean surface warming for the Japan Sea, while proxy data showed little to no warming (2 °C). The results of this study compare better to the climate model of Dowsett et al. (2013) with a m-PWP anomaly of 4–5 °C.

4.5. Conclusions

In this study a robust multi-proxy SST record is presented, providing valuable insight into the Neogene SST history of the Japan Sea. Overall, the findings show that the Japan Sea is a suitable location to study global climate change for the last 18 million years. Exhibiting a trend to colder SST towards the Pleistocene, these temperature changes in the Japan Sea are in line with indicators for global climate change, such as $\delta^{18}O$ of benthic foraminifera and reconstructed CO_2 levels. Therefore, it is suggested that continually falling CO_2 levels throughout the Neogene are the main driver for the long term decline of Japan Sea SSTs, as documented by the TEX_{86} and $U^{K'}_{37}$ records. Superimposed shorter-term changes in $U^{K'}_{37}$ and TEX_{86} are likely due to tectonic changes in the Japan Sea, involving the opening and closure of gateways and thereby causing changes in the dominating water masses. Changes in the East Asian monsoon climate do not show a meaningful control on the SST-records. Throughout the Pleistocene/Pliocene, the TEX_{86} and $U^{K'}_{37}$ records exhibit larger temperature changes at higher frequencies than in the earlier part of the record. These amplitude and frequency changes are hypotesized to be caused by the Milankovich cycles. Resampling the record at a higher resolution is required

to test this hypothesis. It is postulated that the Japan Sea SSTs are controlled by the changing orbital configuration by restricted access of the TWC into the Japan Sea and subsequently expanding of cold waters from the North of the Sea. Due to the sensitivity of the record to changes in climate, the work presented here can be used for climate modeling to improve the predicted impact of global warming especially for the region around the Japan Sea. It is a densely populated region, the increased available heat via increased SSTs is a concern of public health (Patz et al. 2005), increased summer monsoon precipitation could increase thread of landslides (Petley 2010), posing economic strain on the affected regions. Warm SSTs also have their effect on the habitat of fish, threatening the food security of Japan (Uye 2008; Yamano et al. 2011). However, the role of CO_2 forcing on SSTs during mid- and late Miocene cannot be resolved, as the respective proxies are either lacking sensitivity or other greenhouse gasses than CO_2, in example CH_4 or N_2O (Rohling et al. 2012) played the major role in climate change during this time.

5. Compound specific isotope analysis of *n*-alkanes indicate contributions of different source areas to the Japan Sea

Abstract

The Japan Sea lies downwind of the westerly jet, and thus serves as an ideal study area for the characterization of dust and *n*-alkanes derived from central Asia. *n*-Alkanes can be used to reconstruct climate and vegetation changes in central Asia in relation to the Himalaya-Tibetan-Plateau (HTP) uplift, by measuring their stable isotopic signatures, δD and $\delta^{13}C$. Reconstructing the evolution of the East Asian monsoon system and its subsequent changes in relation with enhanced uplift of the HTP at approximately 8 million years is

one of the big challenges in paleoclimate sciences, and one of the scientific objectives of IODP Expedition 346. Here, a continuous record of *n*-alkanes, deposited in the Japan Sea over the last 8 million years, is presented. By measuring δD and δ^{13}C of *n*-alkanes, changes in *n*-alkane source regions, and subsequently precipitation regimes and atmospheric circulation strength, are elucidated. Up until the mid-Pliocene, a single source signal of *n*-alkanes allows an interpretation of the record in terms of climate change of the source area. C_4 plants expanded from 7.4–3 Ma, and the summer monsoon was stronger than present, with a peak activity from 3–5 Ma. Associated with an enhanced HTP uplift is the glacial-interglacial variation of *n*-alkane sources. During glacials, *n*-alkanes are predominantly delivered by the strong winter monsoon, as indicated by δ^{13}C and δD signature of *n*-alkanes. During interglacials, *n*-alkanes from the continental Asian margin are delivered to the Japan Sea by the westerly jet. While this source alternation does not allow a reconstruction of climate and vegetation change in the source areas, the identification of the source area still allows a reconstruction of the glacial-interglacial variation of atmospheric circulation systems, affecting the area around the Japan Sea.

5.1. Introduction

Higher land plants synthesize epicuticular waxes that form the protective layer of leaves and stems (Eglinton and Hamilton 1967), preventing water loss due to evaporation (Jetter, R., Kunst, L. and Samuels 2006). Long-chain *n*-alkanes

(nC$_{27}$- nC$_{35}$), alcohols and fatty acids (Bianchi and Bianchi 1990; Rommerskirchen et al. 2006) are main constituents of this wax layer. *n*-Alkanes of these plants are of odd-over-even predominance (OEP) with one or two preferably produced *n*-alkanes (Eglinton and Hamilton 1967). These *n*-alkanes are readily extractable from the sedimentary record, as the lack of functional groups makes them resistant to degradation. Average chain length (ACL) distributions of *n*-alkanes serve as proxies for aridity or growing temperature (Rommerskirchen et al. 2003; Schefuß et al. 2003; Castañeda et al. 2009; Bush and McInerney 2013). *n*-Alkanes carry a wealth of information about plant community structure, as C_3 and C_4 produce different *n*-alkanes of different chain length (Rommerskirchen et al. 2006). Furthermore, these plants fractionate CO_2 differently (Farquhar et al. 1989), with consequences for their individual carbon isotopic signature (Chikaraishi and Naraoka 2003; Chikaraishi et al. 2004). A more detailed discussion about the stable isotopic signature of *n*-alkanes can be found in Chapter 1.3.1.

Leaf wax components of higher plants found in marine environments are thought to be transported predominantly by winds and dust storms, where the suspended dust particles scrapes the wax off the leaf surface (Simoneit 1977; Schefuß et al. 2003) and considerable amounts of organic matter (Lepple and Brine 1976) and plant wax (Simoneit 1977; Bendle et al. 2006; 2007) are transported in the fine fraction to remote ocean settings. Leaf wax components in Japan Sea sediments are of continental Asian origin (Dersch-Hansmann 1994; Ishiwatari et al. 1999; Yamada and Ishiwatari 1999; Kawamura et al. 2003; Ya-

mamoto et al. 2011), and their variation in their molecular, and isotopic composition, and deposition therefore serves as an indicator of continental Asian climate change, East Asian monsoon variability, and aridity. The main cause for the desertification of central Asia is the Himalaya-Tibetan-Plateau (HTP) uplift, which shields central Asia from inflowing moisture, leading to increasing aridity of the Asian interior. The precise controls on the East Asian summer monsoon are still debated, but in general it is accepted that during the summer, the temperature difference between the HTP and the Indo-Pacific causes the Inner Tropical Convergence Zone (ITCZ) to shift northwards (Wang et al. 2005). The shift of the ITCZ also pulls the moisture bearing south-east trade winds from the southern hemisphere across the equator, where they are deflected by the Coriolis force and start to flow as south-westerlies (Sampe and Xie 2010; Fig. 5.1). Recently it was shown that the position of the westerly jet (WJ) axis has a large influence on the East Asian summer monsoon (EASM) rain band (Schiemann et al. 2009; Sampe and Xie 2010; Nagashima et al. 2011). The westerly jets (polar jet, subtropical jet) form in response to the globally occurring pressure belts, such as Hadley cell, Ferrel cell and Polar cell, and belong to the strongest winds of the atmospheric circulation system. The HTP is under the influence of the subtropical jet, which forms at the border of the Ferrel cell and Hadley cell (at approximately 30°N, Fig. 5.1). In spring, the westerly jet occurs south of the HTP (Schiemann et al. 2009). During summer, the WJ moves northward of the HTP and the rain belt associated with it moves accordingly. The rain belt is continuously fed with moisture by the south-westerlies

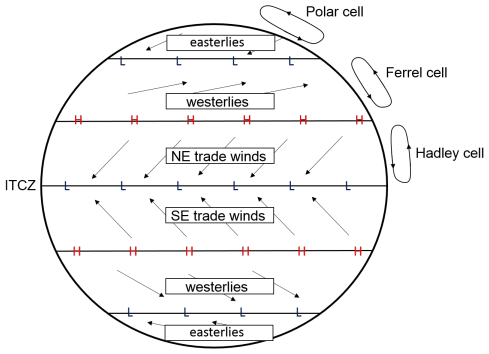

Figure 5.1.: Simple model circulation of the atmosphere and circulation cells. ITCZ=Inner Tropical Convergence Zone (ITCZ), H=subtropcial high pressure zone, L=low pressure zone of the mid-latitudes. H+L also indicate approximate position of the jet streams.

flowing along the South China Sea (Sampe and Xie 2010; Fig. 5.2). The rain belt then disappears, once the WJ is north of the HTP (Sampe and Xie 2010). In winter the situation reverses, and the Siberian High brings strong winds and dust storms blowing from the continents to the ocean (Wang et al. 2005; Fig. 5.2a). The uplift of the HTP is thought to play a major role in the evolution of the East Asian monsoon system (An et al. 2001; Liu and Yin 2002; Lunt et al. 2010), although clear evidence of this is still lacking (Tada et al. 2016). The most recent uplift of parts of the HTP at 3.6 Ma is thought to have caused the WJ to flow in two discrete modes, therefore causing variations in the EASM intensity especially during Dansgaard-Oeschger cycles (DOCs) (Tada 2004). However, the paleo-position of the WJ over East Asia and the Japan Sea is poorly constrained, and reconstructions are limited to the last glacial period (Han et al. 2008; Nagashima et al. 2011).

Changes in the intensity of the East Asian monsoon are not only driven by

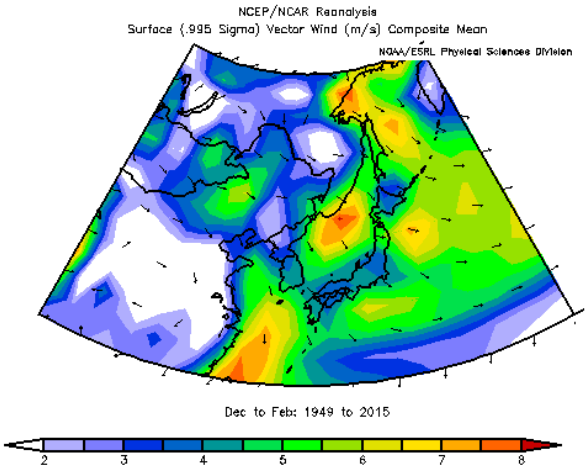

(a) Mean surface winds in (m/s) across E-Asia during the winter (DJF)

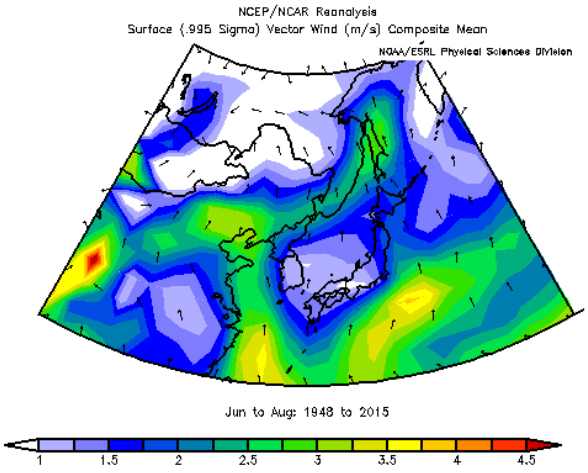

(b) Mean surface winds (m/s) for the same area in summer (JJA)

Figure 5.2.: Seasonal surface winds for the Japan Sea area. Map generated via NOAA/ESRL Physical Science Division, esrl.noaa.gov/psd

changes in tectonic boundary conditions such as enhanced HTP uplift, but also by orbital variations in the climate system (Hovan et al. 1989). This potential for a significant impact of the global climate state on the functioning and strength of the Asian monsoon is important to constrain in order to estimate the impact of future climate change on the monsoon. The isotopic signature of *n*-alkanes deposited in the Japan Sea can reflect how their source region is affected in terms of vegetation and precipitation, driven by the interplay of the uplift of the HTP and changes in monsoon strength.

As a prerequisite for a successful environmental reconstruction using *n*-alkane stable isotope analysis, the source area must be constrained in order to further constrain the impact of environmental factors on the isotope records. When interpreting the $\delta^{13}C$ content of *n*-alkanes, the relative contribution of angiosperms must be constrained, since angiosperms produce ^{13}C enriched *n*-alkanes compared to gymnosperms (Chikaraishi et al. 2004). Usually, $\delta^{13}C$ measurements carried out using nC_{29}, -C_{31} or -C_{33}. The latter two are preferentially produced by C_4 plants, while C_{29} is typical for C_3 plants (Rommerskirchen et al. 2006). Thus first it must be established that environmental effects have the same control on $\delta^{13}C$ derived from the respective *n*-alkanes. Furthermore, the transport mechanism for the *n*-alkanes must be the same, so that measurements do not yield a biased source signal. All these potential effects on carbon isotopic signatures of *n*-alkanes from Site U1425 are discussed in Section 5.4.2. Binary mixing models are usually applied to reconstruct past C_3/C_4 plant contribution, but these mixing models are based on

modern-day end members. This exerts a critical point for the interpretation, because isotopic fractionation of plants changes with changing pCO_2 (Schubert and Jahren 2012; 2015), and the varying isotopic signature of CO_2, $\delta^{13}C_{CO2}$. Thus, end members were likely not the same from the late Miocene to Present (Kürschner et al. 2008; Seki et al. 2010; Tipple et al. 2010). Potential biasing effects on the C_3/C_4 mixing model presented in this study are discussed in Section 5.4.2. The application of *n*-alkane δD analysis also has its pitfalls, as the δD value of the moisture source (marine or continental) influences the *n*-alkane δD value (Mügler et al. 2010). Then, altitude, continental and amount effect also can bias the δD value of *n*-alkanes (Sachse et al. 2012). To date, the effect of aridity and evapotranspiration on the δD value of *n*-alkanes remains controversial (Feakins and Sessions 2010; Thomas et al. 2016). Whether any of these influencing factors are applying to the δD record presented here, is discussed in Section 5.4.3.

Most studies on the Asian monsoon system are based on lake cores and soil samples (Mügler et al. 2010; Xia et al. 2014; Zhuang et al. 2014; Peng et al. 2016). The main assumption in these studies is that the investigated *n*-alkanes stem from the immediate area surrounding the sampling locality, and therefore that the isotopic signature of these *n*-alkanes mainly records environmental change, and not a change in source (locality and subsequently plant) signal. However, the Tibetan Plateau represents an area of a complex interplay between four different important atmospheric circulation features: the Indian and Asian monsoon, the westerlies, and the Siberian High (Araguás-Araguás et al.

1998; Fig. 5.3). Associated with these circulation features is a different isotopic signature of the moisture they deliver. It is also known that *n*-alkanes can be transported via low level winds over long distances (Simoneit 1977; Schefuß et al. 2003; Bendle et al. 2006; 2007; Yamamoto et al. 2011). Some studies have been carried out regarding the transport of terrestrial OM in aerosols to the open Pacific (Zafiriou et al. 1985; Kawamura 1995; Kawamura et al. 2003). *n*-Alkane distributions in aerosols are reflected in surface sediments, suggesting that North Pacific deep-sea sediments are significantly influenced by terrestrial higher land plant waxes (Kawamura 1995). With respect to the deposition mechanism, wet deposition of particles seems to be dominating over dry deposition (Zafiriou et al. 1985). Aerosol fluxes decrease from the west Pacific to the central Pacific (Kawamura 1995), what is then transferred into the ocean is then degraded settles down at the sea floor. During settling, low molecular weight compounds undergo decomposition and remineralization (Kawamura 1995), while high molecular weight compounds are almost constant with depth (Kawamura 1995). These refractory *n*-alkanes are then preserved in the sediments over geological time scales. With respect to aerosol fluxes across the Pacific, Kawamura et al. (2003) recognized a seasonal pattern: *n*-alkane fluxes to open Pacific were high in winter and spring, presumably this reflects the very strong westerlies where air masses were generated over Siberia and Asia. During the summer air masses were generated over the central Pacific and the Far East. These intraseasonal changes of the *n*-alkane source are also reflected in the ACL (Kawamura et al. 2003). When reconstructing past changes

in the Asian monsoon system on the Tibetan Plateau, it is therefore unreasonable to assume that a change in the deuterium isotopic signature only reflects a weak or strong summer monsoon, and that carbon isotopic signature changes indicate vegetation changes at the site. Instead it is possible that deuterium isotopes in *n*-alkanes record alternating moisture sources instead of a weakening/strengthening summer monsoon. It is also possible that *n*-alkanes transported from remote sites to the sampling locality influence the observed isotopic record, which may bias reconstructions of local vegetation changes.

Here, a continuous 8 million year *n*-alkane record from the Japan Sea is presented. By measuring the δD signature of *n*-alkanes, changes in summer monsoon dynamics and therefore precipitation will be elucidated. Furthermore, the results will be evaluated in the context of changing moisture sources or changing source region. Carbon isotope analysis ($\delta^{13}C$) of *n*-alkanes is applied to reconstruct the vegetation change from C_3 to C_4 plants in the context of continental climate change of the Asian interior. As for the deuterium isotopic record, changes in the $\delta^{13}C$ signature will be interpreted in the context of a changing source region. Additionally, the amount of *n*-alkanes will give insight into expansion and contraction of deserts located across the westerly jet path.

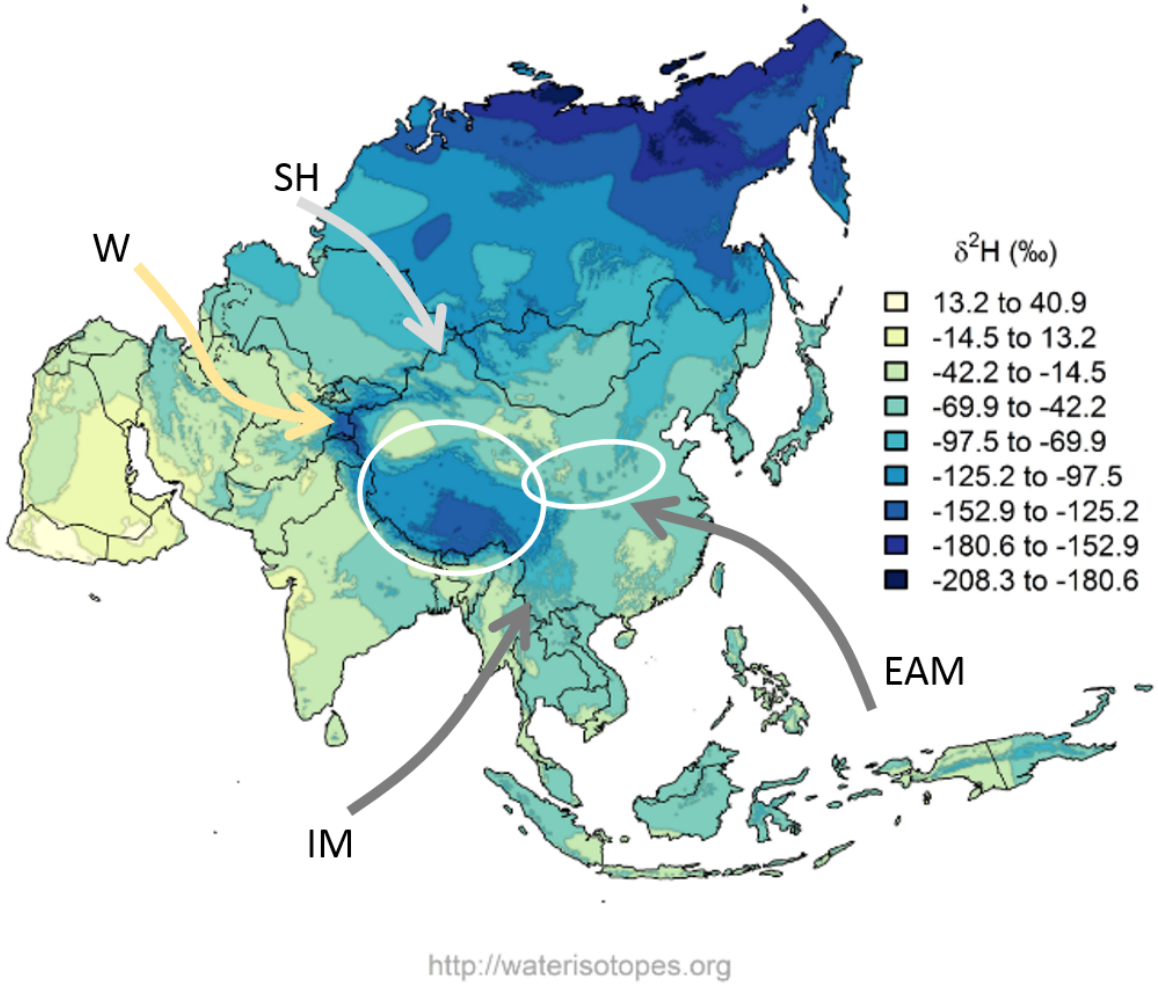

Figure 5.3.: Atmospheric circulation features on the Tibetan Plateau: The Indian and Asian Monsoon, low level westerlies and the Siberian high. W=westerlies, SH=Siberian High, IM=Indian Monsoon, AM=Asian Monsoon. Large circle indicates the approximate location of the Tibet Plateau, the small circle indicates the location of the CLP. Map from waterisotopes.org

5.2. Methods

The methods for standard analyses, such as the quantification of *n*-alkanes, and compound specific isotope measurements can be found in Chapter 2.

5.3. Results

5.3.1. Carbon isotopic values of *n*-alkanes

$\delta^{13}C$ values of nC_{29}-alkanes and nC_{31}-alkanes range between −29.1 ‰ and −32.5 ‰ and −29.3 ‰ and −33.4 ‰ respectively and correlate well with each other (R^2=0.89, Fig. 5.4a). In the late Miocene a steep decline towards ^{13}C depleted nC_{29}-alkanes from 7.9–7.2 Ma is observed (Fig. 5.5). Carbon isotopic signatures range between −29.7 ‰ and −31.8 ‰. After this excursion, nC_{29}-alkanes become increasingly more enriched from 7.2–3.2 Ma, when the $\delta^{13}C$ signatures reach −29.1 ‰. Subsequently nC_{29}-alkanes become more ^{13}C depleted. This trend continues into the Pleistocene. Briefly after the onset of the Pliocene, *n*-alkanes become increasingly enriched, from −31.7 ‰ to −29.4 ‰ at 1.4 Ma. Since then, they have been more depleted, with values ranging between −31 ‰ and −32 ‰.

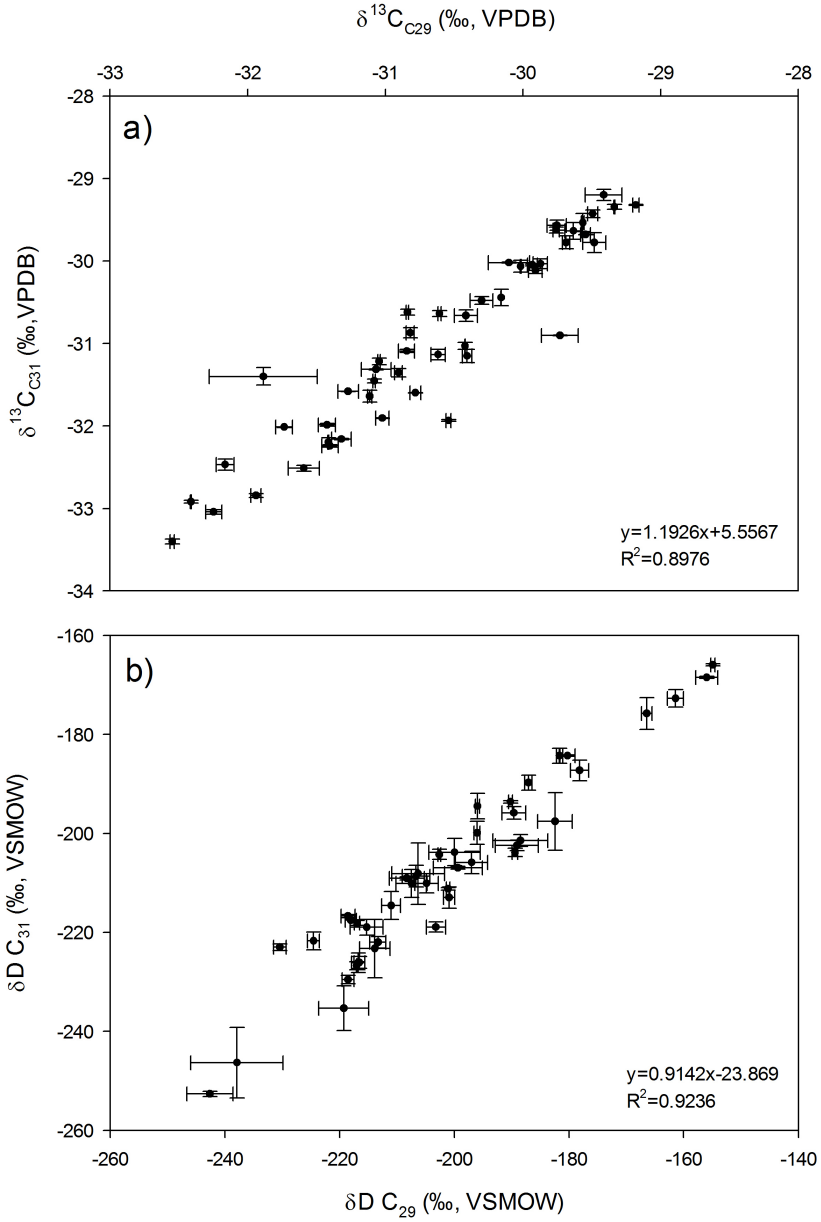

Figure 5.4.: Crossplot of (a) $\delta^{13}C$ and (b) of δD of n-C_{29} and n-C_{31} to exclude a plant community based bias introduced to the isotopic record, by differently fractionating $\delta^{13}C_{CO2}$ and δD of meteoric waters during lipid synthesis.

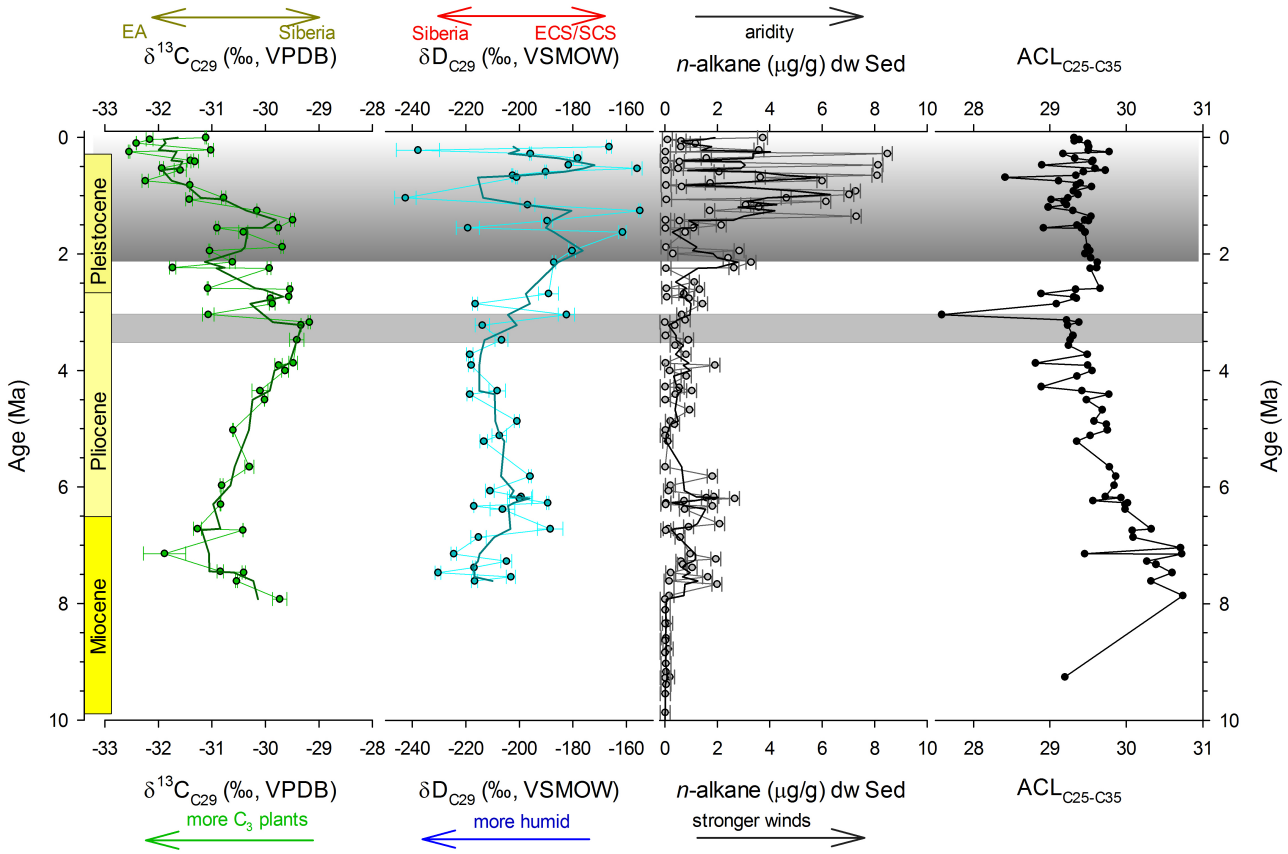

Figure 5.5.: (a) Reconstructed $\delta^{13}C$ of C_{29}-*n*-alkanes detected in core U1425. Dark-green line is the 3-point-running-average (3-PRA). (b) Reconstructed δD of C_{29}-*n*-alkanes detected in core U1425. Dark-blue line is the 33-PRA. (c) *n*-Alkane concentrations detected in core U1425. Black line indicates 3-PRA. (d) Average chain length (ACL) of *n*-alkanes detected in core U1425. Black line indicates 3-PRA. Error bars in all figures indicate the analytical (1σ error). Grey shade area indicates enhanced HTP uplift (Tada et al. 2016; and references therein)

5.3.2. Hydrogen isotopic values of *n*-alkanes

δD values of nC$_{29}$-alkanes and nC$_{31}$-alkanes range between −154.9 ‰ and −242.7 ‰, and −168.4 ‰ and −252.6 ‰ respectively. They correlate very well with each other (R^2=0.92, Fig. 5.4b). In the late Miocene (6.7 Ma, Fig. 5.5), a 20 ‰ shift towards a deuterium enrichment is observed. For the rest of the late Miocene, the isotopic signature remains relatively stable around −210 ‰ and continues to remain so until 4.8 Ma, after which *n*-alkanes become slightly more depleted in deuterium. In the mid-Pliocene, at 3.4 Ma, δD values of nC$_{29}$-alkanes become increasingly enriched, peaking at 2.1 Ma with a δD value of −187.1 ‰. During the Pleistocene from 2–0.1 Ma, the *n*-alkane isotopic signatures fluctuate extremely, being the most depleted with −242.7 ‰ and a rapid recovery within 0.7 Ma to −178.1 ‰. 140 kyr later, *n*-alkanes are depleted in deuterium again, with an isotopic signature of −237.9 ‰.

5.3.3. *n*-alkane concentration and ACL

n-alkane concentrations range from 0.2–8 µg/g ±0.2 µg/g dry weight sediment. Concentrations were low prior to 8 Ma (Fig. 5.11), but show an increase at 8 Ma. After a brief interval of increased *n*-alkane concentrations, they decline during the Pliocene, and only start to increase at approximately 4 Ma. Large changes in amplitude of deposited *n*-alkanes are observed for the Pleistocene, where concentrations frequently vary. Average Chain Length (ACL, Eq. 1.1) ranges from 30.7 to 28.8. ACL shows a long-term decline for almost

5 million years (Fig. 5.11), from the late Miocene to the end of the Pliocene. After a brief excursion to 28.8 at 2.6 Ma, ACL rises quickly to approximately 29, and remains practically stable throughout the Pleistocene, with minor excursions towards shorter ACL at 0.2, 0.4, 0.6, 1.2 and 1.5 Ma.

5.4. Discussion

5.4.1. Source of sedimentary *n*-alkanes

There are two ways that detrital matter is delivered to the oceans: via fluvial or eolian transport (Simoneit 1977; Hedges et al. 1997). The ECSCW water transports river outflow water from the Yangtze and Yellow Rivers into the southern part of the Japan Sea by mixing with the Tsushima Warm Current (TWC) (Ichikawa and Beardsley 2002). A sediment trap study at 1 km depth indicates 'old Asian' terrigenous OM delivery to the Yamato Basin by the TWC (Otosaka et al. 2004). Since this delivery was observed right after the spring bloom, it is also possible that this fluxed was caused by decomposing opal particles (Otosaka et al. 2004). Furthermore, the Yamato Basin also receives a small OM influx from the island arc during autumn and winter (Otosaka et al. 2004). However, lateral transport of particulate organic carbon in the Yamato Basin remains largely unconstrained (Otosaka et al. 2008). It is questionable to which extent these observations are applicable to Site U1425, which is located on a terrace behind Yamato Rise, which peaks at 500 m be-

low the sea surface. The influx of island arc derived organic matter to Site U1425 could be blocked or limited by the Yamato Rise. Given the findings of Otosaka et al. (2004; 2008) *n*-alkane transport via the TWC is possible, but only during times when the sea level was high enough to allow the TWC to enter the Japan Sea (Chapter 4). Thus, *n*-alkane deposition by the TWC is limited to interglacials during the Plio-Pleistocene (Iijima and Tada 1990; Tada 1994). Prior to 2 Ma, a land bridge existed in the south of the Japan Sea, effectively restricting inflow of any river or TWC, and therefore influx of long-chain *n*-alkanes (Iijima and Tada 1990; Kano et al. 1991; Tada 1994; Fig. 3.2). Two Japanese rivers have their outflow in to the northern Japan Sea, which also enables *n*-alkane deposition from the islands to the sea. However, given the direction of the TWC flow (Fig. 3.1), the influence of Japan derived *n*-alkanes at the studied site should be rather low. Furthermore, northern Honshu was only uplifted after approximately 6 Ma, thus these rivers had no influence on the *n*-alkane record presented here. The Amur River discharges into the Okhotsk Sea, which was connected to the Japan Sea up until 3.6 Ma (Xu et al. 2016; Chapter 3). Today, the Amur River discharges its sediment load outside the Mamiya Strait (Stax 1993), thus terrestrial organic carbon derived from this area does not influence the Japan Sea from 3.6 Ma to Present. *n*-Alkane accumulation rates remain low, and steady for the period from 4.5–5 Ma (Fig. 5.11), which is a time where the Amur River discharged at a higher rate into the Japan Sea (Matsuzaki et al., in prep). 68% of terrigenious fluxes in the Yamato Basin were delivered by the Kosa (Chinese loess), the Japanese

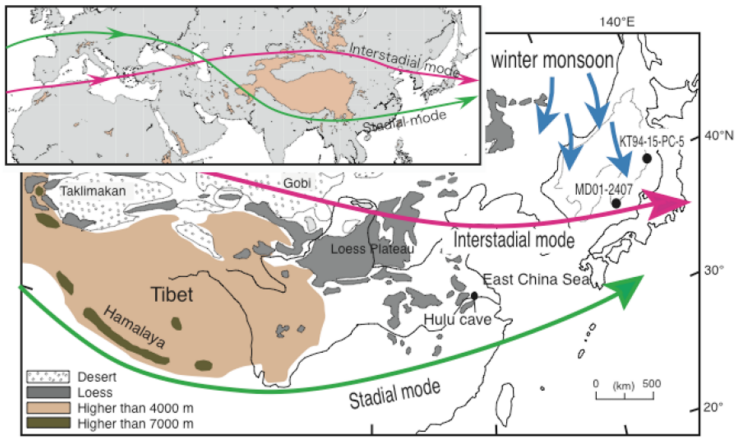

Figure 5.6.: Sketch of westerly jet and its proposed flowing paths in variation with Dansgaard-Oschger-Cycles. Indicated too is the direction of the East Asian winter monsoon, and desert regions of central Asia. Figure taken from IODP proposal 605-Full2.

term for detrital matter delivered by the winter monsoon (Otosaka et al. 2004; Kawamura et al. 2010). Therefore it is concluded that *n*-alkanes at Site U1425 are predominantly delivered by eolian transport pathways.

Substantial amounts of dusts from East and central Asia, especially from the Taklimakan and Gobi Desert, reach the Japan Sea, due to the weakening of the Siberian High in Spring and the resulting shift in air masses (Nagashima et al. 2011). Although the WJ is still south of the HTP during spring, it is meridional dispersed to such a degree that it frequently occurs in the North of the HTP (Schiemann et al. 2009). This extension is the requirement for Gobi- and Taklimakan Desert dust to be air lifted and deposited down wind of the WJ, in the Japan Sea and the North Pacific (Rea et al. 1998; Nagashima et al. 2007b). Therefore, the Japan Sea receives varying contributions of dust from

both deserts, which is dependent on the dominant wind as well as the aridity of the source area (Nagashima et al. 2007a). Dust provenance changes are recorded in the Japan Sea between interstadial and stadial periods (Nagashima et al. 2011), with even Siberian derived dust appearing in some intervals (Nagashima et al. 2007b). The Asian winter monsoon, driven by the intensity of the Siberian High, delivers substantial amounts of dust from Siberia to the Japan Sea (Nagashima et al. 2007b; 2011), and, with the dust, potentially *n*-alkanes. Indeed, Yamamoto et al. (2011) showed that *n*-alkanes in fresh Sapporo snow stem from Siberia. *n*-Alkanes detected at Site U1425 can thus stem from two different regions: central Asia, delivered by the westerly jet, and from Siberia, delivered by the winter monsoon. This source change must be kept in mind during the interpretation of *n*-alkane derived climate records from this region.

5.4.2. Changes in δ^{13}C of terrestrial higher plants

The carbon isotopic signature of *n*-alkanes from higher plants is dependent on the isotopic signature of atmospheric CO_2, and affected by isotopic fractionation during the biosynthesis involved. Furthermore, C_4 plants have been shown to preferably produce longer-chain *n*-alkanes, such as nC_{31} and nC_{33} (Rommerskirchen et al. 2006), while C_3 plants preferably produce nC_{29} (Vogts et al. 2009). Also, the $^{13}C/^{12}C$ ratio has been shown to differ within the homologous series (Collister et al. 1994). Thus, the interpretation of the isotopic record

based on just one *n*-alkane, i.e. nC$_{29}$, can create a bias towards the particular environmental sensitivity of C_3 plants. A cross plot of $\delta^{13}C_{C31}$ and $\delta^{13}C_{C29}$ yields an R^2 of 0.89, indicating that the source areas, source plants, and transport mechanisms are the same for both *n*-alkanes. The following discussion focuses on changes in $\delta^{13}C_{C29}$ alone.

The carbon isotopic signature of CO_2 varied over the last 8 Ma (Tipple et al. 2010), potentially biasing the record towards more depleted or enriched *n*-alkanes. Since CO_2 is the substrate for photosynthesis, its stable isotopic signature is propagated down to the lipid synthesis, therefore causing lipids to be more enriched/depleted in variance with $\delta^{13}C_{CO2}$. This creates a problem for C_3/C_4 plant mixing models, as a bias towards more ^{13}C enriched or depleted *n*-alkanes will over- or underestimate C_4 plant abundance, respectively. $\delta^{13}C_{CO2}$ was reconstructed by Tipple et al. (2010), allowing the subtraction of the isotopic signature of CO_2 ($\delta^{13}C_{CO2}$) from the *n*-alkane carbon isotope records. This enables a discussion of $\delta^{13}C_{C29}$ that is not affected by variations in atmospheric $\delta^{13}C_{CO2}$ ($\epsilon_{C29-CO2}$, Eq. 5.1, Fig 5.7). To fit the data of Tipple et al. (2010) to the data presented here, the $\delta^{13}C_{CO2}$ record was linearly interpolated to derive age points corresponding to the record presented here.

$$\epsilon_{C29-CO2} = \frac{\delta^{13}C_{29} - \delta^{13}C_{CO2}}{\delta^{13}C_{CO2} + 1} \times 1000 \tag{5.1}$$

The $\delta^{13}C$ isotopic signature of *n*-alkanes depends on the biosynthesis of the source plant, with C_4 plants having a more positive $\delta^{13}C$ signature due to

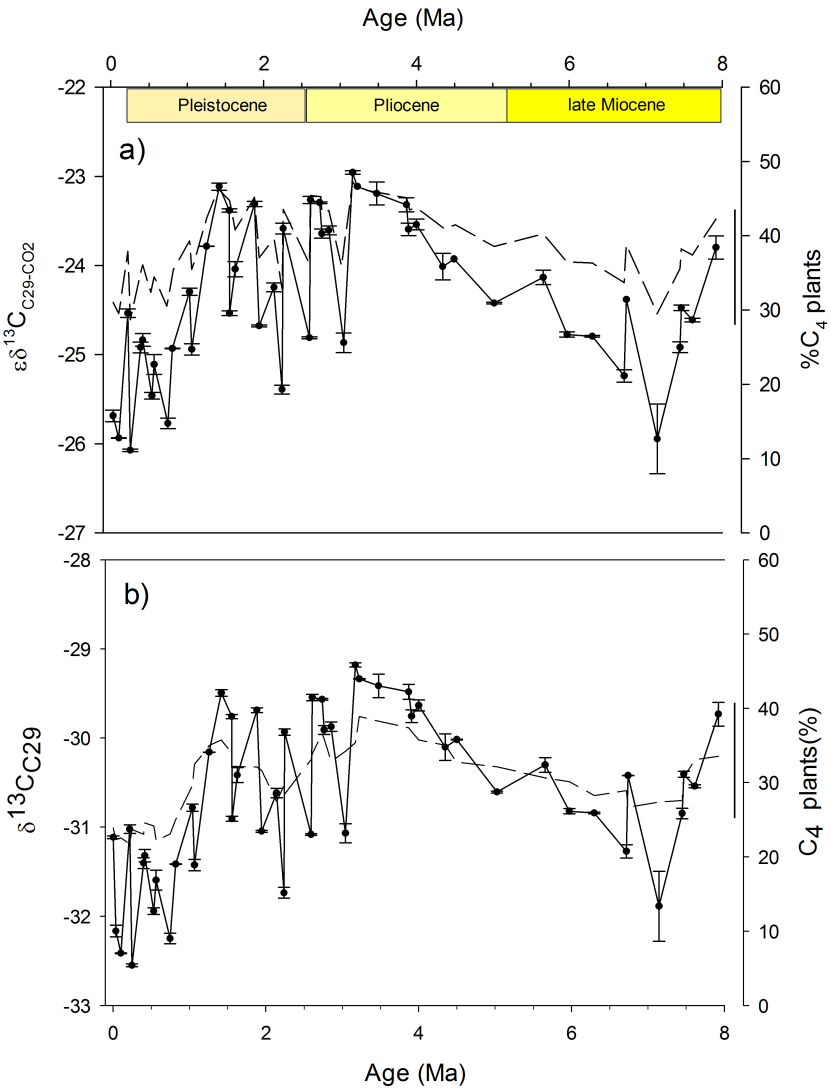

Figure 5.7.: (a) $\delta^{13}C_{29}$ record corrected for the isotopic composition of CO_2 ($\epsilon_{C29-CO2}$), with analytical error (1σ). Black line indicates the 3-point running average, the dashed line represents $\%C_4$ when the end members of the mixing models are also corrected for $\delta^{13}C_{CO2}$. (b) $\delta^{13}C_{29}$ record not corrected for $\delta^{13}C_{CO2}$, with analytical error (1σ). The black line represents the 3-point-running-average of $\delta^{13}C_{29}$. The dashed line represents $\%C_4$ when the end members are not corrected for $\delta^{13}C_{CO2}$.

their pre-concentration of CO_2. This preconcentration give C_4 plants an advantage in low CO_2, hot and arid environments (Sage 2004). This results in the observed isotopic difference between C_3 and C_4 derived *n*-alkanes with $\delta^{13}C$ values of -33.1‰±2.3 and -21.7‰±2.4 for C_3 and C_4 plants respectively (Chikaraishi and Naraoka 2003; Chikaraishi et al. 2004; Rommerskirchen et al. 2006; Vogts et al. 2009). Within C_3 plants, angiosperms display a higher isotopic fractionation than gymnosperms (Chikaraishi and Naraoka 2003). Since the underlying driver for ^{13}C variability in records of leaf wax *n*-alkanes is the relative contribution of C_3 and C_4 plants, changes in plant community composition can be tracked with simple two end member mixing models (Schefuß et al. 2003; Bendle et al. 2006; 2007; Vogts et al. 2012). The isotopic composition of C_3 and C_4 plant end members are assumed to be the modern day isotopic values: -35.1‰ (C_3), and -20‰ (C_4) (global average compiled by Bendle et al. (2007)). Using modern day end members creates a major cavity, as under increased pCO_2 *n*-alkanes are more depleted in ^{13}C (Schubert and Jahren 2012). Thus, in times of higher pCO_2, end members were likely more depleted in ^{13}C than at present (Kürschner et al. 2008; Schubert and Jahren 2012). However, given the large uncertainties in pCO_2 reconstructions, fitting modern day end members to past CO_2 levels is pure guess work. Therefore, modern day global averages are being used. The end member mixing model is calculated as followed:

$$\%C_4 = \frac{\delta^{13}C_{sample} - \delta^{13}C_{C3}}{\delta^{13}C_{C4} - \delta^{13}C_{C3}} \quad (5.2)$$

with $\delta^{13}C_{C3}$=−26.9 ‰ and $\delta^{13}C_{C4}$=−11.8 ‰, which are the end members corrected for the CO_2 effect, using Eq. 5.1. The $\delta^{13}C$ values reported in this study range between −29.1 ‰ to −32.5 ‰ for the uncorrected C_{29} record and between −22.9 ‰ and −26.07 ‰ for the corrected C_{29} *n*-alkane record (Fig. 5.7). Both exhibit the same trends over time. The trend can either be attributed to C_3-plant change or to a change from C_3 to a C_3/C_4 dominated vegetation. The majority of measured isotopic signatures are in the range for C_3 plants (−31.6 ‰±1.7), but are higher than the established average (−33.1 ‰±2.7, (Chikaraishi and Naraoka 2003)). It is possible that $\delta^{13}C$ for the nC_{29}-alkane record presented here reflects changes within the C_3 plant community, i.e. increasing influence of gymnosperms over angiosperms. Gymnosperms fractionate carbon at a lower rate, leading to a ^{13}C enrichment in *n*-alkanes. In a C_3/C_4 mixing models, these $\delta^{13}C$ enriched *n*-alkanes would bias the model towards an increased C_4 plant abundance. However, pollen analysis by Ma et al. (2005) and Jiang and Ding (2008) showed, that if anything, gymnosperms such as *Picea* and *Pinus* were only abundant between 3.7–5.6 Ma, which corresponds to the interval of enriched $\delta^{13}C_{C29}$. Gymnosperms also produce much lower quantities of *n*-alkanes than angiosperms (Bush and McInerney 2013), and so should have less of an impact on the record. Finally, even when gymnosperms are absent from the pollen record, *n*-alkanes show a continu-

ous enrichment in ^{13}C for a much longer period. Subsequently, the isotopic excursions at 2.6 Ma, 1.5–1 Ma and 0.5 Ma are not in concert with conifer expansion. On the basis of pollen data, this gymnosperm scenario can be excluded. Subsequently, changes in the carbon isotope record are interpreted to reflect changes in the C_3/C_4 plant contribution. One example of this plant community change is the global C_4 plant expansion in the late Miocene (Cerling et al. 1997) and their subsequent decline in the Pliocene. The C_4-plant expansion in continental Asia is somewhat ambiguous (Ding and Yang 2000; An et al. 2005; Passey et al. 2009; Jia et al. 2012). An et al. (2005) described reoccurring C_4 expansions on the Chinese Loess Plateau (CLP) well into the Pleistocene, although changes in CO_2 as the main driver for this expansion can be excluded (An et al. 2005). In some studies, the C_4 plant expansion is missing, or is recorded much later in the Pleistocene (Ding and Yang 2000; Jia et al. 2012). The late Miocene C_4 plant expansion is clearly visible in the data presented here, with *n*-alkanes becoming increasingly more enriched in ^{13}C. In the majority of literature, the C_4 plant expansion is constrained to circa 8–4 Ma (Cerling et al. 1997). The onset of the C_4 expansion, as well as the magnitude of expansion agrees with the reconstruction of Quade and Cerling (1995) and Cerling et al. (1997). The end of the major expansion phase, as reconstructed in the Japan Sea agrees with the study results of An et al. (2005) and Suarez et al. (2011). An end member mixing model was applied to both data sets, $\delta^{13}C$ of C_{29} *n*-alkane, and to the record corrected for the effect of $\delta^{13}C_{CO2}$ (Fig. 5.7). There were no changes in trends but in the total abun-

dance of C_4 plants. Overall, the contribution of C_4 plants to the community mix increases from 10 to 25% ±15% at 3.1 Ma, with a decline followed by a peak in the mid Pleistocene, a pattern that is also seen in the data of An et al. (2005) and Passey et al. (2009), increasing the confidence in the data presented here. After another excursion in the Pleistocene, C_4 plants decline to about 10% ±15% which corresponds to the modern day value for the northwest CLP (Sun et al. 2015). From 0–1 Ma, the variation between C_4 and C_3 plant abundance is clearest in the corrected record. Unfortunately the resolution is not high enough to test whether the variation is controlled by orbital forcing (Zhang et al. 2003). Either way, this is an observation that would have been overlooked in the uncorrected $\delta^{13}C_{C29}$ record.

The Plio-Pleistocene variation between ^{13}C enriched and depleted *n*-alkanes suggest a signal from a region with more C_4 or C_3 plants respectively. Decreases in C_4 plant abundance across the Plateau during glacials were found by Zhang et al. (2003), Vidic and Montanez (2004), and An et al. (2005) as response to lower temperatures and altered precipitation pattern. In interglacials, the pattern was reversed (Zhang et al. 2003; Vidic and Montanez 2004). Given the complexity of factors affecting the HTP, the westerly jet path, the position of the Siberian High, global cooling, and Asian monsoon evolution (Nagashima et al. 2007b; Tada et al. 2013; 2016), it should be considered that the source of *n*-alkanes delivered to the Japan Sea was not constant over time. Especially not from 3.6 Ma to Present, when the enhanced HTP uplift (Tada et al. 2016; and references therein) and later enhanced Himalaya uplift altered

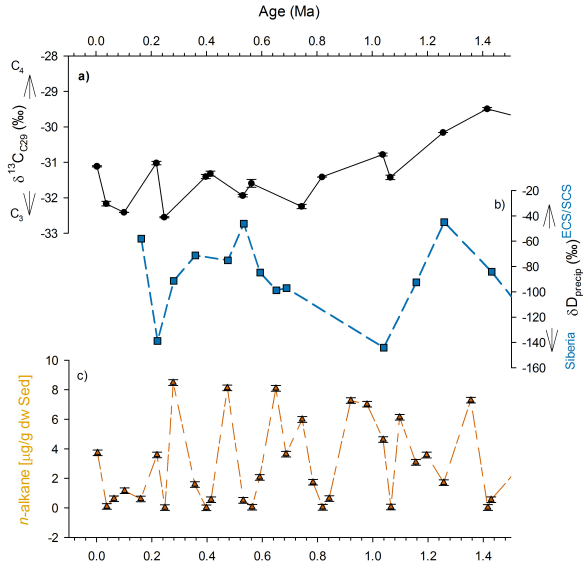

Figure 5.8.: a) $\delta^{13}C$ values of *n*-alkanes derived from U1425, b) Changes in moisture source (δD_{precip}, black line) over the last 2.5 Ma, c) Plio-Pleistocene *n*-alkane fluxes to the Japan Sea at Site U1425

the flow of the westerly jet (Tada et al. 2013), and a reorganization of atmospheric circulation lead to an intensified winter monsoon (Tada et al. 2016). The observed pattern leads to the formulation of the following hypothesis: The alternating influences of the summer monsoon during interglacials and the winter monsoon during glacials (Hovan et al. 1989; Hao et al. 2012; Wang and Chen 2014). An intensified winter monsoon explains the ^{13}C depleted *n*-alkanes (-31 to -32.5‰) in the Plio-Pleistocene record of U1425. Such ^{13}C depleted *n*-alkanes stem most likely from Siberia and northern China (Nagashima et al. 2007b; Yamamoto et al. 2011). Their occurrence during glacial maxima strengthens the formulated hypothesis. In contrast, ^{13}C enriched *n*-

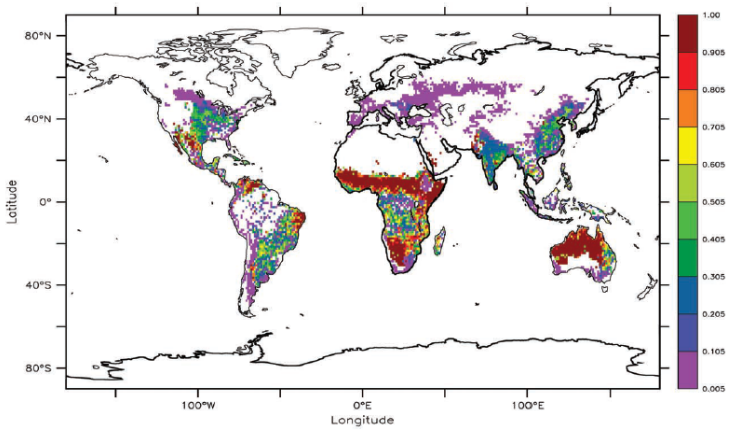

Figure 5.9.: Map of global C_4 plant distribution, taken from Still et al. (2003).

alkanes (-30.5 to -29.5‰) occur during interglacials, which suggest that these are *n*-alkanes delivered from the continental Asian margin, where C_4 plants are abundant during interglacials (Zhang et al. 2003; Vidic and Montanez 2004; An et al. 2005; Fig. 5.9). Therefore it is concluded that since the late Pliocene, the Japan Sea receives *n*-alkane contributions from two different regions: from the continental Asian margin during interglacials, and from Siberia/N-China during glacials. It is difficult to prove whether the enhanced HTP uplift and subsequent alteration of the westerly jet path, or changes in global climate are the cause for such a source shift, because their relation to the Asian monsoon system is not properly understood (Tada et al. 2016). In contrast, the long-term trend towards more ^{13}C enriched *n*-alkanes from 7.4 Ma to 3.1 Ma suggest steady influx from a single source, most likely the continental Asian margin or central Asia, as the C_4 plant expansion did not reach the high latitude environments of Siberia (Passey et al. 2009).

The $\delta^{13}C_{C29}$ record presented here shows the late Miocene C_4 plant expansion from 7.4–3.1 Ma (Hovan et al. 1989; Cerling et al. 1997), and a signal from two different sources from 3.1 Ma onwards. The record also highlights the importance of accounting for the CO_2 effect in order to not overestimate the C_4 plant contribution. The alternating input from 3.1 Ma onwards is caused by the anti-phase behavior of the East Asian monsoon system in response to glacial-interglacial climate variability: the winter monsoon intensifies during glacials, while the summer monsoon is stronger during interglacials (Hovan et al. 1989; Hao et al. 2012).

5.4.3. Changes in δD of terrestrial higher plants

Just as for $\delta^{13}C$ of *n*-alkanes, focusing on just one *n*-alkane (C_{29} or C_{31}) alone can create a bias in interpretations based on δD, as a result of differential fractionation in C_3 and C_4 plants (Wang et al. 2013). A cross-plot of both homologues shows an excellent correlation of δD_{C29} and δD_{C31} (R^2=0.92), again indicating that the mechanism controlling the hydrogen isotopic signatures of the two *n*-alkanes are the same. C_{29} is therefore suitable to use for the interpretation of hydrological changes. δD signatures of bulk organic matter as well as plant-wax components have been used in multiple studies to infer hydrological cycle variability, as their isotopic signature is thought to reflect the isotopic signature of the source water (Sachse et al. 2006; 2012; and references therein). This approach has been established as a robust proxy methodology

for paleohydrology and paleoprecipitation (Liu and Huang 2005; Bai et al. 2009; Aichner et al. 2010; Sachse et al. 2012; Moossen et al. 2015).

The hydrogen isotopic signature of *n*-alkanes (δD_{n-alk}) across the Tibet and Chinese Loess Plateau (CLP) has been used to understand the varying intensities of the East Asian summer monsoon (Liu and Huang 2005; Aichner et al. 2010; Mügler et al. 2010; Bai et al. 2012; Zhuang et al. 2014), with lower D/H ratios interpreted as representing humid conditions in the sampling area. This is taken as an indicator for summer monsoon strength, despite the observation that *n*-alkanes from the HTP are influenced by a multitude of factors (Liu and Huang 2005; Bai et al. 2009), such as aridity and elevation. However, most studies neglect the fact that central Asia is an area where three important atmospheric circulation features meet: the westerlies, Siberian High and the Asian monsoon circulation (Araguás-Araguás et al. 1998). With these distinct circulation features there is also a different isotopic signature of the source water (Fig. 5.3). Maritime air masses derived from the Asian monsoon are more depleted in deuterium than continentally derived air masses from the westerlies. The assumption that δD or $\delta^{18}O$ of climate archives reflect Asian summer monsoon strength is therefore too simplified. Only recently, studies began to consider the differential contribution of different moisture sources and their effect on climate archives (Clemens et al. 2010; Thomas et al. 2016).

Based on findings in Section 5.4.2, it is clear that the influx of *n*-alkanes switched from a single source to at least two sources at around 3 Ma, coinciding with the enhanced HTP uplift, reorganization of atmospheric circulation

and global cooling. The δD signature of *n*-alkanes (δD_{n-alk}) could provide more information about their source region. The signature of δD_{n-alk} is influenced by the δD signature of the source water and environmental factors, such as evaporation and aridity, expressed as fractionation factor $\epsilon_{wax/water}$ (Eq. 5.3). Several studies use the $\epsilon_{wax/water}$ to assess the impact of these environmental conditions on their records, i.e. Bai et al. (2009); Aichner et al. (2010); Zhuang et al. (2014). In this study, the fractionation factor is used to reconstruct the δD value of the source water (δD_{precip}). It is a reasonable approach, since $\epsilon_{wax/water}$ varies across the HTP in a pattern that is not systematically coupled with aridity (Hou et al. 2008; Feakins and Sessions 2010; Garcin et al. 2012; Tipple and Pagani 2013; Gao et al. 2014; Liu et al. 2016), suggesting that aridity only has a minor influence on $\epsilon_{wax/water}$, and is therefore applicable to the geological past (Zhuang et al. 2014; Thomas et al. 2016). Why there is no systematically coupling is not known to date (Zhang et al. 2017).

$$\epsilon_{wax/water} = \frac{\delta D_{n-alk} + 1}{\delta D_{precip} + 1} + 1 \tag{5.3}$$

To calculate δD_{precip}, an $\epsilon_{wax/water}$ of -112.4‰ was used (Aichner et al. 2010; Zhuang et al. 2014). Following the approach of Zhuang et al. (2014) the δD_{n-alk} and $\epsilon_{wax/water}$ were converted to δD_{precip} values, by rearranging Eq. 5.3, to reconstruct moisture contributions from different source areas (Figs 5.3, 5.10, 5.8). δD_{precip} varies between -45 and -145‰ over the studied time interval. Annual weighted δD_{precip} of around -45‰ can be found around the

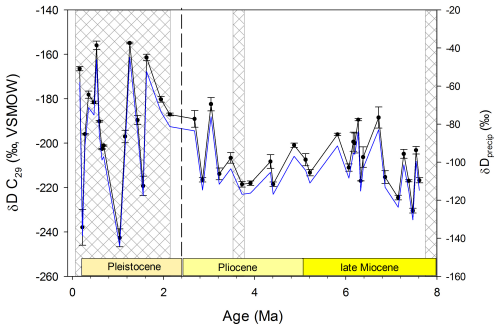

Figure 5.10.: Record of U1425 δD of C_{29}-*n*-alkane (black line) when converted to δD_{precip} (blue line), which allows assessment of precipitation changes alone. Cross-shaded areas indicate tectonic events, the partial uplipft of the TP at 3.6 Ma, and Himalaya uplift at approximately 8, and 1.8 Ma. Dashed black line indicates onset of the northern Hemisphere Glaciation.

Japan Sea, East China Sea (ECS), and South China Sea (SCS), while δD_{precip} of -145‰ and lower are found in Siberia (Fig. 5.3). The δD_{precip} record (Fig. 5.10) is complicated by the shift in deuterium isotopes associated with enhanced Tibetan Plateau uplift, which led to an increased drying of the Asian interior (Peng et al. 2016). At around 3 Ma, a persistent shift towards more deuterium enriched δD_{precip} is observed: from -110 to approximately −70 ‰. Since the enhanced HTP uplift and/or global cooling would have led to the opposite effect, a continuous depletion of deuterium of the source water, this observed 40 ‰ shift is attributed to enhanced drying of continental Asia. Thus on the basis of δD_{precip}, it is concluded that less rain reached the source region. Based on the assumption, that only the amount of precipitation has changed and not the source region itself, the record spanning 3–8 Ma can be corrected

for this 40 ‰ shift. This brings the deuterium record of δD_{precip} up to present day Japan Sea, ECS/SCS values as the moisture source (Fig. 5.8). This reconstructed moisture source is consistent with the theory that the monsoon rain belt is continuously fed with moisture by the south-westerlies flowing along the SCS (Sampe and Xie 2010; Fig. 5.2).

Consistent with the $\delta^{13}C$ record of *n*-alkanes, the record points towards a single source signal until approximately 3 Ma ago. The interval between 7.4–3.1 Ma therefore allows the interpretation of a summer monsoon signal. Based on δD_{precip} it is reasonable to assume that marine derived moisture source has the largest control on the leaf wax lipids' isotopic signature (δD_{n-alk}) at this time. There is a brief period of a rather weakened summer monsoon indicated by δD_{n-alk} from 6–7 Ma, before *n*-alkanes become more depleted in deuterium. A temporary drying of central Asia for this time has also been observed by Peng et al. (2016). Furthermore, D/H ratios are at their lowest between 4.6–5.3 Ma, and 3.3–4 Ma, suggesting a period of a very strong summer monsoon, which is in agreement with other studies (Passey et al. 2009; Suarez et al. 2011; Peng et al. 2016; Zhuang et al. 2014; Xu et al. 2015).

Figure 5.8 shows the variation of the moisture source (δD_{precip}) over the last 1.4 Ma. It is interesting to note that times of extremely depleted δD_{precip} fall into glacial stages, while enriched δD_{precip} fall into interglacial stages. ^{13}C depleted *n*-alkanes also fall into glacial stages, and coincide with deuterium depleted *n*-alkanes. Based on the $\delta^{13}C$ signature of *n*-alkanes it is already established that *n*-alkanes with these signatures stem from the Siberian

area. Furthermore, deuterium signatures of *n*-alkanes in the Okhotsk Sea sediments show similar isotopic signatures of approximately -240‰ (O. Seki, unpubl.), and similar to *n*-alkane δD values measured in the high Arctic (Keisling et al. 2017), strengthening the theory that *n*-alkanes delivered during glacials are delivered from Siberia via strong winter monsoon winds. In contrast, *n*-alkanes in interglacials are delivered from the continental Asian margin, where there are more C_4 plants, and the isotopic signature of the moisture source (East/South China Sea) is recorded in the leaf wax. These *n*-alkanes are delivered into the Japan Sea during the summer, when the westerly jet resides at its position at 40°N (Schiemann et al. 2009), which is approximately on the same latitude as sampling Site U1425.

The calculation of δD_{precip} facilitates the opportunity to look at precipitation changes in the source area alone, at least between 3.1–7.4 Ma. The results suggest that a stronger-than present summer monsoon in the source region existed prior to the Pliocene. An intensified summer monsoon is identified in the beginning and at the end of the Pliocene. At 3.1 Ma, changes in the *n*-alkane δD record coincide with enhanced HTP uplift and global cooling. The δD record presented here, shows large changes in amplitude over the last 2.6 Ma. Based on δD_{precip}, changes in the moisture source can be detected for this interval. From 2.6 Ma onwards, the winter monsoon intensified (Tada et al. 2016; Hovan et al. 1989), delivering isotopically depleted *n*-alkanes from Siberia to the Japan Sea during glacial intervals. During interglacial stages, *n*-alkanes enriched in deuterium are delivered to the Japan Sea when the westerly jet

retreats to the south of the HTP. These results show that precipitation reconstructions based on δD or $\delta^{18}O$ are easily influenced by changes in the moisture source, which is in agreement with findings of Clemens et al. (2010) and Thomas et al. (2016). It should be considered that climate archives do not simply reflect a strengthened/weakened summer monsoon, but also variety in the delivery pathways of moisture.

5.4.4. Changes in *n*-alkane fluxes and chain length

n-alkane fluxes

In a paleoclimatic context, accumulation rates of eolian dust are usually regarded as indicators of aridity in the source region, but can also reflect the strength and changes in atmospheric circulation (Rea 1994; Rea et al. 1998; Nagashima et al. 2011). *n*-Alkanes in the northern Pacific Ocean stem from the Asian interior (Rea et al. 1998; Jia et al. 2012). Leaf wax derived *n*-alkanes are already transported at low wind velocities (Schefuß et al. 2003), and higher velocities facilitate the transport of detrital matter over longer distances (Rea 1994; Rea et al. 1998; Nagashima et al. 2011; Jia et al. 2012). Fluxes of *n*-alkanes concentration (nC_{25}-nC_{35}) show a large variation over time (Fig. 5.11). Since leaf wax components are preferably delivered to the Japan Sea during winter and early spring (Kawamura et al. 2003; Yamamoto et al. 2011) concentrations of *n*-alkanes are additionally regarded as proxy for wind strength, hence winter monsoon or WJ strength. A more precise differentiation based

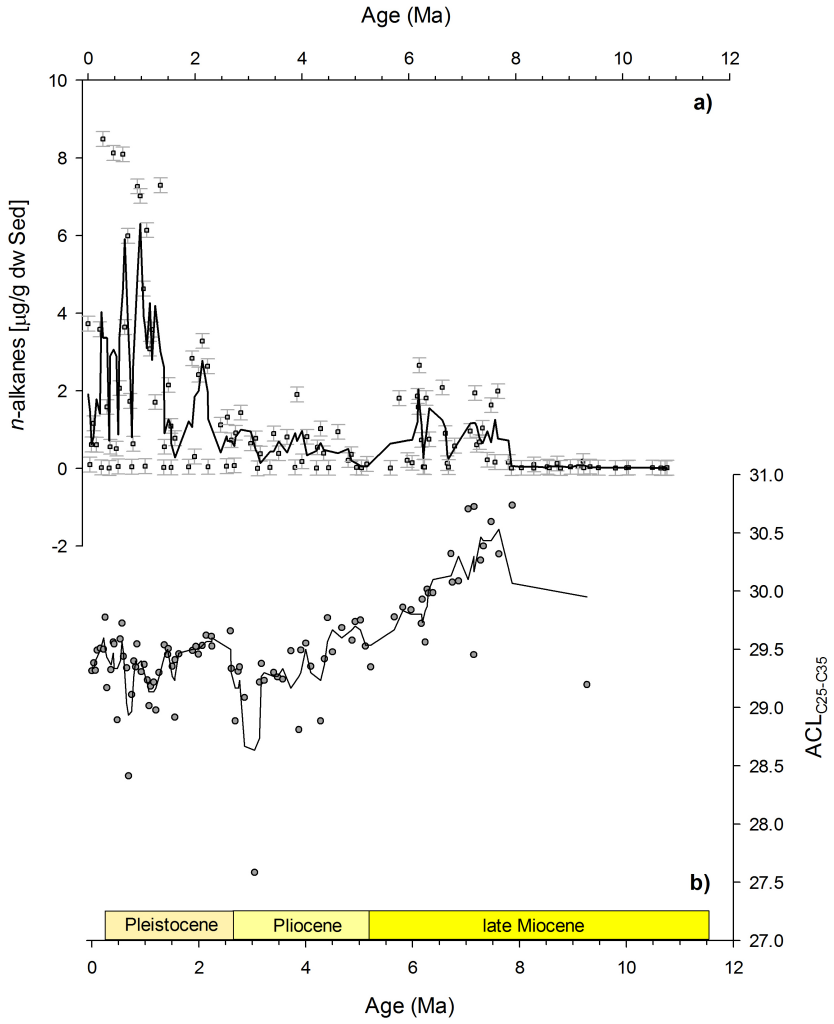

Figure 5.11.: (a) Changes in *n*-alkane concentrations at Site U1425 over time (grey circles, black line represents 3-PRA. Error bars indicate analytical error (1σ) (b) $ACL_{C25-C35}$ reconstructed for Site U1425. Thick black line represents 3-PRA.

on organic geochemistry is impossible. *n*-Alkane concentrations in the Japan Sea prior to 8 Ma are very low (Fig. 5.11), less than 0.1 µg/g dw Sed, with a sudden rise in concentrations at 8 Ma, consistent with the onset of a strong monsoon climate (Zhuang et al. 2014; Xu et al. 2015; Rea et al. 1998; Jia et al. 2012). The period of increased concentrations between 8 Ma and 6 Ma are associated with times of a stronger winter monsoon and a strengthened WJ (Rea et al. 1998; Sun et al. 2008; Jia et al. 2012; Xu et al. 2015).

In the late Miocene to early Pliocene (6–4 Ma), *n*-alkane fluxes to the Japan Sea decreased again, consistent with a weakened winter monsoon (Sun et al. 2008; Xu et al. 2015) as well as a weakening of the westerly circulation (Sun et al. 2008). Another explanation for decreased *n*-alkane contribution is the relatively intense summer monsoon at that time, which lead to increased dust fixation by a dense vegetation cover. It is interesting to note that no increased *n*-alkane contribution to the Japan Sea is recorded between 4.5–5 Ma, when the Amur River discharge and possibly *n*-alkane deposition increased.

At the Plio-Pleistocene border, a steady increase in *n*-alkanes is observed, associated with an enhancement of the winter monsoon (Rea et al. 1998; Jia et al. 2012; Xu et al. 2015) and a progressive strengthening of the westerly jet (Sun et al. 2008). The last 2.5 Ma of the record show large fluctuations in *n*-alkane concentrations, with a timing consistent with orbital-scale cyclicity in Northern Hemisphere glaciation (NHG). As the glacial/interglacial cycles of the Pliocene became established and more pronounced, so did the expansion and contraction of arid areas during glacials and interglacials respectively

(Nagashima et al. 2007a; Rea 1994). The *n*-alkane fluxes presented here exhibit strong maxima during glacials, while they abruptly decrease during interglacials (Fig. 5.8). Dust accumulation is also higher during glacials, suggesting that *n*-alkane fluxes correspond to the expansion of arid areas and increased atmospheric dust load in the air. During interglacials, increased precipitation or dense vegetation fixed the available dust and reduced the associated transport of *n*-alkanes to the Japan Sea.

Average chain length

Changes in ACL are often used to infer past environmental changes affecting the plant community structure (Rommerskirchen et al. 2006), including temperature (Castañeda et al. 2009; Vogts et al. 2012) and precipitation (Moossen et al. 2015). The ACL record presented here (Fig. 5.11), shows a long-term decline to about 3.6 Ma from 30.7 to 29.2. The end of this trend is marked with an abrupt decrease to about 27.5, before the average chain length increases again. According to the aforementioned studies, a decreasing $ACL_{C25-C35}$ is either due to cooling of the source region, a trend towards C_3 plant influence, or a shift towards a more humid climate. In this case, a cooling of the source area is one possibility, in respect to the enhanced uplift of the HTP which shields the Asian interior from the inflow of warm, moist air masses. An increase in seasonal precipitation from 8–3 Ma is observed on the basis of the reconstructed δD_{n-alk}, but the change in $ACL_{C25-C35}$ indicate steadily increasing precipitation

over the same time interval. Further, since the contribution of C_4 plants to the record increases, so should ACL, and thus plant community change cannot be the driving mechanism for decreasing ACL. Instead, it seems most likely that a decrease in temperatures is the main driver for the decreasing $ACL_{C25-C35}$ for this interval.

After 3 Ma, $ACL_{C25-C35}$ exhibits a drastic increase to 29.1 and remained around this value for 1.5 Ma, before showing some smaller variations between 28.4 and 29.5. While the earlier part (3.5–8 Ma) of the $ACL_{C25-C35}$ record displays a good agreement with the cooling of central Asia, the latest part (2.5 Ma–Present) remains enigmatic. With respect to source region changes between glacial and interglacial intervals, there is the possibility that climate specific characteristics from the mid-latitudes and high-latitudes are canceling each other out, making the ACL difficult to interpret from 3 Ma onwards (Kawamura et al. 2003). A comparison with ACL records from the central CLP (Bai et al. 2009) and the NE-TP (Peng et al. 2016) shows no synchronous changes (Fig. 5.12). There might be a similar decreasing trend prior to 5 Ma with records from the central CLP and records from the Lamashan region of the TP. From 5 Ma to near present, other ACL records indicate increasing ACL, while U1425 continues to indicate decreasing ACL. A comparison with ACL records from the Horn of Africa was equally inconclusive (Uno et al. 2016).

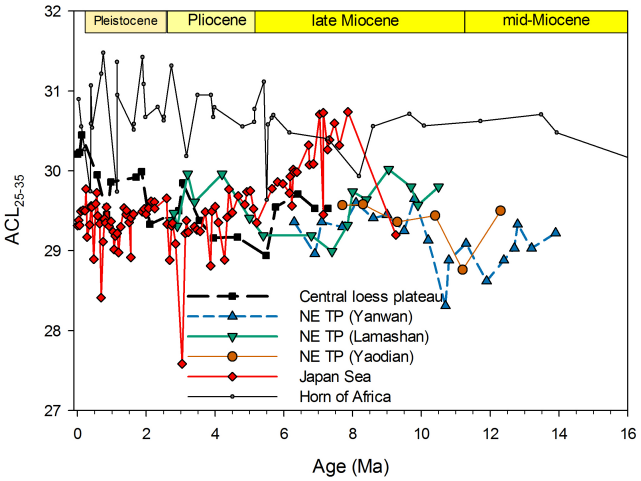

Figure 5.12.: ACL comparison between records from the Japan Sea, the central CLP (Bai et al. 2009), the NE-Tibet Plateau (Peng et al. 2016), and the Horn of Africa (Uno et al. 2016)

5.5. Conclusions

5.5.1. Technical conclusion

This study demonstrates that the Japan Sea is an excellent recorder of changes in the Asian monsoon climate, but the interpretation of $\delta^{13}C$ and δD of *n*-alkanes in the Japan Sea is not straight forward. Prior to enhanced HTP uplift at 3.6 Ma, a steady isotopic signature of δD_{precip} and $\delta^{13}C$ suggest a single source signal. Based on reconstructions of δD_{precip}, the moisture source carries an ECS/SCS-derived signal, consistent with the observation that the Asian monsoon is continuously fed by moisture delivered by the south-westerlies (Schiemann et al. 2009; Sampe and Xie 2010). A correction for the carbon isotopic signature of CO_2 reduces the bias in estimation of C_4 plant contri-

bution to the Japan Sea. The record presented here becomes complicated at around 3 Ma, which marks the timing of enhanced Tibetan Plateau uplift, as well as global cooling and Northern Hemisphere glaciation. Their effect on, or relation with, the summer/winter monsoon system is poorly understood (Tada et al. 2016). The reconstruction of δD_{precip} reflects changing sources of *n*-alkanes deposited in the Japan Sea. The record points to a glacial/interglacial variation between Siberia and SCS/ECS respectively (Fig. 5.8). Corrected *n*-alkanes also show a glacial-interglacial variation between C_3 vegetation and mixed C_3/C_4 vegetation (Fig. 5.8), reflecting *n*-alkane deposition from Siberia and the continental Asian margin respectively.

This approach highlights that the interpretation of precipitation records from the SE-Asian region is oversimplified, as representing either a strengthened or weakened Summer monsoon is problematic. This new record from the Japan Sea shows contributions from multiple moisture sources, which are important to consider when attempting to understand the triangular relationship of HTP uplift, global cooling and Asian monsoon evolution.

5.5.2. Consequences for paleoclimate reconstructions

The Japan Sea is an excellent archive for the reconstruction of the Asian monsoon system. With the resolution of records presented here, this reconstruction is clear until the point of enhanced Tibetan Plateau uplift, when the switch from single to multiple sources occurs. Based on the changes from 3.1–7.4 Ma

a climatic interpretation is only possible for this interval.

During the Mio-Pliocene, the summer monsoon in the source region was likely stronger than present. An intensified summer monsoon occurred, with interruptions, from 3–5 Ma. This increased warm-season precipitation, in combination with declining CO_2 (Seki et al. 2010; Zhang et al. 2013) favored the expansion of C_4 plants in central Asia. The continued expansion of C_4 plants despite a later weakening summer monsoon shows that C_4 plants are also able to thrive in intermediate conditions (Suarez et al. 2011).

For the last 2.6 Ma, increased (decreased) C_4 plant contribution occurred during interglacial (glacial) periods, complemented by deuterium enriched (depleted) precipitation and low (high) accumulation rates of *n*-alkanes in the Japan Sea. It was hypotesized that these characteristics reflect the contribution of two source areas to the Japan Sea. In glacial periods, the Siberian High lasted longer and retreated later (Ding et al. 1995; 1999) delivering more deuterium and ^{13}C depleted *n*-alkanes to the Japan Sea. These signatures reflect the δD_{precip} typical for Siberia, furthermore C_3 vegetation is predominant in the source area (Still et al. 2003; Fig. 5.9). Since the summer- and winter monsoon are in anti-phase for the Plio-Pleistocene (Hao et al. 2012), summer monsoons are stronger in interglacials, and *n*-alkanes from the continental Asian margin are delivered to the Japan Sea, indicated by a $\delta^{13}C$ signal typical for a mixed C_3/C_4 plant community and δD_{precip} characteristic for moisture derived from the ECS/SCS. Since the resolution of the record presented here is low, a more detailed examination of glacial/interglacial changes is not feasible.

n-alkane accumulations accurately reflect dust fluxes reconstructed by Sun et al. (1998); Rea et al. (1998) and Jia et al. (2012), and hence are a good reflector of the drying of the central Asian continent. Dust accumulation started at 8 Ma, marking the onset of the modern Asian monsoon system (Rea et al. 1998; Jia et al. 2012). During the phase of a stronger-than-present summer monsoon, from 3.4–7.4 Ma, dust fluxes are low, indicating that dust suspension was reduced, either due to increased precipitation or a more dense vegetation cover. With the onset of the NHG, *n*-alkane accumulation rates increase once more, with fluxes peaking during glacial periods. During glacials, deserts in central Asia expanded (Nagashima et al. 2007b), with more dust suspension and leaf-waxes transported from vegetation at the continental Asian margin and Siberia to the Japan Sea. In contrast, during interglacials the majority of dust remained fixed, resulting in lower *n*-alkanes transport to and deposition in the Japan Sea. An interpretation in terms of summer monsoon strength and its relation to vegetation change in central Asia is not feasible for the last 3 Ma. The records presented here however, give good insight into the dominant circulation features (westerly jet, Siberian high) at a given time. A high resolution analysis of the last 3 Ma would be required to fully determine the atmospheric pressure system associated with the East Asian monsoon, (summer monsoon, winter monsoon, and westerly jet), and to reconstruct their spatial pattern and interrelationship, on glacial/interglacial timescales.

6. Terrestrial organic matter and depositional environment at the Yamato Rise

Abstract

A sediment core from the Japan Sea were investigated, applying bulk sedimentary research methods and GC, as well as GC-MS analysis of biomarkers. The total organic carbon content of the investigated sediments is generally moderate (~0.7%), but very high during the late Miocene (~4-5%) and Pleistocene (~3%). Mixing models, used to assess the relative contribution of terrestrial organic matter to the Japan Sea gave inconclusive results. A number of triterpenoids were detected, such as 28,30-dinorhopane, suggesting sediment deposition under anoxic conditions during the late Miocene, and eventually Pleistocene. The Lycopane/nC$_{31}$ indicates an anoxic environment during the

late Miocene and late Quaternary.

6.1. Introduction

The aim of this study was to reconstruct the variation in terrestrial organic matter (TOM) delivery and selected biomarkers to reconstruct the environmental history of the Japan Sea. The fate of TOM and past environmental conditions are thought to be closely related to the tectonic evolution of the Japan Sea (Tada et al. 1999; Tada 2004). The contribution of TOM is thought to be decreasing over time, when the Japan Sea changed from a small and shallow sea (Ingle 1992) to its present size with abyssal depths (Xu et al. 2016) and faced semi-isolation from large rivers, such as the Yellow- and Amur Rivers (Ingle 1992; Tada 1994; Xu et al. 2016). Furthermore, the onset and changes in the East Asian monsoon system (EAM) might have driven TOM contribution to the sediment, by altering the continental run-off of detrital matter (Stax and Stein 1994; Tada 1994).

total organic carbon (TOC), C/N and $\delta^{13}C_{org}$ variations measured on these samples are simple, but are only general indicators of sediment properties. Meanwhile, GC and GC-MS analysis provides a more detailed picture, from which it is possible to determine the provenance of organic matter. The contribution of TOM is important to constrain because it represents an important part of global carbon cycle (Eglinton and Repeta 2003) that eventually ends up in ocean. The climate cycle has an important control on TOM delivery to

ocean (Hedges et al. 1997; Eglinton and Repeta 2003). However, the fate of TOM is not well constrained overall, particularly due to the difficult identification of TOM in ocean (Hedges et al. 1997; Eglinton and Repeta 2003). Here, it was attempted to reconstruct the TOM delivery to the Japan Sea for the last 10 Ma, by applying four different end member mixing models. These models are based on the branched index of tetraethers (BIT), the n-alkane/alkenone ratio, $\delta^{13}C_{org}$ and the C/N ratio detected in the analyzed sediments (Moossen et al. 2013; and references therein). These mixing models will help to constrain the influx of TOM and interpret changes in relation to the tectonic evolution of the Japan Sea, and EAM intensity. In principle, the accurate quantification of TOM also allows an estimation of past primary productivity (Knies and Mann 2002), which is another oceanographic factor that would lead to increased understanding of the of the Japan Sea, in respect to the EAM and tectonic evolution of the Japan Sea (Tada et al. 2015).

This study focusses on the analysis of acyclic compounds, and pentacyclic triterpenoids, which are useful indicators of algal contribution and diagenesis respectively. The hopanoids derived from bacteria can contribute substantially to the sedimentary matter post its deposition. Although more information can be derived from polar moieties of the hopanes, it is not feasible to analyse them on GC-MS, thus only apolar compounds analysed for this study. Lycopane (Ly) is an acyclic C_{40} isoprenoid, presumably produced by a marine photoautotrophic organism (Sinninghe Damsté et al. 2003). Lycopane is quickly degraded under oxic conditions (Sinninghe Damsté et al. 2003). The

ly/nC$_{31}$ ratio subsequently indicates the relative abundance lycopane compared to the very stable nC$_{31}$, and can be used as an indicator for paleooxicity (Sinninghe Damsté et al. 2003). 28,30-Dinorhopane (28,30-DNH) is a rather rare C$_{28}$ hopanoid, and C$_{28}$ hopanoids are generally absent from the geochemical record in most studies. It first has been identified in sediments of the Monterey formation (Moldowan et al. 1984). It is contended that it is derived from the 28,30-Dinorhop-13(18)-ene, associated with bacteria residing at the anoxic-oxic interface in low-oxygen marine depositional environments (Sinninghe Damsté et al. 2014). The variation of these markers will be compared to the lithology of both cores, as well as redox-sensitive minerals to evaluate the effect of changing water mass properties on the biomarker record and the depositional environment.

6.2. Methods

The methods for standard analyses, such as determination of bulk parameters, identification and quantification of *n*-alkanes, alkenones, and hopanoids can be found in Chapter 2. Mass spectra of compounds described in this Chapter are found in Appendix A.

6.2.1. Lithology

Core U1425 was divided into 3 lithological units, based on the frequency of alternating dark-light layers (Unit I), diatom content (Unit II) and terrestrial matter as well as lithification (Unit III). The extensive description of the lithology of U1425 can be read in Tada et al. (2015). All summary figures in this study have the lithological subunits plotted with the data presented here. A brief summary can be found in Section 6.4.2.

6.2.2. TOM calculations

Changes in contribution of TOM to the Japan Sea were calculated by using simple binary end member mixing models of C/N, $\delta^{13}C_{org}$, BIT, and *n*-alkane/alkenone ratio, as used by Moossen et al. (2013; and references therein).

$$OC_{terr} = \frac{X_{sample} - X_{terr}}{X_{mar} - X_{terr}} \tag{6.1}$$

X_{sample} is the C/N, BIT or $\delta^{13}C_{org}$ value of the sample, while X_{mar} and X_{terr} are the marine and terrestrial end member respectively).

The application of the *n*-alkane/alkenone mixing model is based on the assumption that long-chain *n*-alkanes are solely produced by higher plants (Eglinton and Hamilton 1967), while alkenones are solely produced by marine haptophyte algae (Volkman et al. 1980). The ratio is calculated using odd-chain *n*-alkanes and C_{37} alkenones, according to Eq. 6.2 (Weijers et al.

2009):

$$\frac{[n-alkanes]}{[n-alkanes]+3[C_{37}-alkenones]} \tag{6.2}$$

6.2.3. MARs

Mass accumulation rates (mass accumulation rate (MAR)) of biomarkers, such as alkenones, and *n*-alkanes, and total organic carbon were calculated as followed:

$$MAR_{[\text{biomarker}]} = (biomarker[\mu g/g]) \times \text{DBD} \times \text{LSR} \tag{6.3}$$

6.3. Results

6.3.1. TOC, $\delta^{13}C_{org}$, C/N

Bulk parameters of Site U1425 are shown in Figure 6.1. The TOC content of sediments recovered from U1425 varies between 0.3 and 5.5 %. Continuously high contents of TOC are measured during the late Miocene (10–6 Ma). This high TOC content coincides with the deposition of clay and quartz (25–27%) from 9.5–10.8 Ma. From 7.4–9.5 Ma high TOC contents are co-occurring with a high diatom content (>25%) and some clay and quartz compounds (Tada et al. 2015). During the Pliocene, high TOC contents are intermittent, during the generally low TOC contents, and the lithological composition is mostly diatomaceous ooze, and some clay. An increased fluctuation of TOC contents is found in the Pleistocene, where the lithological composition is comprised of

terrigenious and biogenic grains, and clay minerals (Tada et al. 2015).

The $\delta^{13}C_{org}$ signature of sediments recovered from U1425 varies between -21.4 ‰ and -25.4 ‰. During the late Miocene (10–5.8 Ma), $\delta^{13}C_{org}$ averaged around -23.1 ‰, these enriched ^{13}C sediments are interrupted by a sudden decline to more depleted $\delta^{13}C_{org}$ at 6.3–5.1 Ma. From 5.8 Ma to Present, average $\delta^{13}C_{org}$ varies around -22.7 ‰, and the amplitude of shifts between more depleted/enriched values increases.

The TOC/N ratio (dimensionless) of the sediments studied here ranged between 4.3 and 20.3. A trend to lower TOC/N ratios is observed during the late Miocene (10.8–6 Ma), where TOC/N rapidly decreases from 12 to approximately 6. Small amplitude changes accompany this decreasing trend. Within a further decreasing trend from 6–2.5 Ma, larger amplitude changes in the TOC/N ratio occur and the ratio varies between 12 and 7. With the onset of the Quaternary (2.5 Ma), drastic increases in the TOC/N ratio are observed, reaching peak values of around 20 at 0.9 Ma.

6.3.2. TOM mixing models

For the mixing models presented here, end members were carefully considered. For the mixing model using the branched index of tetraethers (BIT) based on branched glycerol dialkyl glycerol tetraethers (brGDGTs) (Hopmans et al. 2004; Fig. 6.2a), 0 was the ultimate marine end member, although branched GDGTs are also produced in the water column (Peterse et al. 2009; Fietz et al.

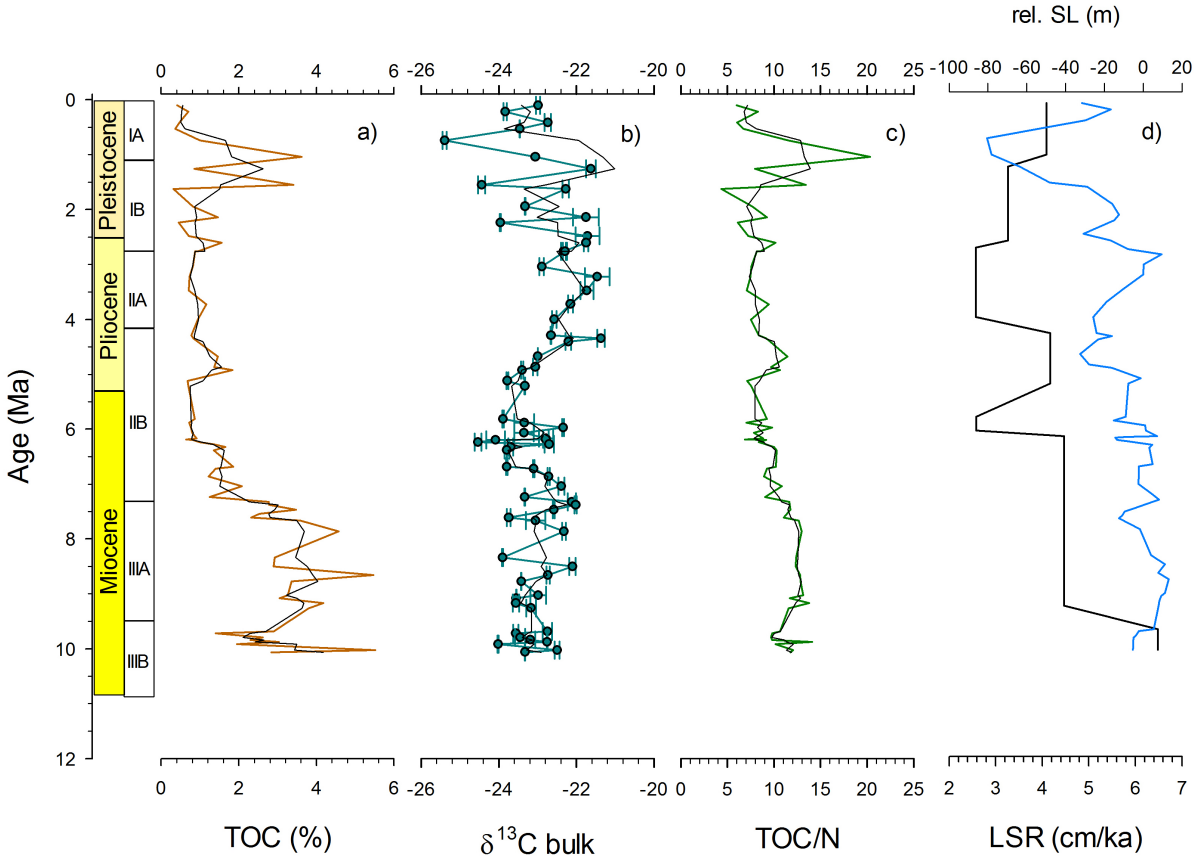

Figure 6.1.: Bulk parameters for Site U1425. The black line indicates the 3 point-running-average for each parameter: a) Total organic carbon in percent, b) $\delta^{13}C_{org}$, c) TOC/N and d) Linear sedimentation rate in cm/ka, and relative sea level (m) after Miller et al. (2005).

2012), and therefore the true end member is likely higher than 0. 0.91 was chosen for the terrestrial end member, because crenarchaeol is produced in soils as well as in the water column (Weijers et al. 2006b). The end member mixing model based on BIT indicates the lowest TOM contribution to the Yamato Rise of all four mixing models, with estimated contribution between 1 and 22%. This is similar to the results of other studies that consider a range of methodologies for estimating the contributions of terrestrial-derived organic carbon to marine systems (i.e. Moossen et al. 2013).

The marine end member in the *n*-alkane/alkenone mixing model is equal to 0, while the terrestrial end member is set to 1. TOM input seems to follow MARs of *n*-alkanes (Fig. 6.2b) and its contribution varies between 10 and 40%. High TOM input is recognized during the late Miocene (8–6 Ma), and during the Pleistocene, which is in agreement with the lithological findings of Tada et al. (2015).

The $\delta^{13}C_{org}$ based mixing model works with end members of −20 ‰ (marine) and −33 ‰ (terrestrial) (Fig. 6.2c). The $\delta^{13}C_{org}$ record, compared to compound-specific carbon isotope records, is very unspecific since the sedimentary record receives input from a variety of sources, such as eukaryotes, cyanobacteria, and methanotrophs, and higher land plants (Meyers 1997; Peters et al. 2005; Bianchi and Canuel 2011). The results of this mixing model only show small variations, the contribution of TOM seems to be varying around 30% for the studied interval. No clear trend emerges from this mixing model.

The TOC/N based mixing model was set up with a marine end member of 3 and a terrestrial end member of 20 (Fig. 6.2d). Small changes in the C/N ratio can cause large variations in TOM estimations (Meyers 1997; Lamb et al. 2006), which might explain the highest %TOM estimates of all mixing models. TOM influx seems to decrease from 60% in the late Miocene to 20% in the late Pliocene, before 100% TOM are detected in the Pleistocene.

In summary, all end member mixing models require thoughtful selection of end members. A consideration of potential offsets between actual terrestrial and marine compositions, and these assumed end member compositions, as well as an awareness of the inter-dependence of summary parameters based on the ratios of two end members is necessary. In the latter case, changes in the flux of only one end member constituent, in this case the accumulation rate of either marine or terrestrial biomarkers, i.e. the *n*-alkane to alkenone ratio, will generate a change in the summary ratio. This is problematic if, for example, a decline in the accumulation rate of alkenones, is wrongly interpreted as an increase in the accumulation of terrestrial-derived organic carbon.

6.3.3. Hopanes

Hopanes in sediments of the Japan Sea are dominated by C_{29}–C_{31} 17β,21β-hopanes, followed by C_{29}-C_{31} 17α,21β-hopanes. Within the moretane series, the C_{29} moretane is the most prominent compound. Smaller abundances of β-trisnorhopane, 17α,21β-, and 17β,21β-bishomohopane were measured too, but

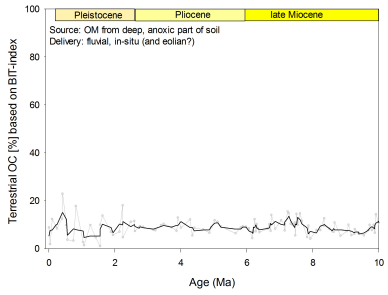

(a) BIT based OC_{terr} mixing model

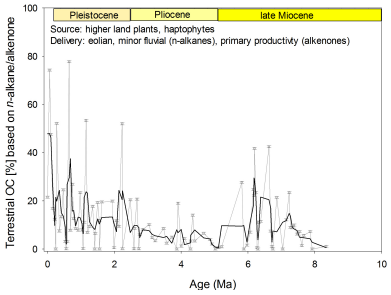

(b) *n*-alkane/alkenone mixing model

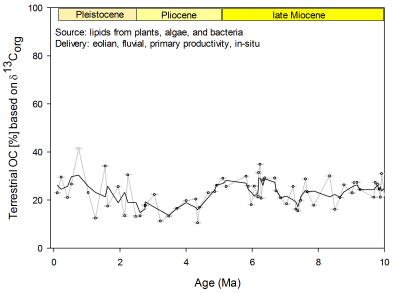

(c) $\delta^{13}C_{org}$ mixing model

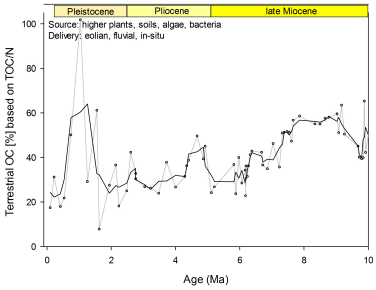

(d) TOC/N mixing model

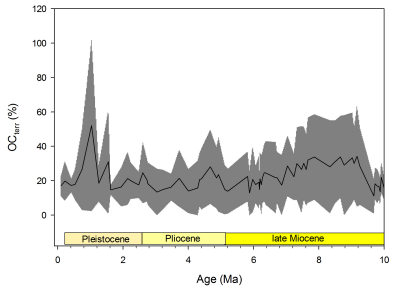

(e) Average of all four mixing models

Figure 6.2.: Terrestrial OC contribution (%) based on a) BIT, b) *n*-alkane/alkenone ratio c) $\delta^{13}C_{org}$, d) TOC/N ratio. e) represents the total variation of all four mixing models (gray area) and the average (solid black line). The end member mixing model bases on Eq. 6.1, end members for each model are described in Section 6.3.2. Black arrows in Figs 6.2a and 6.2d refer to events caused by the East Asian monsoon system.

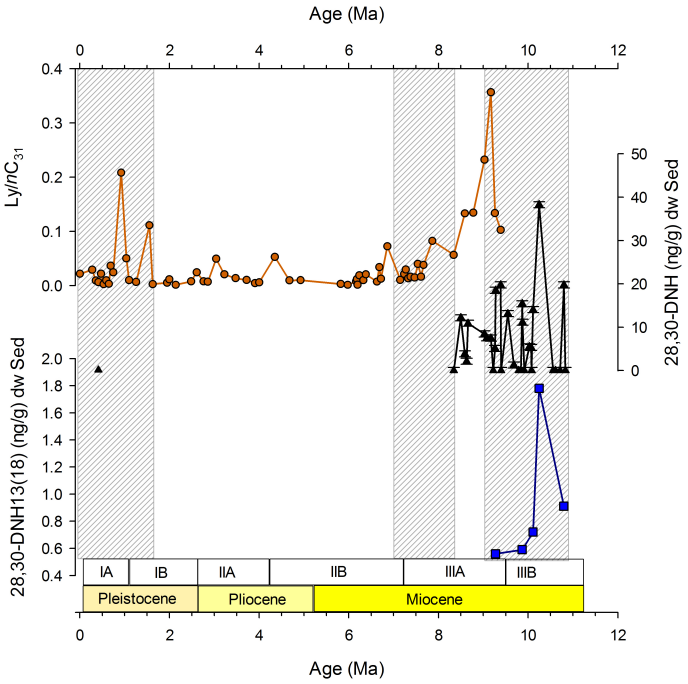

Figure 6.3.: Ly/nC$_{31}$, 28,30-DNH and 28,30-Dinorneohop-13(18)-ene were used as markers for depositional environment changes in the Japan Sea. Given are also the lithological subunits of core U1425 as defined by Tada et al. (2015). Grey shaded areas indicate highly reducing environments, as reconstructed by Masuzawa et al. (1992); Tada (1994) and Kimura et al. (2004).

not were not continuously present throughout the record. 28,30-Dinorhopane (Moldowan et al. 1984; 28,30-DNH) was found in high concentrations of 2–38 ng g^{-1} ±0.7 dw Sed. The presence of 28,30-DNH is limited to 8.3–10.3 Ma (Fig. 6.3). Sometimes, 28,30-Dinorneohop-13(18)-ene co-occurs with 28,30-DNH.

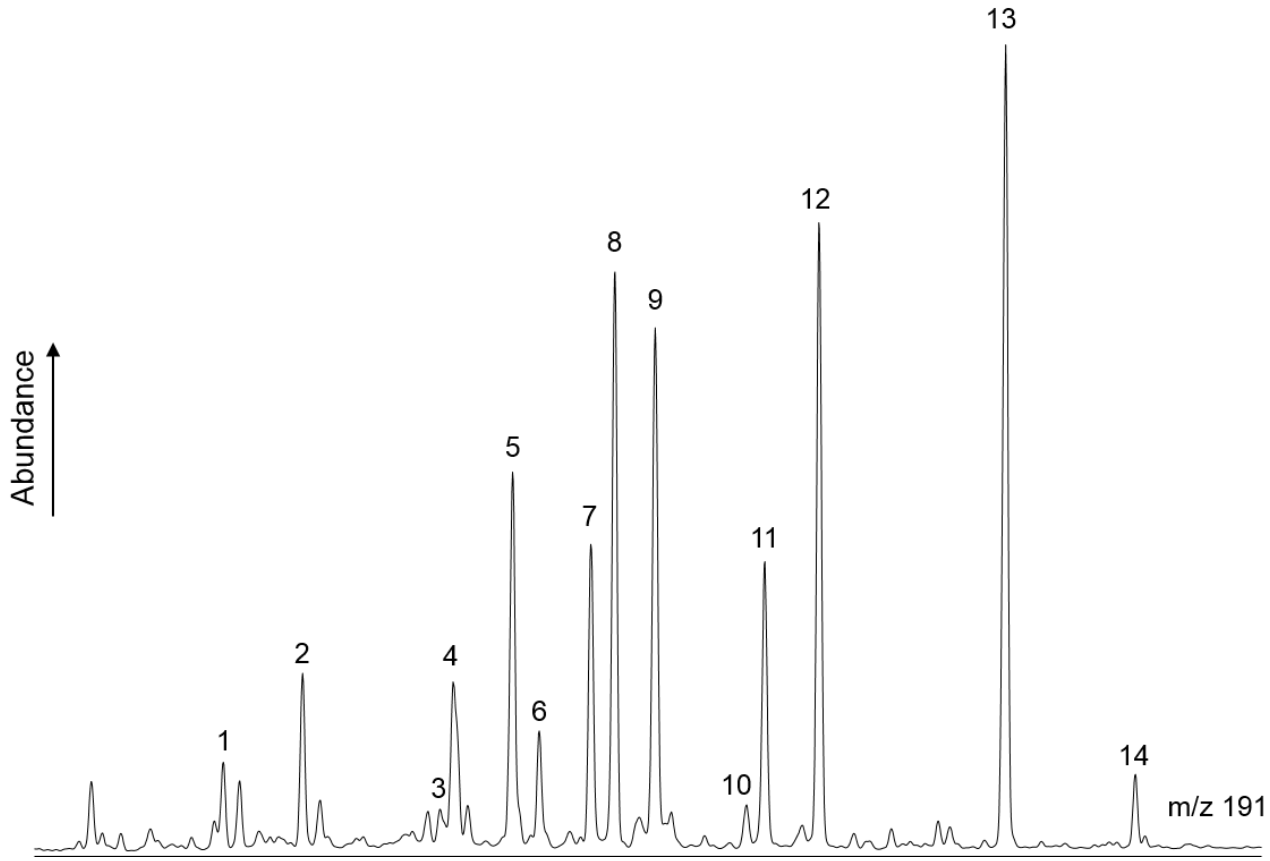

Figure 6.4.: Typical distribution of hopanes and (rearranged) hopenes in sediments of U1425 and 797

Table 6.1.: Identities of hopanes and rearranged hopenes in the aliphatic fraction (10.08 Ma old), labeled in Fig. 6.4

Peak	Identification
1	C_{27} $\Delta^{13(18)}$ hopene [22,29,30-trisnorneohop-13(18)-ene]
2	C_{27} 17β hopane [trinor-17β(H)-hopane]
3	C_{29} $\Delta^{13(18)}$ hopene [30-norneohop-13(18)-ene]
4	C_{29} $\Delta^{17(21)}$ hopene [30-norhop-17(21)-ene]
5	C_{30} $\Delta^{17(21)}$ hopene [hop-17(21)-ene]
6	C_{29} moretane [30-nor-17β(H)-21α(H)-hopane]
7	C_{30} 17α,21β hopane [17α(H),21β(H)-hopane]
8	C_{30} $\Delta^{13(18)}$ hopene [neohop-13(18)-ene]
9	C_{29} 17β,21β hopane [30-norhop-17β(H),21β(H)-ane]
10	Fern-7-ene
11	C_{31} 17α,21β hopane [17α(H),21β(H)-homohopane]
12	C_{30} 17β,21β hopane [17β(H),21β(H)-hopane]
13	C_{31} 17β,21β hopane [17β(H),21β(H)-homohopane]
14	C_{32} 17β,21β hopane [17β(H),21β(H)-bishomohopane]

6.3.4. Aliphatic markers

Lycopane is derived from a marine photoautotrophic organism, but the exact source is unknown. Lycopane is well preserved under anoxic conditions (Sinninghe Damsté et al. 2003) and sporadically occurs throughout the record. Since it is well preserved under anoxic conditions, it serves as a good proxy for paleoxicity of the water column (Sinninghe Damsté et al. 2003). Ly/nC31 ratios are high during the late Miocene, rapidly decline at around 6 Ma, and only start to flucutate between high and low ratios during the Pleistocene (Fig. 6.3).

6.4. Discussion

6.4.1. TOM mixing model efficacy

It should be noted that the TOM mixing models based on ratios are just approximations, and should be treated with caution. In example, a relative change in contribution from one carbon pool decreases, and thus the relative contribution of the other carbon pool must increase, even though its contribution remained constant. Furthermore, models based on biomarkers as representatives of an entire carbon pool are prone to changes in the production and deposition of these biomarkers. Particularly in marine environments, caution should be exercised with respect to the redox state of the water column. Terrestrial carbon is more refractory than marine organic matter (Eglinton and Repeta 2003), and

under oxic conditions will skew the mixing models to increased TOM contribution, since it is simply preserved better.

Since the BIT is an estimation for the amount of soil organic matter that is being delivered to the ocean (Hopmans et al. 2004; Weijers et al. 2006a) it most likely underestimates the contribution of all terrestrial organic matter to the Japan Sea. Furthermore, estimations are skewed by the fact that GDGTs only represent the deep, anoxic part of the soil (Weijers et al. 2006a), thus even underestimate the soil OM delivery to the Japan Sea. Additionally, this TOM mixing model is biased by the in-situ production of brGDGTs (Peterse et al. 2009; Fietz et al. 2012), which influences the end member choice and subsequently model outcome.

The *n*-alkane/alkenone proxy for TOM input is complicated by the fact that terrestrial material is more refractory than marine organic matter (Hedges et al. 1999; Sinninghe Damsté et al. 2002; Eglinton and Repeta 2003), and therefore a potential bias to an increased TOM contribution is possible. Furthermore, this model reflects two different delivery pathways, which is eolian for the *n*-alkanes and in-situ surface production for the alkenones. The eolian deposition of TOM is particularly important for marginal seas downwind of major atmospheric circulation features, which is the case for the Japan Sea (Otosaka et al. 2004; 2008). Exclusively fluvial derived TOM in the Japan Sea is left out of this model. This study found lowest concentrations of alkenones during cold periods, which creates a bias of this TOM mixing model towards more influx of terrestrial organic carbon (Fig. 6.5). Furthermore, the intermittent

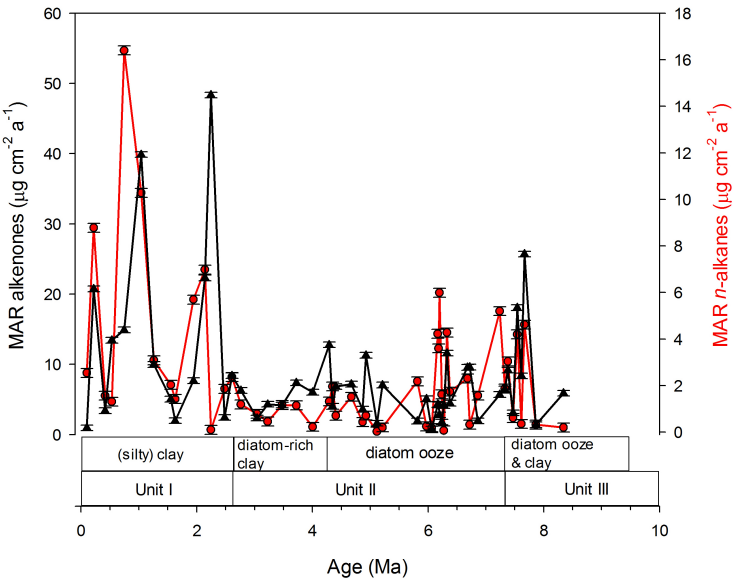

Figure 6.5.: MAR for alkenones and *n*-alkanes in the Japan Sea since the late Miocene, calculated according to Eq. 6.3. Note different scale on both y-axes.

oxic conditions during the early Pliocene and Pleistocene preferentially degrade alkenones over *n*-alkanes (Hoefs et al. 2002; Sinninghe Damsté et al. 2002), skewing the record even further towards increased TOM contribution to the Yamato Rise. These preservation issues create a serious bias for this mixing model.

Since the isotopic siganture for terrestrial and marine organisms is so diverse, TOM estimates based on $\delta^{13}C_{org}$ can be heavily biased. Input of C_4 leaf waxes, with a signature of $-21.7\,‰$ (Farquhar et al. 1989; Chikaraishi and Naraoka 2003), result in biasing the mixing model towards a more marine signal. Soils in Japan also tend to have a positive $\delta^{13}C_{org}$ signature rel-

ative to the assumed terrestrial end member (Hiradate et al. 2004). In the reverse direction, the activity of methanotrophs in the sediment column generates strongly ^{13}C depleted organic matter (Whiticar 1999; Thiel et al. 2003), and would falsely bias this $\delta^{13}C_{org}$ mixing model towards an increased contribution of TOM. Changes based on this mixing model should thus be carefully constrained, where possible, by the analysis of additional biomarkers that can help to resolve the major sources of organic carbon or identify the presence of methanotrophy.

Nitrogen is very labile and is rapidly degraded (Lamb et al. 2006), which can bias the TOC/N ratio towards higher TOM input. It is clear that small changes in organic carbon or nitrogen abundance can cause large shifts in the TOC/N ratio (Meyers 1997), and that end member choice can have large influences on the outcome of the mixing model. Sedimentary particle size can also affect the C/N ratio of bulk organic matter (Meyers 1997), with fine sediments having a low C/N ratio, as they contain the clay fraction, which can absorb ammonium lowering the C/N ratio. This could be a problem for the Yamato Rise, as the lithology is dominated by clay, silty clay, and siliceous claystone (Tada et al. 2015). The terrestrial end member for this mixing model is hard to chose. A low TOC content (<0.3%) can also influence the nitrogen quantification (Meyers 1997), but this is unlikely a problem at the Yamato Rise, where TOC content is typically >0.7%. TOC/N of organic matter within paleosols from the Chinese Loess Plateau (CLP) varies around 9.5±1.3, the interbedded loess has a ratio of 5.6±1 (Vidic and Montanez 2004). C/N ratios of organic matter

in the Yangtze River vary between 9 (surface) and 14 (near bottom) (Zhang et al. 2007). The Yangtze River and paleosols as well as loess from the CLP are sources of terrestrial organic carbon that ends up in the Japan Sea (Oba 1991; Dersch-Hansmann 1994; Nagashima et al. 2007a). Their TOC/N ratios are very close to the marine end member, defined by Meyers (1997) and Lamb et al. (2006), and they are close to the ratios measured in this study. With these potential end member values it is difficult to explain where the TOC/N ratio of 20 (1.0 Ma) at the Yamato Rise comes from. Furthermore, overall estimates of TOM input come with a large uncertainty, since the terrestrial end member cannot be constrained.

The combination of all four mixing models suggest an increased contribution of TOM during the late Miocene, from 9–7 Ma, averaging approximately 30%, before it slightly declines to 15–25% from 7–5 Ma. This is in agreement with the lithological description of U1425 (Tada et al. 2015). A brief peak in OC_{terr} fluxes is found from 4–5 Ma (Fig. 6.2e, Section 5.4.3), coinciding with a strong summer monsoon and presumed increased Amur River discharge. This suggest that more TOM was washed into the Japan Sea by an intensified summer monsoon. Highest variations of terrestrial organic carbon fluxes can be found in the Pleistocene, with 30-50% contribution from continentally derived organic matter. Increased abundance of terrigenious matter is also found by Tada et al. (2015). These fluctuations could mirror the alternating influence of the Tsushima Warm Current and East China Sea Coastal Water (ECSCW) inflow after 2.5 Ma. The ECSCW brings terrestrially de-

rived organic carbon to the Japan Sea by mixing with waters from the Yellow River and Yangtze River (Oba 1991; Tada et al. 1999). The differing delivery pathways of biomarkers, as different influencing factors, such as contributing organisms, surface water changes, and end member choice make it difficult to reconstruct the TOM contribution in a dynamic environment such as the Japan Sea. This has consequences for the determination of paleoproductivity (Stax 1993). Given these highly problematic factors, TOM contribution cannot be accurately determined with the methods applied here, and reconstructions are consequently deemed unsuccessful. It is therefore not attempted to reconstruct paleo primary productivity.

6.4.2. Paleodepositional environment

Changes in surface water properties in relation to tectonic changes of the Japan Sea were detected (Oba 1991; Tada 1994; Tada et al. 1999; Itaki 2016). This includes changes in nutrient supply due to N-Honshu uplift, which restricts Pacific oxygen minimum zone (OMZ) inflow (Tada 1994). Additional change in bottom water oxygenation occur when the OMZ was restricted either due to sea level change or uplift (Tada 1994; Kimura et al. 2004). The Japan Sea entered its compressional stage at circa 10 Ma (Kano et al. 1991; Xu et al. 2016). It was open to the north, while the southern channel was closed, and an eastern channel was intermittently open. The eastern channel offered a way in for the OMZ, which silled in during sea level high stands (Tada 1994). Sub-

sequently, bottom waters fluctuated between euxinic and suboxic (Tada 1994). This fluctuation is reflected in alternating parallel laminations of the siliceous claystone, and a high pyrite content (5-25%) (Tada et al. 2015). Mo/Al ratios, total sulfur (TS), and $\delta^{34}S$ of pyrites indicate highly reducing bottom waters from 9–10.6 Ma (Masuzawa et al. 1992; Kimura et al. 2004). The next major change is the onset of the N-Honshu uplift, starting at circa 8 Ma (K. Horikawa, pers. comm.) and ended at circa 6 Ma (Tada 1994). At 6 Ma the eastern channel was completely closed, so was the southern channel. Thus, the Japan Sea was only open to the north. Apart from intermittent burrows no sedimentary features are recognizable during this time (Tada et al. 2015). Very subtle color changes from dark gray to dark brown on meter scale are described, and the lithology is mostly comprised of diatoms (>75%) (Tada et al. 2015). The last fine laminations of the late Miocene are found in organic rich layers at around 7.7 Ma (Tada et al. 2015). These laminations fall into the interval when bottom waters were highly reducing (Kimura et al. 2004). The pyrite content was decreasing towards 6 Ma. Total sulfur and $\delta^{34}S$ values suggest a variation between less oxic and less euxinic conditions (Masuzawa et al. 1992). The Japan Sea was tectonically quiescent until the Pliocene, when Hokkaido was uplifted and separated the Japan Sea from the Okhotsk Sea (Xu et al. 2016). The lithology indicates a decreasing flux of TOM to the Japan Sea, and heavily bioturbated diatomaceous ooze (70-95%), with very few clay intervals (Tada et al. 2015). Mo/Al ratios, and TS decrease to close to 0, indicating steadily oxic conditions during the very late Miocene to mid Pliocene (Masuzawa et al.

1992; Kimura et al. 2004).

After 3.5 Ma, surface water flows were altered by eustatic sea level change rather than uplift and compression (Tada 1994; 2004; Kitamura and Kimoto 2006). Sea surface salinity (SSS), reconstructed using $\delta^{18}O$ and diatom stratigraphy, drastically decreased during sea level low stands, because relatively more fresh water was delivered to the Japan Sea through the Tsushima Strait (Oba 1991; Tada et al. 1999). The resulting density stratification promoted the development of euxinic bottom waters and the deposition of dark, organic carbon-rich layers (Stax 1993; Tada et al. 1999). With this mechanism, it is expected that deep-water ventilation is related to sea surface salinity changes, and the subsequent restriction of down welling of these water masses in winter (Zou et al. 2012; Tada et al. 2013). The lithology of the Quaternary comprises distinctive sedimentary features. The most obvious is the alternating-ing of decimeter-scale color-banded bedding. Dark, organic-rich layers are inter-bedded in lighter-colored, organic poor layers (Tada et al. 2015). The relative frequency is higher in the 0.8 Ma-Present interval than in the older part >0.8 Ma (Tada et al. 2015). The darker layers are also characterized by a higher TS content (>2%), and low $\delta^{34}S$ of pyrite, indicating euxinic conditions (Masuzawa et al. 1992; Tada et al. 2015). The light, organic-poor layers during the Quaternary are heavily bioturbated, and have a low TS content (<0.3%), suggesting oxic bottom water conditions (Masuzawa et al. 1992; Tada et al. 2015).

28,30-DNH and its precursor were detected in concentrations from 1–40 ng g^{-1}

dw Sed, from 8.3–10.7 Ma (Fig. 6.3), thus falls into a time where inorganic proxies suggest highly reducing bottom waters (Masuzawa et al. 1992; Kimura et al. 2004). Thus, 28,30-DNH and 28,30-Dinorhop-13(18)-ene seem indeed to be sensitive to anoxic bottom water conditions. The trend in reducing bottom waters indicated by these two biomarkers even roughly mirrors bottom water state indicated by Mo/Al ratios of Kimura et al. (2004). However, 28,30-DNH is absent from the record during the anoxic conditions after 8 Ma, when the last organic-rich layers with fine laminations were deposited (Kimura et al. 2004; Tada et al. 2015), or conditions were not viable for the 28,30-DNH producers. This could be due to differences in the age model used over the three different studies (Masuzawa et al. 1992; Kimura et al. 2004; and this study). In the Quaternary, where bottom water conditions were thought to fluctuate between oxic and euxinic, 28,30-DNH could only be detected once, and in a comparatively small amount: 0.1 ng g^{-1} dw Sed at circa 0.41 Ma. This either implies that the bottom water redox state was not reducing as currently assumed, or that the living conditions for the 28,30-DNH producers were favorable enough.

The application of the Ly/nC$_{31}$ proxy is an alternative approach to assess the paleoxcitiy of the water column (Sinninghe Damsté et al. 2003). Lycopane was not detected prior to circa 9 Ma (Fig. 6.3), from which on the Ly/nC$_{31}$ ratio decreases rapidly until 6 Ma. Ly/nC$_{31}$ ratios are generally low from the late Miocene throughout the Pliocene, with exceptions at 4.3 Ma and 3 Ma. The lithology indicates homogeneous diatomaceous ooze in both cases, thus

is little helpful here (Tada et al. 2015). No redox-sensitive mineral record of U1425 is available yet that could give insight into the redox state at this time. It is intriguing that both peaks occur during a salinity minimum in the Japan Sea, eventually caused by a strong summer monsoon (Tada et al. 2016; Ch. 7). It is hypothesized that a density stratification, as a result of a fresh water cap formation, might have lowered available oxygen at greater depths, causing the Ly/nC$_{31}$ excursions. This hypothesis shoould be tested, as soon as appropriate redox records become available. The Ly/nC$_{31}$ ratio increases again in Quaternary, but unfortunately the resolution is too low to test a relation with eustatic sea level change and subsequent changes in bottom water oxygenation. Both peaks lie close to a glacial as indiacted by (Lisiecki and Raymo 2005), thus the increased Ly/nC$_{31}$ ratio would be plausible given the at least anoxic state of the bottom water (Tada et al. 1999).

6.5. Conclusions

This study has shown that the mixing models presented here, are complicated by the fact that the terrestrial matter influx cannot be reliably constrained, due to variability and poor constraints on terrestrial end members, such as for the C/N mixing model. $\delta^{13}C_{org}$ records all organic matter input, which is complicated when particular constituents of marine organic matter have carbon isotopic signatures that overlap with the terrestrial end-member (for example cyanobacteria), and vice versa. While the eolian transport is the most impor-

tant pathway for terrestrial organic matter delivery to the Yamato Rise, the monsoon intensity as well as the tectonic setting play major roles in delivering TOM, and nutrients to the Japan Sea. Ly/nC$_{31}$ and 28,30-DNH indicated a bottom water oxygen deficiency for the late Miocene. But increased ratios of Ly/nC$_{31}$ beyond 8 Ma show that Ly/nC$_{31}$ might be sensitive even to suboxic conditions, for example during the intensified summer monsoon, while 28,30-DNH only indicates strongly stratified/anoxic bottom waters. Overall, 28,30-DNH and Ly/nC$_{31}$ do help to constrain the paleoxicity of the water column at the Yamato Rise over the last 10 Ma.

7. Using alkenone stable isotopes as CO_2 proxy in the Japan Sea

Abstract

The roles of atmospheric greenhouse gases, such as CO_2 and CH_4, in the Earth's energy budget are relatively well understood in the modern system. In contrast, detailed coupling of CO_2 and long-term climate changes over the geological record is poorly constrained. One reason for this are the contrasting results of different CO_2 reconstruction methods, such as those based on soil carbonates, alkenone paleobarometry or leaf stomata size. Available CO_2 proxies lack the accuracy and precision to investigate a link between global climate change and atmospheric CO_2 concentrations. This study applied alkenone paleobarometry, using the $\delta^{13}C$ signature of alkenones to re-

construct pCO_2 changes since the late Miocene. The late Miocene is of particular interest, since proxies point to substantial warmth, but low pCO_2 levels. Since alkenone-based paleobarometry requires assumptions about a number of associated environmental and physiological parameters, such as algal carbon fixation mechanisms and growth rates, the pCO_2 reconstructions generated are explored subject to a range of feasible assumptions. The δD signature of alkenones was used to correct the pCO_2 record for changes in sea surface salinity, which affects the solubility of CO_2 in sea water. Independent of the choice of boundary parameters, all records show a drastic pCO_2 decline in the late Miocene (8–6 Ma), from >500 to around 380–320 µatm. Pliocene trends in pCO_2 are in agreement with other studies. Pleistocene pCO_2 estimates are most likely overestimated, due to the lack of available estimates of $\delta^{13}C_{CO2}$. The late Miocene decline from >500 to around 300 µatm falls into the required range for the C_4 plant expansion, which occurs shortly after the detected pCO_2 decline. This decline also falls into the time range when large coccoliths start to react to a CO_2 limitation. This is the first record that shows the late Miocene pCO_2 decline in the required range for these large scale marine and terrestrial changes.

7.1. Introduction

Greenhouse gases (GHGs) are an important component of the atmosphere, as they absorb thermal radiation emitted by the Earth's surface, and thereby raise

the global mean temperature (Lacis et al. 2010). The effect of GHGs on the surface temperature is easily demonstrated by Lacis et al. (2010), who removed long living GHGs (CO_2, CH_4, O_3, N_2O, CFCs) from the AR5 climate model. The results show that the mean surface temperature would drop to −21 °C within just 50 years, thus demonstrating that the radiative forcing of GHGs and aerosols are essential to sustain a viable climate. The radiative effect of GHGs, such as CO_2, on the Earths' heat budget is known since 1896 (Arrhenius 1896). Of all GHGs mixed in the atmosphere today, CO_2 exerts the strongest radiative forcing, with $1.82\,W\,m^{-2}\pm0.19$ relative to 1750 (Myhre et al. 2013). The influence of increased CO_2 emissions on today's global warming is well understood (Myhre et al. 2013), but its effect is difficult to constrain for past climate changes. Ice cores from Antarctica and Greenland show CO_2 fluctuations over glacial-interglacial cycles for the last 800,000 years, but the driving processes for this variation are not fully understood (Lacis et al. 2010; Masson-Delmotte et al. 2013). CO_2 was not the trigger or pacemaker for these cycles, but presumably played an important feedback role (Masson-Delmotte et al. 2013). CO_2 is considered to be an important driver of long-term climate change (Lacis et al. 2010; Beerling and Royer 2011). A long-term cooling trend over the last 65 Ma has been reconstructed by using the stable isotopic composition ($\delta^{18}O$) of benthic foraminifera (Zachos et al. 2001; 2008). This cooling trend broadly follows a decline in CO_2 (Beerling and Royer 2011). A closer examination of the relation between long-term climate change and long-term concentrations of CO_2 is currently not feasible, because currently available records lack ac-

curacy and precision of ancient pCO_2 estimates (Beerling and Royer 2011). Within these constrains lie two major scientific research goals: the more accurate reconstruction of ancient pCO_2 levels and subsequently constraining the global climate response to changing pCO_2 levels.

Two examples of current problems with reconstructions of pCO_2 are (1) the inter-proxy mismatch and the (2) problem of the apparent mismatch between apparent low pCO_2 conditions and substantially enhanced surface temperatures. Regarding the inter-proxy mismatch, the most prominent example is the reconstruction of mid- to late Miocene CO_2 concentrations using soil carbonates, boron isotopes, leaf stomata data and alkenone paleobarometry. While the first few proxies indicate increased pCO_2, and a subsequent decline for the mid-Miocene Climate Optimum (MMCO) (17–15 Ma), the alkenone pCO_2 proxy displays a flat line (Fig. 4.1) (Pagani et al. 1999a; Kürschner et al. 2008; Beerling and Royer 2011; Foster et al. 2012). The respective problem of the apparent mismatch between pCO_2 and surface temperature are also found in the mid- and late Miocene. LaRiviere et al. (2012) suggested the mid- to late Miocene oceanic warmth to be decoupled from pCO_2 concentrations, and argued that warm conditions were feasible due to deep global thermocline, and a subsequent reduction in low latitude climate gradients. This idea is rebuked by authors of other studies (e.g. Bolton and Stoll 2013; Herbert et al. 2016), because it does not explain the large environmental reorganization on land reconstructed at the same time. The late Miocene is known for sustained warmth (Seki et al. 2012; LaRiviere et al. 2012; Zhang et al. 2014; Herbert et al. 2016),

expansion of C_4 plants (Cerling et al. 1997), lack of Northern Hemisphere ice sheets, but low atmospheric pCO_2 (Pagani et al. 1999a).

The SST records from the Northern and Southern Hemisphere, compiled by Herbert et al. (2016), show a drop in temperatures in the late Miocene (7.6–5.5 Ma) and occurred at the same time in both hemispheres, strengthening the authors' argument that global changes in the marine and terrestrial environment were a direct consequence of a decline in late Miocene pCO_2 levels. Based on findings of other studies (Ehleringer et al. 1997; Diester-Haass et al. 2006; Bolton and Stoll 2013) they suggested that during the late Miocene atmospheric carbon dioxide concentrations descended to a critical pCO_2 level from 500 to below 350 ppm, which favored C_4 over C_3 plants (Ehleringer et al. 1997; Herbert et al. 2016), although proxy records suggesting such a drop are sparse. Recently, Bolton and Stoll (2013) attributed the onset of strong vital effects in both the $\delta^{18}O$ and carbon isotopes of coccoliths produced by large cells as a response to limitations on carbon uptake with lower surface ocean dissolved inorganic carbon as atmospheric CO_2 declines. Interestingly, this divergence starts to become very pronounced in the late Miocene, close to the expansion of C_4 plants. Bolton and Stoll (2013) suggest that terrestrial and marine photosynthesizers show adaptation at a common pCO_2 threshold of circa 500 ppm, and that a decline below such a level caused the synchronous response of both photosynthesizers to this decline. These findings indirectly infer that late Miocene pCO_2 declines from above 500 ppm to less than 500 ppm. Thus new records, which provide direct evidence of a mid- to late Miocene

pCO_2 decline are required.

7.1.1. Alkenone paleobarometry

Direct CO_2 measurements only span back to the 1950s (Keeling et al. 1989). CO_2 reconstructions for the last 800 000 years are based on direct measurements of ice-core gas bubbles (Lüthi et al. 2008). Beyond this time, methods for pCO_2 reconstructions include boron isotopes (Foster et al. 2012), fossil leaf stomata (Kürschner et al. 2008), soil carbonates (Cerling 1992), and carbon isotopes of alkenones (Jasper and Hayes 1990; Pagani et al. 1999a). A compilation of these records shows that for the same interval, reconstructed pCO_2 can vary extremely, sometimes by the factor of 2 (Fig. 4.1, (Pagani et al. 1999b; Zhang et al. 2013)). A strong relationship exists between ^{13}C of algal matter and $[CO_2]$ (Rau et al. 1992; Raven et al. 1993; Goericke and Fry 1994), thus the carbon isotopic signature of organic matter was used to reconstruct pCO_2 for the last glacial-interglacial cycle (Jasper and Hayes 1990), the Quaternary (Hayes 1993), or Phanerozoic (Popp et al. 1989). As discussed in Chapter 6, $\delta^{13}C_{org}$ is the isotopic signal of a variety of source organisms, including terrestrial matter (Pagani et al. 1999a), and thus mixes a broad range of isotopic compositions, biasing the pCO_2 reconstruction. A biomarker based pCO_2 reconstruction, for example by utilizing alkenones, narrows down biases in pCO_2 estimations, because alkenones are highly source specific and reflect a single source signal, in contrast to $\delta^{13}C_{org}$. Furthermore, once the effect of

cell size and cell geometry on alkenone $\delta^{13}C$ values can be constrained, their effect on the alkenone based pCO_2 reconstruction can be constrained. However, this requires a micropaleontological investigation of nannofossils present in the respective sample, and is an aspect that is not accounted for in all studies applying the alkenone paleobarometry. Ambient CO_{2aq} in sea water relatively low (10–30 µmol), which is below the half saturation constant for Rubisco in haptophytes (30–60 µmol) (Pagani 2014). Unless algae can take up carbon actively, CO_2 limitation is widespread in the global ocean (Pagani 2014). Most algae can take up carbon actively, by the release of a carbonic anhydrase, leading to the dehydration of HCO_3^- to CO_{2aq}, direct uptake of HCO_3^- or a mix of both. A direct uptake of HCO_3^- would have a large impact on ϵ_p, since HCO_3^- is 10 ‰ heavier than CO_{2aq} (Pagani 2014). CCMs are weakly expressed in *Emiliania huxleyi* and *Gephyrocapsa Oceanica*, the species that originated under low CO_2 concentrations during the Quaternary. Whether CCM was active in ancient alkenone producers is simply unknown (Pagani 2014). Although the presence of CCMs in haptophytes has been implied in chemostat experiments and field data, it is assumed that *Emiliania huxleyi* is dependent on a diffusive supply of carbon to the cell (Bidigare et al. 1997; Pagani 2014). A CCM in coccolithophores could explain the relative invariance of alkenone based pCO_2 reconstructions during the early Miocene (Pagani et al. 1999b; Zhang et al. 2013). But the current working assumption is that a diffusive supply is the main mechanism for carbon supply in coccoliths, thus they should have a $\delta^{13}C$ signature closest to $CO_{2(aq)}$. Furthermore, alkenones are less affected

by the diagenetic alteration of the isotopic signal than $\delta^{13}C_{org}$ (Pagani et al. 1999a). The relationship of isotopic fractionation between a source organism and $CO_{2(aq)}$ is described by Eq. 7.4. It is based on the assumption that CO_2 is transported to the cell mainly by passive diffusion, thus the diffusion model is similar to the C_3 plant fractionation model by Farquhar et al. (1989; Fig. 1.1a). Despite the close relationship between ϵ_p and $CO_{2(aq)}$ (Bidigare et al. 1997), ϵ_p (Eq. 7.4) can be affected by cell size and geometry (Popp et al. 1998; Laws et al. 2002) and irradiance (Rost et al. 2002). Data from experiments and modern samples of particulate organic carbon (POC) have shown that haptophyte growth rates, and the associated physiological *b*-factor, can be related to the phosphate concentrations $[PO_4^{3-}]$ of the growth medium (Bidigare et al. 1997). Developing this relationship, Bidigare et al. (1997); Popp et al. (1998); Laws et al. (2002) and Pagani (2014) introduced a global calibration for the *b*-factor with respect to surface ocean $[PO_4^{3-}]$. Although useful for alkenone-based estimates of pCO_2, this relationship ignores the potential for regional, or other environmental variations, that cause a divergence from this empirical *b*-factor vs $[PO_4^{3-}]$ relationship. Further, even with this relationship, there are currently no proxy methods available for the estimation of past surface ocean $[PO_4^{3-}]$. This is particularly problematic for times in the Japan Sea, where $[PO_4^{3-}]$ values were likely higher, i.e. at circa 8 Ma (Masuzawa et al. 1992; Tada 1994). Increased $[PO_4^{3-}]$ values will affect ϵ_p, and therefore pCO_2 estimates. As a result, alkenone-based pCO_2 reconstructions are often based on the assumption that $[PO_4^{3-}]$ of the mixed layer (top 50–100 m) in ancient oceans were equal to

modern values, which is almost certainly not the case (Seki et al. 2010; Pagani et al. 2011; Zhang et al. 2013). Other studies have used biogeochemical models to estimate past phosphate concentrations, but these models themselves are also highly unconstrained (Pagani et al. 2011). Uncertainties regarding the factor of enzymatic fractionation, ϵ_f (Eq. 7.4) stem from the enzymes being involved in carbon fixation during carbon uptake. Studies suggest that the principal enzyme involved in carbon fixation in coccoliths is 'Rubisco ID' (Badger and Bek 2008). Maximum isotopic fractionation appears to occur at high $CO_{2(aq)}$, very low growth rates or high temperatures (Pagani et al. 1999a). Goericke and Fry (1994) found ϵ_f to vary between 25–28 ‰, and Wong and Sackett (1978) determined an ϵ_f of 27 ‰ for haptophytes. Most studies use an ϵ_f of 25–27 ‰. Problems arise when the difference between ϵ_f and ϵ_p is small, which makes uncertainties in $[PO_4^{3-}]$ and sea surface temperatures (SSTs) estimations increasingly significant for pCO_2 reconstructions (Pagani 2014). The selection of $[PO_4^{3-}]$ and ϵ_f thus need careful consideration to limit the associated uncertainties for alkenone paleobarometry.

This study used the opportunity to analyze sedimentary alkenone δD and $\delta^{13}C$ from the same core from a single locality. This is the first study using alkenone paleobarometry that also accounts for changes in sea surface salinity by using the deuterium isotopic signature of alkenones, instead of assuming a constant salinity of 35–36 (Pagani et al. 1999a; Seki et al. 2010). The Japan Sea most likely experienced stark changes in sea surface salinity, due to opening and closure of the Tsushima Strait (Oba 1991; Tada 1994), as well as

intensified summer monsoon (Chapter 5) and increased discharge of the Amur River into the Japan Sea (Chapter 6). Here, $\delta^{13}C$ and δD of the $C_{37:2}$ alkenone are used to reconstruct changes in pCO_2 since the late Miocene. δD is converted to sea surface salinity (SSS), and changes in salinity are then used to select appropriate solubility coefficients of CO_2 in saline solutions, based on Weiss (1974). Since salinity affects CO_2 solubility, this approach should improve the reconstruction of atmospheric pCO_2. Within the temperature range indicated by $U^{K'_{37}}$ 4, effect of salinity on the solubility of CO_2 is expected to be small (Weiss 1974), especially when the effect is compared to the $[PO_4^{3-}]$ range presented here. No other study so far compared salinity corrected and uncorrected pCO_2 reconstructions with each other. The Japan Sea is an excellent recorder of global climate change, thus this study is based on the theory that signals of changes in pCO_2 are also preserved in the sedimentary record of the Japan Sea, i.e. via the $\delta^{13}C$ signature of alkenones. The selected time span (0.3–8 Ma) is particularly interesting, as it should include the hypothesized decline in pCO_2 in the late Miocene, that caused large changes in the marine and terrestrial environment, as suggested by Ehleringer et al. (1997); Diester-Haass et al. (2006); Bolton and Stoll (2013) and Herbert et al. (2016).

7.2. Methods

7.2.1. Alkenone barometry

After the compound specific isotopes were calibrated to the VPDB and VSMOW standard (see Chapter 2), the photosynthetic isotopic fractionation between $\delta^{13}C_{CO2}$ and $\delta^{13}C_{37:2}$ can be calculated, and is described as:

$$\epsilon_p = \left(\frac{\delta^{13}C_{CO2(aq)} + 1000}{\delta^{13}C_{37:2} + 1000} - 1 \right) \times 1000 \tag{7.1}$$

Due to the lack of well preserved carbonate microfossils in the Japan Sea, $\delta^{13}C_{CO2}$ from dissolved inorganic carbon (DIC) cannot be determined. Therefore, $CO_{2(aq)}$ is assumed to be of the same isotopic composition as $CO_{2(g)}$ (Deuser and Degens 1967; Deuser et al. 1968). Tipple et al. (2010) reconstructed benthic foraminifera $\delta^{13}C$ and $\delta^{18}O$ records from a global data set to reconstruct the carbon isotopic signature of CO_2 ($\delta^{13}C_{CO2}$) and subsequently, $\delta^{13}C_{CO2}$ data is taken from Tipple et al. (2010). A comparison with bulk carbonate $\delta^{13}C$ from IODP site U1338 Reghellin et al. (2015) shows the same trends, but yields higher pCO_2 estimates 7.5. The isotopic fractionation between $CO_{2(aq)}$ and $CO_{2(g)}$ was calculated according to Pagani et al. (1999a):

$$\epsilon_{CO2(aq)-CO2(g)} = \left(\frac{\delta^{13}C_{CO2(aq)}}{\delta^{13}C_{CO2(g)}} - 1 \right) \times 1000 \tag{7.2}$$

$$\epsilon_{CO2(aq)-CO2(g)} = \frac{-373}{T(^{\circ}K)} + 0.19 \tag{7.3}$$

ϵ_p from Eq. 7.1 is also related to $[CO_{2(aq)}]$:

$$\epsilon_p = \epsilon_f - \frac{b}{[CO_{2(aq)}]} \tag{7.4}$$

where ϵ_f represents the isotopic fractionation within the cell, and varies between 25–27 ‰ (Goericke and Fry 1994; Laws et al. 2002). While ϵ_f has to be estimated, b is globally calibrated, and needs to be calculated for every ϵ_f (Pagani et al. 1999a; Pagani 2014). b is the sum of all biological factors affecting the carbon isotopic fractionation within the cell. Studies using batch cultures have shown that b is particularly sensitive to $[PO_4^{3-}]$ concentrations (Bidigare et al. 1997). b was calculated according to Pagani et al. (1999a), and $[PO_4^{3-}]$ concentrations were taken from the data archives of the Japan Oceanography Data Center (JODC). Since the Japan Sea is characterized by eddies and seasonal currents, a site specific determination of $[PO_4^{3-}]$ is not feasible. Therefore, the lowest and highest $[PO_4^{3-}]$ close to Site U1425 were chosen. For this purpose, $[PO_4^{3-}]$ of the first 20 m of the water column were averaged, yielding $[PO_4^{3-}]$ of 0.14 µmol l^{-1}. For the error calculation, an upper limit of $[PO_4^{3-}]$=0.26 µmol l^{-1}, and a lower limit of $[PO_4^{3-}]$=0.05 µmol l^{-1} were used. Equations 7.5, 7.6, 7.7 calculate b and its associated error for ϵ_f=25‰.

$$b = 118.5 \times [PO_4^{3-}] + 84.07 \tag{7.5}$$

$$b_{\max} = 4.17 \times [PO_4^{3-}]^2 + (113.79 \times [PO_4^{3-}]) + 88.63 \quad (7.6)$$

$$b_{\min} = -4.14 \times [PO_4^{3-}]^2 + (120.14 \times [PO_4^{3-}]) + 74.21 \quad (7.7)$$

Equations 7.8, 7.9, 7.10 calculate b and its associated error for ϵ_f=27‰.

$$b = 128.96 \times [PO_4^{3-}] + 101.37 \quad (7.8)$$

$$b_{\max} = 4.35 \times [PO_4^{3-}]^2 + (125.65 \times [PO_4^{3-}]) + 108.89 \quad (7.9)$$

$$b_{\min} = -4.35 \times [PO_4^{3-}]^2 + (132.27 \times [PO_4^{3-}]) + 93.85 \quad (7.10)$$

Since all neccesary variables are now known, Eq. 7.4 can be rearranged to:

$$[CO_2(aq)] = \frac{b}{\epsilon_f - \epsilon_p} \quad (7.11)$$

$[CO_{2(aq)}]$ from Eq. 7.11 can then be converted to $[CO_{2(atm)}]$ by using Eq. 7.12:

$$[CO_2(aq)] = pCO_2 \times K_H \quad (7.12)$$

K_H is the solubility coefficient of CO_2, dependent on salinity as well as tem-

perature. K_H for each sample was determined using data from Weiss (1974).

7.2.2. Paleo-sea surface salinity

The relationship between $\delta D_{alkenones}$ of *E. huxleyi* and salinity in batch cultures studies by Schouten et al. (2006) can be described as:

$$\delta D_{\text{alkenones}} = 4.8 \times S - 347 \tag{7.13}$$

where S is the salinity of the culture water. The knowledge of SSS, converted to practical salinity units (psu) is used to select the appropriate K_H from Weiss (1974)

7.3. Results

7.3.1. Deuterium isotopes of the $C_{37:2}$ alkenone

The alkenone δD signature varies considerably over the last 10 Ma (Fig. 7.1), between −165 ‰ to −240 ‰. The late Miocene shows small variations in amplitude in alkenone δD, between −180 ‰ to −208 ‰ (5.8–10 Ma), before δD of $C_{37:2}$ decreases markedly to −240 ‰ at 5.2 Ma. $C_{37:2}$ alkenones become increasingly enriched in deuterium after this excursion. The D/H ratio varies again between −190 ‰ to −216 ‰ (3–5 Ma), before they steeply increase. δD of $C_{37:2}$ alkenones then ranges between −180 ‰ to −190 ‰ in the

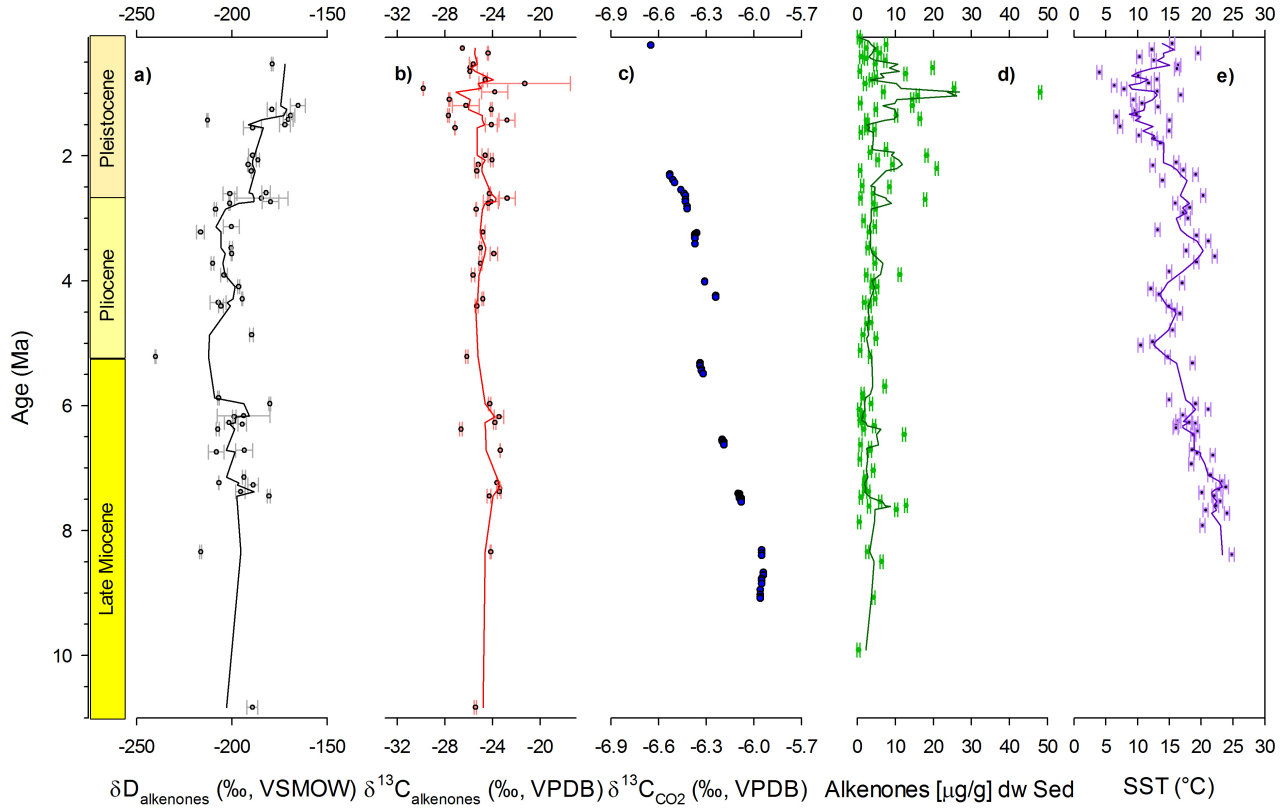

Figure 7.1.: Deuterium isotopic (a) and carbon isotopic (b) composition of alkenones, alongside with (c) CO_2 (Tipple et al. 2010), $U^{K'}_{37}$-SST (d) and alkenone concentrations (e) for Site U1425, over the last 8 Ma.

late Pliocene, before D/H ratios increase again to −170 ‰ to −180 ‰ in the early Pleistocene.

7.3.2. Carbon isotopes of the $C_{37:2}$ alkenone

The ^{13}C content of the $C_{37:2}$ alkenone remains stable from 3–10 Ma, varying between −23 ‰ to −25 ‰ (Fig. 7.1). Considerable variation occurs in the mid-Pleistocene, when $^{13}C/^{12}C$ ratios in alkenones start to vary between −29 ‰ to −21 ‰ within a very short time.

7.3.3. pCO_2 reconstruction

When an ϵ_f of 25 ‰ is used, pCO_2 reconstructions show a larger range than reconstructions using an ϵ_f of 27 ‰ (Figs 7.2a, 7.2b). Overall, for the ϵ_f=25‰ scenario, reconstructed pCO_2 ranges between 500 and 400 µatm during the late Miocene (8 Ma) and shows a decreasing trend towards 318–412 µatm at 6 Ma (Fig. 7.2a). pCO_2 rises to approximately 400 and 600 µatm from 5–4 Ma. Around 4 Ma, reconstructed pCO_2 shows large variations between 320 and 500 µatm, but the overall trend in pCO_2 is decreasing (Fig. 7.2a). For ϵ_f=27‰, the overall reconstructed pCO_2 ranges between 557 and 200 µatm (Fig. 7.2b), with the highest pCO_2 of 557 µatm limited to the late Miocene. The trends for pCO_2 reconstructions using ϵ_f=27‰ are identical but off-set compared to ϵ_f=25‰: considerable variation in pCO_2 is recognized from 4 Ma onwards, where pCO_2 generally trends to lower values, but still reaches values above

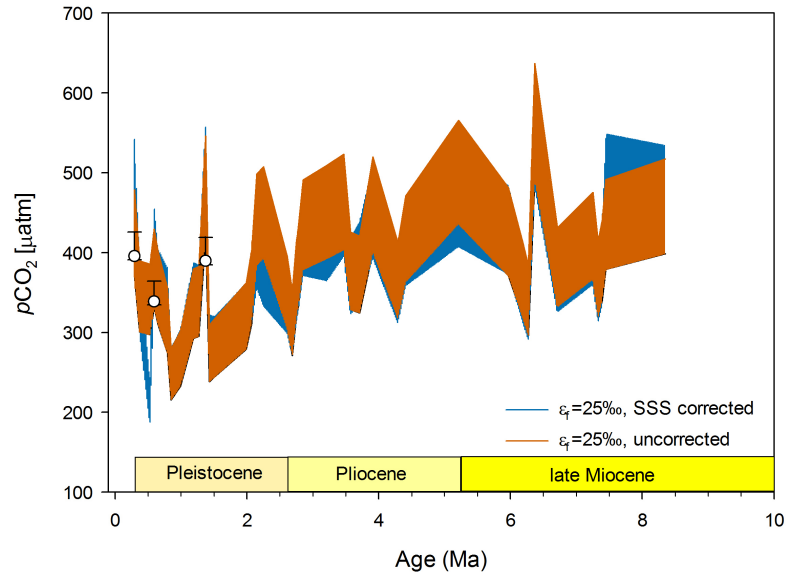

(a) ϵ_f=25‰

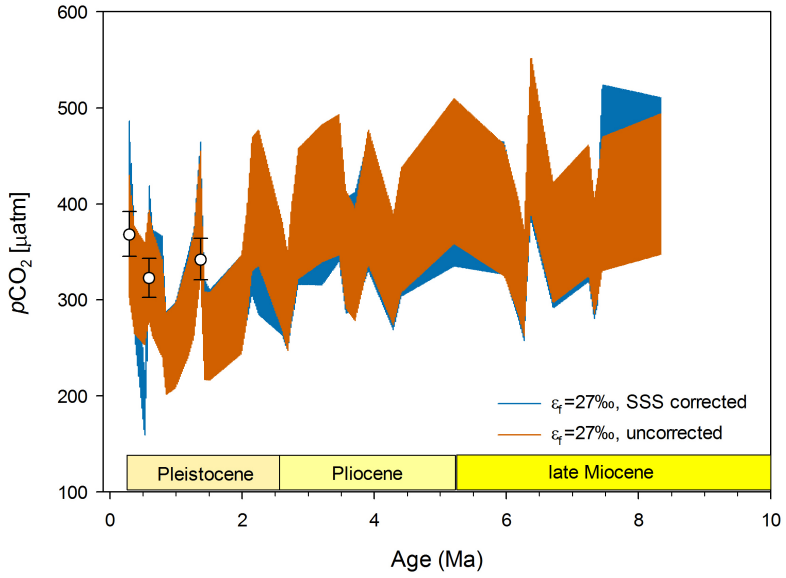

(b) ϵ_f=27‰

Figure 7.2.: Different pCO_2 reconstruction scenarios uncorrected (orange) and corrected for salinity (blue). White circles indicated data points corrected for glacial $\delta^{13}C_{CO2}$.

400 µatm in the late Pleistocene (Fig. 7.2b).

7.4. Discussion

7.4.1. Sea surface salinity reconstruction

Recently, δD of C_{37}-alkenones as proxy for SSS was introduced (Schouten et al. 2006; van der Meer et al. 2008; Kasper et al. 2014). Incubation experiments by Schouten et al. (2006) showed a good correlation of alkenone δD and the salinity of the growth medium (Eq. 7.13, R^2=0.86), which was applied to the data set presented here. A better estimation of paleosalinity is achieved when calculating the fractionation factor α between δD_{water} and $\delta D_{alkenones}$, and accounting for growth rates. However, δD_{water} is unavailable for the Japan Sea, and the estimation of growth rates is based on $\delta^{13}C_{alkenones}$, which would create a circular argument in this study, since $\delta^{13}C_{alkenones}$ is already used for the pCO_2 reconstructions. Thus, using Eq. 7.13 by Schouten et al. (2006) was the most favorable option to reconstruct paleo-SSS. Overall, the Japan Sea shows a trend towards increased SSS from the late Miocene to the Pleistocene: from 33 psu in the late Miocene, to approximately 35 psu during the Pleistocene (Fig. 7.3). The present day SSS ranges around 34.3 psu (Talley et al. 2004), which is precisely within the error of the most recent sample. Interestingly, SSS is at its lowest between 3 and 5 Ma, which coincides with the intensified summer monsoon (Chapter 5) and increased Amur River discharge (Matsusaki, in

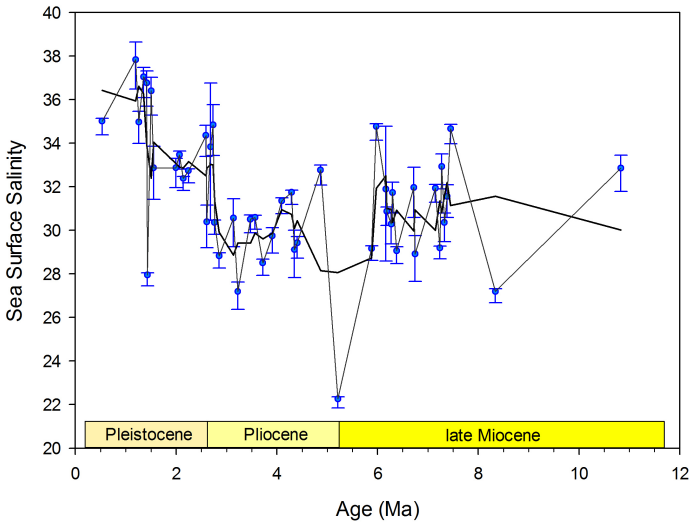

Figure 7.3.: Sea Surface Salinity (SSS), calculated from alkenone δD using Eq. 7.13. Error bars indicate the error of every δD measurements and associated salinity changes.

prep). SSS reaches a reconstructed SSS of 27 psu at 3.2 Ma, and 22 psu at 5.2 Ma. A moderate correlation between δD of alkenones and δD of *n*-alkanes (p=0.002, r=0.45), suggests that they are largely influenced by the same driver, in this case the summer monsoon (see Chapter 5). van der Meer et al. (2013) suggested the combined measurement of $C_{37:2}$ and $C_{37:3}$ alkenones, since the deuterium isotopic fractionation of individual alkenones can differ by about 40‰. The difference in hydrogen isotopes is mainly driven by the abundance, which is driven by temperature (van der Meer et al. 2013). In this study, most depleted signals are complemented by low alkenone abundance of the respective alkenones. However, in this case it is argued that alkenone abundances are low due to the massive freshening of surface waters by increased run-off.

There are only a few coccolith species living in fresh water or low salinity waters (Thierstein 2004). However, SSS of the Japan Sea is most likely overestimated here, since this study uses only $C_{37:2}$ alkenones, which fractionate between source water and lipid at a lower rate. Therefore the deuterium isotopic signature of this alkenone can indicate a lower salinity than was actually present. The increasing influence of the saline waters from the Tsushima Warm Current (Nakada et al. 2005) could explain the increasing SSS since the end of the Pliocene (Oba 1991; Tada 1994), SSS minima during this interval are probably associated with a sea level low stand, when surface freshening occurred (Tada 1994), but the data resolution is too low to validate such a hypothesis. After δD of $C_{37:2}$ alkenones was converted to SSS using Eq. 7.13, they were ready to be used to correct the pCO_2 record for salinity changes.

7.4.2. CO_2 reconstruction

Many factors determine pCO_2 reconstructions, such as the choice of ϵ_f, and therefore its associated *b*-factor (Pagani et al. 1999a; Pagani 2014; Eq. 7.5-7.10). Subsequently, pCO_2 was reconstructed using an ϵ_f of 25 and 27‰ (Figs 7.2a, 7.2b), which are reasonable assumptions (Goericke and Fry 1994; Pagani et al. 1999a; 2011) and the outcomes will be compared to each other. Furthermore, both pCO_2 scenarios were also corrected for changes in sea surface salinity (Figs 7.2a, 7.2b, Eqs 7.13, 7.12). The minimum pCO_2 error was calculated based on lowest reconstructed SST and lowest $[PO_4^{3-}]$ ($0.05\,\mu mol\,l^{-1}$),

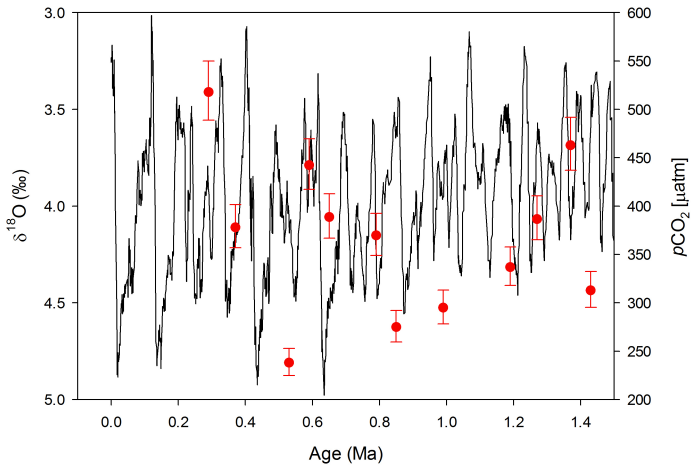

Figure 7.4.: Glacial-to-interglacial variations of $\delta^{18}O$, co-plotted with pCO_2 reconstructions (red circles).

while the maximum error was calculated based on highest SST and highest $[PO_4^{3-}]$ (0.26 µmol l^{-1}) concentrations. There is a lack of suitable data from 0.5–1.5 Ma for $\delta^{13}C_{CO2}$ (Fig. 7.1) in the data set of Tipple et al. (2010) that can be used to calculate pCO_2 (Eqs 7.1, 7.4). This is especially problematic for the glacial to interglacial variations of pCO_2, which also affects the isotopic composition of carbon dioxide. Studies suggest that glacial $\delta^{13}C_{CO2}$ was 0.4–0.5 ‰, in some cases even 1.5 ‰ (Marino et al. 1992; Schulte et al. 2003; Schneider et al. 2013) more depleted than reconstructed by Tipple et al. (2010). Especially over the 0.5–1.5 Ma span, reconstructed pCO_2 regularly exceeds 400 µatm. Plotting benthic foraminfera $\delta^{18}O$ together with reconstructed pCO_2 (Fig. 7.4) roughly suggests that these extreme values are falling into glacial stages. For these points, $\delta^{13}C_{CO2}$ was lowered to −7.04 ‰, which is a 0.4 ‰ difference from Tipple et al. (2010). It lowered reconstructed pCO_2

by 20 µatm for ϵ_f=27‰ and by 60 µatm for ϵ_f=25 ‰ (Fig. 7.2, white circles). Available $\delta^{13}C_{CO2}$ data that can be considered for the sampling site only spans back to 8.4 Ma (Tipple et al. 2010; Reghellin et al. 2015), thus data points from this study beyond this age cannot be accounted for in this reconstruction. The following discussion focuses on the choice of different parameters for pCO_2 reconstructions, and how the results are affected by it.

Impact of isotopic calibration

The choice of method for the isotopic calibration determines the $\delta^{13}C$ signature of C_{37} alkenones. ϵ_p expresses the fractionation between CO_2 and the cell, thus ϵ_p is also dependent on the respective carbon isotope calibration against Vienna Pee Dee Belemnite (VPDB) and will change accordingly. $[CO_{2(aq)}]$ then depends on ϵ_f-ϵ_p difference (Eq. 7.11), which, depending on the calibration can be smaller or larger, leading to an over- or underestimation of past CO_2. Alkenone $\delta^{13}C_{37}$ in this study differs from the $\delta^{13}C$ composition of alkenones measured by Bae et al. (2015) further south in the Japan Sea (Δ=2–4‰), but they also differ from the $\delta^{13}C$ content of alkenones in the western N-Pacific, measured by Yamamoto et al. (2007). Both studies found comparatively ^{13}C enriched alkenones, which are typical of the warm waters they stem from (Deuser et al. 1968), while the range of $\delta^{13}C$ depleted alkenones in this study is expected to be found in colder waters (Deuser et al. 1968; Goericke and Fry 1994). Alkenones of a similar carbon isotopic range to the ones pre-

sented here were found by van der Meer et al. (2008) in the Black Sea. ϵ_p (Eq. 7.1) of this study ranges around 18, even for the most recent ones, while ϵ_p calculated by Bae et al. (2015) ranges around 12. Pagani (2014) argues that samples with an ϵ_p above 18 are due to lower growth rates, while samples with an ϵ_p as found by Bae et al. (2015) are due to higher growth rates. It is important to constrain growth rates, as growth rates and intracellular CO_2 are interrelated, with consequences for ϵ_p, thus growth rates can confound pCO_2 estimates. Presently, the sampling location of Bae et al. (2015) is more productive than the Yamato Rise (Yamada et al. 2005), thus the difference in the isotopic composition of alkenones could stem from there. The observed difference in ϵ_p and $\delta^{13}C$ of alkenones could also be due to differences in the carbon isotopic calibration against VPDB. This is difficult to assess, since most publications do not provide a detailed description of their calibration methods (Chapter 2.3.2). Presently it is not clear why the $C_{37:2}$-alkenones are comparatively depleted, but it does have an effect on ϵ_p, and therefore on the error of pCO_2 estimates, since the difference between ϵ_f and ϵ_p is narrowed, and therefore SST and $[PO_4^{3-}]$ estimates significantly increase their impact on the reconstructions (Pagani et al. 2011; Pagani 2014). The working assumption of this study considers the ϵ_p of the data set presented here to suggest low growth rates (Pagani 2014) at Site U1425. Direct evidence for low growth rates could be provided by micropaleontological evidence, however, micro- and nannofossils are poorly preserved at Site U1425 (Tada et al. 2015), and other sites with better records indicate higher growth rates of alkenones, based on $\delta^{13}C_{alkenone}$

(Yamamoto et al. 2007; Bae et al. 2015).

Impact of choice of carbonate data

Since Japan Sea Site U1425 only comprises poorly preserved carbonate microfossils (Tada et al. 2015), it is impossible to reconstruct $\delta^{13}C$ of DIC for $\delta^{13}C_{CO2}$ estimates. Thus, a substitute for $\delta^{13}C_{CO2}$ estimates is necessary. Certainly, most suitable would be DIC data from the open Pacific, to get a signal as close to the Japan Sea as possible. However, DIC data records spanning the last 8 Ma are very sparse. The only suitable record is provided by Reghellin et al. (2015) in the form of a bulk carbonate $\delta^{13}C$ record from an upwelling site (IODP U1338). Another $\delta^{13}C_{CO2}$ record is provided by Tipple et al. (2010), who compiled a global data set of well constrained benthic foraminifera $\delta^{13}C$, and subsequently derived $\delta^{13}C_{CO2}$. pCO_2 estimates of this study were calculated based on both $\delta^{13}C_{CO2}$ data sets (Tipple et al. 2010; Reghellin et al. 2015). The overlap of both records is quite large (Fig. 7.5), with the Reghellin et al. (2015) based data set resulting in slightly higher pCO_2 estimates. In the end, the decision was made to base pCO_2 reconstructions on $\delta^{13}C_{CO2}$ estimates by Tipple et al. (2010), since it is a source specific record, and the effect of non-equilibrium factors on the benthic foraminifera record is excluded. Furthermore, the Tipple et al. (2010) data set is not derived from an upwelling region, in contrast to Reghellin et al. (2015), thus the effect of the disequilibrium of $CO_{2(aq)}$ and $CO_{2(atm)}$ on the pCO_2 reconstructions is avoided.

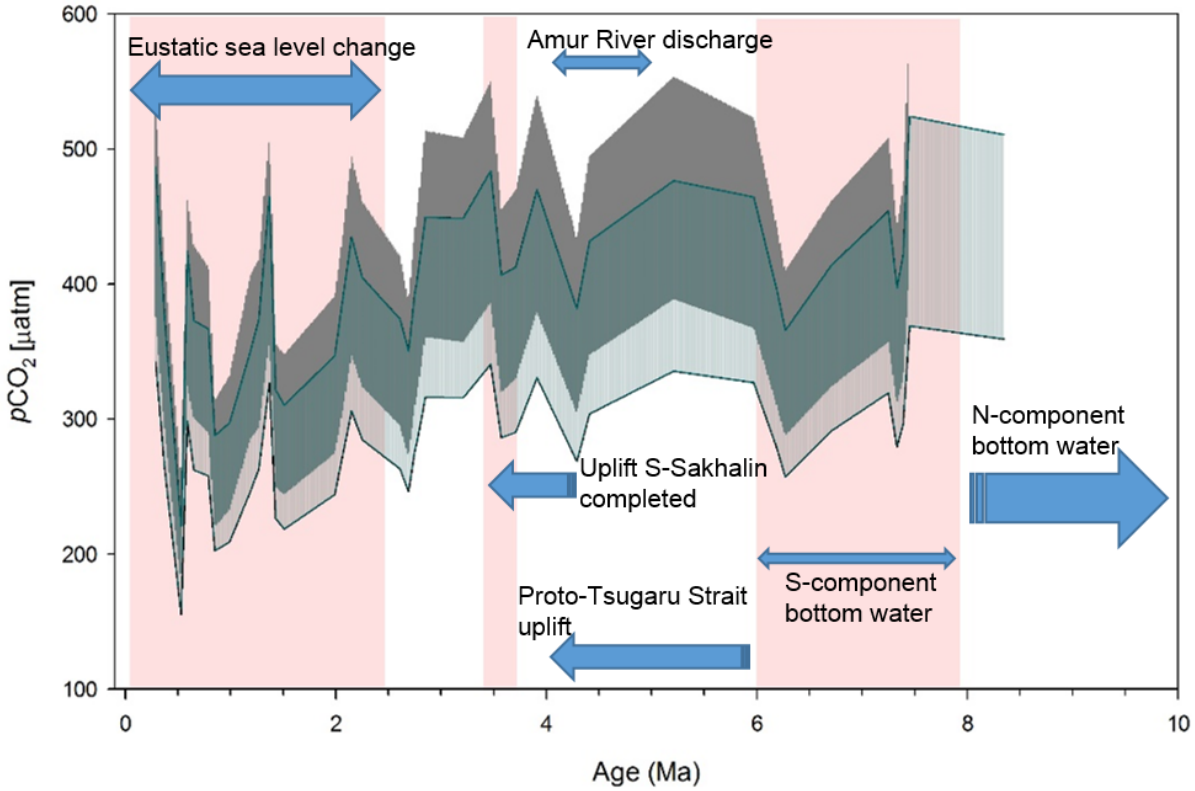

Figure 7.5.: pCO_2 reconstructions using bulk carbonate $\delta^{13}C$ from the Pacific (Reghellin et al. 2015; gray) and globally distributed benthic foraminfera $\delta^{13}C$ (Tipple et al. 2010; blue). Red bands and arrows indicate major circulation and tectonic changes in the Japan Sea that could have affected $[PO_4^{3-}]$ over time.

Impact of varying ϵ_f and *b*

Next to temperature estimates, estimations of $[PO_4^{3-}]$ and therefore *b*-factor and errors in estimation have a large influence on $CO_{2(aq)}$ estimates. The *b*-factor is globally calibrated, and can be calculated with site specific $[PO_4^{3-}]$ data (Pagani 2014). In contrast, ϵ_f needs to be estimated, and is strongly dependent on the enzymes involved with carbon fixation. The choice of ϵ_f then determines the slope of *b* (Pagani et al. 1999a). Most ϵ_f of phytoplankton fall into the range of 25–28 ‰ (Goericke and Fry 1994), and most studies using alkenone paleobarometry assume an ϵ_f of 25‰ (Pagani et al. 1999a; 2010; Seki et al. 2010; Pagani et al. 2011; Badger et al. 2013a). The effect of an ϵ_f of 25‰ or ϵ_f of 27‰ only makes a difference of 15 µatm (Pagani et al. 1999a), and therefore the effect on reconstructed pCO_2 is small. Nonetheless, ϵ_f requires careful consideration, as a small difference in ϵ_f and ϵ_p can cause errors of SST and $[PO_4^{3-}]$ estimations to become increasingly significant, affecting the pCO_2 reconstruction (Pagani et al. 1999a).

The Japan Sea surface waters are generally depleted in nutrients (Talley et al. 2004). The Japan Sea is also affected by eddies (Isoda 1994), pulling up nutrients from the nutricline to the surface, and altering the primary productivity. It is therefore challenging to find suitable $[PO_4^{3-}]$ to represent Site U1425, since site specific data is not available. $[PO_4^{3-}]$ concentrations in summer nearly are homogenous for the Japan Sea, varying around 0.2 µmol l^{-1} over the first 50 m of the water column (Talley et al. 2004). Site specific, depth

averaged (0–20 m) data from 135.9°E, 39.1°N was chosen, as it is close to Site U1425 (134.4°E, 39.4°N). The minimum $[PO_4^{3-}]$ yields 0.05 µmol l^{-1} (JODC). With an estimation of ϵ_f=25‰, this results in a *b*-factor of 87, while it ranges around 108 with an ϵ_f=27‰. *b* rises to 112 and 135 respectively, when the maximum $[PO_4^{3-}]$ estimation of 0.26 µmol l^{-1} is used. Primary productivity and nutrient supply changed drastically over the last 10 Ma in the Japan Sea. Especially, when shoaling of the proto-Tsugaru Strait, and changes in bottom water provenance restricted the inflow of nutrient rich waters from the Pacific (Tada 1994). Furthermore, the intermittent restriction of the proto-Tsushima Warm Current from the South was also able to lower the nutrient supply to the Japan Sea (Bae et al. 2015). An intensified summer monsoon and increased Amur River discharge from 5–3 Ma also impacted the nutrient concentration of the Japan Sea, either by intensified upwelling or increased run-off from land. Both processes are difficult to constrain with the proxy data available here, but could have a large influence on $[PO_4^{3-}]$ estimations. $[PO_4^{3-}]$ during the late Miocene were most likely higher than 0.26 µmol l^{-1}. A higher *b* associated with increased $[PO_4^{3-}]$ during the late Miocene would also result in higher reconstructed pCO_2. Thus pCO_2 presented here for the late Miocene is probably underestimated. Therefore, the modern-ocean relationship between *b* and $[PO_4^{3-}]$, which is the foundation of many alkenone paleobarometry studies, might not hold true for these times in the Japan Sea.

Comparing ϵ_f=25‰ (Fig. 7.2a) and ϵ_f=27‰ (Fig. 7.2b), shows a very similar trend for both records. The error margin for ϵ_f=25‰ is slightly larger.

Overall the upper range of ϵ_f=25‰ is approximately 50 µatm higher than with ϵ_f=27‰. A similar offset for both ϵ_f is found in the lower range of the pCO_2 reconstructions. During the Pliocene, both scenarios show large fluctuation in pCO_2, reaching up to 500 µatm. Amongst concentration of external CO_2 and $[PO_4^{3-}]$, factors like cell size, cell geometry and irradiation can influence ϵ_p and therefore pCO_2 reconstructions. During glacial stages, coccolith growth rates are very low (Xing et al. 2011), and oceanic conditions did not favor coccolith growth. Thus, it is likely that other factors than $CO_{2(aq)}$ had an influence on ^{13}C discrimination in coccoliths. The average changes between different ϵ_f of 25 µatm are slightly larger than the 15 µatm suggested by Pagani et al. (1999a). Still, this is a smaller variation than the variation caused by erroneous $[PO_4^{3-}]$ and SST estimations. It is noteworthy that highest pCO_2 levels are reconstructed for the time span from 6–6.3 Ma. Other proxies suggest that during this time a severe environmental perturbation of the Japan Sea took place, affecting productivity and phytoplankton communities (Chapters 4, 6). It is therefore questionable, whether this peak in pCO_2 really indicates increased CO_2 concentrations, or whether other environmental factors were driving ^{13}C discrimination in coccoliths.

Applying a different ϵ_f to the data set presented here shows on average mostly no difference, when a K_H with a fixed salinity of 34 is used. Reconstructions covering the time span 0–2 Ma are not very distinguished from each other, since this time span lacks continuous $\delta^{13}C_{CO2}$ data. This hampers the accuracy in pCO_2 reconstructions in the Japan Sea. Assuming a depletion of

$\delta^{13}C_{CO2}$ data by 0.4‰ reduces reconstructed pCO_2 by 70 µatm. Uncertainties in $[PO_4^{3-}]$ estimations increase the upper error margin of pCO_2 reconstructions, while the lower error margin for both scenarios is in a similar range. Both records show a decreasing trend in pCO_2 after 4 Ma, which is in agreement with other studies (Pagani et al. 2010; Seki et al. 2010; Bolton and Stoll 2013; Zhang et al. 2013). The application of different ϵ_f (25–27 ‰) suggests that late Miocene pCO_2 levels declined from 517–474 µatm to 412–373 µatm respectively, if the upper error margin is considered. For the lower error margin, a pCO_2 level decline is reconstructed from 398–347 µatm to 318–264 µatm. Interestingly, the upper error margin of pCO_2 matches the decline that is required to trigger the late Miocene C_4 plant expansion (Herbert et al. 2016). The overall trend of pCO_2 indicates decreasing concentrations of the greenhouse gas in the Pliocene and Pleistocene. It is noted that pCO_2 undergoes large changes in magnitude during the Pleistocene, which are also observed for other proxies in this study, such as SST, SSS, TOC and $\delta^{13}C_{org}$, suggesting that other environmental factors than $CO_{2(aq)}$ are affecting the alkenone paleobarometry.

Correction for sea surface salinity

The reconstruction of $CO_{2(atm)}$ requires knowledge of the solubility coefficient K_H (Eq. 7.12), which describes the solubility of CO_2 in water under different temperature and salinity regimes (Weiss 1974). Most alkenone-based pCO_2 reconstructions so far assumed a constant salinity of 35–36 psu (Pagani et al.

1999a; Seki et al. 2010; Zhang et al. 2013), or used another proxy to constrain salinity (Badger et al. 2013b). These sites experienced only small changes in surface salinity over time, and assuming a relatively constant salinity of 35 psu is reasonable. Changes in sea surface salinity in the Japan Sea were rather drastic (Oba 1991; Tada 1994), and are mostly determined by the opening and closure of the Tsushima Strait, as well as summer monsoon intensity and Amur River discharge. Thus it is even more important to constrain salinity changes at Site U1425 over the studied interval to improve the pCO_2 reconstruction. For this purpose, sea surface salinity was reconstructed using δD of alkenones (Sec. 7.4.1). Changes in salinity could then be accounted for by selecting the appropriate K_H by Weiss (1974; Eq. 7.12). Both pCO_2 reconstructions, using an ϵ_f of 25 and 27 ‰ were corrected for salinity changes. The comparison of all four models shows that salinity corrected pCO_2 (Fig. 7.2a, 7.2b) levels for 7.3–8 Ma are higher than their uncorrected counterparts. Upper range pCO_2 reconstructions changed from 534–412 µatm to 510–359 µatm respectively.

As for the uncorrected record, the salinity corrected record shows large changes in magnitude during the Pleistocene. Again, other proxies for this interval show also large changes in magnitude, suggesting that other environmental factors than $CO_{2(aq)}$ are affecting the alkenone paleobarometry. The lower error margin has just shifted by 6–9 µatm for both pCO_2 scenarios when compared to the uncorrected pCO_2 records. The correction for salinity shows that sea surface salinity plays a considerable role in pCO_2 reconstruction, as concentrations are easily underestimated by 30–40 µatm in the uncorrected

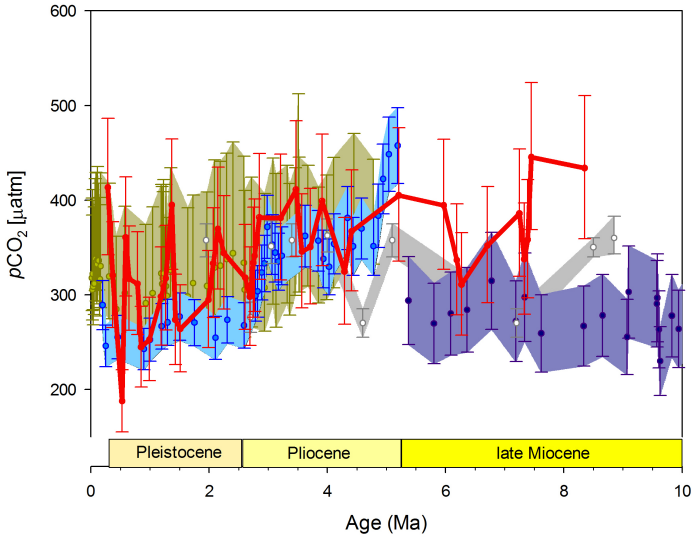

Figure 7.6.: CO_2 reconstructions from this study (red) in comparison with CO_2 reconstructions of other studies: (Seki et al. 2010; turqouise), (Pagani et al. 1999a; purple), (Zhang et al. 2013; khaki), (Beerling and Royer 2011; gray).

scenarios. However, there was no drastic change in pCO_2 trends, as the declining trend during the Pliocene and Pleistocene still remains.

7.4.3. Comparison with data from the literature

The salinity corrected pCO_2 record with an ϵ_f=27‰ was compared to data from other studies (Fig. 7.6). It was selected because it had the narrowest error margin and smallest fluctuation in the Pleistocene, and the most reasonable concentrations overall. The data point at 6.3 Ma was excluded, since it is likely not representing pCO_2, but another factor driving the ^{13}C discrimination in coccoliths. The pCO_2 records reconstructed here are the longest, continu-

ous pCO_2 reconstructions so far, spanning from 0.2–8.4 Ma. It is therefore not possible to compare it to similarly derived records. For the late Miocene, a critical interval, where large perturbations in the terrestrial and marine environments are detected (Pagani et al. 1999b; LaRiviere et al. 2012), the role of CO_2 is ambiguous (Pagani et al. 1999a;b; Herbert et al. 2016). Pagani et al. (1999a) reconstructed increasing pCO_2, while Beerling and Royer (2011) reconstructed a phase of decreased pCO_2. Furthermore, both records are approximately 90 to 120 µatm lower than the record presented here (Fig. 7.6). The most obvious discrepancy of the compiled pCO_2 records is observed between the Pagani et al. (1999b) study and the record generated for this study. For their record, Pagani et al. (1999b) used the carbon isotopic signature of shallow dwelling foraminfera. As pointed out by Tipple et al. (2010), a $\delta^{13}C_{CO2}$ reconstruction based on shallow dwelling foraminfera is complicated by biological, diagenetic and temperature effects that vary in time, and are difficult to account for. According to Tipple et al. (2010), these factors add uncertainty to $\delta^{13}C_{CO2}$ estimates, and thus benthic foraminifera are the preferred organisms for $\delta^{13}C_{CO2}$ estimates. Furthermore, Pagani et al. (1999b) does not provide a SST record for their sampling site DSDP 588, thus it is impossible to assess the impact of temperature on their pCO_2 record. The study presented here uses the $\delta^{13}C$ signature of benthic foraminifera, whose isotopic signature is less affected by diagenetic processes and thus remains more stable over geological time scales than planktonic foraminifera (Tipple et al. 2010). Secondly, the study here provides an excellent temperature control, improving the accuracy

of reconstructed pCO_2 estimates. These two constraints, temperature and $\delta^{13}C$ of benthic foraminifera, are the probable reason why this study provides the proposed pCO_2 decline in the late Miocene. To test for the temperature control hypothesis, alkenone paleobarometry should be carried out on the compiled data sets by Herbert et al. (2016), as they also show the extensive late Miocene cooling. So far, the record presented here is the only record showing decreasing pCO_2 concentrations from approximately 8 to 6 Ma. The agreement of different CO_2 records improves from the Pliocene onwards, where all records show a generally decreasing trend (Seki et al. 2010; Beerling and Royer 2011; Zhang et al. 2013) in CO_2 concentrations. During the Pleistocene, all four records show a consistent change in trends. The lower error margin and average of the record presented here is mostly consistent with data from Zhang et al. (2013). Generally, the record presented here is not unreasonable, but reconstructed pCO_2 concentrations are likely overestimated for this Pleistocene time span. The for glacial states corrected CO_2 (Sec. 7.4.2) record agrees well with Pleistocene pCO_2 data from Zhang et al. (2013), but occasionally overestimates reconstructions from Seki et al. (2010) by up to 165 µatm. Overall, the reconstructed pCO_2 concentrations at Site U1425 show a good agreement with data from other studies, where data is available. The generated record suggests that CO_2 concentrations declined markedly in the late Miocene, and were decreasing from 4 Ma to Present. The offset between the generated record presented here and other studies might be explained best by other influencing factors on alkenone paleobarometry in the Japan Sea, such as drastically

changing [PO_4^{3-}].

Something that is hard to reconcile with the apparent low pCO_2 record of Pagani et al. (1999b) is the lack of evidence for the glaciation of Greenland during the earlier part of the late Miocene. As Lunt et al. (2008) demonstrated, CO_2 is the main driver for the late Pliocene glaciation of Greenland. A draw down of CO_2 from 400 ppm to 280 ppm was sufficient to trigger the glaciation of East Greenland during the Plio-Pleistocene Transition (Lunt et al. 2008). This is a shift that is also observed in the record here (Fig. 7.6). Events such as the late Cenozoic uplift, Panama seaway closure or termination of El Niño had no 'priming' effect leading to this glaciation (Lunt et al. 2008). Larsen et al. (1994) report the deposition of glacio-marine sediments around Greenland for the last 7 Ma. If CO_2 was as low as Pagani et al. (1999b) suggested, and the main driver of the glaciation of Greenland is indeed pCO_2 Lunt et al. (2008) the glaciation of Greenland should have occurred earlier, and likewise the deposition of glacio-marine sediments. Thus the pCO_2 record presented here reconciles with the deposition of these sediments and the glaciation of Greenland, and climate models, and therefore challenges the pCO_2 reconstructions generated by Pagani et al. (1999b).

7.4.4. Comparison with ice core data

The accuracy of pCO_2 estimates derived from the Japan Sea can be tested by comparing the results against the well constrained ice core CO_2 data (Lüthi

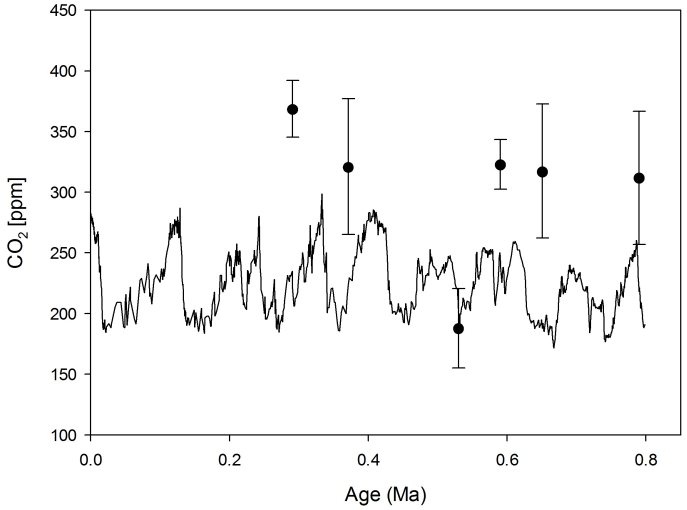

Figure 7.7.: Results of reconstructed pCO_2 compared to ice core CO_2 measurements by Lüthi et al. (2008)

et al. 2008; Fig. 7.7). Out of the six data points available for the Pleistocene, only two agree with ice core CO_2 data, at 0.79 and 0.53 Ma (Fig. 7.7). The other estimates are off-set by at least 60 µatm, and up to 100 µatm, in interglacials as well as glacial periods. There are some problems in the Quaternary Japan Sea that are affecting the alkenone paleobarometry: warm alkenone SSTs even during glacials for unknown reasons (Ishiwatari et al. 2001; Fujine et al. 2006; Lee et al. 2008) have been reconstructed, which influences the chosen solubility coefficient for pCO_2 reconstructions (Weiss 1974). Repeated opening and closure of the Tsushima Strait in the context of eustatic sea level change does affect nutrient properties of the surface water (Tada 1994; Fig. 7.5), and adds to the uncertainty of $[PO_4^{3-}]$ estimates and hence pCO_2 reconstructions. Furthermore, the $\delta^{13}C_{CO2}$ record of Tipple et al. (2010)

needed linear interpolation, due to lack of high-resolution data for the Pleistocene. Errors in $\delta^{13}C_{CO2}$ estimates thus affect the reconstruction of pCO_2 in the Japan Sea, especially during glacial periods, when $\delta^{13}C_{CO2}$ was up to 0.4–0.5 ‰ more depleted than values reconstructed by Tipple et al. (2010) (Marino et al. 1992; Schulte et al. 2003; Schneider et al. 2013). Especially SST and $[PO_4^{3-}]$, which have the largest influence on pCO_2 estimates (Pagani et al. 1999a; Pagani 2014) are poorly constrained during the Pleistocene, and thus add to the mismatch between ice core and reconstructed CO_2 concentrations of this study. Since the cause for increased SSTs during glacials in the Japan Sea is unknown, and $[PO_4^{3-}]$ cannot be reconstructed, it is questionable whether the Pleistocene part of the pCO_2 record presented here can ever be accurately estimated. For the reconstruction of pCO_2 on shorter time scales, marine sediments are not very useful, due to the large integrated time signal.

7.5. Conclusion

The study presented here is the first continuous, single site pCO_2 reconstruction spanning the last 8.4 Ma. pCO_2 was reconstructed using two different ϵ_f (25 and 27 ‰) and the results were compared to each other. The error of pCO_2 estimates with ϵ_f=25‰ was slightly larger, and pCO_2 estimations were higher than with ϵ_f=27‰. Furthermore, pCO_2 estimations were corrected for changes in salinity, using δD of $C_{37:2}$-alkenones. Almost all studies assume a constant surface salinity in the range of 35–36 psu. Paleoceanographic studies from

the Japan Sea suggest that the surface salinity varied drastically over glacial and interglacial states (Oba 1991; Tada 1994), as well as long term, due to the restriction of the TWC. It was therefore necessary to correct pCO_2 for salinity changes. The comparison shows that the uncorrected pCO_2 records underestimate pCO_2 on average by 5 µatm, in the late Miocene even by approximately 25 µatm. The late Miocene decline in pCO_2 reconstructed in this study seems to explain the profound changes in the terrestrial environment around this time, as well as drastic cooling of sea surface temperatures across both hemispheres (Herbert et al. 2016), and the beginning deposition of glacio-marine sediments around Greenland and Alaska (Krissek 1995; Larsen et al. 1994). pCO_2 for the Pleistocene is slightly increased, but agrees at least trend wise with studies from Seki et al. (2010); Beerling and Royer (2011) and Zhang et al. (2013). Although indicating a decreasing trend, pCO_2 estimations from the Japan Sea are likely overestimated, at least occasionally for the last 4 Ma. It could indicate that other factors than $CO_{2(aq)}$ influenced the ^{13}C content of coccoliths. The overestimation could also be due to the lack of appropriate $\delta^{13}C_{CO2}$ which represents a global signal (Tipple et al. 2010) instead of a regional signal. $\delta^{13}C_{DIC}$ records from the East Equatorial Pacific are similarly sparse for the critical time spans (e.g. Reghellin et al. 2015), thus the problem could not be circumvented. Therefore, this study should be repeated with a higher sampling density of $\delta^{13}C_{CO2}$. Future work should also focus on the constraint of alkenone growth rates, which equally influences pCO_2 and SSS reconstructions. Nonetheless, the pCO_2 record is fairly reasonable and accurately reflects

the proposed trend changes in pCO_2 since the late Miocene.

8. Summary and future work

The aim of this thesis was to reconstruct paleoenvironmental changes in central Asia, such as the C_4 plant expansion, and the East Asian monsoon evolution with respect to the uplift of the Himalaya-Tibetan-Plateau (HTP). Furthermore, it was the aim to reconstruct paleoceanographic changes in the Japan Sea, such as circulation changes due to tectonic changes of the marginal sea, and sea surface temperatures in the context of global climate change and the East Asian monsoon system. For this purpose, an extensive biomarker record from sediments in the Japan Sea was generated, using *n*-alkanes, alkenones, branched and isoprenoidal GDGTs, as well as hopanoids and steroids. Some of these records presented here are the most extensive records that have been generated for the Japan Sea. The results presented in this thesis show that the deposition of these biomarkers is controlled by climate change as well as regional changes in the tectonic setting. The key reconstructions of this study are summarized in Fig. 8.1.

The following section presents the main results of this study, and recommends further work that should be undertaken to improve the records presented

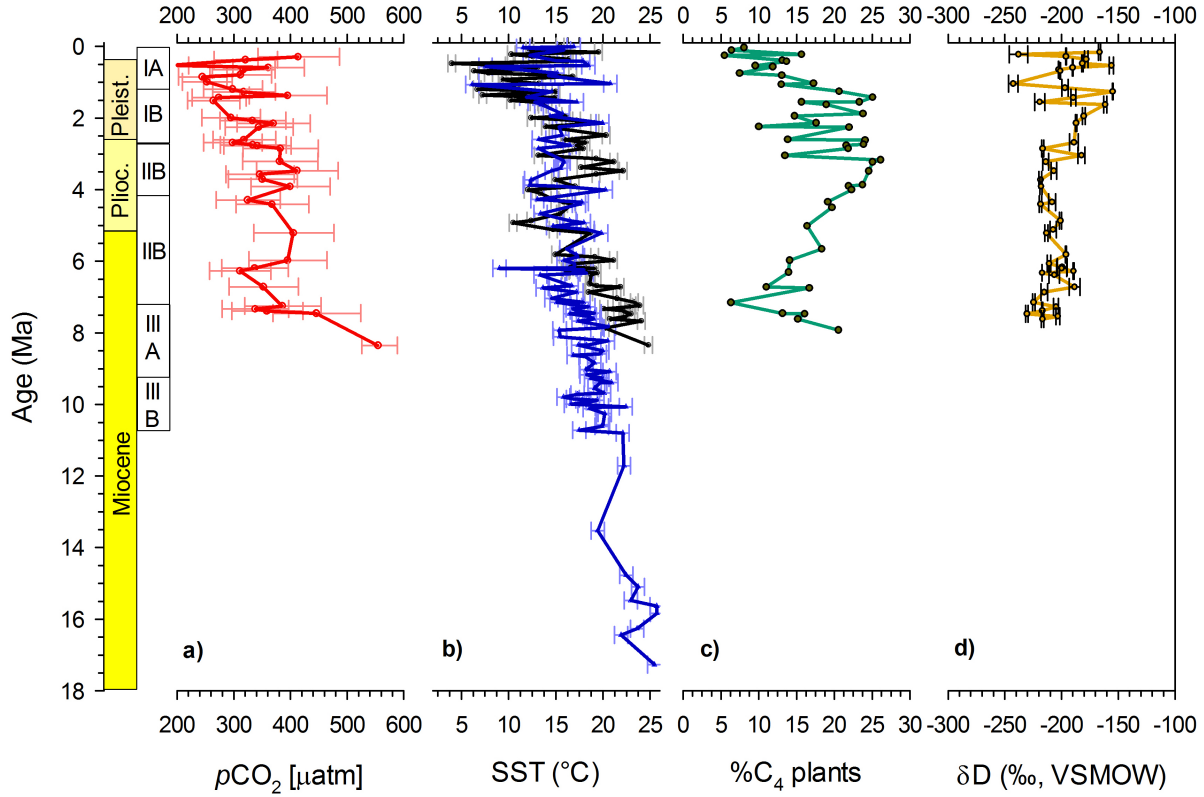

Figure 8.1.: Summary of key reconstructions at site U1425 and 797: a) reconstructed pCO_2 (ϵ_f=27 ‰, SSS corrected scenario), b) TEX_{86}- (blue) and $U^{K'}_{37}$ (black)-SSTs, c) C_4 plant expansion and d) reconstructed precipitation changes based on δD_{C29}.

here.

The tetraether index of tetraethers consisting of 86 carbons (TEX_{86}) and unsaturation index of C_{37}-ketones ($U^{K'}_{37}$), used as sea surface temperature (SST) proxies, were applied to reconstruct SST changes in the Japan Sea since the mid-Miocene. The TEX_{86}-SST record suggested that SSTs were substantially warmer during the mid-Miocene, by approximately 10 °C compared to today. The mid-Miocene Climate Transition (MMCT) from 14.5 Ma is well displayed in TEX_{86}-SSTs, and showed a cooling by 3 °C. $U^{K'}_{37}$ and TEX_{86}-SSTs showed a pronounced cooling by 7 °C in the late Miocene (7–5 Ma), which has recently been named the late Miocene cooling (LMC) (Herbert et al. 2016). The cooling observed in the Japan Sea ranged within the observed magnitude of Herbert et al. (2016). This suggested that the Japan Sea is indeed sensitive to global climate change (Tada 2004). Regional tectonic events affected the records occasionally. Overall, the temperature changes in the Japan Sea were in agreement with indicators for global climate change, such as $\delta^{18}O$ of benthic foraminifera, and reconstructed CO_2 levels. Therefore, it was suggested that continuously falling CO_2 levels throughout the Neogene were the main driver for the long term decline of Japan Sea SSTs. Throughout the Pliocene/Pleistocene, the TEX_{86} and $U^{K'}_{37}$ records exhibited larger temperature changes at higher frequencies than in the earlier part of the record. These amplitude and frequency changes were hypothesized to reflect the response to orbital forcing.

The stable carbon isotopic signature of *n*-alkanes in the Japan Sea was an-

alyzed to track the vegetation change from a C_3 dominated to a mixed C_3/C_4 vegetation in an unknown source area. The deuterium isotopic signature of *n*-alkanes was reconstructed to gain insight into the variability of the summer monsoon. Surprisingly, the interpretation of the stable isotope records in terms of vegetation change and summer monsoon intensity was only possible until approximately 3 Ma ago. A mixing model based on the $\delta^{13}C$ signature of *n*-alkanes showed a steady expansion of C_4 plants since approximately 7.5 Ma. The deuterium isotopic signature of *n*-alkanes suggested an intensifying summer monsoon over the interval of the C_4 plant expansion. Correcting δD of *n*-alkanes for the fractionation factor between wax and water ($\epsilon_{wax/water}$) to calculate δD of the source water enabled the identification of the moisture source for the precipitation in the source region. For the period from 8–3 Ma, the δD signature of the source water pointed to the East China Sea (ECS)/South China Sea (SCS) as moisture source for the precipitation in the source region. At 3 Ma, the westerly jet changed its flow mode into two discrete modes during glacials and interglacials, with profound impact on the monsoon intensity and variability. The $\delta^{13}C$ and δD record of *n*-alkanes shows large fluctuations after 3 Ma. It was subsequently hypothesized that during glacial stages, the Siberian High became very pronounced and lasted longer than during interglacials, and hence facilitate the increased deposition of Siberia derived *n*-alkanes in the Japan Sea. In contrast, during interglacials, the Siberian High was weaker than in glacial stages, and relatively less *n*-alkanes from Siberia are deposited in the Japan Sea.

The application of four different mixing models to evaluate the relative input of marine versus terrestrial organic matter was not successful. This was due to the inability to constrain appropriate terrestrial end members. The depositional environment of Site U1425 was reconstructed using 28,30-Dinorhopane (28,30-DNH) and the Lycopane/nC$_{31}$ (Ly/nC$_{31}$) ratio. Both proxies show increased abundance from 10.8 to circa 8 Ma, which is in agreement with other records (Kimura et al. 2004). 28,30-DNH is absent from the record at 8–7 Ma, although reducing conditions prevailed. This could indicate that living conditions for the 28,30-DNH were not viable anymore. Meanwhile, Ly/nC$_{31}$ continues to decline, in agreement with the increasingly oxygenated water column at 6 Ma (Kimura et al. 2004; Tada et al. 2015). During the Pleistocene, 28,30-DNH was detected once more, although at a much smaller concentration than during the Miocene. The Ly/nC$_{31}$ ratio fluctuates, in agreement with fluctuating oxic/anoxic conditons in the Japan Sea (Tada et al. 1999). Thus, both biomarkers are suitable tools to reconstruct the depositional environment at Site U1425.

In this study, it was attempted to reconstruct atmospheric CO_2 concentrations over the last 8 Ma, using the stable isotopic composition of $C_{37:2}$-alkenones from the Japan Sea. Different nutrient and enzymatic fractionation scenarios were considered, in order to constrain the fidelity of an alkenone-based pCO_2 record from the Japan Sea. Furthermore, the deuterium isotopic signature of the same biomarker was used to constrain the impact of sea surface salinity on the pCO_2 record. The results showed an overall declining

pCO_2 trend from 8 Ma to Present, with a distinct decline from approximately 520 to 300 µatm in the time from 8–6 Ma. The lack of appropriate $\delta^{13}C_{CO2}$ during the Pliocene, as well as very dynamic nutrient fluctuations, probably in response to summer monsoon variability and glacio-eustatic sea level change, complicated the Pleistocene part of the pCO_2 record presented here. The pCO_2 record presented here is the first pCO_2 record that captures the required decline in pCO_2 to trigger the C_4 plant expansion, and explains the observed changes in inorganic carbon allocation in large coccoliths. However, it is unclear whether a pCO_2 decline triggered the onset of the LMC, or whether cooling SSTs acted as a positive feedback for a declining pCO_2 as proposed by Herbert et al. (2016).

8.1. Future work

Future work should focus on increasing the sampling resolution of the TEX_{86} record, to fully capture the mid-Miocene Climate Optimum (MMCO) and MMCT. However, this study showed that the TEX_{86} record for this interval is affected by non-thermal factors (Fig. 4.3d), thus this attempt might prove difficult. Increasing the SST resolution of both proxy records, $U^{K'}_{37}$ and TEX_{86}, is necessary to constrain the effect of eustatic sea level changes on SSTs in the Japan Sea, and to test the hypothesis that the fluctuations are caused by these sea level changes.

At present, the environmental reconstruction based on stable isotopes of *n*-

alkanes cannot provide an answer to whether the variability of the East Asian monsoon was caused by enhanced HTP uplift, or the onset of the Northern Hemisphere glaciation, as both events happened around the same time, and their interrelationship is still poorly understood (Tada et al. 2016). Furthermore, the part of the record spanning 3 Ma to Present lacks a high sample resolution. Increasing the resolution of the carbon and deuterium isotopic signature record of *n*-alkanes can be used to constrain the dominant atmospheric circulation feature (westerly jet or Siberian High), and their spatial extent in variation with glacial-interglacial cycles. The paleo position of both atmospheric circulation features should be used to re-evaluate monsoon records from East Asia and the maritime continent, to further improve the understanding of the monsoon system.

Future work should focus on generating a nannofossil record of coccolithophores in the Japan Sea (i.e. from Site U1428) to constrain the effect of cell size on the presented pCO_2 record. It should also focus on increasing the sampling resolution of the $\delta D_{alkenone}$ record, and on the constraint of growth rates for more accurate pCO_2 estimates. There should also be a focus on generating a higher resolution $\delta^{13}C_{CO2}$ record of benthic foraminifera, to correct for its variation in glacial and interglacial periods. This will improve the alkenone based pCO_2 estimates in the Japan Sea during the Plio- Pleistocene. Subsequently, the pCO_2 record should be expanded to further elucidate the lag and lead relationship of SSTs and pCO_2.

Expedition 346 was just the onset of a whole set of cruises around SE-

Asia which target the evolution of the Asian monsoons. More expeditions were conducted, to investigate the Indian Monsoon rainfall (IDOP 353), the Bengal Fan (354), the Arabian Sea monsoon (355) and the Maledives monsoon (359). A compilation of biomarker records, such as of SSTs, *n*-alkane δD and $\delta^{13}C$ of higher plants will build an integrated picture of the EAM and its subsequent evolution. Conveniently, the C_4 plant expansion, which is somewhat ambiguous across East Asia can be integrated into a whole picture, to answer question where it did start when, and when it was terminated again. Results from Expedition 377 to the Arctic Ocean, which intends to drill back to Oligocene, are also interesting to compare the records generated here to. This expedition has the potential to generate more MMCO SST records, which will provide the opportunity to establish a latitudinal temperature gradient. Furhtermore, alkenone paleobarometry should be carried out on the same records used by Herbert et al. (2016) for their $U^{K'_{37}}$-SST reconstruction during the late Miocene, to test for the hypothesis of a better constrained temperature record and its effect on pCO_2 reconstructions, as proposed in this dissertation.

References

Ageta, H., Shiojima, K., and Arai, Y. (1987). Acid-Induced Rearrangement of Triterpenoid Hydrocarbons Belonging to the Hopane and Migrated Hopane Series. *Chemical and Pharmaceutical Bulletin*, 35(7):2705–2716.

Aichner, B., Wilkes, H., Herzschuh, U., Mischke, S., and Zhang, C. (2010). Biomarker and compound-specific δ^{13}C evidence for changing environmental conditions and carbon limitation at Lake Koucha, eastern Tibetan Plateau. *Journal of Paleolimnology*, 43(4):873–899.

An, Z., Huang, Y., Liu, W., Guo, Z., Clemens, S., Li, L., Prell, W., Ning, Y., Cai, Y., Zhou, W., Lin, B., Zhang, Q., Cao, Y., Qiang, X., Chang, H., and Wu, Z. (2005). Multiple expansions of C_4 plant biomass in East Asia since 7 Ma coupled with strengthened monsoon circulation. *Geology*, 33(9):705–708.

An, Z., Kutzbach, J. E., Prell, W. L., and Porter, S. C. (2001). Evolution of Asian monsoons and phased uplift of the Himalaya-Tibetan plateau since Late Miocene times. *Nature*, 411:62–66.

Araguás-Araguás, L., Froehlich, K., and Rozanski, K. (1998). Stable isotope composition of precipitation over southeast Asia. *Journal of Geophysical Research*, 103(D22):28721.

Arrhenius, S. (1896). On the influence of carbonic acid in the air upon temperature of the ground. *Philosophical Magazine*, 41(5):237–276.

Arrigo, K. R. (2005). Marine microorganisms and global nutrient cycles. *Nature*, 437:349–355.

Backman, J., Raffi, I., Rio, D., and Fornaciari, E. (2012). Biozonation and biochronology of Miocene through Pleistocene calcareous nannofossils from low and middle latitudes. *Newsletters on Stratigraphy*, 47:131–181.

Badger, M. P. S., Lear, C. H., Pancost, R. D., Foster, G. L., Bailey, T. R., Leng, M. J., and Abels, H. A. (2013a). CO_2 drawdown following the middle Miocene expansion of the Antarctic Ice Sheet. *Paleoceanography*, 28(1):42–53.

Badger, M. P. S., Schmidt, D. N., Mackensen, A., and Pancost, R. D. (2013b). High-resolution alkenone palaeobarometry indicates relatively stable pCO_2 during the Pliocene (3.3-2.8 Ma). *Philosophical transactions. Series A, Mathematical, Physical, and Engineering Sciences*, 371.

Badger, M. R. and Bek, E. J. (2008). Multiple Rubisco forms in proteobacteria

- their functional significance in relation to CO_2 acquisition by the CBB cycle. *Journal of Experimental Botany*, 59(7):1525–1541.

Bae, S. W., Lee, K. E., and Kim, K. (2015). Use of carbon isotopic composition of alkenone as a CO_2 proxy in the East Sea/Japan Sea. *Continental Shelf Research*, 107:24–32.

Bai, Y., Fang, X., Nie, J., Wang, Y., and Wu, F. (2009). A preliminary reconstruction of the paleoecological and paleoclimatic history of the Chinese Loess Plateau from the application of biomarkers. *Palaeogeography, Palaeoclimatology, Palaeoecology*, 271:161–169.

Bai, Y., Fang, X., and Tian, Q. (2012). Spatial patterns of soil *n*-alkane δD values on the Tibetan Plateau: Implications for monsoon boundaries and paleoelevation reconstructions. *Journal of Geophysical Research Atmospheres*, 117(20).

Balsam, W., Ji, J., and Chen, J. (2004). Climatic interpretation of the Luochuan and Lingtai loess sections, China, based on changing iron oxide mineralogy and magnetic susceptibility. *Earth and Planetary Science Letters*, 223:335–348.

Beerling, D. J. and Royer, D. L. (2011). Convergent Cenozoic CO_2 history. *Nature Geoscience*, 4(7):418–420.

Bendle, J., Kawamura, K., Yamazaki, K., and Niwai, T. (2007). Latitudinal

distribution of terrestrial lipid biomarkers and *n*-alkane compound-specific stable carbon isotope ratios in the atmosphere over the western Pacific and Southern Ocean. *Geochimica et Cosmochimica Acta*, 71(24):5934–5955.

Bendle, J. A., Kawamura, K., and Yamazaki, K. (2006). Seasonal changes in stable carbon isotopic composition of *n*-alkanes in the marine aerosols from the western North Pacific: Implications for the source and atmospheric transport. *Geochimica et Cosmochimica Acta*, 70:13–26.

Bereiter, B., Eggleston, S., Schmitt, J., Nehrbass-Ahles, C., Stocker, T. F., Fischer, H., Kipfstuhl, S., and Chappellaz, J. (2015). Revision of the EPICA Dome C CO_2 record from 800 to 600 kyr before present. *Geophysical Research Letters*, 42(2):542–549.

Berggren, W., Kent, D., Flynn, J., and van Couvering, J. (1985). Cenozoic geochronology. *Geological Society of America Bulletin*, 96(11):1407–1418.

Bianchi, A. and Bianchi, G. (1990). Surface lipid composition of C_3 and C_4 plants. *Biochemical Systematics and Ecology*, 18:533–537.

Bianchi, T. S. and Canuel, E. A. (2011). *Chemical biomarkers in aquatic ecosystems*. Princeton University Press, Princeton.

Bidigare, R. R., Fluegge, A., Freeman, K. H., Hanson, K. L., Hayes, J. M., Hollander, D., Jasper, J. P., King, L. L., Laws, E. A., Milder, J., Millero, F. J., Pancost, R., Popp, B. N., Steinberg, P. A., and Wakeham, S. G. (1997). Con-

sistent fractionation of ^{13}C in nature and in the laboratory: Growth-rate effects in some haptophyte algae. *Global Biogeochemical Cycles*, 11(2):279–292.

Bjerknes, J. (1964). Atlantic Air-Sea Interaction. In Landsberg, H. E. and Mieghem, J. V., editors, *Advances in Geophysics*, volume 10 of *Advances in Geophysics*, chapter 1, pages 1–82. Academic Press, New York and London.

Bolton, C., Hernández-Sánchez, M., Fuertes, M.-Á., González-Lemos, S., Abrevaya, L., Mendez-Vicente, A., Flores, J.-A., Probert, I., Giosan, L., Johnson, J., and Stoll, H. (2016). Decrease in coccolithophore calcification and CO_2 since the middle Miocene. *Nature Communications*, 7.

Bolton, C. T. and Stoll, H. M. (2013). Late Miocene threshold response of marine algae to carbon dioxide limitation. *Nature*, 500:558–562.

Brassell, S. C., Eglinton, G., Marlowe, I. T., Pflaumann, U., and Sarnthein, M. (1986). Molecular stratigraphy: A new tool for climatic assessment. *Nature*, 320:129–133.

Breecker, D. O., Sharp, Z. D., and McFadden, L. D. (2010). Atmospheric CO_2 concentrations during ancient greenhouse climates were similar to those predicted for A.D. 2100. *Proceedings of the National Academy of Sciences*, 107(2):576–580.

Burkhardt S; Riebesell, U. Z. I. (1999). Effects of growth rate, CO_2 concen-

tration, and cell size on the stable carbon isotope fractionation in marine phytoplankton. *Geochimica et Cosmochimica Acta*, 63(22):3729–3741.

Bush, R. T. and McInerney, F. A. (2013). Leaf wax *n*-alkane distributions in and across modern plants: Implications for paleoecology and chemotaxonomy. *Geochimica et Cosmochimica Acta*, 117:161–179.

Caballero, R. and Huber, M. (2013). State-dependent climate sensitivity in past warm climates and its implications for future climate projections. *Proceedings of the National Academy of Sciences*, 110(35):14162–14167.

Castañeda, I. S., Werne, J. P., Johnson, T. C., and Filley, T. R. (2009). Late Quaternary vegetation history of southeast Africa: The molecular isotopic record from Lake Malawi. *Palaeogeography Palaeoclimatology Palaeoecology*, 275:100–112.

Cerling, T. E. (1991). Carbon dioxide in the atmosphere; evidence from Cenozoic and Mesozoic Paleosols. *American Journal of Science*, 291(4):377–400.

Cerling, T. E. (1992). Use of carbon isotopes in paleosols as an indicator of the $p\mathrm{CO}_2$ of the paleoatmosphere. *Global Biogeochemical Cycles*, 6(3):307–314.

Cerling, T. E., Harris, J. M., Macfadden, B. J., Leakey, M. G., Quadek, J.,

Eisenmann, V., and Ehleringer, J. R. (1997). Global vegetation change through the Miocene/Pliocene boundary. *Nature*, 389(6647):153–158.

Chen, W., Mohtadi, M., Schefuß, E., and Mollenhauer, G. (2014). Organic-geochemical proxies of sea surface temperature in surface sediments of the tropical eastern Indian Ocean. *Deep Sea Research Part I: Oceanographic Research Papers*, 88:17–29.

Chen, W., Mohtadi, M., Schefuß, E., and Mollenhauer, G. (2016). Concentrations and abundance ratios of long-chain alkenones and glycerol dialkyl glycerol tetraethers in sinking particles south of Java. *Deep Sea Research Part I: Oceanographic Research Papers*, 112:14–24.

Chikaraishi, Y. and Naraoka, H. (2003). Compound-specific δD-δ^{13}C analyses of *n*-alkanes extracted from terrestrial and aquatic plants. *Phytochemistry*, 63(3):361–371.

Chikaraishi, Y., Naraoka, H., and Poulson, S. R. (2004). Hydrogen and carbon isotopic fractionation of lipid biosynthesis among terrestrial (C_3, C_4 and CAM) and aquatic plants. *Phytochemistry*, 65(10):1369–1381.

Chivall, D., M'Boule, D., Sinke-Schoen, D., Sinninghe Damsté, J. S., Schouten, S., and van der Meer, M. T. J. (2014). The effects of growth phase and salinity on the hydrogen isotopic composition of alkenones produced by coastal haptophyte algae. *Geochimica et Cosmochimica Acta*, 140:381–390.

Clemens, S. C., Prell, W. L., and Sun, Y. (2010). Orbital-scale timing and mechanisms driving Late Pleistocene Indo-Asian summer monsoons: Reinterpreting cave speleothem δ^{18}O. *Paleoceanography*, 25(4).

Collister, J. W., Rieley, G., Stern, B., Eglinton, G., and Fry, B. (1994). Compound-specific δ^{13}C analyses of lead lipids from plants with differing carbon dioxide metabolisms. *Organic Geochemistry*, 21(6):619–627.

Conte, M. H., Sicre, M. A., Rühlemann, C., Weber, J. C., Schulte, S., Schulz-Bull, D., and Blanz, T. (2006). Global temperature calibration of the alkenone unsaturation index ($U^{K'}_{37}$) in surface waters and comparison with surface sediments. *Geochemistry, Geophysics, Geosystems*, 7(2).

Cranwell, P. A. (1981). Diagenesis of free and bound lipids in terrestrial detritus deposited in a lacustrine sediment. *Organic Geochemistry*, 3(3):79–89.

D'Andrea, W. J., Liu, Z., Alexandre, M. D. R., Wattley, S., Herbert, T. D., and Huang, Y. (2007). An efficient method for isolating individual long-chain alkenones for compound-specific hydrogen isotope analysis. *Analytical Chemistry*, 79(9):3430–3435.

De Rosa, M. and Gambacorta, A. (1988). The lipids of archaebacteria. *Progress in Lipid Research*, 27:153–175.

Dersch-Hansmann, M. (1994). *Zur Klimaentwicklung in Ostasien wahrend*

der letzten 5 Millionen Jahre: Terrigener Sedimenteintrag in die Japan See (ODP Ausfahrt 128). PhD thesis, Universität Bremen.

Deuser, W. G. and Degens, E. T. (1967). Carbon Isotope Fractionation in the System $CO_{2(gas)}$-$CO_{2(aqueous)}$-$HCO^{-}_{3\,(aqueous)}$. *Nature*, 215:1033–1035.

Deuser, W. G., Degens, E. T., and Guillard, R. R. L. (1968). Carbon isotope relationships between plankton and sea water. *Geochimica et Cosmochimica Acta*, 32:657–660.

Diester-Haass, L., Billups, K., and Emeis, K. C. (2006). Late Miocene carbon isotope records and marine biological productivity: Was there a (dusty) link? *Paleoceanography*, 21(4).

Ding, Z. L., Liu, T., Rutter, N., Yu, Z., and Zhu, R. (1995). Ice-volume forcing of East Asian Winter Monsoon Variation in the Past 800,000 Years. *Quaternary Research*, 44:149–159.

Ding, Z. L., Ren, J. Z., Yang, S. L., and Liu, T. S. (1999). Climate instability during the penultimate glaciation: Evidence from two high-resolution loess records, China. *Journal of Geophysical Research B: Solid Earth*, 104(B9):20123–20132.

Ding, Z. L. and Yang, S. L. (2000). C_3/C_4 vegetaiton evolution over the last 7.0 Myr in the Chinese Loess Plateau: eivdence from pedogenic carbonate δ^{13}C. *Palaeogeography, Palaeoclimatology, Palaeoecology*, 160:291–299.

Douka, E., Koukkou, A. I., Drainas, C., Grosdemange-Billiard, C., and Rohmer, M. (2001). Structural diversity of the triterpenic hydrocarbons from the bacterium *Zymomonas mobilis*: The signature of defective squalene cyclization by the squalene/hopene cyclase. *FEMS Microbiology Letters*, 199(2):247–251.

Dowsett, H. J., Foley, K. M., Stoll, D. K., Chandler, M., Sohl, L. E., Bentsen, M., Otto-Bliesner, B. L., Bragg, F. J., Chan, W.-L., Contoux, C., Dolan, A. M., Haywood, A. M., Jonas, J., Jost, A., Kamae, Y., Lohmann, G., Lunt, D. J., Nisancioglu, K. H., Abe-Ouchi, A., Ramstein, G., Riesselman, C. R., Robinson, M. M., Rosenbloom, N. A., Salzmann, U., Stepanek, C., Strother, S. L., Ueda, H., Yan, Q., and Zhang, Z. (2013). Sea surface temperature of the mid-Piacenzian ocean: a data-model comparison. *Scientific Reports*, 3.

Eglinton, G. and Hamilton, R. J. (1967). Leaf epicuticular waxes. *Science*, 156:1322–1335.

Eglinton, T. I. and Repeta, D. J. (2003). Organic Matter in the Contemporary Ocean - Treatise on Geochemistry. In Elderfield, H., editor, *Treatise on Geochemistry*, volume 6 of *Teatrise on Geochemistry*, chapter 6.06, pages 145–180. Elsevier–Pergamon Oxford, Oxford.

Ehleringer, J. R., Cerling, T. E., and Helliker, B. R. (1997). C_4 photosynthesis, atmospheric CO_2, and climate. *Oecologia*, 112(3):285–299.

Elling, F. J., Könneke, M., Mußmann, M., Greve, A., and Hinrichs, K.-U.

(2015). Influence of temperature, pH, and salinity on membrane lipid composition and TEX_{86} of marine planktonic thaumarchaeal isolates. *Geochimica et Cosmochimica Acta*, 171:238–255.

Eltgroth, M. L., Watwood, R. L., and Wolfe, G. V. (2005). Production and cellular localization of neutral long-chain lipids in the haptophyte algae *Isochrysis galbana* and *Emiliania huxleyi*. *Journal of Phycology*, 41(5):1000–1009.

Ensminger, A., Albrecht, P., Ourisson, G., Kimble, B. J., Maxwell, J. R., and Eglinton (1972). Homohopane in messel oil shale: First identification of a C_{31} pentacyclic triterpane in nature Bacterial origin of some triterpanes in ancient sediments? *Tetrahedron Letters*, 13(36):3861–3864.

Epstein, B. L., D'Hondt, S., Quinn, J. G., Zhang, J., and Hargraves, P. E. (1998). An effect of dissolved nutrient concentrations on alkenone based temperature estimates. *Paleoceanography*, 13(2):122–126.

Farquhar, G. D., Ehleringer, and Hubick (1989). Carbon isotope discrimination and photosynthesis. *Annual Review of Plant Physiology and Plant Molecular Biology*, 40(1):503–537.

Feakins, S. J. and Sessions, A. L. (2010). Controls on the D/H ratios of plant leaf waxes in an arid ecosystem. *Geochimica et Cosmochimica Acta*, 74(7):2128–2141.

Fietz, S., Huguet, C., Bendle, J., Escala, M., Gallacher, C., Herfort, L., Jamieson, R., Martínez-Garcia, A., McClymont, E. L., Peck, V. L., Prahl, F. G., Rossi, S., Rueda, G., Sanson-Barrera, A., and Rosell-Melé, A. (2012). Co-variation of crenarchaeol and branched GDGTs in globally-distributed marine and freshwater sedimentary archives. *Global and Planetary Change*, 92:275–285.

Foster, G. L., Lear, C. H., and Rae, J. W. B. (2012). The evolution of $p\mathrm{CO}_2$, ice volume and climate during the middle Miocene. *Earth and Planetary Science Letters*, 341:243–254.

Foster, G. L. and Rae, J. W. B. (2016). Reconstructing Ocean pH with Boron Isotopes in Foraminifera. *Annual Review of Earth and Planetary Sciences*, 44(1):207–237.

Fujine, K., Yamamoto, M., Tada, R., and Kido, Y. (2006). A salinity-related occurrence of a novel alkenone and alkenoate in Late Pleistocene sediments from the Japan Sea. *Organic Geochemistry*, 37(9):1074–1084.

Gamo, T. (1999). Global warming may have slowed down the deep conveyor belt of a marginal sea of the northwestern Pacific: Japan Sea. *Geophysical Research Letters*, 26(20):3137–3140.

Gao, L., Edwards, E. J., Zeng, Y., and Huang, Y. (2014). Major evolutionary trends in hydrogen isotope fractionation of vascular plant leaf waxes. *PLoS ONE*, 9(11).

Garcin, Y., Schwab, V. F., Gleixner, G., Kahmen, A., Todou, G., Séné, O., Onana, J.-M., Achoundong, G., and Sachse, D. (2012). Hydrogen isotope ratios of lacustrine sedimentary *n*-alkanes as proxies of tropical African hydrology: Insights from a calibration transect across Cameroon. *Geochimica et Cosmochimica Acta*, 79:106–126.

Goericke, R. and Fry, B. (1994). Variations of marine plankton δ^{13}C with latitude, temperature, and dissolved CO_2 in the world ocean. *Global Biogeochemical Cycles*, 8(1):85–90.

Gordon, E. S. and Goñi, M. A. (2003). Sources and distribution of terrigenous organic matter delivered by the Atchafalaya River to sediments in the northern Gulf of Mexico. *Geochimica et Cosmochimica Acta*, 67(13):2359–2375.

Gradstein, F. and Ogg, J. (2012). The Geological Timescale. *Newsletters on Stratigraphy*, 45(2):171–188.

Guo, Z. T., Ruddiman, W. F., Hao, Q. Z., Wu, H. B., Qiao, Y. S., Zhu, R. X., Peng, S. Z., Wei, J. J., Yuan, B. Y., and Liu, T. S. (2002). Onset of Asian desertification by 22 Myr ago inferred from loess deposits in China. *Nature*, 416(6877):159–163.

Hamon, N., Sepulchre, P., Donnadieu, Y., Henrot, A. J., Francois, L., Jaeger, J. J., and Ramstein, G. (2011). Growth of subtropical forest in Miocene

Europe: The role of carbon dixoide and Antarctic ice volume. *Geology*, 40(6):567–570.

Han, Y., Fang, X., Kang, S., Wang, H., and Kang, F. (2008). Shifts of dust source regions over central Asia and the Tibetan Plateau: Connections with the Arctic oscillation and the westerly jet. *Atmospheric Environment*, 42(10):2358–2368.

Hao, Q., Wang, L., Oldfield, F., Peng, S., Qin, L., Song, Y., Xu, B., Qiao, Y., Bloemendal, J., and Guo, Z. (2012). Delayed build-up of Arctic ice sheets during 400,000-year minima in insolation variability. *Nature*, 490:393–396.

Hartman, D., Klein Tank, A., Rusticucci, M., Alexander, L. V., Brönnimann, S., Charabi, Y., Dentener, F., Dlugokency, E., Easterling, D., Kaplan, A., Soden, B., Thorne, P., Wild, M., and Zhai, P. (2013). Observations: Atmosphere and Surface. In Stocker, T. F., Qin, D., Plattner, G.-K., Tignor, M., Allen, S. K., Boschung, J., Nauels, A., Xia, Y., Bex, V., and Midgley, P., editors, *Climate Change 2013: The Physical Science Basis. Contribution of Working Group I to the Fifth Assessment Report of the Intergovernmental Panel on Climate Change*, chapter 2, pages 159–254. Cambridge University Press, Cambridge, United Kingdom and New York, NY, USA.

Harvey, H. R., Tuttle, J. H., and Bell, J. T. (1995). Kinetics of phytoplankton decay during simulated sedimentation: Changes in biochemical composi-

tion and microbial activity under oxic and anoxic conditions. *Geochimica et Cosmochimica Acta*, 59(16):3367–3377.

Hayes, J. M. (1993). Factors controlling ^{13}C contents of sedimentary organic compounds: Principles and evidence. *Marine Geology*, 113(1):111–125.

Hays, J. D., Imbrie, J., and Shackleton, N. J. J. (1976). Variations in the Earth's Orbit : Pacemaker of the Ice Ages. *Science*, 194:1121–1132.

Hedges, J. I., Baldock, J. A., Gelinas, Y., Lee, C., Peterson, M., and Wakeham, S. G. (2001). Evidence for non-selective preservation of organic matter in sinking marine particles. *Nature*, 409:801–804.

Hedges, J. I., Hu, F. S., Devol, A. H., Hartnett, H. E., Tsamakis, E., and Keil, R. G. (1999). Sedimentary organic matter preservation: A test for selective degradation under oxic conditions. *American Journal of Science*, 299:529–555.

Hedges, J. I., Keil, R. G., and Aransas, P. (1997). What happens to terrestrial organic matter in the ocean? *Organic Geochemistry*, 27(5):195–212.

Herbert, T. D., Lawrence, K. T., Tzanova, A., Peterson, L. C., Caballero-Gill, R., and Kelly, C. S. (2016). Late Miocene global cooling and the rise of modern ecosystems. *Nature Geoscience*, 9(11):843–847.

Herfort, L., Schouten, S., Boon, J. P., and Sinninghe Damsté, J. S. (2006).

Application of the TEX_{86} temperature proxy to the southern North Sea. *Organic Geochemistry*, 37:1715–1726.

Hernandez-Sanchez, M. T., Woodward, E. M. S., Taylor, K. W. R., Henderson, G. M., and Pancost, R. D. (2014). Variations in GDGT distributions through the water column in the South East Atlantic Ocean. *Geochimica et Cosmochimica Acta*, 132:337–348.

Herold, N., Huber, M., Müller, R. D., and Seton, M. (2012). Modeling the Miocene climatic optimum: Ocean circulation. *Paleoceanography*, 27(1):1–22.

Hiradate, S., Nakadai, T., Shindo, H., and Yoneyama, T. (2004). Carbon source of humic substances in some Japanese volcanic ash soils determined by carbon stable isotopic ratio, $\delta^{13}C$. *Geoderma*, 119(1):133–141.

Ho, S. L. and Laepple, T. (2015). Glacial cooling as inferred from marine temperature proxies TEX_{86}^{H} and $U_{37}^{K'}$. *Earth and Planetary Science Letters*, 409:15–22.

Hodell, D. A. and Woodruff, F. (1994). Variations in the strontium isotopic ratio of seawater during the Miocene: Stratigraphic and geochemical implications. *Paleoceanography*, 9(3):405–426.

Hoefs, M. J. L., Rijpstra, W. I. C., and Sinninghe Damsté, J. S. (2002). The influence of oxic degradation on the sedimentary biomarker record I: Evi-

dence from Madeira Abyssal Plain turbidites. *Geochimica et Cosmochimica Acta*, 666:2719–2735.

Hoefs, M. J. L., Sinninghe Damsté, J. S., de Lange, G. J., and de Leeuw, J. W. (1998a). Changes in kerogen composition across an oxidation front in Madeira Abyssal Plain turbidites as revealed by pyrolysis GC-MS. In Weaver, P. P., Schmincke, H.-U., Firth, J. V., and Duffield, W., editors, *Proceedings of the Ocean Drilling Program, Scientific Results, Vol. 157*, chapter 35, pages 591–607. College Station, (TX Ocean Drilling Program), College Station.

Hoefs, M. J. L., Versteegh, G. J. M., Rijpstra, W. I. C., de Leeuw, J. W., and Sinninghe Damsté, J. S. (1998b). Postdepositional oxic degradation of alkenones: Implications for the measurement of paleo sea surface temperatures. *Paleoceanography*, 13:42–49.

Hönisch, B., Hemming, N., Archer, D., Siddall, M., and McManus, J. F. (2009). Atmospheric carbon dioxide concentration across the mid-Pleistocene transition. *Science*, 324:1551–1554.

Hopmans, E. C., Schouten, S., Pancost, R. D., van Der Meer, M. T. J., and Sinninghe Damsté, J. S. (2000). Analysis of intact tetraether lipids in archaeal cell material and sediments by high performance liquid chromatography/atmospheric pressure chemical ionization mass spectrometry. *Rapid Communications in Mass Spectrometry*, 14(7):585–589.

Hopmans, E. C., Weijers, J. W. H., Schefuß, E., Herfort, L., Sinninghe Damsté, J. S., and Schouten, S. (2004). A novel proxy for terrestrial organic matter in sediments based on branched and isoprenoid tetraether lipids. *Earth and Planetary Science Letters*, 224:107–116.

Hori, M. E. and Ueda, H. (2006). Impact of global warming on the East Asian winter monsoon as revealed by nine coupled atmosphere-ocean GCMs. *Geophysical Research Letters*, 33(3).

Hou, J., D'Andrea, W. J., and Huang, Y. (2008). Can sedimentary leaf waxes record D/H ratios of continental precipitation? Field, model, and experimental assessments. *Geochimica et Cosmochimica Acta*, 72(14):3503–3517.

Hovan, S. A., Rea, D. K., Pisias, N. G., and Shackleton, N. J. (1989). A direct link between the China loess and marine δ^{18}O records: aeolian flux to the north Pacific. *Nature*, 340:296–298.

Hulthe, G., Hulth, S., and Hall, P. O. J. (1998). Effect of oxygen on degradation rate of refractory and labile organic matter in continental margin sediments. *Geochimica et Cosmochimica Acta*, 62(8):1319–1328.

Hurley, S. J., Elling, F. J., Könneke, M., Buchwald, C., Wankel, S. D., Santoro, A. E., Lipp, J. S., Hinrichs, K.-U., and Pearson, A. (2016). Influence of ammonia oxidation rate on thaumarchaeal lipid composition and

the TEX_{86} temperature proxy. *Proceedings of the National Academy of Sciences*, 113(28):7762–7767.

Ichikawa, H. and Beardsley, R. C. (2002). The current system in the Yellow and East China Seas. *Journal of Oceanography*, 58(1):77–92.

Iijima, A. and Tada, R. (1990). Evolution of Tertiary sedimentary basins of Japan in reference to opening of the Japan Sea. *Journal of the Faculty of Science, University of Tokyo*, 22:121–171.

Ingle, J. C. (1992). Subsidence of the Japan Sea: Stratigraphic Evidence From Odp Sites and Onshore Sections. In Tamaki, K., Suyehiro, K., Allan, J., and McWilliams, M., editors, *Proceedings of the Ocean Drilling Program*, volume 127/128, chapter 76, pages 1197–1218. College Station, (TX Ocean Drilling Program).

Inglis, G. N., Farnsworth, A., Lunt, D., Foster, G. L., Hollis, C. J., Pagani, M., Jardine, P. E., Pearson, P. N., Markwick, P., Galsworthy, A. M. J., Raynham, L., Taylor, K. W. R., and Pancost, R. D. (2015). Descent toward the Icehouse: Eocene sea surface cooling inferred from GDGT distributions. *Paleoceanography*, 30(7):1000–1020.

IPCC (1990). Introduction. In Houghton, J. T., Jenkins, G. J., and Ephraums, J. J., editors, *Climate change. The IPCC Scientific Assessment*, chapter 1. Cambridge University Press, Cambridge.

Ishiwatari, R., Houtatsu, M., and Okada, H. (2001). Alkenone-sea surface temperatures in the Japan Sea over the past 36 kyr: Warm temperatures at the last glacial maximum. *Organic Geochemistry*, 32(1):57–67.

Ishiwatari, R., Yamada, K., Matsumoto, K., Houtatsu, M., and Naraoka, H. (1999). Organic molecular and carbon isotopic records of the Japan Sea over the past 30 kyr. *Paleoceanography*, 14(2):260–270.

Isoda, Y. (1994). Warm eddy movements in the eastern Japan Sea. *Journal of Oceanography*, 50(1):1–15.

Itaki, T. (2016). Transitional changes in microfossil assemblages in the Japan Sea from the Late Pliocene to Early Pleistocene related to global climatic and local tectonic events. *Progress in Earth and Planetary Science*, 3(1):11.

Jasper, J. P. and Hayes, J. M. (1990). A carbon isotope record of CO_2 levels during the late Quaternary. *Nature*, 347:462–464.

Jetter, R., Kunst, L. and Samuels, A. L. (2006). Composition of Plant Cuticular Wax. *Annual Plant Reviews, Biology of Pant Cuticle*, 23:145.

Jia, G., Li, Z., Peng, P., and Zhou, L. (2012). Aeolian *n*-alkane isotopic evidence from North Pacific for a Late Miocene decline of C_4 plant in the arid Asian interior. *Earth and Planetary Science Letters*, 321:32–40.

Jiang, H. and Ding, Z. (2008). A 20 Ma pollen record of East-Asian sum-

mer monsoon evolution from Guyuan, Ningxia, China. *Palaeogeography, Palaeoclimatology, Palaeoecology*, 265:30–38.

Jolivet, L., Tamaki, K., and Fournier, M. (1994). Japan Sea, opening history and mechanism: A synthesis. *Journal of Geophysical Research*, 99(11):22237–22259.

Kano, K., Kato, H., Yanagisawa, Y., and Yoshida, F. (1991). *Stratigraphy and geologic history of the Cenozoic of Japan*, volume 274. Geological Survey of Japan, Ibaraki.

Karner, M. B., DeLong, E. F., and Karl, D. M. (2001). Archaeal dominance in the mesopelagic zone of the Pacific Ocean. *Nature*, 409:507–510.

Kasper, S., Van Der Meer, M. T. J., Mets, A., Zahn, R., Sinninghe Damsté, J. S., and Schouten, S. (2014). Salinity changes in the Agulhas leakage area recorded by stable hydrogen isotopes of C_{37} alkenones during Termination I and II. *Climate of the Past*, 10(1):251–260.

Kawamura, K. (1995). Land-derived lipid class compounds in the deep-sea sediments and marine aerosols from North Pacific. In Nozaki, Y. and Sakai, H., editors, *Biogeochemical Processes and Ocean Flux in the Western Pacific*, chapter 3, pages 31–51. Terra Scientific Publishing Company, Tokyo.

Kawamura, K., Ishimura, Y., and Yamazaki, K. (2003). Four years' observa-

tions of terrestrial lipid class compounds in marine aerosols from the western North Pacific. *Global Biogeochemical Cycles*, 17(1):1–19.

Kawamura, K., Matsumoto, K., Uchida, M., and Shibata, Y. (2010). Contributions of modern and dead organic carbon to individual fatty acid homologues in spring aerosols collected from northern Japan. *Journal of Geophysical Research: Atmospheres*, 115(D22).

Keeling, C. D., Bacastow, R. B., Carter, A. F., Piper, S. C., Whorf, T. P., Heimann, M., Mook, W. G., and Roeloffzen, H. (1989). A three-dimensional model of atmospheric CO_2 transport based on observed winds: 1. Analysis of observational data. *Geophysical Monograph*, 55:165–236.

Keil, R. G., Montlucon, D. B., Prahl, F. G., and Hedges, J. I. (1994). Sorptive preservation of labile organic matter in marine sediments. *Nature*, 370:549–552.

Keisling, B. A., Castañeda, I. S., and Brigham-Grette, J. (2017). Hydrological and temperature change in Arctic Siberia during the intensification of Northern Hemisphere Glaciation. *Earth and Planetary Science Letters*, 457:136–148.

Kender, S., Peck, V. L., Jones, R. W., and Kaminski, M. A. (2009). Middle Miocene oxygen minimum zone expansion offshore West Africa: Evidence for global cooling precursor events. *Geology*, 37(8):699–702.

Killops, S. D. and Killops, V. J. (2005). *Introduction to Organic Geochemistry*. Blackwell Publishing Ltd, Oxford.

Kim, J. H., Schouten, S., Hopmans, E. C., Donner, B., and Sinninghe Damsté, J. S. (2008). Global sediment core-top calibration of the TEX_{86} paleothermometer in the ocean. *Geochimica et Cosmochimica Acta*, 72(4):1154–1173.

Kim, J. H., Schouten, S., Rodrigo-Gámiz, M., Rampen, S., Marino, G., Huguet, C., Helmke, P., Buscail, R., Hopmans, E. C., Pross, J., Sangiorgi, F., Middelburg, J. B. M., and Sinninghe Damsté, J. S. (2015). Influence of deep-water derived isoprenoid tetraether lipids on the TEX_{86}^{H} paleothermometer in the Mediterranean Sea. *Geochimica et Cosmochimica Acta*, 150:125–141.

Kim, J. H., van der Meer, J., Schouten, S., Helmke, P., Willmott, V., Sangiorgi, F., Koç, N., Hopmans, E. C., and Sinninghe Damsté, J. S. (2010). New indices and calibrations derived from the distribution of crenarchaeal isoprenoid tetraether lipids: Implications for past sea surface temperature reconstructions. *Geochimica et Cosmochimica Acta*, 74(16):4639–4654.

Kimura, S., Shikazono, N., Kashiwagi, H., and Nohara, M. (2004). Middle Miocene-early Pliocene paleo-oceanic environment of Japan Sea deduced from geochemical features of sedimentary rocks. *Sedimentary Geology*, 164(1):105–129.

Kitamura, A. and Kimoto, K. (2006). History of the inflow of the warm Tsushima Current into the Sea of Japan between 3.5 and 0.8 Ma. *Palaeogeography, Palaeoclimatology, Palaeoecology*, 236:355–366.

Knies, J. and Mann, U. (2002). Depositional environment and source rock potential of Miocene strata from the central Fram Strait: Introduction of a new computing tool for simulating organic facies variations. *Marine and Petroleum Geology*, 19(7):811–828.

Koga, Y., Kyuragi, T., Nishihara, M., and Sone, N. (1998). Did archaeal and bacterial cells arise independently from noncellular precursors? A hypothesis stating that the advent of membrane phospholipid with enantiomeric glycerophosphate backbones caused the separation of the two lines of descent. *Journal of Molecular Evolution*, 46(1):54–63.

Koizumi, I. (1990). Successional changes of middle Miocene diatom assemblages in the northwestern Pacific. *Palaeogeography, Palaeoclimatology, Palaeoecology*, 77(3-4):181–193.

Koizumi, I. (1992a). Biostratigraphy and paleoceanography of the Japan Sea based on diatoms: ODP leg 127. In Tsuchi, R. and Ingle, J. C., editors, *Pacific Neogene: Environment, Evolution and Events*, pages 15–24. University Tokyo Press, Tokyo.

Koizumi, I. (1992b). Diatom biostratigraphy of the Japan Sea: Leg 127. In

Pisciotto, K. A., Ingle, J. C., von Breymann, M. T., and Barron, J., editors, *Proc. ODP Sci. Res 127/128*, pages 249–289.

Kolstad, E. W. and Bracegirdle, T. J. (2008). Marine cold-air outbreaks in the future: An assessment of IPCC AR4 model results for the Northern Hemisphere. *Climate Dynamics*, 30:871–885.

Koopmans, M. P., Köster, J., Van Kaam-Peters, H. M. E., Kenig, F., Schouten, S., Hartgers, W. A., De Leeuw, J. W., and Sinninghe Damsté, J. S. (1996). Diagenetic and catagenetic products of isorenieratene: Molecular indicators for photic zone anoxia. *Geochimica et Cosmochimica Acta*, 60(22):4467–4496.

Krapp, M. and Jungclaus, J. H. (2011). The Middle Miocene climate as modelled in an atmosphere-ocean-biosphere model. *Climate of the Past*, 7(4):1169–1188.

Krissek, L. A. (1995). Late Cenozoic ice-rafting records from Leg 145 sites in the North Pacific: Late Miocene onset, late Pliocene intensification, and Pliocene-Pleistocene events. In Rea, D. K., Basov, L. A., Scholl, D. W., and Allan, J. F., editors, *Proceedings of the Ocean Drilling Program, Scientific Results*, volume 145, pages 179–194. Ocean Drilling Program, College Station, (TX Ocean Drilling Program).

Kürschner, W. M., Kvacek, Z., and Dilcher, D. L. (2008). The impact of Miocene atmospheric carbon dioxide fluctuations on climate and the evo-

lution of terrestrial ecosystems. *Proceedings of the National Academy of Sciences*, 105(2):449–53.

Lacis, A. A., Schmidt, G. A., Rind, D., and Ruedy, R. A. (2010). Atmospheric CO_2: principal control knob governing Earth's temperature. *Science*, 330:356–359.

Lamb, A. L., Wilson, G. P., and Leng, M. J. (2006). A review of coastal palaeoclimate and relative sea-level reconstructions using $\delta^{13}C$ and C/N ratios in organic material. *Earth Science Reviews*, 75:29–57.

LaRiviere, J. P., Ravelo, C., Crimmins, A., Dekens, P. S., Ford, H. L., Lyle, M., and Wara, M. W. (2012). Late Miocene decoupling of oceanic warmth and atmospheric carbon dioxide forcing. *Nature*, 486:97–100.

Larsen, H. C., Saunders, A. D., Clift, P. D., Beget, J., Wei, W., Spezzaferri, S., and ODP Leg 152 Scientific Party (1994). Seven Million Years of Glaciation in Greenland. *Science*, 264:952–955.

Laws, E. A., Popp, B. N., Cassas, N., and Tanimoto, J. (2002). ^{13}C discrimination patterns in oceanic phytoplankton: likely influence of CO_2 concentrating mechanisms, and implications for palaeoreconstructions. *Functional plant biology*, 29:323–333.

Lee, K. E., Bahk, J. J., and Choi, J. (2008). Alkenone temperature estimates

for the East Sea during the last 190,000 years. *Organic Geochemistry*, 39(6):741–753.

Lee, K. E., Bahk, J. J., and Narita, H. (2003). Temporal variations in productivity and planktonic ecological structure in the East Sea (Japan Sea) since the last glaciation. *Geo-Marine Letters*, 23(2):125–129.

Lee, K. E., Khim, B.-K., Otosaka, S., and Noriki, S. (2011). Sediment trap record of alkenones from the East Sea (Japan Sea). *Organic Geochemistry*, 42(3):255–261.

Lee, K. E. and Schneider, R. (2005). Alkenone production in the upper 200m of the Pacific Ocean. *Deep Sea Research Part I: Oceanographic Research Papers*, 52(3):443–456.

Lehmann, M. F., Bernasconi, S. M., Barbieri, A., and McKenzie, J. A. (2002). Preservation of organic matter and alteration of its carbon and nitrogen isotope composition during simulated and in situ early sedimentary diagenesis. *Geochimica et Cosmochimica Acta*, 66(20):3573–3584.

Lepple, F. K. and Brine, C. J. (1976). Organic constituents in eolian dust and surface sediments from northwest Africa. *Journal of Geophysical Research*, 81(6):1141–1147.

Lipp, J. S. and Hinrichs, K. U. (2009). Structural diversity and fate of in-

tact polar lipids in marine sediments. *Geochimica et Cosmochimica Acta*, 73(22):6816–6833.

Lisiecki, L. E. and Raymo, M. E. (2005). A Pliocene-Pleistocene stack of 57 globally distributed benthic δ^{18}O records. *Paleoceanography*, 20.

Liu, J., Liu, W., An, Z., and Yang, H. (2016). Different hydrogen isotope fractionations during lipid formation in higher plants: Implications for paleohydrology reconstruction at a global scale. *Scientific Reports*, 6.

Liu, W. and Huang, Y. (2005). Compound specific D/H ratios and molecular distributions of higher plant leaf waxes as novel paleoenvironmental indicators in the Chinese Loess Plateau. *Organic Geochemistry*, 36(6):851–860.

Liu, X. and Yin, Z. Y. (2002). Sensitivity of the East Asian monsoon climate to the uplift of the Tibetan Plateau. *Palaeogeography, Palaeoclimatology, Palaeoecology*, 183:223–245.

Liu, Z., Pagani, M., Zinniker, D., DeConto, R., Huber, M., Brinkhuis, H., Shah, S. R., Leckie, R. M., and Pearson, A. (2009). Global Cooling During the Eocene-Oligocene Climate Transition. *Science*, 323:1187–1190.

Lunt, D. J., Flecker, R., and Clift, P. D. (2010). The impacts of Tibetan uplift on palaeoclimate proxies. *Geological Society, London, Special Publications*, 342(1):279–291.

Lunt, D. J., Foster, G. L., Haywood, A. M., and Stone, E. J. (2008). Late Pliocene Greenland glaciation controlled by a decline in atmospheric CO_2 levels. *Nature*, 454:1102–1105.

Lüthi, D., Le Floch, M., Bereiter, B., Blunier, T., Barnola, J.-M., Siegenthaler, U., Raynaud, D., Jouzel, J., Fischer, H., Kawamura, K., and Stocker, T. F. (2008). High-resolution carbon dioxide concentration record 650,000-800,000 years before present. *Nature*, 453:379–382.

Ma, Y., Wu, F., Fang, X., Li, J., An, Z., and Wang, W. (2005). Pollen record from red clay sequence in the central Loess Plateau between 8.10 and 2.60 Ma. *Chinese Science Bulletin*, 50(19):2234.

Marino, B., McElroy, M., Salawitch, R., and Spaulding, W. (1992). Glacial-to-interglacial variations in the carbon isotopic composition of atmospheric CO_2. *Nature*, 357:461–466.

Martínez-Botí, M. A., Foster, G. L., Chalk, T. B., Rohling, E. J., Sexton, P. F., Lunt, D. J., Pancost, R. D., Badger, M. P. S., and Schmidt, D. N. (2015). Plio-Pleistocene climate sensitivity evaluated using high-resolution CO_2 records. *Nature*, 518:49–54.

Massana, R., Murray, E., Preston, C. M., and DeLong, E. F. (1997). Vertical distribution and phylogenetic characterization of marine planktonic Archaea in the Santa Barbara Channel. *Applied and Environmental Microbiology*, 63(1):50–56.

Masson-Delmotte, V., Schulz, M., Abe-Ouchi, A., Beer, J., Ganopolski, A., González Rouco, J. F., Jansen, E., Lambeck, K., Luterbacher, J., Naish, T., Osborn, T., Otto-Bliesner, B., Quinn, T., Ramesh, R., Shao, X., and Timmermann, A. (2013). Information from Paleoclimate Archives. In Stocker, F., Qin, D., Plattner, G.-K., Tignor, M., Allen, S. K., Boschung, J., Nauels, A., Xia, Y., Bex, V., and Midgley, P., editors, *Climate Change 2013: The Physical Science Basis. Contribution of Working Group I to the Fifth Assessment Report of the Intergovernmental Panel on Climate Change*, chapter 5, pages 383–464. Cambridge University Press, Cambridge, United Kingdom and New York, NY, USA.

Masuzawa, T., Takada, J., and Matsushita, R. (1992). 41. Trace element geochemistry of sediments and sulfur isotope geochemistry from framboidal pyrite from Site 795, Leg 127, Japan Sea. In Pisciotto, K. A., Ingle, J. C., von Breymann, M. T., and Barron, J., editors, *Proceedings of the Ocean Drilling Program, Scientific Results, Vol. 127/128*, chapter 41, pages 705–717.

McKay, D. I., Tyrrell, T., Wilson, P. A., and Foster, G. L. (2014). Estimating the impact of the cryptic degassing of Large Igneous Provinces: A mid-Miocene case-study. *Earth and Planetary Science Letters*, 403:254–262.

Meyers, P. A. (1997). Organic geochemical proxies of paleoceanographic,

plaeolimnologic, and plaeoclimatic processes. *Organic Geochemistry*, 27(5):213–250.

Micheels, A., Bruch, A. A., Eronen, J., Fortelius, M., Harzhauser, M., Utescher, T., and Mosbrugger, V. (2011). Analysis of heat transport mechanisms from a Late Miocene model experiment with a fully-coupled atmosphere-ocean general circulation model. *Palaeogeography Palaeoclimatology Palaeoecology*, 304:337–350.

Miller, K. G., Kominz, M. A., Browning, J. V., Wright, J. D., Mountain, G. S., Katz, M. E., Sugarman, P. J., Cramer, B. S., Christie-Blick, N., and Pekar, S. F. (2005). The Phanerozoic record of global sea-level change. *Science*, 310:1293–1298.

Moldowan, J. M., Seifert, W. K., Arnold, E., and Clardy, J. (1984). Structure proof and significance of stereoisomeric 28,30-bisnorhopanes in petroleum and petroleum source rocks. *Geochimica et Cosmochimica Acta*, 48(8):1651–1661.

Mollenhauer, G., Basse, A., Kim, J.-h., Sinninghe, J. S., and Fischer, G. (2015). A four-year record of $U_{37}^{K'}$- and TEX_{86}-derived sea surface temperature estimates from sinking particles in the filamentous upwelling region off Cape Blanc, Mauritania. *Deep-Sea Research Part I: Oceanographic Research Papers*, 97:67–79.

Moossen, H., Abell, R., Quillmann, U., and Bendle, J. (2013). Holocene

changes in marine productivity and terrestrial organic carbon inputs into an Icelandic fjord: Application of molecular and bulk organic proxies. *The Holocene*, 23(12):1699–1710.

Moossen, H., Bendle, J., Seki, O., Quillmann, U., and Kawamura, K. (2015). North Atlantic Holocene climate evolution recorded by high-resolution terrestrial and marine biomarker records. *Quaternary Science Reviews*, 129:111–127.

Mügler, I., Gleixner, G., Günther, F., Mäusbacher, R., Daut, G., Schütt, B., Berking, J., Schwalb, A., Schwark, L., Xu, B., Yao, T., Zhu, L., and Yi, C. (2010). A multi-proxy approach to reconstruct hydrological changes and Holocene climate development of Nam Co, Central Tibet. *Journal of Paleolimnology*, 43(4):625–648.

Mügler, I., Sachse, D., Werner, M., Xu, B., Wu, G., Yao, T., and Gleixner, G. (2008). Effect of lake evaporation on δD values of lacustrine *n*-alkanes: A comparison of Nam Co (Tibetan Plateau) and Holzmaar (Germany). *Organic Geochemistry*, 39(6):711–729.

Müller, P. J., Kirst, G., Ruhland, G., von Storch, I., and Rosell-Mele, A. (1998). Calibration of the alkenone paleotemperature index $U^{K'}_{37}$ based on core-tops from the eastern South Atlantic and the global ocean (60°N-60°S). *Geochimica et Cosmochimica Acta*, 62(10):1757–1772.

Müller, P. J. and Suess, E. (1979). Productivity, sedimentation rate, and sedi-

mentary organic matter in the oceans-I. Organic carbon preservation. *Deep Sea Research Part A*, 26(12):1347–1362.

Myhre, G., Shindell, D., Breon, F.-M., Collins, W., Fuglestvedt, J., Huang, J., Koch, D., Lamarque, J. F., Lee, D., Mendoza, B., Nakajima, T., Robock, A., Stephens, G., Takemura, T., and Zhang, H. (2013). Anthropogenic and Natural Radiative Forcing. In Stocker, F., Qin, D., Plattner, G.-K., Tignor, M., Allen, S. K., Boschung, J., Nauels, A., Xia, Y., Bex, V., and Midgley, P., editors, *Climate Change 2013: The Physical Science Basis. Contribution of Working Group I to the Fifth Assessment Report of the Intergovernmental Panel on Climate Change*, chapter 8, pages 659–740. Cambridge University Press, Cambridge, United Kingdom and New York, NY, USA.

Nagashima, K., Tada, R., Matsui, H., Irino, T., Tani, A., and Toyoda, S. (2007a). Orbital- and millennial-scale variations in Asian dust transport path to the Japan Sea: Quaternary Paleoceanography of the Japan Sea and its linkage with Asian Monsoon. *Palaeogeography, Palaeoclimatology, Palaeoecology*, 247:161.

Nagashima, K., Tada, R., Tani, A., Sun, Y., Isozaki, Y., Toyoda, S., and Hasegawa, H. (2011). Millennial-scale oscillations of the westerly jet path during the last glacial period. *Journal of Asian Earth Sciences*, 40(6):1214–1220.

Nagashima, K., Tada, R., Tani, A., Toyoda, S., Sun, Y., and Isozaki, Y.

(2007b). Contribution of aeolian dust in Japan Sea sediments estimated from ESR signal intensity and crystallinity of quartz. *Geochemistry, Geophysics, Geosystems*, 8(2).

Nakada, S., Isoda, Y., and Uchiyama, I. (2005). Seasonal variations of water properties and the baroclinic flow pattern in Toyama Bay under the influence of the Tsushima Warm Current. *Journal of Oceanography*, 61(5):943–952.

Nytoft, H. P. and Larsen, B. (2001). Triterpenoids and other organic compounds as markers of depositional conditions in the Baltic Sea deep basins during the Holocene. *Baltica*, 14(1):95–107.

Oba, T. (1991). Paleoenvironmental changes in the Japan Sea during the last 85 000 years. *Paleoceanography*, 6(4):499–518.

O'Brien, C. L., Foster, G. L., Martínez-Botí, M., Abell, R., Rae, J. W. B., and Pancost, R. D. (2014). High sea surface temperatures in tropical warm pools during the Pliocene. *Nature Geoscience*, 7(8):606–611.

Ogasawara, K. (1994). Neogene paleogeography and marine climate of the Japanese Islands based on shallow-marine molluscs. *Palaeogeography, Palaeoclimatology, Palaeoecology*, 108:335–351.

Ohkouchi, N., Kawamura, K., Kawahata, H., and Okada, H. (1999). Depth range of alkenone production in the central Pacific Ocean. *Global Biochemical Cycles*, 13(2):695–704.

Ohkushi, K., Itaki, T., and Nemoto, N. (2003). Last Glacial-Holocene change in intermediate water ventilation in the Northwestern Pacific. *Quarternary Science Reviews*, 22:1477–1484.

Otofuji, Y. and Matsuda, T. (1983). Paleomagnetic evidence for the clockwise rotation of Southwest Japan. *Earth and Planetary Science Letters*, 62(3):349–359.

Otofuji, Y., Matsuda, T., and Nohda, S. (1985). Paleomagnetic evidences for the Miocene counter clockwise rotation of northeast Japan - rifting process of the Japan arc. *Earth and Planetary Science Letters*, 75:265–277.

Otosaka, S., Tanaka, T., Togawa, O., Amano, H., Karasev, E. V., Minakawa, M., and Noriki, S. (2008). Deep sea circulation of particulate organic carbon in the Japan Sea. *Journal of Oceanography*, 64(6):911–923.

Otosaka, S., Togawa, O., Baba, M., Karasev, E., Volkov, Y. N., Omata, N., and Noriki, S. (2004). Lithogenic flux in the Japan Sea measured with sediment traps. *Marine Chemistry*, 91(1):143–163.

Ourisson, G. and Albrecht, P. (1992). Hopanoids. 1. Geohopanoids: the most abundant natural products on Earth? *Accounts of Chemical Research*, 25(3):398–402.

Ourisson, G., Albrecht, P., and Rohmer, M. (1979). The hopanoids: palaeo-

chemistry and biochemistry of a group of natural products. *Pure and Applied Chemistry*, 51(4):709–729.

Pagani, M. (2014). Biomarker-Based Inferences of Past Climate: The Alkenone pCO_2 Proxy. In Holland, H. and Turekian, K., editors, *Teatrise on Organic Geochemistry*, chapter 12.13, pages 361–378. Elsevier, Amsterdam, 2 edition.

Pagani, M., Arthur, M. A., and Freeman, K. H. (1999a). Miocene evolution of atmospheric carbon dioxide. *Paleoceanography*, 14(3):273–292.

Pagani, M., Freeman, K. H., and Arthur, M. A. (1999b). Late Miocene Atmospheric CO_2 Concentrations and the Expansion of C_4 Grasses. *Science*, 285(5429):867–879.

Pagani, M., Huber, M., Liu, Z., Bohaty, S. M., Henderiks, J., Sijp, W., Krishnan, S., and DeConto, R. M. (2011). The Role of Carbon Dioxide During the Onset of Antarctic Glaciation. *Science*, 334:1261–1265.

Pagani, M., Liu, Z., LaRiviere, J., and Ravelo, A. C. (2010). High Earth-system climate sensitivity determined from Pliocene carbon dioxide concentrations. *Nature Geoscience*, 3(1):27–30.

PALAEOSENS (2012). Making sense of palaeoclimate sensitivity. *Nature*, 491:683–691.

Passey, B. H., Ayliffe, L. K., Kaakinen, A., Zhang, Z., Eronen, J. T., Zhu, Y., Zhou, L., Cerling, T. E., and Fortelius, M. (2009). Strengthened East Asian summer monsoons during a period of high-latitude warmth? Isotopic evidence from Mio-Pliocene fossil mammals and soil carbonates from northern China. *Earth and Planetary Science Letters*, 277:443–452.

Patz, J. A., Campbell-Lendrum, D., Holloway, T., and Foley, J. A. (2005). Impact of regional climate change on human health. *Nature*, 438:310–317.

Peng, T., Li, J., Song, C., Guo, B., Liu, J., Zhao, Z., and Zhang, J. (2016). An integrated biomarker perspective on Neogene-Quaternary climatic evolution in NE Tibetan Plateau: Implications for the Asian aridification. *Quaternary International*, 399:174–182.

Peters, K. E., Walters Clifford C, and Moldowan, J. M. (2005). *The Biomarker Guide, biomarkers and Isotopes in Petroleum Exploration and Earth Histroy, Volume 2*. Cambridge University Press New York, Cambridge, 2 edition.

Peterse, F., Kim, J.-H., Schouten, S., Klitgaard, D., Koç, N., and Sinninghe, J. S. (2009). Organic Geochemistry Constraints on the application of the MBT/CBT palaeothermometer at high latitude environments (Svalbard, Norway). *Organic Geochemistry*, 40(6):692–699.

Peterse, F., van der Meer, J., Schouten, S., Weijers, J. W. H., Fierer, N., Jackson, R. B., Kim, J.-H., and Sinninghe Damsté, J. S. (2012). Revised

calibration of the MBT-CBT paleotemperature proxy based on branched tetraether membrane lipids in surface soils. *Geochimica et Cosmochimica Acta*, 96:215–229.

Petley, D. N. (2010). On the impact of climate change and population growth on the occurrence of fatal landslides in South, East and SE Asia. *Quarterly Journal of Engineering Geology and Hydrogeology*, 43(4):487–496.

Popp, B., Takigiku, R., Hayes, J. M., Louda, J. W., and Baker, E. A. (1989). The post-paleozoic chronology and mechanism of ^{13}C depletion in primary marine organic matter. *American Journal of Science*, 289:436–454.

Popp, B. N., Laws, E. a., Bidigare, R. R., Dore, J. E., Hanson, K. L., and Wakeham, S. G. (1998). Effect of phytoplankton cell geometry on carbon isotopic fractionation. *Geochimica et Cosmochimica Acta*, 62(1):69–77.

Pound, M. J., Haywood, A. M., Salzmann, U., Riding, J. B., Lunt, D. J., and Hunter, S. J. (2011). A Tortonian (Late Miocene, 11.61-7.25 Ma) global vegetation reconstruction. *Palaeogeography, Palaeoclimatology, Palaeoecology*, 300:29–45.

Prahl, F. G., Hayes, J. M., and Xie, T. M. (1992). Diploptene: An indicator of terrigenous organic carbon in coastal sediments. *Limnology and Oceanography*, 37(6):1290–1300.

Prahl, F. G., Muehlhausen, L. A., and Zahnke, D. L. (1988). Further evalua-

tion of long-chain alkenones as indicators of paleoceanographic conditions. *Geochimica et Cosmochimica Acta*, 52:2303–2310.

Prahl, F. G. and Wakeham, S. G. (1987). Calibration of unsaturation patterns in long chain ketone compositions for paleotemperature assesments. *Nature*, 330:367–369.

Qin, W., Carlson, L. T., Armbrust, E. V., Devol, A. H., Moffett, J. W., Stahl, D. A., and Ingalls, A. E. (2015). Confounding effects of oxygen and temperature on the TEX_{86} signature of marine Thaumarchaeota. *Proceedings of the National Academy of Sciences*, 112(35):10979–10984.

Quade, J. and Cerling, T. E. (1995). Expansion of C_4 grasses in the Late Miocene of Northern Pakistan - evidence from stable isotopes in paleosols. *Palaeogeography Palaeoclimatology Palaeoecology*, 115:91–116.

Ransom, B., Kim, D., Kastner, M., and Wainwright, S. (1998). Organic matter preservation on continental slopes: importance of mineralogy and surface area. *Geochimica et Cosmochimica Acta*, 62(8):1329–1345.

Rau, T., Takahashi, K., Des Marais, D. J., and Martin, J. H. (1992). The relationship between $\delta^{13}C$ of organic matter and $[CO_{2(aq)}]$ in ocean surface water: Data from a JGOFS site in the northeast Atlantic Ocean and a model. *Geochimica et Cosmochimica Acta*, 56:1413–1419.

Raven, J. A., Johnston, A. M., and Turpin, D. H. (1993). Influence of changes

in CO_2 concentration and temperature on marine phytoplankton $^{13}C/^{12}C$ ratios: an analysis of possible mechanisms. *Global and Planetary Change*, 8.

Rea, D. K. (1994). The paleoclimatic record provided by eolian deposition in the deep sea: The geologic history of wind. *Reviews of Geophysics*, 32(2):159–195.

Rea, D. K., Snoeckx, I., and Joseph, L. H. (1998). Late Cenozoic Eolian deposition in the North Pacific: Asian drying, Tibetan uplift, and cooling of the northern hemisphere. *Paleoceanography*, 13(3):215–224.

Reghellin, D., Coxall, H. K., Dickens, G. R., and Backman, J. (2015). Carbon and oxygen isotopes of bulk carbonate in sediment deposited beneath the eastern equatorial Pacific over the last 8 million years. *Paleoceanography*, 30(10):1261–1286.

Reinert, D. J., Balliano, G., and Schulz, G. E. (2004). Conversion of Squalene to the Pentacarbocyclic Hopene. *Chemistry and Biology*, 11(1):121–126.

Rhein, M., Rintoul, S., Aoki, S., Campos, E., Chambers, D., Feely, R., Gulev, S., Johnson, G. C., Josey, S. A., Kostianoy, A., Mauritzen, C., Roemmich, D., Talley, L., and Wang, F. (2013). Observations: Oceans. In Stocker, F., Qin, D., Plattner, G.-K., Tignor, M., Allen, S. K., Boschung, J., Nauels, A., Xia, Y., Bex, V., and Midgley, P., editors, *Climate Change 2013: The Physical Science Basis. Contribution of Working Group I to the Fifth Assessment*

Report of the Intergovernmental Panel on Climate Change, chapter 3, pages 255–315. Cambridge University Press, Cambridge, United Kingdom and New York, NY, USA.

Riebesell, U., Revill, A. T., Holdsworth, D. G., and Volkman, J. K. (2000). The effects of varying CO_2 concentration on lipid composition and carbon isotope fractionation in *Emiliania huxleyi*. *Geochimica et Cosmochimica Acta*, 64(24):4179–4192.

Robinson, M. M., Dowsett, H. J., and Chandler, M. A. (2008). Pliocene role in assessing future climate impacts. *Eos*, 89(49):501–502.

Rohling, E. J., Medina-Elizalde, M., Shepherd, J. G., Siddall, M., and Stanford, J. D. (2012). Sea surface and high-latitude temperature sensitivity to radiative forcing of climate over several glacial cycles. *Journal of Climate*, 25(5):1635–1656.

Rohmer, M., Bouvier-Nave, P., and Ourisson, G. (1984). Distribution of hopanoid triterpenes in prokaryotes. *Microbiology*, 130(5):1137–1150.

Rommerskirchen, F., Eglinton, G., Dupont, L., Güntner, U., Wenzel, C., and Rullkötter, J. (2003). A north to south transect of Holocene southeast Atlantic continental margin sediments: Relationship between aerosol transport and compound-specific δ^{13}C land plant biomarker and pollen records. *Geochemistry, Geophysics, Geosystems*, 4(12).

Rommerskirchen, F., Plader, A., Eglinton, G., Chikaraishi, Y., and Rullkötter, J. (2006). Chemotaxonomic significance of distribution and stable carbon isotopic composition of long-chain alkanes and alkan-1-ols in C_4 grass waxes. *Organic Geochemistry*, 37(10):1303–1332.

Rost, B., Zondervan, I., and Riebesell, U. (2002). Light-dependent carbon isotope fractionation in the coccolithophorid *Emiliania huxleyi*. *Limnology and Oceanography*, 47(1):120–128.

Rueda, G., Rosell-Melé, A., Escala, M., Gyllencreutz, R., and Backman, J. (2009). Comparison of instrumental and GDGT-based estimates of sea surface and air temperatures from the Skagerrak. *Organic Geochemistry*, 40(2):287–291.

Sachse, D., Billault, I., Bowen, G. J., Chikaraishi, Y., Dawson, T. E., Feakins, S. J., Freeman, K. H., Magill, C. R., McInerney, F., van der Meer, M. T. J., Polissar, P., Robins, R. J., Sachs, J. P., Schmidt, H.-L., Sessions, A. L., White, J. W., West, J. B., and Kahmen, A. (2012). Molecular paleohydrology: interpreting the hydrogen-isotopic composition of lipid biomarkers from photosynthesizing organisms. *Annual Review of Earth and Planetary Sciences*, 40:221–249.

Sachse, D., Radke, J., and Gleixner, G. (2006). δD values of individual *n*-alkanes from terrestrial plants along a climatic gradient - Implications for the sedimentary biomarker record. *Organic Geochemistry*, 37(4):469–483.

Sage, R. F. (2004). The evolution of C_4 photosynthesis. *New Phytologist*, 161(2):341–370.

Sampe, T. and Xie, S. P. (2010). Large-scale dynamics of the Meiyu-Baiu rainband: Environmental forcing by the westerly jet. *Journal of Climate*, 23(1):113–134.

Schefuß, E., Ratmeyer, V., Stuut, J.-B. W., Jansen, J. H. F., and Sinninghe Damsté, J. S. (2003). Carbon isotope analyses of *n*-alkanes in dust from the lower atmosphere over the central eastern Atlantic. *Geochimica et Cosmochimica Acta*, 67(10):1757–1767.

Schiemann, R., Lüthi, D., and Schär, C. (2009). Seasonality and interannual variability of the westerly jet in the Tibetan Plateau region. *Journal of Climate*, 22:2940–2957.

Schneider, R., Schmitt, J., Köhler, P., Joos, F., and Fischer, H. (2013). A high resolution record of atmospheric carbon dioxide and its stable carbon isotopic composition from the penultimate glacial maximum to the glacial inception. *Climate of the Past Discussions*, 9(2):2015–2057.

Schouten, S., Hopmans, E. C., Schefuß, E., and Sinninghe Damsté, J. S. (2002). Distributional veriations in marine crenarchaeol membrane lipids: a new tool for reconstructing ancient sea water temperatures? *Earth and Planetary Science Letters*, 204:265–274.

Schouten, S., Hopmans, E. C., and Sinninghe Damsté, J. S. (2004). The effect of maturity and depositional redox conditions on archaeal tetraether lipid palaeothermometry. *Organic Geochemistry*, 35(5):567–571.

Schouten, S., Hopmans, E. C., and Sinninghe Damsté, J. S. (2013). The organic geochemistry of glycerol dialkyl glycerol tetraether lipids: A review. *Organic Geochemistry*, 54:19–61.

Schouten, S., Huguet, C., Hopmans, E. C., Kienhuis, M. V. M., and Sinninghe Damsté, J. S. (2007). Analytical methodology for TEX_{86} paleothermometry by high-performance liquid chromatography/atmospheric pressure chemical ionization-mass spectrometry. *Analytical Chemistry*, 79(7):2940–2944.

Schouten, S., Ossebaar, J., Schreiber, K., Kienhuis, M. V. M., Langer, G., Benthien, A., and Bijma, J. (2006). The effect of temperature, salinity and growth rate on the stable hydrogen isotopic composition of long chain alkenones produced by *Emiliania huxleyi* and *Gephryocapsa oceanica*. *Biogeosciences*, 3(1):113–119.

Schouten, S., Pitcher, A., Hopmans, E. C., Villanueva, L., van Bleijswijk, J., and Sinninghe Damsté, J. S. (2012). Intact polar and core glycerol dibiphytanyl glycerol tetraether lipids in the Arabian Sea oxygen minimum zone: I. Selective preservation and degradation in the water column and consequences for the TEX_{86}. *Geochimica and Cosmochimica Acta*, pages 228–243.

Schubert, B. A. and Jahren, A. H. (2012). The effect of atmospheric CO_2 concentration on carbon isotope fractionation in C_3 land plants. *Geochimica et Cosmochimica Acta*, 96:29–43.

Schubert, B. A. and Jahren, A. H. (2015). Global increase in plant carbon isotope fractionation following the Last Glacial Maximum caused by increase in atmospheric pCO_2. *Geology*, 43(5):435–438.

Schulte, S., Benthien, A., Andersen, N., Müller, P., Rühlemann, C., and Schneider, R. (2003). Stable Carbon Isotopic Composition of the $C_{37:2}$ Alkenone: A Proxy for $CO_{2(aq)}$ Concentration in Oceanic Surface Waters? In Wefer, G., Mulitza, S., and Ratmeyer, V., editors, *The South Atlantic in the Late Quaternary: Reconstruction of Material Budgets and Current Systems*, chapter 10, pages 195–211. Springer Berlin Heidelberg, Heidelberg.

Seifert, W. K. and Moldowan, J. M. (1980). The effect of thermal stress on source rock quality as measured by hopane stereochemistry. *Physics and Chemistry of The Earth*, 12:229–237.

Seki, O., Foster, G. L., Schmidt, D. N., Mackensen, A., Kawamura, K., and Pancost, R. D. (2010). Alkenone and boron-based Pliocene pCO_2 records. *Earth and Planetary Science Letters*, 292(1):201–211.

Seki, O., Schmidt, D. N., Schouten, S., Hopmans, E. C., Sinninghe Damsté, J. S., and Pancost, R. D. (2012). Paleoceanographic changes in the Eastern Equatorial Pacific over the last 10 Myr. *Paleoceanography*, 27(3).

Sessions, A., Zhang, L., Welander, P., Doughty, D., Summons, R., and Newman, D. (2013). Identification and quantification of polyfunctionalized hopanoids by high temperature gas chromatography-mass spectrometry. *Organic Geochemistry*, 56:120–130.

Shackleton, J. and Opdyke, N. D. (1973). Oxygen isotope and paleomagnetic stratigraphy of equatorial core V28-238: oxygen isotope temperature and ice volumes on a 10^5 and 10^6 year scale. *Quaternary Research*, 3:39–55.

Shackleton, N. J. and Kennett, J. P. (1976). Paleotemperature history of the Cenozoic and the initiation of Antarctic glaciation; Oxygen and carbon isotope analyses in DSDP sites 277, 279 and 281. Technical report, Joint Oceanographic Institutions for Deep Earth Sampling (JOIDES).

Siedenburg, G. and Jendrossek, D. (2011). Squalene-hopene cyclases. *Applied and Environmental Microbiology*, 77(12):3905–3915.

Sikes, E. L., O'Leary, T., Nodder, S. D., and Volkman, J. K. (2005). Alkenone temperature records and biomarker flux at the subtropical front on the Chatham Rise, SW Pacific Ocean. *Deep-Sea Research Part I: Oceanographic Research Papers*, 52(5):721–748.

Sikes, E. L., Volkman, J. K., Robertson, L. G., and Pichon, J.-J. (1997). Alkenones and alkenes in surface waters and sediments of the Southern Ocean: Implications for paleotemperature estimation in polar regions. *Geochimica et Cosmochimica Acta*, 61(7):1495–1505.

Simoneit, B. R. T. (1977). Concepts in Marine Organic Chemistry: Organic matter in eolian dusts over the Atlantic Ocean. *Marine Chemistry*, 5(4):443–464.

Sinninghe Damsté, J. S., Eglinton, T. I., De Leeuw, J. W., and Schenck, P. A. (1989). Organic sulfur in macromolecular sedimentary organic matter: I. Structure and origin of sulfur-containing moieties in kerogen, asphaltenes, and coal as revealed by flash pyrolysis. *Geochimica et Cosmochimica Acta*, 53(4):873–889.

Sinninghe Damsté, J. S., Kuypers, M. M., Schouten, S., Schulte, S., and Rullkötter, J. (2003). The lycopane/C_{31} *n*-alkane ratio as a proxy to assess palaeoxicity during sediment deposition. *Earth and Planetary Science Letters*, 209(1-2):215–226.

Sinninghe Damsté, J. S., Rijpstra, W. I. C., and Reichart, G.-J. (2002). The influcence of oxic degradation on the sedimentary biomarker record II. Evidence from Arabian Sea sediments. *Geochimica et Cosmochimica Acta*, 66(15):2737–2754.

Sinninghe Damsté, J. S. and Schouten, S. (1997). Is there evidence for a substantial contribution of prokaryotic biomass to organic carbon in Phanerozoic carbonaceous sediments? *Organic Geochemistry*, 26:517–530.

Sinninghe Damsté, J. S., Schouten, S., and Volkman, J. K. (2014). C_{27}-C_{30} neohop-13(18)-enes and their saturated and aromatic derivatives in sedi-

ments: Indicators for diagenesis and water column stratification. *Geochimica et Cosmochimica Acta*, 133:402–421.

Smith, F. A. and Freeman, K. H. (2006). Influence of physiology and climate on δD of leaf wax *n*-alkanes from C_3 and C_4 grasses. *Geochimica et Cosmochimica Acta*, 70(5):1172–1187.

Solomon, S. (2007). *Climate Change 2007–The Physical Science Basis: Working Group I contribution to the fourth assessment report of the IPCC*, volume 4. Cambridge University Press, Cambridge.

Stax, R. (1993). *Zyklische Sedimentation von organischem Kohlenstoff in der Japan See: Anzeiger fuer Anderungen von Paleozeanographie und Paleoklima im Spaatkanozoikum*. PhD thesis, Universität Bremen.

Stax, R. and Stein, R. (1994). Quaternary organic carbon cycles in the Japan Sea (ODP-site 798) and their paleoceanographic implications. *Palaeogeography, Palaeoclimatology, Palaeoecology*, 108:509–521.

Still, C. J., Berry, J. A., Collatz, G. J., and DeFries, R. S. (2003). Global distribution of C_3 and C_4 vegetation: Carbon cycle implications. *Global Biogeochemical Cycles*, 17(1).

Stocker, T. F. (2013). *The physical science basis. Contribution of working group I to the fifth assessment report of the intergovernmental panel on climate change*. Cambridge University Press, Cambridge.

Suarez, M. B., Passey, B. H., and Kaakinen, A. (2011). Paleosol carbonate multiple isotopologue signature of active East Asian summer monsoons during the late Miocene and Pliocene. *Geology*, 39(12):1151–1154.

Summons, R. E., Bradley, A. S., Jahnke, L. L., and Waldbauer, J. R. (2006). Steroids, triterpenoids and molecular oxygen. *Philosophical Transactions of the Royal Society B*, 361:951–968.

Summons, R. E., Jahnke, L. L., Hope, J. M., and Logan, G. A. (1999). 2-Methylhopanoids as biomarkers for cyanobacterial oxygenic photosynthesis. *Nature*, 400:554–557.

Sun, B., Liu, W., Sun, Y., and An, Z. (2015). The precipitation threshold value on C_4/C_3 abundance of the Loess Plateau, China. *Science Bulletin*, 60(7):718–725.

Sun, D., Su, R., Bloemendal, J., and Lu, H. (2008). Grain-size and accumulation rate records from Late Cenozoic aeolian sequences in northern China: Implications for variations in the East Asian winter monsoon and westerly atmospheric circulation. *Palaeogeography, Palaeoclimatology, Palaeoecology*, 264:39–53.

Sun, D. H., Shaw, J., An, Z. S., Cheng, M. Y., and Yue, L. P. (1998). Magnetostratigraphy and paleoclimate interpretation of a continuous 7.2 Ma Late Cenozoic eolian sediments from the Chinese Loess Plateau. *Geophysical Research Letters*, 25(1):85–88.

Tada, R. (1994). Paleoceanographic evolution of the Japan Sea. *Palaeogeography, Palaeoclimatology, Palaeoecology*, 108:487–508.

Tada, R. (2004). *Onset and Evolution of Millennial-Scale Variability in the Asian Monsoon and Its Impact on Paleoceanography of the Japan Sea*, pages 283–298. American Geophysical Union, Washington D.C.

Tada, R., Irino, T., and Koizumi, I. (1999). Land-ocean linkages over orbital and millennial timescales recorded in late Quaternary sediments of the Japan Sea. *Paleoceanography*, 14(2):236–247.

Tada, R., Murray, R., Alvarez Zarikian, C., Anderson, W. J., Bassetti, M.-A., Brace, B., Clemens, S., da Costa Gurgel, M., Dickens, G., Dunlea, A., Gallagher, S., Giosan, L., Henderson, A., Holbourn, A., Ikehara, K., Irino, T., Itaki, T., Karasuda, A., Kinsley, C., Kubota, Y., Lee, G., Lee, K., Lofi, J., Lopes, C., Peterson, L., Saavedra-Pellitero, M., Sagawa, T., Singh, R., Sugisaki, S., Toucanne, S., Wan, S., Xuan, C., Zheng, H., and Ziegler, M. (2015). Site U1425. In Tada, R., Murray, R., and Alvarez Zarikian, C., editors, *Proceedings of IODP Expedition 346*. College Station, TX (Integrated Ocean Drilling Program).

Tada, R., Murray, R. W., and Zarikian, C. A. A. (2013). Asian Monsoon: onset and evolution of millennial-scale variability of Asian Monsoon and its possible relation with the Himalaya and Tibetan plateau uplift. *IODP Scientific Prospectus*, 346.

Tada, R., Zheng, H., and Clift, P. D. (2016). Evolution and variability of Asian monsoon and its potential linkage with the Himalayas-Tibetan Plateau uplift. *Progress in Earth and Planetary Science*, 3.

Talley, L. D., Lobanov, V., Ponomarev, V., Salyuk, A., Tishchenko, P., Zhabin, I., and Riser, S. (2003). Deep convection and brine rejection in the Japan Sea. *Geophysical Research Letters*, 30(4):1159.

Talley, L. D., Min, D. H., Lobanov, V. B., Luchin, V. A., Ponomarev, V. I., Salyuk, A. N., Shcherbina, A. Y., Tishchenko, P. Y., and Zhabin, I. (2006). Japan/East Sea water masses and their relation to the sea's circulation. *Oceanography*, 19(3):32–49.

Talley, L. D., Tishchenko, P., Luchin, V., Nedashkovskiy, A., Sagalaev, S., Kang, D. J., Warner, M., and Min, D. H. (2004). Atlas of Japan (East) Sea hydrographic properties in summer, 1999. *Progress in Oceanography*, 61:277–348.

Tamaki, K., Suyehiro, K., Allan, J., and McWilliams, M. (1992). *Proceedings ODP, Scientific Results*, volume 127/128. College Station, (TX Ocean Drilling Program), College Station.

Taylor, K. W. R., Huber, M., Hollis, C. J., Hernandez-Sanchez, M. T., and Pancost, R. D. (2013). Re-evaluating modern and Palaeogene GDGT distributions: Implications for SST reconstructions. *Global and Planetary Change*, 108:158–174.

Tegelaar, E., de Leeuw, J., Derenne, S., and Largeau, C. (1989). A reappraisal of kerogen formation. *Geochimica et Cosmochimica Acta*, 53(11):3103–3106.

Thiel, V., Blumenberg, M., Pape, T., Seifert, R., and Michaelis, W. (2003). Unexpected occurrence of hopanoids at gas seeps in the Black Sea. *Organic Geochemistry*, 34(1):81–87.

Thierstein, H. (2004). *Coccolithophores from molecular processes to global impact*. Springer, Berlin, Heidelberg.

Thomas, E. K., Huang, Y., Clemens, S. C., Colman, S. M., Morrill, C., Wegener, P., and Zhao, J. (2016). Changes in dominant moisture sources and the consequences for hydroclimate on the northeastern Tibetan Plateau during the past 32 kyr. *Quaternary Science Reviews*, 131:157–167.

Tierney, J. E. (2014). Biomarker-Based Inferences of Past Climate: The TEX_{86} Paleotemperature Proxy. In Holland, H. D. and Turekian, K. K., editors, *Treatise on Geochemistry (Second Edition)*, chapter 12.14, pages 379–393. Elsevier, Amsterdam, 2 edition.

Tierney, J. E. and Tingley, M. P. (2014). A Bayesian, spatially-varying calibration model for the TEX_{86} proxy. *Geochimica et Cosmochimica Acta*, 127:83–106.

Tipple, B. J., Meyers, S. R., and Pagani, M. (2010). Carbon isotope ratio of

Cenozoic CO_2: A comparative evaluation of available geochemical proxies. *Paleoceanography*, 25(3).

Tipple, B. J. and Pagani, M. (2013). Environmental control on eastern broadleaf forest species' leaf wax distributions and D/H ratios. *Geochimica et Cosmochimica Acta*, 111:64–77.

Turich, C., Schouten, S., Thunell, R. C., Varela, R., Astor, Y., and Wakeham, S. G. (2013). Comparison of TEX_{86} and $U^{K'}_{37}$ temperature proxies in sinking particles in the Cariaco Basin. *Deep-Sea Research Part I: Oceanographic Research Papers*, 78:1–19.

Uda, I., Sugai, A., Itoh, Y. H., and Itoh, T. (2001). Variation in Molecular Species of Polar Lipids from Thermoplasma acidophilum Depends on Growth Temperature. *Lipids*, 36(1):103–105.

Uno, K. T., Polissar, P. J., Jackson, K. E., and DeMenocal, P. B. (2016). Neogene biomarker record of vegetation change in eastern Africa. *Proceedings of the National Academy of Sciences*, 113(23):6355–6363.

Utescher, T., Bruch, A., and Micheels, A. (2011). Cenozoic climate gradients in Eurasia - a palaeo-perspective on future climate change? *Palaeogeography,*, 304:351–358.

Uye, S. (2008). Blooms of the giant jellyfish *Nemopilema nomurai*: a threat

to the fisheries sustainability of the East Asian Marginal Seas. *Plankton and Benthos Research*, 3:125–131.

van der Meer, M. T. J., Benthien, A., Bijma, J., Schouten, S., and Sinninghe Damsté, J. S. (2013). Alkenone distribution impacts the hydrogen isotopic composition of the $C_{37:2}$ and $C_{37:3}$ alkan-2-ones in *Emiliania huxleyi*. *Geochimica et Cosmochimica Acta*, 111:162–166.

van der Meer, M. T. J., Benthien, A., French, K. L., Epping, E., Zondervan, I., Reichart, G.-J., Bijma, J., Damsté, J. S. S., and Schouten, S. (2015). Large effect of irradiance on hydrogen isotope fractionation of alkenones in *Emiliania huxleyi*. *Geochimica et Cosmochimica Acta*, 160:16–24.

van der Meer, M. T. J., Sangiorgi, F., Baas, M., Brinkhuis, H., Sinninghe Damsté, J. S., and Schouten, S. (2008). Molecular isotopic and dinoflagellate evidence for Late Holocene freshening of the Black Sea. *Earth and Planetary Science Letters*, 267:426–434.

Venkatesan, M. I. (1988). Diploptene in Antarctic sediments. *Geochimica et Cosmochimica Acta*, 52(1):217–222.

Verado, D. J., Froelich, P.N. and McIntyre, A. (1990). Determination of organic carbon and nitrogen in marine sediments using the Carlo Erba NA-1500 Analyser. *Deep-Sea Research Part I: Oceanographic Research Papers*, 37(1):157–165.

Versteegh, G. J. M., De Leeuw, J. W., Taricco, C., and Romero, A. (2007). Temperature and productivity influences on $U_{37}^{K'}$ and their possible relation to solar forcing of the Mediterranean winter. *Geochemistry, Geophysics, Geosystems*, 8(9).

Vidic, N. J. and Montanez, I. P. (2004). Climatically driven glacial-interglacial variations in C_3 and C_4 plant proportions on the Chinese Loess Plateau. *Geology*, 32(4):337–340.

Villanueva, L., Damsté, J. S. S., and Schouten, S. (2014). A re-evaluation of the archaeal membrane lipid biosynthetic pathway. *Nature reviews. Microbiology*, 12(6):438–48.

Villanueva, L., Schouten, S., and Sinninghe Damsté, J. S. (2015). Depth-related distribution of a key gene of the tetraether lipid biosynthetic pathway in marine Thaumarchaeota. *Environmental microbiology*, 17(10):3527–3539.

Vincent, E. and Berger, W. H. (1985). Carbon Dioxide and Polar Cooling in the Miocene: The Monterey Hypothesis. In Sundquist, E. and Broecker, W. S., editors, *The Carbon Cycle and Atmospheric CO_2: Natural Variations Archean to Present*. American Geophysical Union, Washington D.C.

Vogts, A., Moossen, H., Rommerskirchen, F., and Rullkötter, J. (2009). Distribution patterns and stable carbon isotopic composition of alkanes and alkan-

1-ols from plant waxes of African rain forest and savanna C_3 species. *Organic Geochemistry*, 40(10):1037–1054.

Vogts, A., Schefuß, E., Badewien, T., and Rullkötter, J. (2012). *n*-Alkane parameters from a deep sea sediment transect off southwest Africa reflect continental vegetation and climate conditions. *Organic Geochemistry*, 47:109–119.

Volkman, J. K. (2006). Lipid biomarkers for marine organic matter. In Volkman, J. K., editor, *Marine Organic Matter: Biomarkers, Isotopes and DNA*, chapter 2, pages 27–70. Springer Berlin Heidelberg, Berlin.

Volkman, J. K., Barrett, S. M., Blackburn, S. I., and Sikes, E. L. (1995). Alkenones in Gephyrocapsa oceanica - Implications for Studies of Paleoclimate. *Geochimica et Cosmochimica Acta*, 59(3):513–520.

Volkman, J. K., Eglington, G., Corner, E. D. S., and Forsberg, T. E. V. (1980). Long chain alkenes and alkenones in the coccolithophorid *Emiliania huxleyi*. *Phytochemistry*, 19(12):2619–2622.

Wakham, S. G., Gagan, M. K., Corrége, T., Schott-Gagan, H., Cowley, J., and Hantoro, W. S. (2003). Archaea mediated anaerobic oxidation of methane in deep euxinic waters of the Black Sea. *Geochimica et Cosmochimica Acta*, 6 7(7):1359–1373.

Wang, L. and Chen, W. (2014). An Intensity Index for the East Asian Winter Monsoon. *Journal of Climate*, 27(6):2361–2374.

Wang, Y., Cheng, H., Lawrence Edwards, R., He, Y., Kong, X., An, Z., Wu, J., Kelly, M. J., Dykoski, C. A., and Li, X. (2005). The Holocene Asian Monsoon: Links to Solar Changes and North Atlantic Climate. *Science*, 308:854–857.

Wang, Y. V., Larsen, T., Leduc, G., Andersen, N., Blanz, T., and Schneider, R. R. (2013). What does leaf wax δD from a mixed C_3/C_4 vegetation region tell us? *Geochimica et Cosmochimica Acta*, 111:128–139.

Warden, L., van der Meer, M. T. J., Moros, M., and Sinninghe Damsté, J. S. (2016). Sedimentary alkenone distributions reflect salinity changes in the Baltic Sea over the Holocene. *Organic Geochemistry*, 102:30–44.

Wei, Y., Wang, J., Liu, J., Dong, L., Li, L., Wang, H., Wang, P., Zhao, M., and Zhang, C. L. (2011). Spatial variations in archaeal lipids of surface water and core-top sediments in the South China Sea and their implications for paleoclimate studies. *Applied and Environmental Microbiology*, 77(21):7479–7489.

Weijers, J. W. H., Schouten, S., Hopmans, E. C., Geenevasen, J. A. J., David, O. R. P., Coleman, J. M., Pancost, R. D., and Sinninghe Damsté, J. S. (2006a). Membrane Lipids of Mesophilic Anaerobic Bacteria Thriving in Peats have Typical Archeal Traits. *Environmental Microbiology*, 8:648–657.

Weijers, J. W. H., Schouten, S., Schefuß, E., Schneider, R. R., and Sinninghe Damsté, J. S. (2009). Disentangling marine, soil and plant organic carbon contributions to continental margin sediments: A multi-proxy approach in a 20,000 year sediment record from the Congo deep-sea fan. *Geochimica et Cosmochimica Acta*, 73(1):119–132.

Weijers, J. W. H., Schouten, S., Spaargaren, O. C., and Sinninghe Damsté, J. S. (2006b). Occurrence and distribution of tetraether membrane lipids in soils; implications for the use of the TEX_{86} proxy and the BIT index. *Organic Geochemistry*, 37(12):1680–1693.

Weijers, J. W. H., Schouten, S., van den Donker, J. C., Hopmans, E. C., and Sinninghe Damsté, J. S. (2007). Environmental controls on bacterial tetraether membrane lipid distribution in soils. *Geochimica et Cosmochimica Acta*, 71(3):703–713.

Weijers, J. W. H., Steinmann, P., Hopmans, E. C., Schouten, S., and Sinninghe Damsté, J. S. (2011). Bacterial tetraether membrane lipids in peat and coal: Testing the MBT-CBT temperature proxy for climate reconstruction. *Organic Geochemistry*, 42(5):477–486.

Weiss, R. F. (1974). Carbon Dioxide in Water and Sea Water: The Solubility of a Non-Ideal Gas. *Marine Chemistry*, 2:203–215.

Werne, J. P., Hollander, D. J., Behrens, A., Schaeffer, P., Albrecht, P., and Sinninghe Damsté, J. S. (2000). Timing of early diagenetic sulfurization of

organic matter: A precursor-product relationship in Holocene sediments of the anoxic Cariaco Basin, Venezuela. *Geochimica et Cosmochimica Acta*, 64(10):1741–1751.

Werner, R. A. and Brand, W. A. (2001). Referencing strategies and techniques in stable isotope ratio analysis. *Rapid Communications in Mass Spectrometry*, 15(7):501–519.

Whiticar, M. J. (1999). Carbon and hydrogen isotope systematics of bacterial formation and oxidation of methane. *Chemical Geology*, 161:291–314.

Wong, W. W. and Sackett, W. M. (1978). Fractionation of stable carbon isotopes by marine phytoplankton. *Geochimica et Cosmochimica Acta*, 42(12):1809–1815.

Woodruff, F., Savin, S. M., and Douglas, R. G. (1981). Miocene stable isotope record: a detailed deep Pacific Ocean study and its paleoclimatic implications. *Science*, 212:665–668.

Woodward, F. I. (1987). Stomatal numbers are sensitive to increases in CO_2 from pre-industrial levels. *Nature*, 327:617–618.

Wu, L., Cai, W., Zhang, L., Nakamura, H., Timmermann, A., Joyce, T., McPhaden, M. J., Alexander, M., Qiu, B., Visbeck, M., Chang, P., and Giese, B. (2012). Enhanced warming over the global subtropical western boundary currents. *Nature Climate Change*, 2(3):161–166.

Wuchter, C., Schouten, S., Wakeham, S. G., and Damsté, J. S. S. (2006). Archaeal tetraether membrane lipid fluxes in the northeastern Pacific and the Arabian Sea: Implications for TEX_{86} paleothermometry. *Paleoceanography*, 21(4).

Wuchter, C., Schouten, S., Wakeham, S. G., and Sinninghe Damsté, J. S. (2005). Temporal and spatial variation in tetraether membrane lipids of marine Crenarchaeota in particulate organic matter: Implications for TEX_{86} paleothermometry. *Paleoceanography*, 20(3).

Xia, D., Jia, J., Li, G., Zhao, S., Wei, H., and Chen, F. (2014). Out-of-phase evolution between summer and winter East Asian monsoons during the Holocene as recorded by Chinese loess deposits. *Quaternary Research*, 81(3):500–507.

Xing, L., Zhang, R., Liu, Y., Zhao, X., Liu, S., Shi, X., and Zhao, M. (2011). Biomarker records of phytoplankton productivity and community structure changes in the Japan Sea over the last 166 kyr. *Quaternary Science Reviews*, 30(19-20):2666–2675.

Xu, S., Ye, Q., Li, S., Somerville, I., Feng, H., Tang, Z., Shu, D., and Bi, H. (2016). Sequential patterns in Cenozoic marginal basins of the Northwest Pacific. *Geological Journal*, 51:387–415.

Xu, Y., Li, J., Yue, L., Jiang, J., Sun, F., and Zhang, L. (2015). Grain-size characteristics of red clay deposits on the eastern edge of Chinese Loess

Plateau and its implications for Neogene evolution of East Asian winter monsoon. *Environmental Earth Sciences*, 73(11):7445–7456.

Yamada, K. and Ishiwatari, R. (1999). Carbon isotopic compositions of long-chain *n*-alkanes in the Japan Sea sediments: implications for paleoenvironmental changes over the past 85 kyr. *Organic Geochemistry*, 30(5):367–377.

Yamada, K., Ishizaka, J., and Nagata, H. (2005). Spatial and temporal variability of satellite primary production in the Japan Sea from 1998 to 2002. *Journal of Oceanography*, 61(5):857–869.

Yamamoto, M., Shimamoto, A., Fukuhara, T., Naraoka, H., Tanaka, Y., and Nishimura, A. (2007). Seasonal and depth variations in molecular and isotopic alkenone composition of sinking particles from the western North Pacific. *Deep-Sea Research Part I: Oceanographic Research Papers*, 54(9):1571–1592.

Yamamoto, M., Shimamoto, A., Fukuhara, T., Tanaka, Y., and Ishizaka, J. (2012). Glycerol dialkyl glycerol tetraethers and TEX_{86} index in sinking particles in the western North Pacific. *Organic Geochemistry*, 53:52–62.

Yamamoto, M. and Watanabe, Y. (1995). Molecular geochemical approach to the paleoceanographic assessment of Neogene sediments of Yashima area, Akita Basin, Japan. *Journal of the Japanese Association for Petroleum Technology*, 60(1):27–38.

Yamamoto, S., Kawamura, K., and Seki, O. (2011). Long-range atmospheric transport of terrestrial biomarkers by the Asian winter monsoon: Evidence from fresh snow from Sapporo, northern Japan. *Atmospheric Environment*, 45(21):3553–3560.

Yamano, H., Sugihara, K., and Nomura, K. (2011). Rapid poleward range expansion of tropical reef corals in response to rising sea surface temperatures. *Geophysical Research Letters*, 38(4).

Yang, H., Lohmann, G., Wei, W., Dima, M., Ionita, M., and Liu, J. (2016). Intensification and poleward shift of subtropical western boundary currents in a warming climate. *Journal of Geophysical Research: Oceans*, 121(7):4928–4945.

Yeh, S.-W., Park, Y.-G., Min, H., Kim, C.-H., and Lee, J.-H. (2010). Analysis of characteristics in the sea surface temperature variability in the East/Japan Sea. *Progress in Oceanography*, 85:213–223.

You, Y., Huber, M., Müller, R. D., Poulsen, J., and Ribbe, J. (2009). Simulation of the Middle Miocene Climate Optimum. *Geophysical Research Letters*, 36(4).

Zachos, J., Pagani, M., Sloan, L., Thomas, E., and Billups, K. (2001). Trends, Rhythms, and Aberrations in Global Climate 65 Ma to Present. *Science*, 292:686–693.

Zachos, J. C., Dickens, G. R., and Zeebe, R. E. (2008). An early Cenozoic perspective on greenhouse warming and carbon-cycle dynamics. *Nature*, 451:279–283.

Zafiriou, O. C., Gagosian, R. B., Peltzer, E. T., Alford, J. B., and Loder, T. (1985). Air-to-sea fluxes of lipids at Enewetak Atoll. *Journal of Geophysical Research: Atmospheres*, 90:2409–2423.

Zhang, J., Wu, Y., Jennerjahn, T. C., Ittekkot, V., and He, Q. (2007). Distribution of organic matter in the Changjiang (Yangtze River) Estuary and their stable carbon and nitrogen isotopic ratios: Implications for source discrimination and sedimentary dynamics. *Marine Chemistry*, 106:111–126.

Zhang, X., Xu, B., Günther, F., Mügler, I., Lange, M., Zhao, H., Li, J., and Gleixner, G. (2017). Hydrogen isotope ratios of terrestrial leaf wax *n*-alkanes from the Tibetan Plateau: Controls on apparent enrichment factors, effect of vapor sources and implication for altimetry. *Geochimica et Cosmochimica Acta*, 211:10–27.

Zhang, Y. G., Pagani, M., and Liu, Z. (2014). A 12-Million-Year Temperature History of the Tropical Pacific Ocean. *Science*, 344:84–87.

Zhang, Y. G., Pagani, M., Liu, Z., Bohaty, S. M., and Deconto, R. (2013). A 40-million-year history of atmospheric CO_2. *Philosophical transactions. Series A, Mathematical, Physical, and Engineering Sciences*, 371.

Zhang, Y. G., Pagani, M., and Wang, Z. (2016). Ring Index: A new strategy to evaluate the integrity of TEX_{86} paleothermometry. *Paleoceanography*, 31(2):220–232.

Zhang, Y. G., Zhang, C. L., Liu, X. L., Li, L., Hinrichs, K. U., and Noakes, J. E. (2011). Methane Index: A tetraether archaeal lipid biomarker indicator for detecting the instability of marine gas hydrates. *Earth and Planetary Science Letters*, 307(3-4):525–534.

Zhang, Z., Zhao, M., Lu, H., and Faiia, A. M. (2003). Lower temperature as the main cause of C_4 plant declines during the glacial periods on the Chinese Loess Plateau. *Earth and Planetary Science Letters*, 214:467–481.

Zhu, C., Wakeham, S. G., Elling, F. J., Basse, A., Mollenhauer, G., Versteegh, G. J., Könneke, M., and Hinrichs, K. U. (2016). Stratification of archaeal membrane lipids in the ocean and implications for adaptation and chemotaxonomy of planktonic archaea. *Environmental Microbiology*, 18(12):4324–4336.

Zhu, C., Weijers, J. W. H., Wagner, T., Pan, J.-M., Chen, J.-F., and Pancost, R. D. (2011). Sources and distributions of tetraether lipids in surface sediments across a large river-dominated continental margin. *Organic Geochemistry*, 42(4):376–386.

Zhuang, G., Brandon, M. T., Pagani, M., and Krishnan, S. (2014). Leaf wax

stable isotopes from Northern Tibetan Plateau: Implications for uplift and climate since 15 Ma. *Earth and Planetary Science Letters*, 390:186–198.

Zou, J., Shi, X., Liu, Y., Liu, J., Selvaraj, K., and Kao, S. J. (2012). Reconstruction of environmental changes using a multi-proxy approach in the Ulleung Basin (Sea of Japan) over the last 48 ka. *Journal of Quaternary Science*, 27(9):891–900.

A. Mass Spectra of triterpenoids

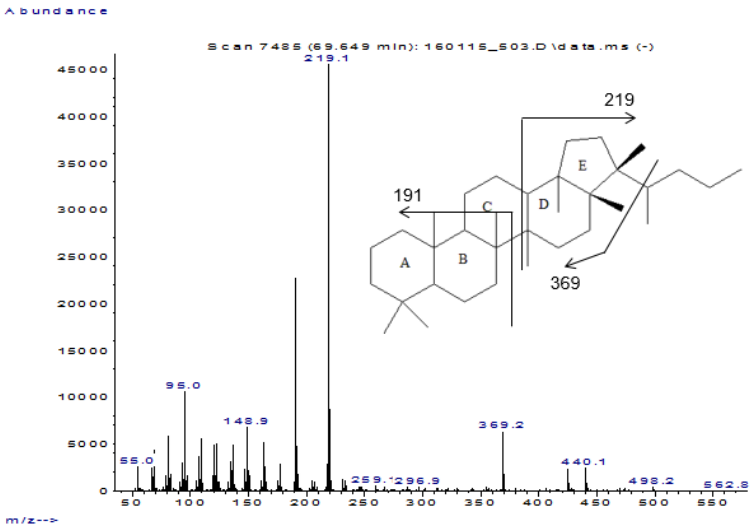

Figure A.1.: C_{32} 17β,21β hopane [17β(H),21β(H)-bishomohopane]. Sample U1425D-39H-1W, 145–147 cm.

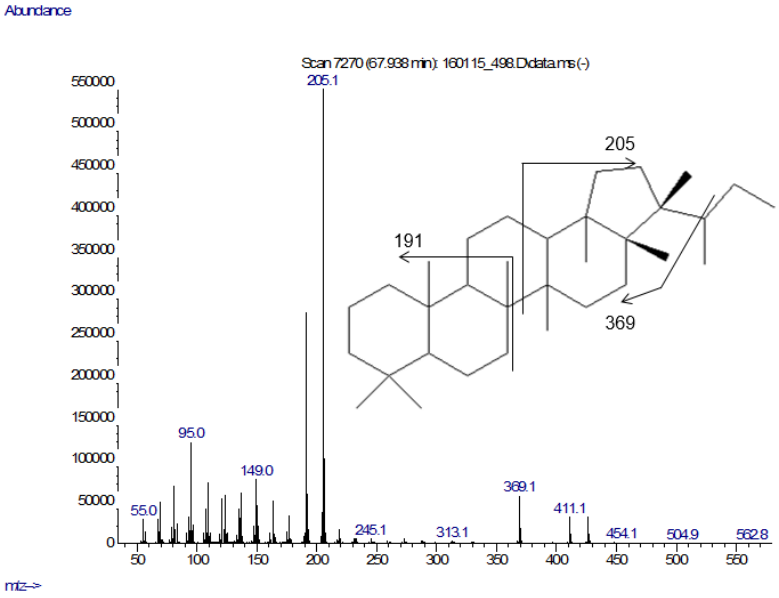

Figure A.2.: C_{31} 17β,21β hopane[17β(H),21β(H)-homohopane]. Sample U1425D-28H-4W, 45–47 cm.

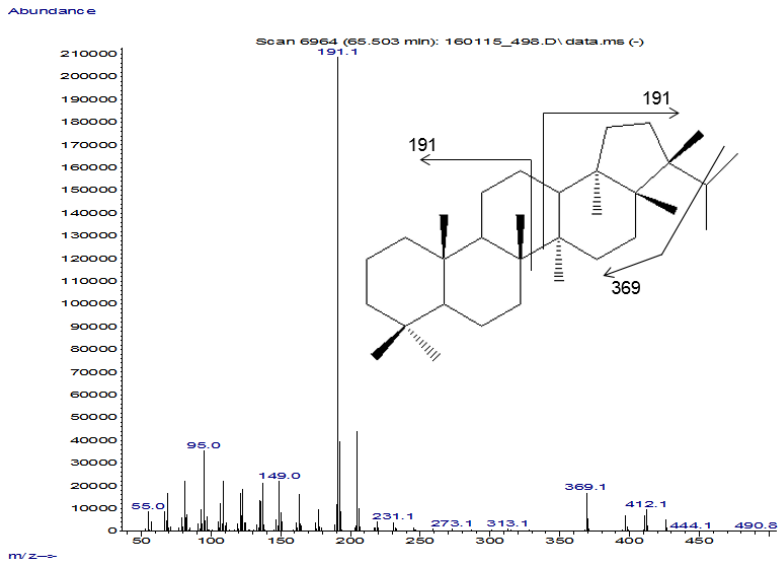

Figure A.3.: C_{30} 17β,21β hopane [17β(H),21β(H)-hopane]. Sample U1425D-28H-4W, 45–47 cm.

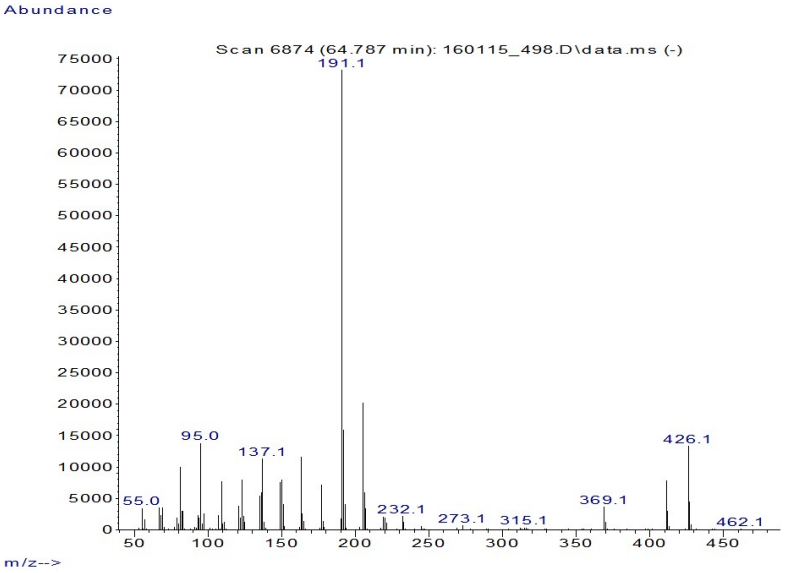

Figure A.4.: C_{31} 17α,21β hopane [17α(H),21β(H)-homohopane]. Sample U1425D-28H-4W, 45–47 cm.

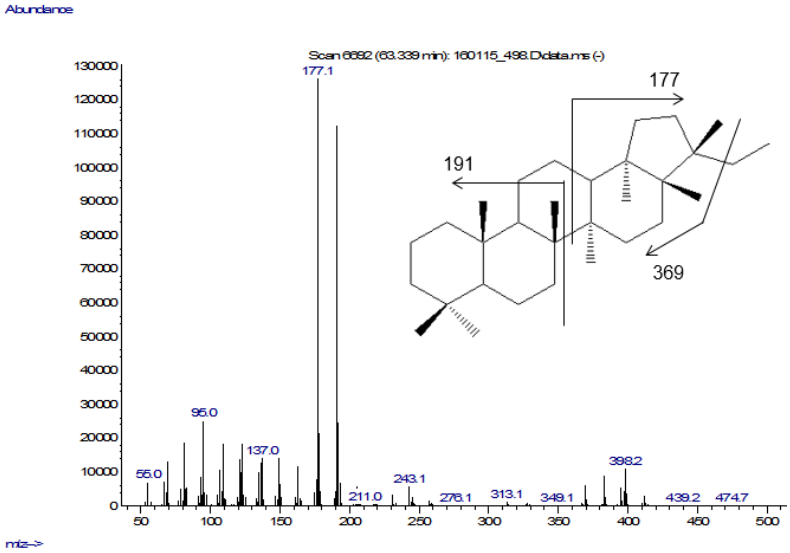

Figure A.5.: C_{29} 17β,21β hopane [17β(H),21β(H)-hopane]. Sample U1425D-28H-4W, 45–47 cm.

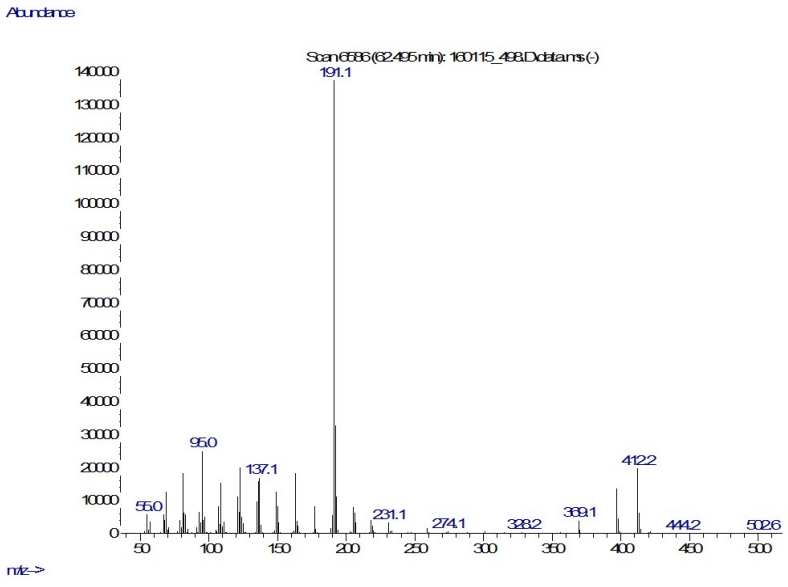

Figure A.6.: C_{30} 17α,21β hopane [17α(H),21β(H)-hopane]. Sample U1425D-28H-4W, 45–47 cm.

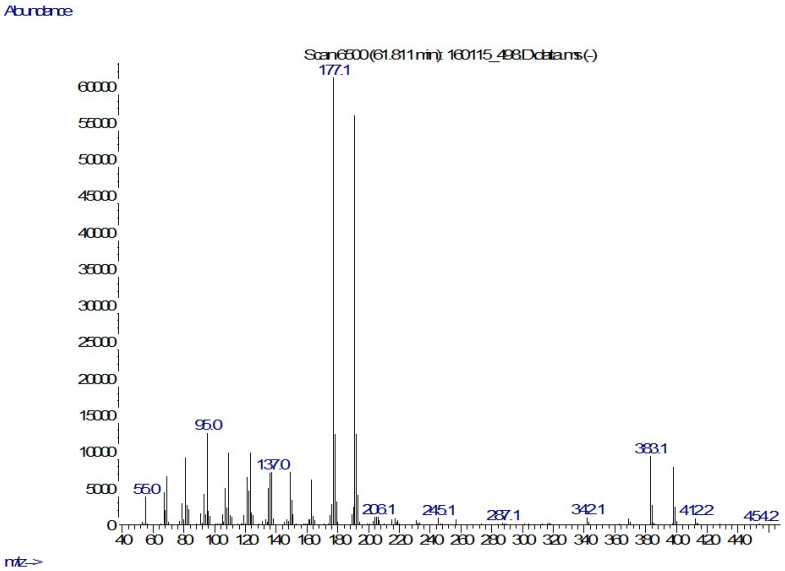

Figure A.7.: C_{29} 17β,21α hopane [17β(H),21α(H)-hopane]. Sample U1425D-28H-4W, 45–47 cm.

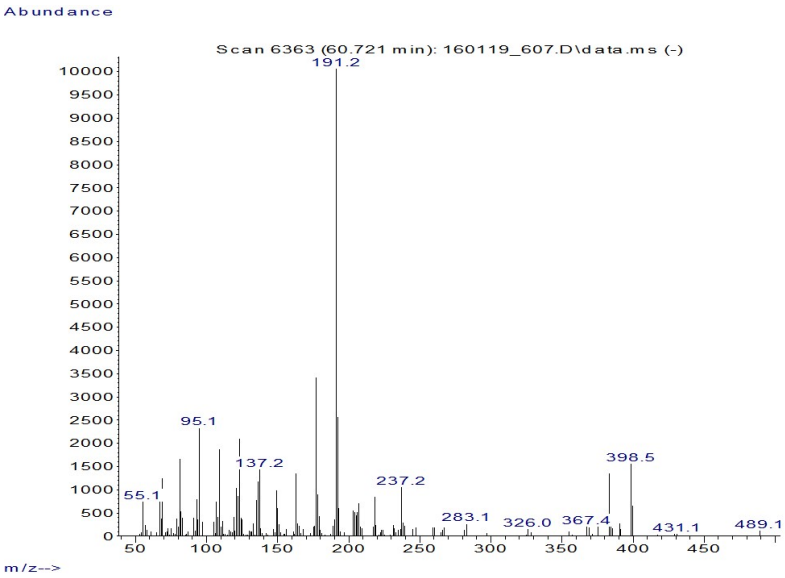

Figure A.8.: C_{29} 17α,21β hopane [17α(H),21β(H)-hopane]. Sample U1425D-6H-4W, 17–19 cm.

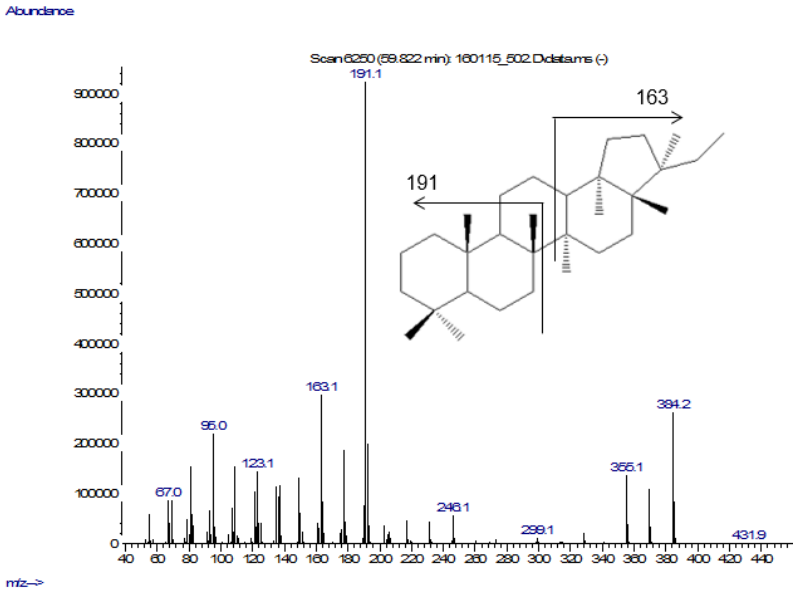

Figure A.9.: C_{28} 17β,21α hopane [17β(H),21α(H)-dinorhopane]. Sample U1425D-52H-1W, 65–67 cm.

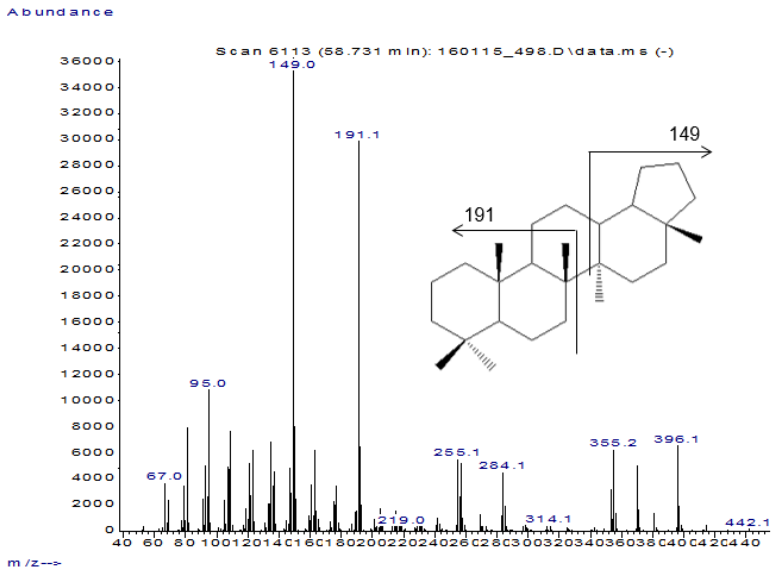

Figure A.10.: C_{27} 17β hopane [17β(H),21α(H)-trinorhopane]. Sample U1425D-28H-4W, 45–47 cm.

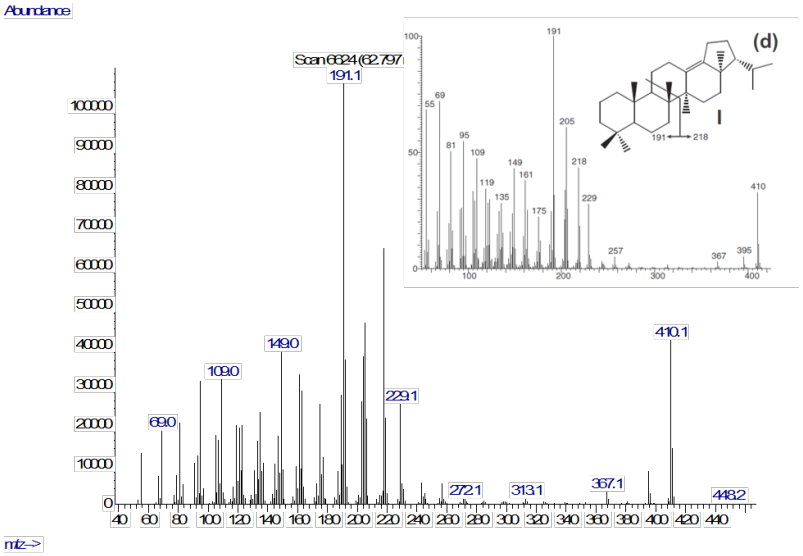

Figure A.11.: C_{30} $\Delta^{13(18)}$ hopene [neohop-13(18)-ene]. Spectrum from Sinninghe Damsté et al. (2014). Sample U1425D-28H-4W, 45–47 cm.

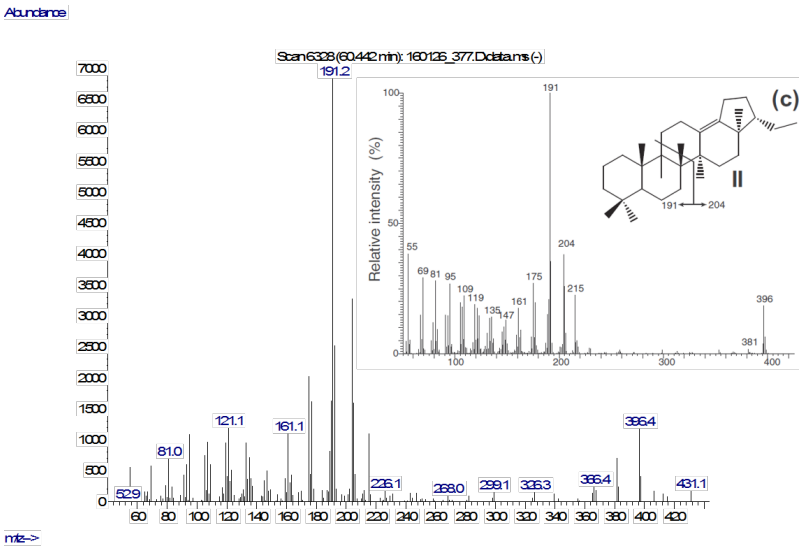

Figure A.12.: C_{29} $\Delta^{13(18)}$ hopene [30-norneohop-13(18)-ene]. Spectrum from Sinninghe Damsté et al. (2014). Sample 797B-41X-2W, 6–8 cm.

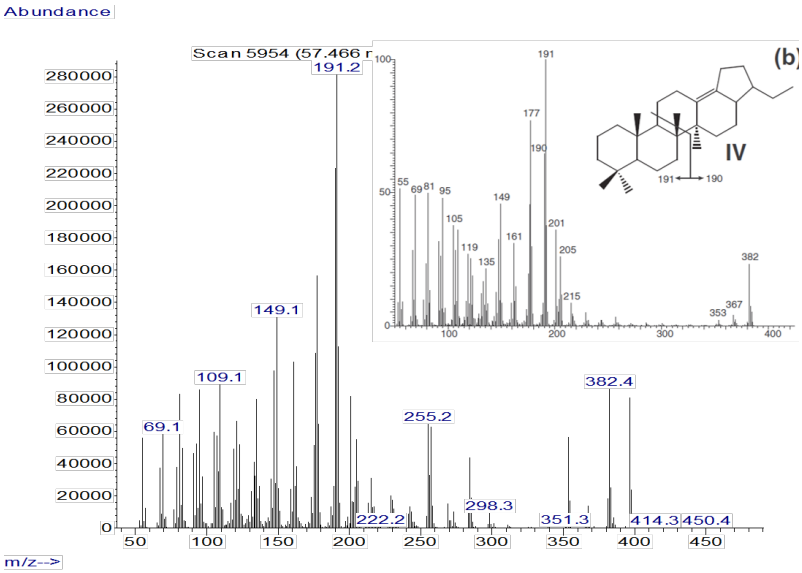

Figure A.13.: C_{28} $\Delta^{13(18)}$hopene [28,30-dinorneohop-13(18)-ene]. Spectrum from Sinninghe Damsté et al. (2014). Sample U1425D-57H-1W.

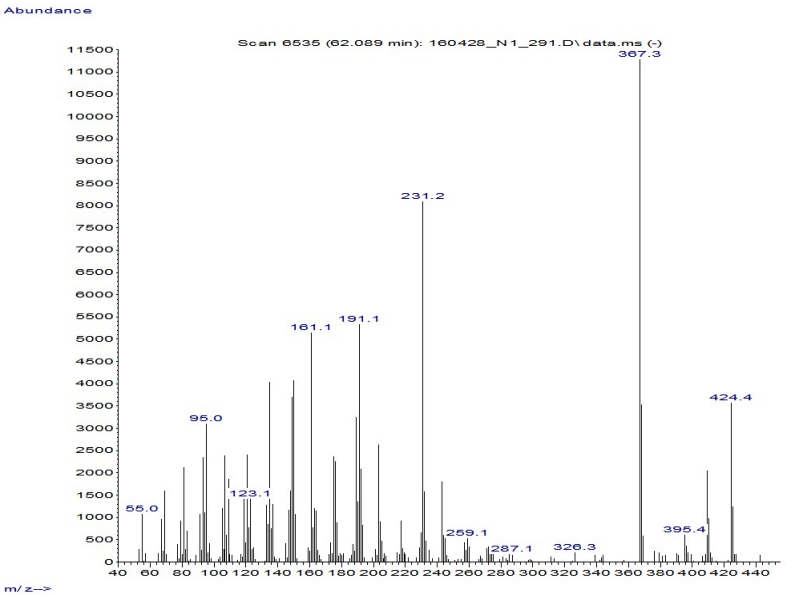

Figure A.14.: C_{31} $\Delta^{13(18)}$ hopene [homohop-17(21)-ene]. Sample U1425B-61X-1W.

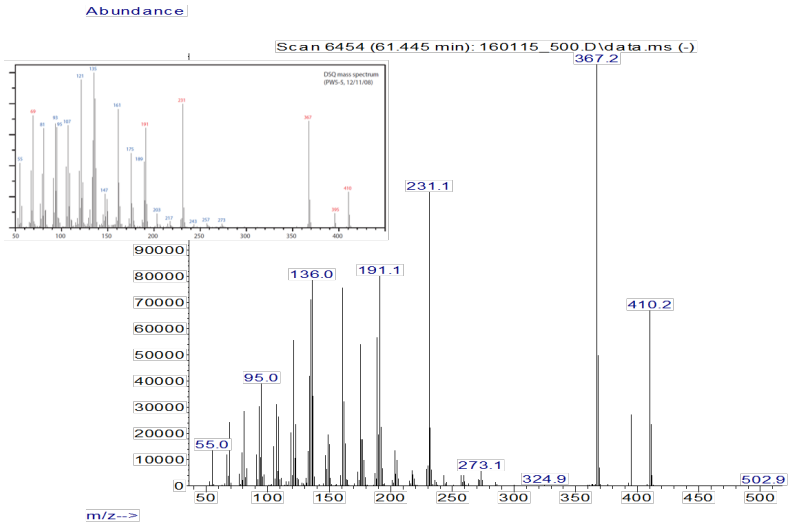

Figure A.15.: C_{30} $\Delta^{13(18)}$ hopene [hop-17(21)-ene], spectrum from (Sessions et al. 2013; SI). Sample U1425D-32H-2W, 123–125 cm.

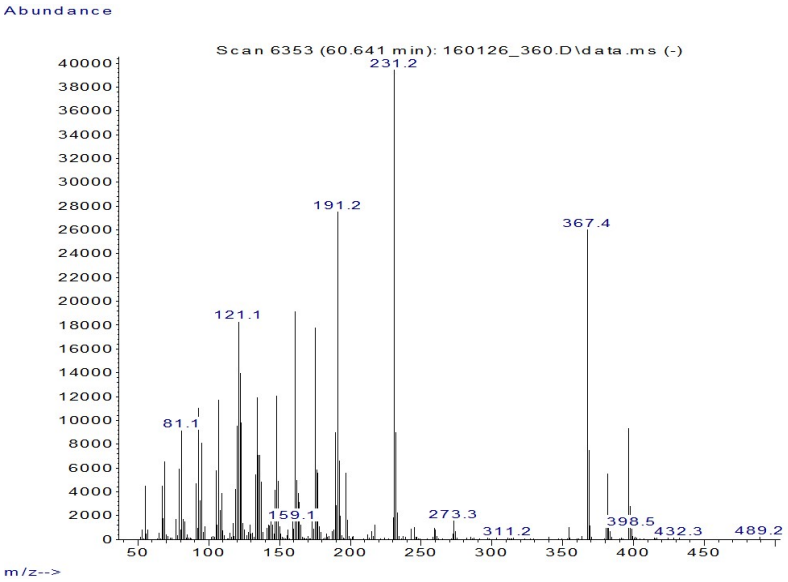

Figure A.16.: C_{29} $\Delta^{13(18)}$ hopene [30-norhop-17(21)-ene]. Sample U797B-37X-1W, 50–52 cm.

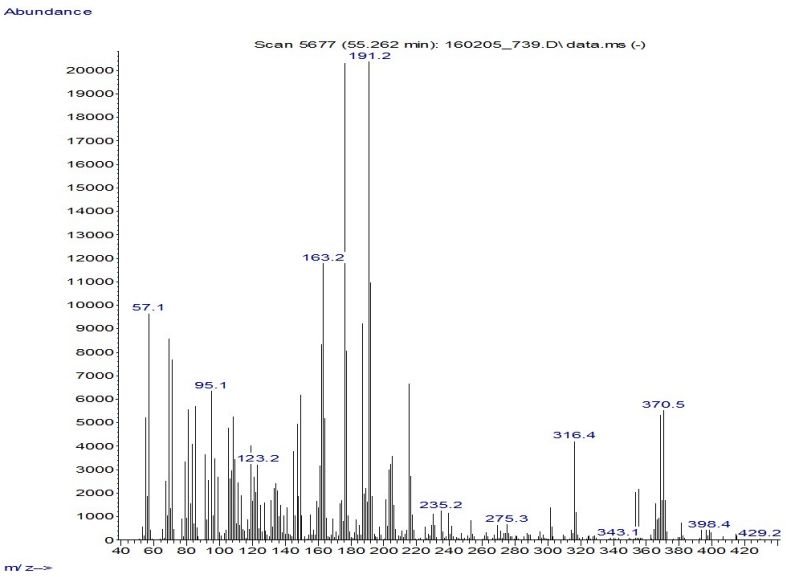

Figure A.17.: C_{27} $\Delta^{17(21)}$ hopene [22,29,30-trisnorneohop-17(21)-ene], based on RT from Nytoft and Larsen (2001). Sample U1425D-46H-3W, 95–97 cm.

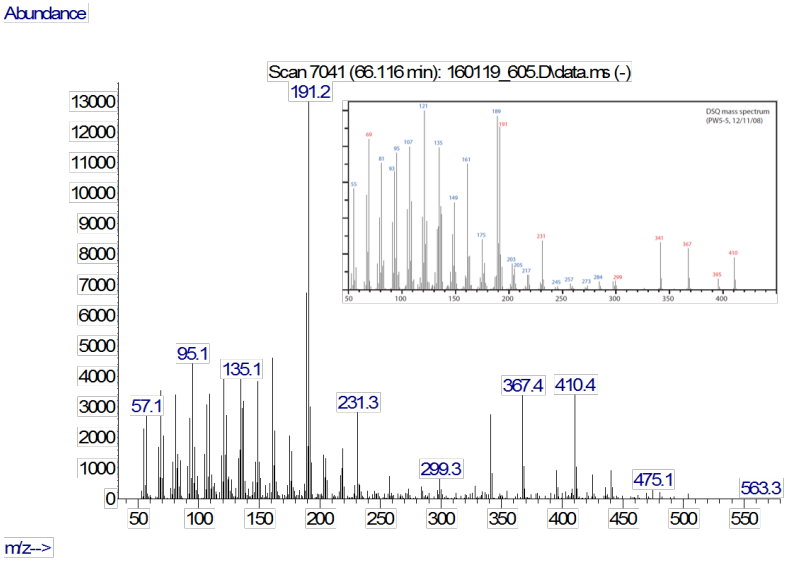

Figure A.18.: C_{30} Δ^{21} hopene [hop-21-ene], spectrum from Sessions et al. (2013; SI). Sample U1425D-1H-1W, 18–20 cm.

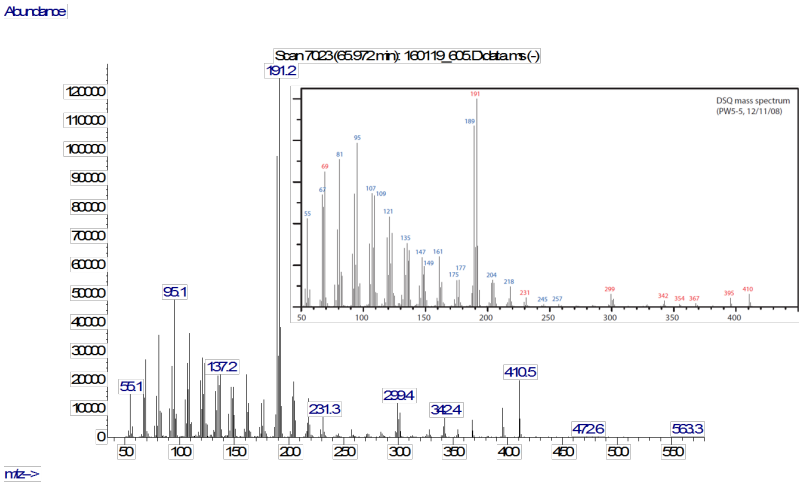

Figure A.19.: C_{30} $\Delta^{22(29)}$ hopene [hop-22(29)-ene], spectrum from Sessions et al. (2013; SI). Sample U1425D-1H-1W, 18–20 cm.

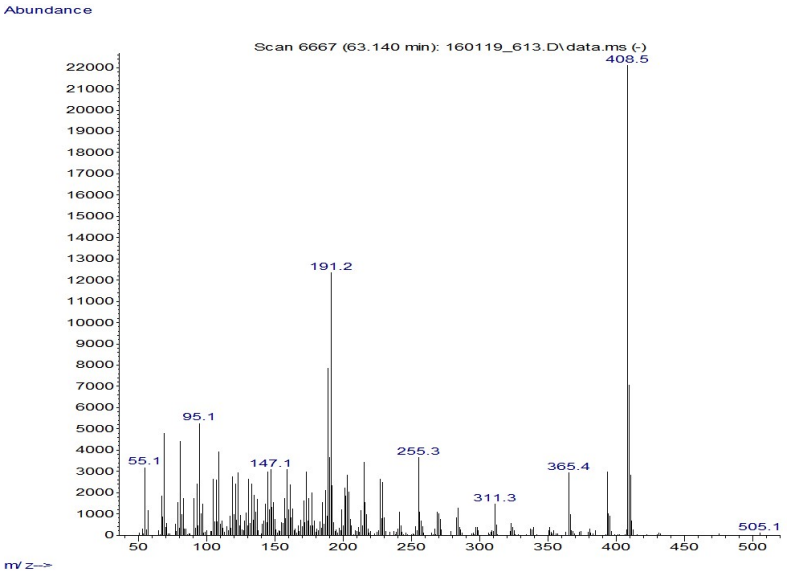

Figure A.20.: C_{30} ββ-hopadiene. Sample U1425D-7H-3W, 23–25 cm.

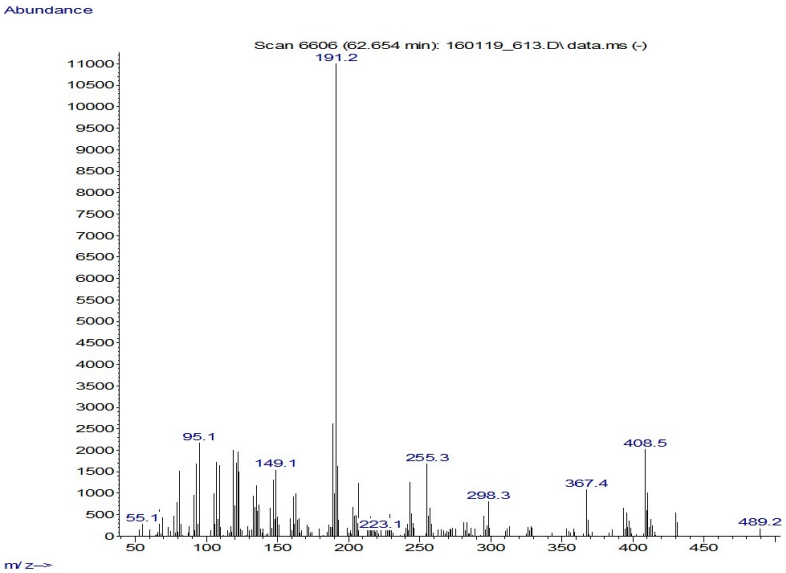

Figure A.21.: C_{30} βα-hopadiene. Sample U1425D-7H-3W, 23–25 cm.

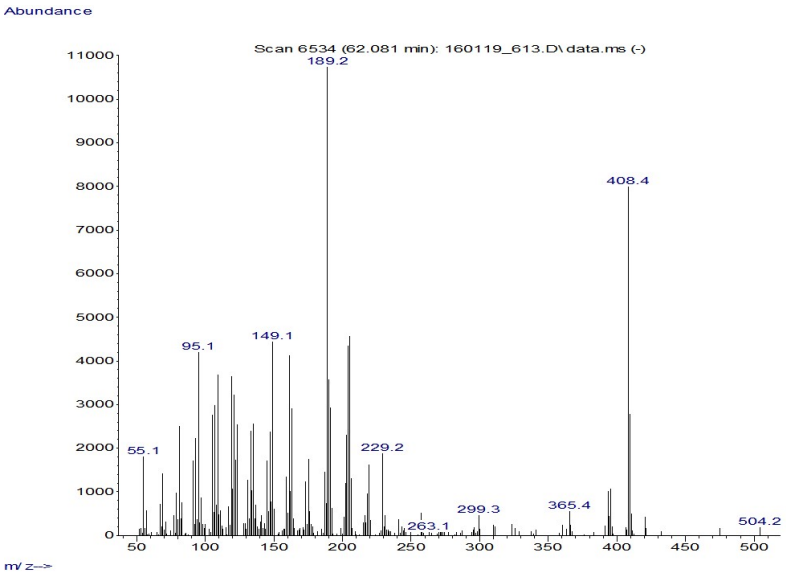

Figure A.22.: C_{30} αβ-hopadiene. Sample U1425D-7H-3W, 23–25 cm.

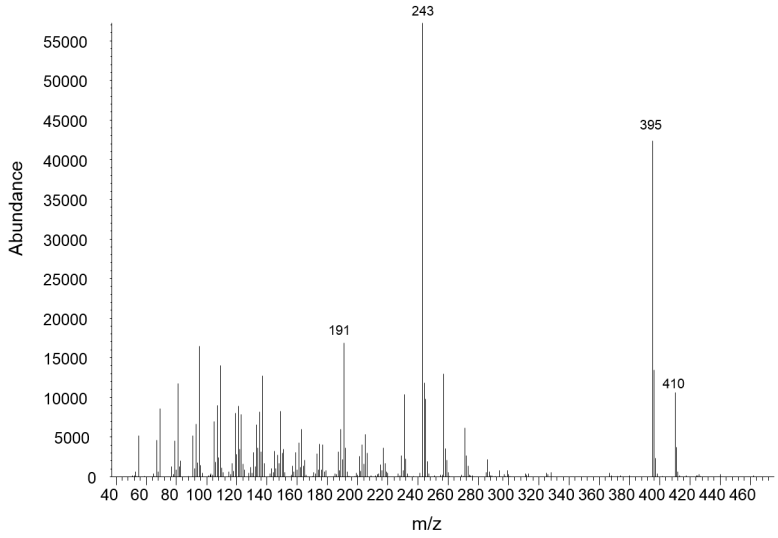

Figure A.23.: Fern-7-ene. Sample U1425D-41H-2W, 127–128 cm.

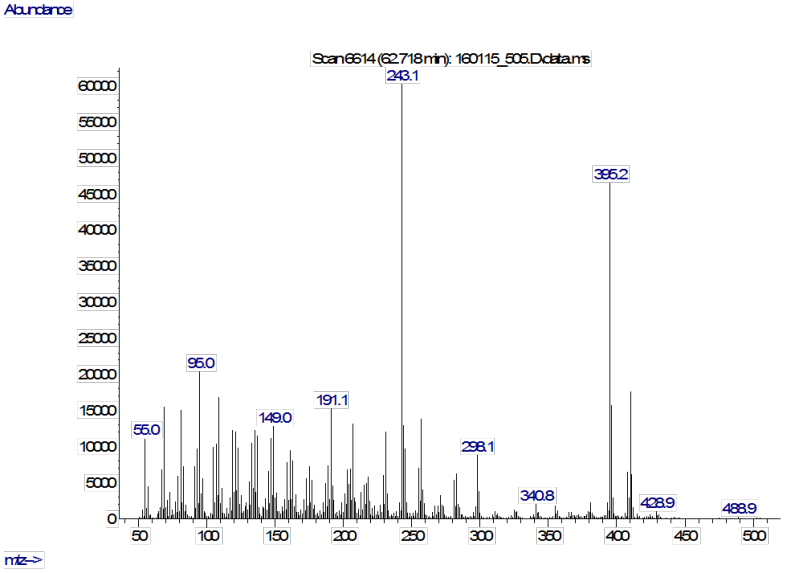

Figure A.24.: Fern-8-ene. Sample U1425D-41H-2W, 127–128 cm.

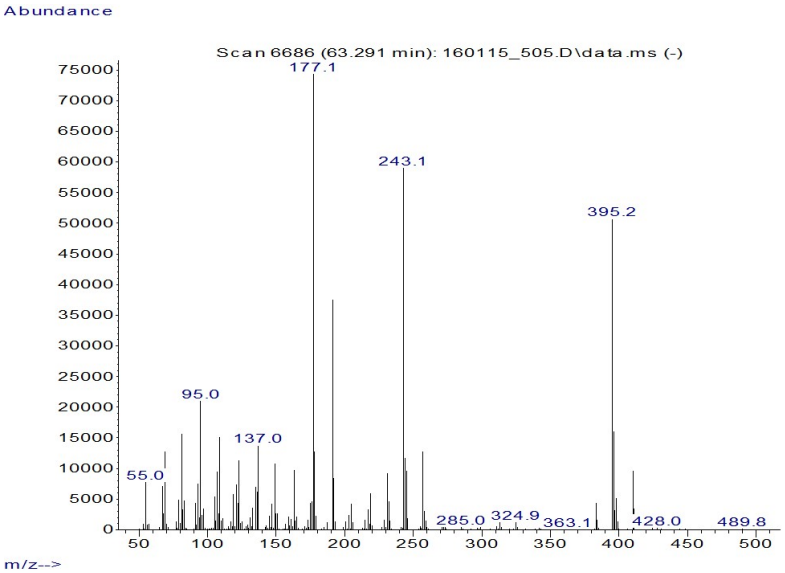

Figure A.25.: Sample U1425D-41H-2W, 127–128 cm.